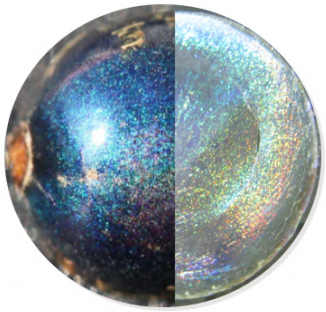

Structural Colour in Fruits

Rox MIDDLETON

Doctoral Thesis
University of Cambridge
St John's College

Submitted: *September 28th 2018*
Supervisor: Dr. Silvia VIGNOLINI

Abstract

Structural Colour in Fruits

Rox MIDDLETON

Structural colour arises from the constructive interference of light with a material structured on a lengthscale corresponding to optical wavelengths. This phenomenon is responsible for the appearance of many of the brightest colours in nature and recently the existence of structural colouration in plants has been demonstrated across multiple species. This thesis extends our understanding of the effect specifically in fruit epidermal tissues, it uses the physical principles underlying structural colour to understand biological development and it extracts design ideas from biological tissues to enhance the optical response of biomimetic materials.

In more detail, this thesis reports the optical characteristics and architecture of structural colour in several fruits of the genera *Pollia* and *Viburnum*. Previous work showed that the external cells of *Pollia condensata* fruits have extremely thick cell walls which act as photonic crystals to reflect circular polarised light. Here, the spectral and morphological characteristics of photonic cell walls in this and three other *Pollia* species are reported and it is shown that the unusual right handed circular polarisation reflection is apparent in only *P. condensata*. It is also shown that the occurrence of right circular polarisation is associated with longer wavelength reflection. This thesis extends this analysis by demonstrating the use of structural colour to observe the development of thickened cell walls in *Pollia condensata* and *Pollia japonica* using optical microscopy. It is shown that during development, cell wall material is built up gradually and with a fixed structural periodicity in both species, and that significant cell wall growth occurs in the earliest stages of the long fruit maturation period. In the other genus investigated, structural colour analysis is extended to the fruits of *Viburnum tinus* and *Viburnum davidii*, and found to arise from layers of globular vesicles in the specialised cell wall. Inspired by these studies, a novel templating technique for reflective self-assembled cellulose nanocrystal films is described, which mimics the morphology of *Pollia* cells by successfully introducing a curvature in the photonic multilayer whilst maintaining its optical response. Enhancement of the angular independence of light reflected from this curved surface is demonstrated.

Declaration

- This dissertation is the result of my own work and includes nothing which is the outcome of work done in collaboration except as clearly specified in the text.
- It is not substantially the same as any that I have submitted, or, is being concurrently submitted for a degree or diploma or other qualification at the University of Cambridge or any other University or similar institution. I further state that no substantial part of my dissertation has already been submitted, or, is being concurrently submitted for any such degree, diploma or other qualification at the University of Cambridge or any other University or similar institution.
- It does not exceed 60,000 words, including summary/abstract, tables, footnotes and appendices.

Dr Holly Middleton and Dr Dorothy Collins

Acknowledgements

I would like to acknowledge the help of my supervisor Silvia Vignolini and thank her for training, inspiration and support.
I'd also like to acknowledge the help of Edwige Moyroud, Paula Rudall, Bonan Zhu, Miranda Sinnott-Armstrong, Richard Parker, Yu Ogawa, Rebecca Karanja and Beverley Glover who contributed scientifically to the projects presented in this thesis as specified in the text, and the biophotonics research community whose work has motivated me.
I'm very grateful to the publicly funded EPSRC for my stipend which allowed me the opportunity to carry out this research, the experience of which has been invaluable to me and I have really enjoyed. Also the Cambridge Philosophical Society and Silvia Vignolini for additional funding.
I would like to thank Gen Kamita, Giulia Guidetti and Villads Johansen for their help in the lab and Julia Spindel, Sandra Cortijo, Olimpia Onelli, Giulia Guidetti, Bruno Frka-Petešić and especially Richard Parker, Beverley Glover and Silvia Vignolini for helpful reading and feedback on earlier drafts of this thesis.
I'd like to thank all the members of the Bio Inspired Photonics group for support, particularly those mentioned above and also Lisa, Cyan, Alyssa and Katie.
I'd like to thank all the above for their friendship, as well as many other inspirational people: Lucy and Aisha, Carmen, Chess and Jess, Ciaran and Douglas, Wilf and Leo, my parents and past & present members of the CGIS, Gangu, CYL & Market Labour, NanoDTC c2013, CUCU, FoFF, Senrab Col. and Ebbisham, the Pit and 111 King St.
In relation to the completion of this manuscript I would particularly like to thank Ellen Pilsworth and Máire Ní Leathlobhair.

Additional Work and Publications

The research reported in this thesis was carried out entirely with the Bio Inspired Photonics group in the Department of Chemistry at the University of Cambridge, except for the fieldwork with Dr Rebecca Karanja at the Kakamega Forest National Reserve and the National Museum of Kenya described in chapter 2. The opportunity to carry out this fieldwork was extremely valuable, and was made possible by the grant awarded by the ALBORADA research fund to carry out the research. Zeiss also supported this work by the donation of a microscope.[1] The collaboration with Dr Rebecca Karanja improved the ecological understanding and Dr Silvia Vignolini supported the advancement of the collaboration. Without the establishment of this collaboration, the developmental work on *P. condensata* in chapter 4 would not have been possible.

The work presented represents a significant amount of the research I carried out between October 2014 - October 2018. Beyond the subjects presented here, I have also contributed to work on other projects which are largely not included in this thesis. Some of this work has resulted in publications. Publications during my PhD are detailed below because my other work has been relevant to the formation of my ideas either in technique development, themes or in some cases the topics explored in the text.

Publications during doctoral research

- JPH Rivett, LZ Tan, MB Price, S Bourelle, NJLK Davis, Z Xiao, Y Zou, **R Middleton**, B Sun, AM Rappe, D Credgington, F Deschler. Long-lived polarization memory in the electronic states of lead-halide perovskites from local structural dynamics, *Nature Communications* (2018) 9, 3531 (DOI: 10.1038/s41467-018-06009-3)

  We found that photo-excited charge carriers in perovskite crystals maintain an initial polarization anisotropy for several picoseconds, independent of crystallite size and composition. Understanding the principles of perovskite crystal charge carriers is crucial to the development of high performance photovoltaic

cells. I contributed polarisation and optical microscopy analysis of the steady state devices in order to assess the device isotropy.

- **R Middleton**, X Li, J Shepherd, Z Li, W Wang, SM Best, RE Cameron, YYS Huang. Near-field Electrospinning Patterning Polycaprolactone and Polycaprolactone/Collagen Interconnected Fiber Membrane, *Macromolecular Materials and Engineering* (2018) 303, 1700463, (DOI:10.1002/mame.201700463)

  We showed the successful rapid production of large scale ultra-fine spatially controlled and interlinked mesh made via near-field electrospinning of polymer-biopolymer composite fibres. The composite was shown to be well integrated and the mesh mechanically robust and promising for application in tissue scaffolding. I carried out all the fabrication of solution and mesh, the optical and confocal analysis and the stress-testing reported. As first author I wrote the majority of the paper.

- E Moyroud, T Wenzel, **R Middleton**, PJ Rudall, H Banks, A Reed, G Mellers, P Killoran, MM Westwod, U Steiner, S Vignolini, BJ Glover. Disorder in convergent floral nanostructures enhances signaling to bees, *Nature* (2017) 550, 469, (DOI:10.1038/nature24285)

  We showed that a disordered striation pattern on the surface of flower petals across most angiosperm lineages produces a wide angle structurally coloured blue reflection or blue halo. An artificial model of this disordered striation was demonstrated to enhance bee foraging with respect to both perfectly ordered striations and flat surfaces. The work comprises optical and morphological assessment of petal surfaces, production of artificial floral mimics and bee behaviour studies. I performed all the optical analysis of floral and artificial samples that is presented in the paper using angular resolved spectroscopy. This represents a significant body of work, and the largest section of work which I have chosen not to report in this thesis, although some results are reported in chapter 2.

- BD Wilts, AG Dumanli, **R Middleton**, P Vukusic, S Vignolini. Chiral Optics of helicoidal cellulose nanocrystal films, *APL Photonics* (2017) 2, 040801, (DOI: 10.1063/1.4978387)

  We reported the optical characterisation of self-assembled cellulose nanocrystal films displaying structural colour. Within this work, I contributed angular resolved spectroscopy which showed strong angular dependence in the wavelength reflected from the film. This is relevant to the work on enhancing the structure and optical response of these films in chapter 6.

- **R Middleton**, U Steiner, S Vignolini. Bio-Inspired Polymers ch.17 Bio-mimetic Structural Colour using Biopolymers(2016), 555-585, (DOI: 10.1039/9781782626664-00555)

I contributed a chapter to the book Bio-Inspired polymers. This is a review focused on self-assembled polymers, particularly cellulose nanocrystals and the use of its helicoidal structure to develop structurally coloured pigments. The chapter offers a similar introduction to the optical theory which is produced here in chapter 1 although it constitutes a distinct work. The publication is also relevant to chapter 6. I wrote this chapter with additions and contributed sections from the senior co-authors.

Publications in Preparation

Since the completion of this thesis, work in chapters 5 and 6 has been completed and prepared for publication in the following articles.

- **R. Middleton**, T. Zhao, R. Qi, A. Taylor, R. M. Parker, C. A. Williams, S. Guldin, S. Vignolini. Bio-inspired hierarchical structure of cellulose nanocrystal films for pigment application. *(Expected submission date November 2018.)*

  We show that using a hemispheric array inspired by fruit cell morphology, angular independence of structural colour is enhanced in cellulose nanocrystal films, making it a suitable technique for the production of biocompatible structurally coloured films. Work in collaboration has recently produced results which make use of the enhanced angular reflection reported in chapter 6 while suppressing extraneous reflection, extending the report in this thesis from biomimesis to macroscale appearance. I developed the morphology and the technique through the work reported in chapter 6 and produced templates for patterning. I optically characterised the work we will present.

- **R. Middleton**, M. Sinnott-Armstrong, Y. Ogawa, G. Iacucci, P. Rudall, E. Moyroud, B. Glover, M. Donoghue, S. Vignolini. Lipid-cellulose Matrix Generates Structural Colour in *Viburnum tinus*. *(Expected submission date November 2018)*

  Structural colour is observed in the fruit of a common species. The optical response is analysed and correlated to the material nanostructure which is responsible for its reflection. This publication will report the results in chapter 5.

- **R. Middleton**, E. Moyroud, P. Rudall, B. Glover, S. Vignolini. Observation of incremental cellulose cell wall growth via structural colour analysis. *(Expected submission date December 2018)*

  Cell wall development is observed in vivo in the fruits of structurally coloured species. This publication will report the results of chapter 2.

Contents

List of Abbreviations

CNC	Cellulose Nanocrystal
DI	De-Ionised (water)
FDTD	Finite Difference Time Domain
L	Left (circular handedness)
NA	Numerical Aperture
R	Right (circular handedness)
SEM	Scanning Electron Microscopy
SWA	Scalar Wave Approximation
TEM	Transmission Electron Microscopy
um	10^{-6} m
wt%	Weight Percent

Chapter 1

Optics of Helicoidal Materials

The research presented in this thesis uses optical microscopy for analysis of small fruit displaying bright, durable or metallic-appearing colour from the *Pollia* and *Viburnum* genera. Simple optical models are used to understand how the material in the outer cells of these fruit produce their unusual appearances.

Initially I analyse *Pollia* fruits using optical and electron microscopy and identify characteristics of their cells' spectral reflection. I then observe the development of these cells in living tissues in two species of the same genus *P. japonica* and *P. condensata*. I use analysis of their structural colour to understand the changes that occur in the outer cell walls during maturation of the fruit on the plant. I investigate the optical characteristics of reflection from *Viburnum* fruits, particularly *V. tinus* and *V. davidii* and demonstrate the structural origin of their colouration. Finally, I demonstrate the development of a hierarchically structured artificial material to reproduce some of the optical effects observed in the fruits analysed.

The unifying theme of this thesis is the investigation of structural colour in fruit cells. Structural colour is what occurs when light interacts with a spatially periodic dielectric material with a similar lengthscale to its own wavelength. In this event, an interference effect causes bright iridescent colours to be reflected.

In order to contextualise the research, I begin with an introduction to principles of optics, reflection by periodic nanostructures and polarisation. I discuss helicoidal architectures and models for representing them.

In this chapter I introduce a basic wave description of light and structural colour mechanisms, and a more in-depth description of the particular material architecture that will be the subject of research. This theoretical background is designed to enable the reader to understand the assumptions and framework for the experimental results that follow.

This chapter ends with an introduction to the experimental techniques employed throughout the thesis. These are numerical modelling and optical and electron microscopy for analysis, with an emphasis on polarisation microscopy.

We start with the basic principles of wave optics.

1.1 Electromagnetism

Light is a transverse electromagnetic wave with two components: the electric and magnetic field, which oscillate perpendicular to each other and to the direction of propagation of the wave.

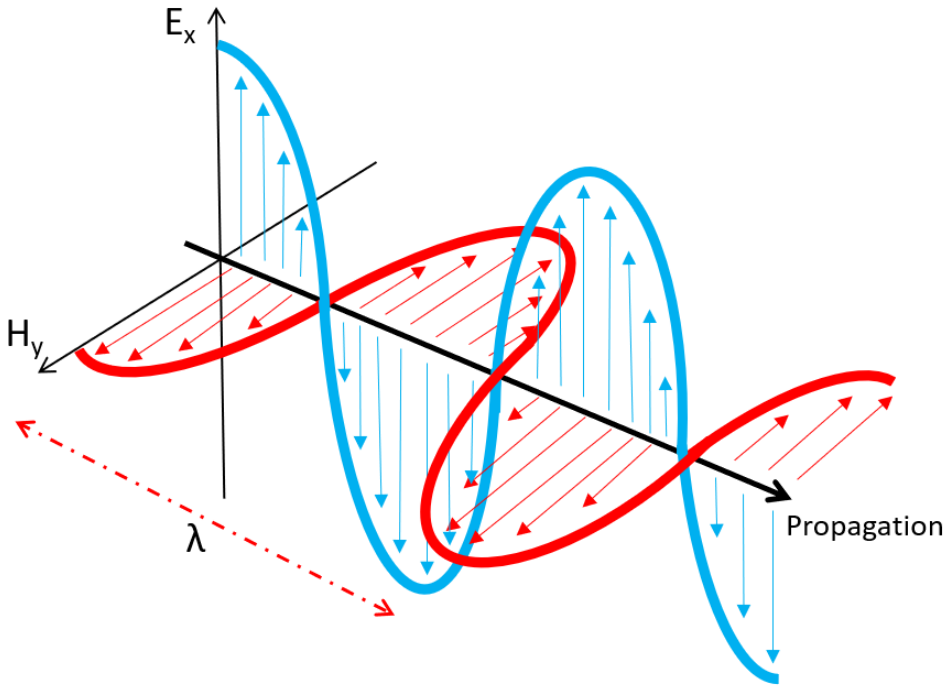

FIGURE 1.1: A simple linearly polarised wave with orthogonal E and H fields schematised. Adapted from a schematic at electronic-shub.org

Mathematically, we describe waves using a trigonometric expression, which can also be expressed using the Euler identity.

$$e^{ik.r} = \cos(\boldsymbol{k}.\boldsymbol{r}) + i\sin(\boldsymbol{k}.\boldsymbol{r}). \tag{1.1}$$

Here r is the vector of spatial propagation of the wave, and $\boldsymbol{k}$ is the wavevector, which in simplest terms accounts for the fact that since cos and sin are periodic,

$$\sin(x) = \sin(x + 2\pi n)$$

.

The wave conception of light is understood through the most fundamental equations of electromagnetism, Maxwell's equations. [2]

$$\nabla \times \boldsymbol{E} + \frac{\partial \boldsymbol{B}}{\partial t} = 0 \tag{1.2}$$

$$\nabla \times \boldsymbol{H} - \frac{\partial \boldsymbol{D}}{\partial t} = \boldsymbol{J} \tag{1.3}$$

$$\nabla \cdot \boldsymbol{D} = \rho \tag{1.4}$$

$$\nabla \cdot \boldsymbol{B} = 0 \tag{1.5}$$

In these equations, $\boldsymbol{E}$ and $\boldsymbol{H}$ are the electric and magnetic field vectors. $\boldsymbol{J}$ is the current density (moving charges) and ρ is the static charge density. $\boldsymbol{D}$ and $\boldsymbol{B}$ are respectively electric displacement and magnetic induction, quantities that account for the interaction of matter with the electric and magnetic fields, which they are related by:

$$\boldsymbol{D} = \varepsilon \boldsymbol{E} = \boldsymbol{\varepsilon_0 E} + \boldsymbol{P}$$
$$\boldsymbol{B} = \boldsymbol{\mu H} = \mu_0 \boldsymbol{H} + \boldsymbol{M}$$

ε and μ are characteristics of the material through which the electromagnetic is passing, and are tensors of dielectric permittivity and magnetic permeability.

$\boldsymbol{P}$ and $\boldsymbol{M}$ are the electric and magnetic polarisations of the material, that is, the induced polarisation from the electromagnetic field in question when it is different from ε and μ. In fact, in the non-magnetic, dielectric materials under low electromagnetic stimulation conditions that we will consider, we will assume the additional permeability of the material compared to free space to be negligible. Furthermore, in these dielectrics, we will also assume the case where there is no static or flowing charge (i.e. $\boldsymbol{J} = \rho = 0$).

In order to simplify the equations, and for many applications, ε and μ are taken to be scalar rather than tensor quantities and $\mu = \mu_r \mu_0$, $\varepsilon = \varepsilon_r \varepsilon_0$. However, especially for the case explored in this thesis, the system must be treated in full in three dimensions, and therefore require tensor analysis. We will return to this later in section 1.2.3.

We combine equations 1.2 and 1.3 with 1.1 and apply to the first case the curl ($\times$), and to the second the time derivative to produce wave equations for $\boldsymbol{H}$ and $\boldsymbol{E}$:

$$\nabla \times (\frac{1}{\mu} \nabla \times \boldsymbol{E}) + \frac{\partial}{\partial t} \nabla \times \boldsymbol{H} = 0 \tag{1.6}$$

$$\nabla \times (\frac{1}{\mu} \nabla \times \boldsymbol{E}) + \varepsilon \frac{\partial^2 \boldsymbol{E}}{\partial t^2} = 0 \tag{1.7}$$

Normally, in an introduction to electromagnetism, these wave equations are simplified in the assumption of a homogeneous isotropic material to give a pair of identical

simple harmonic wave equations in $\boldsymbol{E}$ and $\boldsymbol{H}$. The spatial and temporal parts of the solution are solved independently and a small extension of the expression 1.1 shows that Maxwell's equations are solved by a plane wave solution:

$$\psi = Ae^{i(\omega t \pm \boldsymbol{k}.\boldsymbol{r})} \tag{1.8}$$

This is the description of the propagation of electromagnetic waves in a vacuum. In this expression ω is the plane wave's angular frequency, and is the temporal analogue of k in 1.1. For a plane wave of light in a non-dispersive medium

$$\omega = 2\pi\frac{c}{\lambda}, \tag{1.9}$$

where c is the speed of light in a vacuum and λ is its wavelength.

We can relate the parameters of the plane wave to the physical parameters of Maxwell's equations. The speed of propagation of light in a vacuum is

$$c = \frac{1}{\sqrt{\mu_0\varepsilon_0}} \tag{1.10}$$

i.e. the permittivity and permeability of free space are the definition of the speeds of propagation of the electric and magnetic field oscillations. In a non-vacuum medium then, the altered speed of light c_m depends on the variable permittivity and permeability of the electromagnetic field:

$$c_m = \frac{1}{\sqrt{\mu\varepsilon}} \tag{1.11}$$

The speed of light in a material is a quantity that we traditionally identify relative to the speed of light in a vacuum, by using the refractive index n, where

$$n = \frac{c}{c_m} = \left(\frac{\mu\varepsilon}{\mu_0\varepsilon_0}\right)^{\frac{1}{2}} \tag{1.12}$$

In a non-magnetic material, as mentioned above, diamagnetism is usually very weak so the permeability μ is approximated to μ_0 and

$$n = \sqrt{\frac{\varepsilon}{\varepsilon_0}} \tag{1.13}$$

Having introduced the simple classical wave description of light in vacuum, the same expression can be used to analyse the interaction of light in a non-homogeneous medium.

1.1.1 Bloch Waves

The periodicity in a dielectric is in optical terms characterised by the changing refractive index, or electromagnetic potential, in the medium. The solution to the problem of a plane wave travelling through such a periodic potential is taken from electronic band structure theory and is mathematically identical [2] to the Kronig-Penney [3] model of Bloch electrons. [4]

A material with a periodic potential relies on the dielectric function $\varepsilon(\boldsymbol{r}) = \varepsilon(\boldsymbol{r} + \boldsymbol{R})$, where $\boldsymbol{r}$ is the spatial vector and $\boldsymbol{R}$ is the period of the lattice. The solution to 1.6 and 1.7 therefore must be invariant with a translation of $\boldsymbol{R}$.

The eigenvector solutions can be expressed as

$$E(\boldsymbol{r}) = \boldsymbol{u_k}(\boldsymbol{r})e^{i\boldsymbol{k}\boldsymbol{r}} \tag{1.14}$$

where $\boldsymbol{u_k}$ is periodic with a period $\boldsymbol{R}$, that is

$$\boldsymbol{u_k}(\boldsymbol{r}) = \boldsymbol{u_k}(\boldsymbol{r} + \boldsymbol{R}) \tag{1.15}$$

In order to solve this problem, the Scalar Wave Approximation (SWA) is used. [5] This holds that the electric field in the medium is a scalar quantity, and expands the Bloch sum over the reciprocal lattice vectors $\boldsymbol{G}$, [6]

$$E(\boldsymbol{r}) = \sum_{\boldsymbol{G}}\sum_{\boldsymbol{k}} C_{\boldsymbol{k}-\boldsymbol{G}} e^{i(\boldsymbol{k}-\boldsymbol{G})\cdot\boldsymbol{r}}. \tag{1.16}$$

Here the second sum is over $\boldsymbol{k}$, the first Brillouin zone wave vectors. The dielectric function is expanded similarly:

$$\varepsilon(\boldsymbol{r}) = \varepsilon_{avg} + \sum_{\boldsymbol{G}} U_{\boldsymbol{G}} e^{i\boldsymbol{G}\cdot\boldsymbol{r}}. \tag{1.17}$$

The result of combining these descriptions with 1.7 and 1.6 is a system of coupled equations which give an eigenvalue problem for the wave vector $k(\omega)$ and dispersion relation inside the periodic material.

Determining the real and imaginary limitations of $k(\omega)$ identifies the amplitude and phase of any wave propagating in the material. Furthermore, in a periodic photonic crystal, it indicates the range of values for $k(\omega)$ for which the wave inside the material is entirely imaginary, i.e. evanescent and non-propagating. This indicates a photonic band gap, analogous to an electronic band gap, where light waves will be entirely reflected from the material.

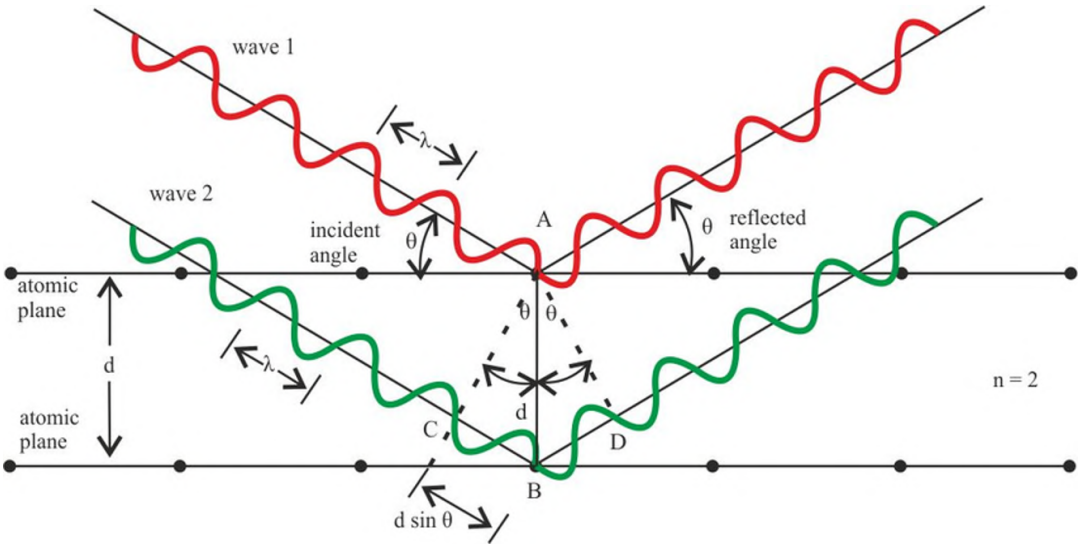

FIGURE 1.2: A diagram reproduced from [11] showing the path difference of light reflected from adjacent planes in terms of the characteristic lengthscales of the periodic material. In this diagram, the planes are atomic planes within a solid, but in the photonic crystal case we consider, the relevant distance is between planes of refractive index contrast.

The Scalar Wave Approximation assumes that the problem may be considered along one particular set of lattice planes, corresponding to the shortest reciprocal lattice vector for a given direction. This reduces the problem to a one dimensional analytic form with a wave vector expressed in terms of lattice characteristics.

Photonic band-gaps that are identified in the SWA may occur only along one direction as a pseudo band-gap, or in multiple directions as a full photonic band gap. [7] Despite its shortcomings, the application of SWA Bloch solutions to photonic crystals has been successfully demonstrated both in theory and experimentally [8] [9], [10] initially in the context of Anderson localisation, the trapping of photons inside periodic dielectrics. However, it has been very successful in describing the full reflection of narrow wavebands of visible light from photonic crystals to produce vibrant colour.

The strongest criticism of SWA, that it has been demonstrated to be incorrect when applied to off-axis propagation, is also true of earlier theory used in the understanding of reflection from periodic dielectrics. [6]

1.1.2 Bragg Reflection

Prior to the application of Bloch's theorem to photonic crystals in 1987 [10], the interaction of light with periodic dielectrics was treated using Bragg's law [12] and its extension in dynamical diffraction theory.

Bragg's law for the reflection of light of wavelength λ incident at angle θ from a material with periodic potential d is

$$n\lambda = 2d \sin\theta \tag{1.18}$$

where n is an integer number. The law was developed for X-ray diffraction from crystals, but to a first approximation is extremely effective for predicting reflection from photonic crystals.

Bragg's law is easily derived from a geometrical analysis of the path difference between light reflected from neighbouring parallel planes. A diagram reproduced from [11] is shown in 1.2 in which the geometrical derivation is shown. The diagram shows the case where waves are reflected from atomic planes, but the same description can be applied in the case of visible wavelengths being reflected from a periodic photonic crystal. For the angle at which the path difference between adjacent planes is equal to an integer number of wavelengths, light is strongly reflected due to constructive interference of the relevant wavelength of light, and destructive interference of wavelengths which would otherwise be partially reflected.

Historically, Bragg's law has been extended through the use of dynamical diffraction theory to get a better insight into propagation in dielectric media. This requires assumptions, including the same made in SWA. It is also assumed that the refractive index in the crystal is a small perturbation from 1 and considered only at first order. Dynamical diffraction theory makes predictions that vary from the SWA predictions increasingly with a increasing refractive index contrast in the material. Although the predicted positions of the photonic band gaps are the same, they are predicted to be wider and to have a stronger dissipative effect in the dynamical diffraction theory. [6]

1.1.3 Multilayer Interference

Extending analysis of reflection interference from the simple lattice formulation treated in the Bloch waves and Bragg reflection models allows us to understand how light is reflected from surfaces and films. [13]

Light incident on a thin film is reflected at the both the top and bottom refractive index boundary, and the reflections from the two surfaces interfere with each other. Assuming that the light is incident from air on the first surface, the interference condition depends on the distance between the interfaces and the refractive index contrast at the second surface. When light is reflected at an interface with a higher refractive index, as for an anti-reflective coating, its phase is changed by 180^{o}. When the second refractive index change is to a lower refractive index, as in a soap bubble, the phase is not inverted.

The same interference condition applies to produce constructive or destructive interference, depending on the second boundary condition. The constructive interference condition for a soap-bubble in air and an anti-reflective coating are respectively

$$\begin{aligned} 2n_b d\cos\theta_b &= (m-1/2)\lambda \\ 2n_b d\cos\theta_b &= m\lambda \end{aligned} \tag{1.19}$$

where n_b and θ_b are the refractive index and angle of refraction in the film material b. This model treats only the interference from a single reflection at each interface. A reflection at the interface between material a (air) and b (film) introduces reflection and transmission amplitudes r_{ab} and t_{ab} as a function of incidence and the respective refractive indices via Snell's and Fresnel's laws. [14] The third material is denoted c.

Taking into account multiple reflections at both interfaces, the exact amplitude of reflection and transmittance is given by

$$\begin{aligned} r &= r_{ab} + t_{ab}r_{bc}t_{ba}\mathrm{e}^{i\phi} + \cdots = r_{ab} + t_{ab}r_{bc}t_{ba}\mathrm{e}^{i\phi}\kappa \\ t &= t_{ab}t_{bc}\mathrm{e}^{i\phi/2} + t_{ab}r_{bc}t_{bc}\mathrm{e}^{3i\phi/2} + \cdots = t_{ab}t_{bc}\mathrm{e}^{i\phi/2}\kappa \end{aligned} \tag{1.20}$$

using $\kappa = 1/(1 - r_{bc}r_{ba}\mathrm{e}^{i\phi})$ and $\phi = 4\pi n_b d\cos(\theta_b)/\lambda$. For real refractive indices, the reflectivity and transmittance are given by $R = |r|^2$ and $T = (n_c/n_a)|t|^2$ and $R + T = 1$.

Thin film interference may be modelled in this way, and the reflectance shown to be weak and with a broad reflection spectrum that is only weakly dependent on wavelength. The reflectivity is increased with increasing angle making colours more clearly visible at large angles, as observed in soap bubbles. [15]

Enhanced thin film reflectivity is produced by increased reflectance at each interface via a larger refractive index contrast, such as those seen in oxide layers coating some metals. [16] Visible colouration in these circumstances is only seen when interference of wavelengths satisfying the destructive condition suppresses total reflectivity such that narrow band spectral colours or non-spectral mixed-colour reflections are visible.

The analysis of thin film interference is extended to multilayers with a small refractive index contrast ($\Delta n \approx 0.05$) by considering a stack of alternating material layers, A and B with thicknesses d_A and d_B and refractive indices $n_A > n_B$, as shown in the schematic in figure 1.3. Light is reflected at every interface, with a 180° phase

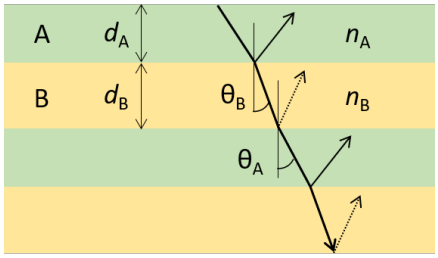

FIGURE 1.3: Schematic after [13] showing a multilayer stack of alternating films A and B. The single-headed arrows denote an incident and reflected light rays.

shift at the B-A boundary. Therefore, for maximum reflection from an 'ideal multilayer', relations similar to the soap bubble and anti-reflective coating constructive conditions,

$$\begin{aligned} 2(n_A d_A \cos\theta_A + n_B d_B \cos\theta_B) &= m\lambda \\ 2n_A d_A \cos\theta_A &= (m' - 1/2)\lambda \end{aligned} \tag{1.21}$$

should be satisfied for the same wavelength, where $m' \leqslant m$.

Multilayers with larger refractive index contrasts may be treated using transfer matrix methods. Solution of multilayer reflection via transfer matrix methods have shown [13] that for normal incidence light, maximum reflectivity occurs when the relation $2n_A d_A = 2n_B d_B = (m' - 1/2)\lambda$ is satisfied, at which wavelength the amplitude reflectivity satisfies

$$\begin{aligned} &r = (1-\gamma)/(1+\gamma) \\ &\gamma = (n_t/n_i)\cdot(n_A/n_B)^N \qquad \text{for N even} \\ &\gamma = n_A^2/(n_t n_i)\cdot(n_A/n_B)^{N-1} \qquad \text{for N odd} \end{aligned}$$

where n_i and n_t are the refractive indices for the media in the incident and transmitted spaces respectively.

1.1.4 Transfer Matrices

For complex materials, where the number of layers becomes very large, propagation of light can be approached using transfer matrices to discretise Maxwell's equations. This approach is particularly successful for periodic structures, and is useful for computer modelling. There are no limitations placed on the form of the target material, and this method will be used in the rest of this chapter. [2]

The transfer matrix method was first introduced [17] in order to approach optically active materials, that is, material in which the polarisation of electromagnetic waves

in two dimensions (transverse to the direction of propagation) is important. The materials that are the subject of the research in this thesis are optically active, but are also themselves chiral. This necessitates an approach which fully describes their orientation, and interaction with electromagnetic waves as three dimensional dynamic phenomena. However, our understanding of this model relies on a fundamental understanding of the general approach to photonic crystals with Maxwell's equations extended using transfer matrices.

We will now approach the materials themselves, and then apply the electromagnetic equations covered in the previous sections via transfer matrices.

1.2 Helicoidal Structures

The materials considered in this research are helicoidal photonic crystals. Having discussed generalisations of photonic crystal reflection, this section introduces helicoidal structures.

1.2.1 Polarisation and Optical Activity

We return to the wave expression for an optical wave as set out in 1.1, but now taking the wave as a transverse vector in two-dimensions. An electromagnetic wave oscillating in the plane transverse to its direction of propagation z can be represented as a vector in $x-y$ co-ordinates using Jones vector representation $\boldsymbol{J}$. A schematic showing the superposition of out of phase linear components is shown in figure 1.4. $\boldsymbol{J}$ is a complex vector and therefore retains all information about the wave's amplitude and phase of which the electric field vector $\boldsymbol{E}$ is only the real part. [17] [2]

$$\boldsymbol{E}(z,t) = \boldsymbol{Re}[\boldsymbol{A}e^{i(\omega t - kz)}] = \boldsymbol{Re}\left[\begin{pmatrix} \boldsymbol{A}_x e^{i\delta_x} \\ \boldsymbol{A}_y e^{i\delta_y} \end{pmatrix}\right] = \boldsymbol{Re}[\boldsymbol{J}] \tag{1.22}$$

The polarisation of a general wave may therefore be expressed with a normalised (unit length) Jones vector where ϕ is the azimuth angle of the oscillation with respect to the x axis, and δ is the phase offset between the x and y field components.

$$\boldsymbol{J}(\phi,\delta) = \begin{pmatrix} \cos\phi \\ e^{i\delta}\sin\phi \end{pmatrix} \tag{1.23}$$

This vector traces out a generalised ellipse, special cases of which occur at $\frac{n\pi}{2}$ radian intervals in ϕ and δ. These special cases, where the the phase and azimuth angle of

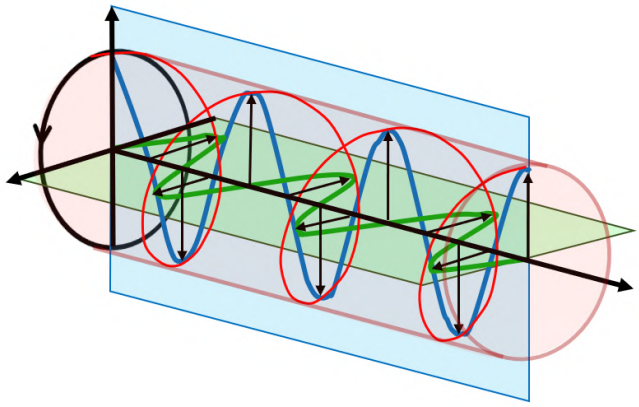

FIGURE 1.4: Diagram, redrawn and adapted from [18], showing the interpretation of a circular polarised wave in terms of superposition of linear polarised waves. I define the polarisation such that this is a left handed wave. It should be noted that the vector at a single point eg. the axes intercept, rotates clockwise as viewed from the source, and counter-clockwise as viewed from the receiver.

polarisation in x and y are pure linearly or circularly polarised light, as shown in 1.5.

The use of $x - y$ coordinates is adopted to simplify our expressions but it should be noted that just as circularly polarised light may be expressed as a complex (i.e. out of phase) combination of equal parts of vertical and horizontal linear polarisations, linear polarised light may be expressed as equal parts of left and right circularly polarised light.

By defining the electromagnetic field directions in x and y, we can also orient our anisotropic material. Crystalline materials are anisotropic, due to the orientation of atoms with respect to each other in a crystal lattice, which produces directional electromagnetic permeability and permittivity, which was previously ignored after equation 1.1.

As an electromagnetic wave passes through any anisotropic medium, the relative phase of the x and y oscillation components changes, because a different refractive index for each crystalline direction slows the oscillation anisotropically. A birefringent material therefore converts linearly polarised light into elliptically or circularly polarised light, because of its refractive index anisotropy. This is useful for interconversion of different polarisations of light experimentally. An anisotropic slab of a defined thickness, like a quarter-wave plate can be used to interconvert light between linear and circular polarisations. Optical components like this may be characterised using a two dimensional Jones vector, as in the table in figure 1.5. The Jones vector for each polarisation is also the transformation vector equivalent to the optical component that converts vertical linear polarised light into that polarisation.

Polarization	Jones vector	Illustration
Linearly polarized: vertical	$\begin{bmatrix} 1 \\ 0 \end{bmatrix}$	
Linearly polarized: horizontal	$\begin{bmatrix} 0 \\ 1 \end{bmatrix}$	
Linearly polarized: +45°	$\frac{1}{\sqrt{2}}\begin{bmatrix} 1 \\ 1 \end{bmatrix}$	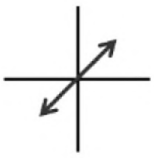
Linearly polarized: –45°	$\frac{1}{\sqrt{2}}\begin{bmatrix} 1 \\ -1 \end{bmatrix}$	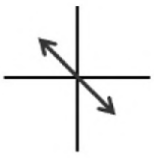
Circularly polarized: left	$\frac{1}{\sqrt{2}}\begin{bmatrix} 1 \\ -i \end{bmatrix}$	
Circularly polarized: right	$\frac{1}{\sqrt{2}}\begin{bmatrix} 1 \\ i \end{bmatrix}$	

FIGURE 1.5: Normalised Jones vectors for common polarisations, from [19]

1.2.2 Chiral Nematic Materials

Liquid crystals were isolated in the end of the nineteenth century. [20] They are materials comprised of anisotropic molecules or nanoparticles showing long range order due to alignment whilst remaining a liquid. One orientation structure found in liquid crystals is the chiral nematic phase in which molecules are arranged in a pseudo-planar geometry (not aligned in true planes, but sharing orientation with others in their planar cross-section), with each molecule oriented at a slight angle from the one below, as in figure 1.6.

The development of the optical response of chiral cholesterics from Friedel, Oseen [21] and subsequently de Vries [22] has described the reflection from these materials that is observed experimentally. This successful approach took each plane of the cholesteric material as an infinitesimally narrow slab with an anisotropic refractive index, and demonstrated that the results hold for any width of slab.

FIGURE 1.6: Rods arranged in a chiral nematic orientation, image by Dr Gen Kamita.

It was shown that chiral nematics have an effective band gap and reflection range for one circular polarisation of light, corresponding to the pitch of 180^o rotation of the molecules, analogous to the band-gaps and Bragg law reflection criteria discussed earlier in section 1.1.2. [21]

De Vries' approach demonstrates solutions to Maxwell's equations in a material made up of slabs of arbitrary width. It is shown that there exist values of λ and corresponding pitch lengths for which the wave inside the material is purely imaginary and therefore corresponds to an evanescent, non-propagating wave. The mathematical derivation is not given here, but is easily followed in [22] [23] [24] and [25].

Polarisation-retention in Reflection

One important feature of the reflected light is that it retains its chirality on reflection, because the electrical vector is reversed, unlike reflection of circularly polarised light from homogeneous refractive-index boundaries. This is easily observed experimentally by looking at normal incidence through a circularly polarising filter into a mirror.

In order to understand the chirality retention in reflection, the interaction of light at each crystal boundary is considered for both of the crystal birefringent axes. At every partially-reflecting boundary only the polarisation of light on the axis transitioning to the higher refractive index (the fast ray) will undergo phase reversal. The light crossing a boundary to a lower refractive index (the slow ray) will retain the same phase. The reflected light that is the circularly polarised superposition therefore has induced in it a change in the relative phase, or reversal of the direction of the electric vector. A reversal of the electric vector and a reversal of the direction of the wave together mean that the circular polarisation retains its direction. The reflected wave therefore has the same circular polarisation as the incident wave.

Rotatory Power

It was also demonstrated that chiral nematics have extremely strong rotatory power, up to thousands of degrees per mm. Rotatory power is a consequence of a material's chirality which turns the polarisation direction of linear polarised light [26]. For comparison, quartz in which rotatory power was first observed has a rotatory power of only 24^o/mm [22] and ordinary organic liquids have a rotatory power of 300^o/mm. [27] Either side of the reflected bandgap this rotatory power is extremely enhanced in opposite directions. The expression for disallowed wavelengths in the bandgap gives infinite rotatory power.

Handedness Conventions

The relative handedness of the reflected light and the chirality of the material has been the subject of unacknowledged conflict. The primary results fail in my opinion to make explicit whether the same direction or opposite direction wave is reflected from the material. This is not helped by the use of exact opposite or mixed naming conventions in different fields and within the same field [28] or even the same paper. [22] Often in the earlier papers the chirality of the material is not made explicit while the handedness of the light reflected is.

The biggest source of confusion appears to be that the spatial handedness of the circular polarised wave (i.e. the chirality traced by directions of the adjacent electric vectors carrying the wave relative to each other) and the temporal handedness of a vector at any one point are opposite. A circularly left handed spatial wave has a circularly right handed rotating vector. This means that the described circular orientation can sometimes be unclear. Spatial and temporal handedness are compared in figures 1.4 and 1.7.

Highly cited seminal papers which have established the mathematical description of the reflection and respected textbooks [24] [25] [22] [23] fig 3, [29] fig 3.2, [30] [31] contain unclear or clear but contradictory summaries of their results. Although the helicity of the material and the wave is clear mathematically, the non-mathematical description and therefore communication to non-theorists has been weak. There is very little discussion of this conflict.

1.2.3 Berreman Formulation

We now approach the solution to Maxwell's equations for a helicoidal photonic crystal using Berreman's matrix formulation of Maxwell's equations which built on the original characterisation by Oseen and de Vries. This approach demonstrates the

existence of reflective bandgaps in a chiral nematic material, and will form the basis for our understanding of the chiral nematic materials under investigation.

The transfer matrix technique for solving reflection and transmission by stratified (or continuously varying i.e. infinitesimal strata) is impressive in its ability to conserve higher dimensional optical properties, and handle systems with low optical symmetry. We start with a formulation of Maxwell's equations of the electromagnetic field vectors $\boldsymbol{E}, \boldsymbol{H}, \boldsymbol{D}$ and $\boldsymbol{B}$ in three dimensions as a 6x6 matrix, and then derive a 4x4 matrix which allows us to find solutions for chiral nematic materials. [32] The full worked solution may be found in [33].

Equations 1.2 to 1.5 can be expressed

$$\begin{pmatrix} 0 & 0 & 0 & 0 & -\frac{\partial}{\partial z} & \frac{\partial}{\partial y} \\ 0 & 0 & 0 & \frac{\partial}{\partial z} & 0 & -\frac{\partial}{\partial x} \\ 0 & 0 & 0 & -\frac{\partial}{\partial y} & \frac{\partial}{\partial x} & 0 \\ 0 & \frac{\partial}{\partial z} & \frac{\partial}{\partial x} & 0 & 0 & 0 \\ -\frac{\partial}{\partial z} & 0 & \frac{\partial}{\partial y} & 0 & 0 & 0 \\ \frac{\partial}{\partial y} & \frac{\partial}{\partial x} & 0 & 0 & 0 & 0 \end{pmatrix} \begin{pmatrix} \boldsymbol{E}_x \\ \boldsymbol{E}_y \\ \boldsymbol{E}_z \\ \boldsymbol{H}_x \\ \boldsymbol{H}_y \\ \boldsymbol{H}_z \end{pmatrix} = \frac{1}{c}\frac{\partial}{\partial t} \begin{pmatrix} \boldsymbol{D}_x \\ \boldsymbol{D}_y \\ \boldsymbol{D}_z \\ \boldsymbol{B}_x \\ \boldsymbol{B}_y \\ \boldsymbol{B}_z \end{pmatrix} \tag{1.24}$$

The symmetrical non-zero elements of the matrix are the curl operators for $\boldsymbol{H}$ and $\boldsymbol{E}$. This can be rewritten as

$$\boldsymbol{RG} = \frac{1}{c}\frac{\partial}{\partial t}\boldsymbol{C} \tag{1.25}$$

By ignoring nonlinear effects, we assume a linear relationship between $\boldsymbol{G}$ and $\boldsymbol{C}$ giving

$$\boldsymbol{G} = \boldsymbol{MC} \tag{1.26}$$

We define the time dependence with an exponential factor $e^{-i\omega t}$ and the transformation matrix $\boldsymbol{M}$

$$\boldsymbol{M} = \begin{pmatrix} \boldsymbol{\varepsilon} & \boldsymbol{\rho} \\ \boldsymbol{\rho'} & \boldsymbol{\mu} \end{pmatrix} \tag{1.27}$$

where each of the four quadrants in $\boldsymbol{M}$ define a 3x3 tensor for optical rotation (quadrants I and III), dielectric (permittivity) and (magnetic) permeability. From this we arrive at the spatial wave equation for the frequency ω:

$$\boldsymbol{R\Gamma} = \frac{-i\omega}{c}\boldsymbol{M\Gamma} \tag{1.28}$$

We will take the case of a plane wave incident obliquely in the x,y plane so that $\boldsymbol{M}$ is a function of z only. We can therefore expand the wave equation and combine the resulting expressions to give four first-order linear differential equations and two linear algebraic equations which can be expressed

$$-\frac{ic}{\omega}\frac{\partial}{\partial z}\begin{pmatrix}0&0&0&1\\0&0&-1&0\\0&-1&0&0\\1&0&0&0\end{pmatrix}\begin{pmatrix}E_x\\E_y\\H_x\\H_y\end{pmatrix}=\boldsymbol{S}\begin{pmatrix}E_x\\E_y\\H_x\\H_y\end{pmatrix} \tag{1.29}$$

Apply the inverse 4x4 matrix and rearrange to give the equivalent

$$\frac{\partial}{\partial z}\begin{pmatrix}E_x\\H_y\\E_y\\-H_x\end{pmatrix}=\frac{i\omega}{c}\begin{pmatrix}S_{41}&S_{44}&S_{42}&-S_{43}\\S_{11}&S_{14}&S_{12}&-S_{13}\\-S_{31}&-S_{34}&-S_{32}&S_{33}\\S_{21}&S_{24}&S_{22}&-S_{23}\end{pmatrix}\begin{pmatrix}E_x\\E_y\\H_x\\H_y\end{pmatrix} \tag{1.30}$$

where the components of $\boldsymbol{S}$ are expressions using M_{ij}. We further abbreviate to

$$\frac{\partial}{\partial z}\psi=\frac{i\omega}{c}\Delta\psi \tag{1.31}$$

If Δ is approximately independent of z over a small distance δz (taking an increment), the four periodic solutions are of the form

$$\psi_j(\delta z)=e^{iq_j\delta z}\psi_j(0) \tag{1.32}$$

and are found by solving the characteristic equation

$$Det\Big(\frac{\omega}{c}\Delta-q\boldsymbol{I}\Big)=0, \tag{1.33}$$

where $\boldsymbol{I}$ is the 4x4 identity matrix. Further, if Δ is independent of z over distance h then by integrating equation 1.31 we find

$$\psi(z+h)=\boldsymbol{P}(h)\psi(z). \tag{1.34}$$

We find $\boldsymbol{P}(h)$ by taking the eigenvector matrix $\boldsymbol{\Psi}$ inserted into equation1.31

$$\boldsymbol{\Psi K}(h)=\boldsymbol{P}(h)\boldsymbol{\Psi} \tag{1.35}$$

If

$$K_{ij}=e^{iq_jh} \tag{1.36}$$

then

$$\boldsymbol{P}(h) = \boldsymbol{\Psi}\boldsymbol{K}(h)\boldsymbol{\Psi}^{-1} \tag{1.37}$$

Exact eigenmodes may be found analytically for systems where $\boldsymbol{M}$ is periodic, for example in the case of an electromagnetic wave aligned with the director of a flat single domain chiral nematic material.

Finding solutions for this case, we assume that the optical activity of each plane is negligible compared to the optical rotation of the structure. This is in fact the case, as described earlier. Oseen [21] gives unit permeability, no optical rotation in the plane and

$$\boldsymbol{\varepsilon} = \begin{pmatrix} \epsilon + \delta\cos 2\beta z & \delta \sin 2\beta z & 0 \\ \delta \sin 2\beta z & \epsilon - \delta\cos 2\beta z & 0 \\ 0 & 0 & \epsilon_3 \end{pmatrix} \tag{1.38}$$

This represents a dielectric tensor with two principle axes normal to z of which the x axis length is $(\epsilon + \delta)$ at $z = 0$ and spiralling with increasing z with a pitch

$$\lambda = 2\pi/\beta. \tag{1.39}$$

From there we derive the components of $\boldsymbol{S}$ so that

$$\boldsymbol{\Delta}(z) = \begin{pmatrix} 0 & 1 - X^2/\epsilon_3 & 0 & 0 \\ \epsilon + \delta\cos 2\beta z & 0 & \delta \sin 2\beta z & 0 \\ 0 & 0 & 0 & 1 \\ \delta \sin 2\beta z & 0 & \epsilon - X^2 - \delta\cos(2\beta z) & 0 \end{pmatrix}, X = \frac{c\zeta}{\omega} \tag{1.40}$$

where ζ is the propagation vector component in the x direction. If we take this to be 0, then we can extract eigenmodes analytically. The eigenvectors are

$$\psi = e^{i(q+\beta)z}\begin{pmatrix} A \\ A' \\ -iA \\ -iA' \end{pmatrix} + e^{i(q-\beta)z}\begin{pmatrix} B \\ B' \\ -iB \\ -iB' \end{pmatrix} \tag{1.41}$$

where A and B values are to be found.

Using matrix multiplication in this case,

$$\boldsymbol{\Delta\psi} = e^{i(q+\beta)z}\begin{pmatrix} A \\ \epsilon A' + \delta B \\ -iA \\ -i(\epsilon A' + \delta B) \end{pmatrix} + e^{i(q-\beta)z}\begin{pmatrix} B \\ \epsilon B' + \delta A \\ -iB \\ -i(\epsilon B' + \delta A) \end{pmatrix} \tag{1.42}$$

and by differentiation,

$$-i\frac{c}{\omega}\frac{\partial\psi}{\partial z} = e^{i(q+\beta)z}\begin{pmatrix} A \\ A' \\ -iA \\ -iA' \end{pmatrix}\frac{c}{\omega}(q+\beta) + e^{i(q-\beta)z}\begin{pmatrix} B \\ B' \\ -iB \\ -iB' \end{pmatrix}\frac{c}{\omega}(q-\beta). \tag{1.43}$$

We know that 1.42 and 1.43 are equal, thanks to 1.31, so by equating the sides we can find four expressions. From them we can find non-trivial solutions for the case where q has one of four eigenvalues:

$$q = \pm\left(\beta^2 \pm 2\beta\frac{\omega}{c}\sqrt{\epsilon + \frac{\frac{\delta^2}{\epsilon}\left(\frac{\omega}{c}\right)^2}{4\beta^2}} + \left(\frac{\omega}{c}\right)^2\epsilon\right)^{\frac{1}{2}} \tag{1.44}$$

This provides a full solution with either A or B specified.

This approach also yields the two important optical effects along with the full solutions. For small values of ω, the eigenvectors corresponding to eigenvalues of q are approximately circularly polarised, and affected by strong optical rotation from the chiral material, which is optically active on a different scale to ordinary molecular optical activity.

Furthermore, when the electromagnetic wavelength in the medium is approximately half the pitch length,

$$\omega \approx \frac{c\beta}{\sqrt{\epsilon}} \tag{1.45}$$

the eigenvectors are no longer circularly polarised and one pair of eigenvalues from equation 1.44 becomes imaginary for a band around that frequency, giving an attenuated forward mode and amplified backward mode for its respective eigenvectors. The part of the light that excites these attenuated modes, in a thick and perfectly ordered material is therefore completely reflected, whilst the light in the other mode passes through the crystal. This happens in optical chiral nematic materials, where the matching wavelength of light with the anti-rotating electric vector to the spatial rotation of the field is fully reflected making the material brightly coloured. [34]

A schematic illustrating the circular polarisation modes and their transmission and reflection by a helicoidal photonic crystal is shown in figure 1.7.

Although other weaker bands near higher integral multiples of the fundamental frequency band give secondary order reflections, [27] these are generally irrelevant to the visible reflection from materials with optical wavelength first order modes. Light incident at off-normal incidence is subject to a longer periodicity in the material, causing an iridescent effect. The numerical models in this thesis are based on an application of this Berreman method, justified by the use of a low refractive index contrast material with a chiral nematic structure. The transfer matrix approach means that rays that are incident obliquely on the surface of a chiral nematic material can be treated, yielding nontrivial elliptical polarisation. For normal incidence however, we may use Bragg's law to indicate the photonic bandgaps in one polarisation.

Analogy with Non-twisted Photonic Crystals

The existence of Bragg-like photonic bandgaps in a helicoidal material is a consequence of a periodic refractive index. We have treated the specific case of a periodically twisted anisotropic material. As an intuitive analogy, the result of this model can be compared to the isotropic multilayer approach discussed in section 1.1.3 by viewing a birefringent, but not twisted, multilayer from the rotating frame of a circularly polarised light wave.

To simplify, we take the case of the two circularly polarised waves with the same wavelength (in the material) as the pitch. In the frame of a wave with *temporal* field vectors rotating in the same direction as the material's spatial handedness, at any one time the material appears simply birefringent without periodicity. Inversely, if the wave's *temporal* electric vectors have the opposite handedness the material appears to have a spatially periodic birefringence matching half the wave's own length.

Crucially, we define the handedness of the wave by its spatial and not its temporal chirality, because this definition is independent of the emitter / receiver perspective. Left handed materials therefore reflect light of the same (spatial) chirality as themselves. A schematic summary of transmission and reflection chirality is given in figure 1.7.

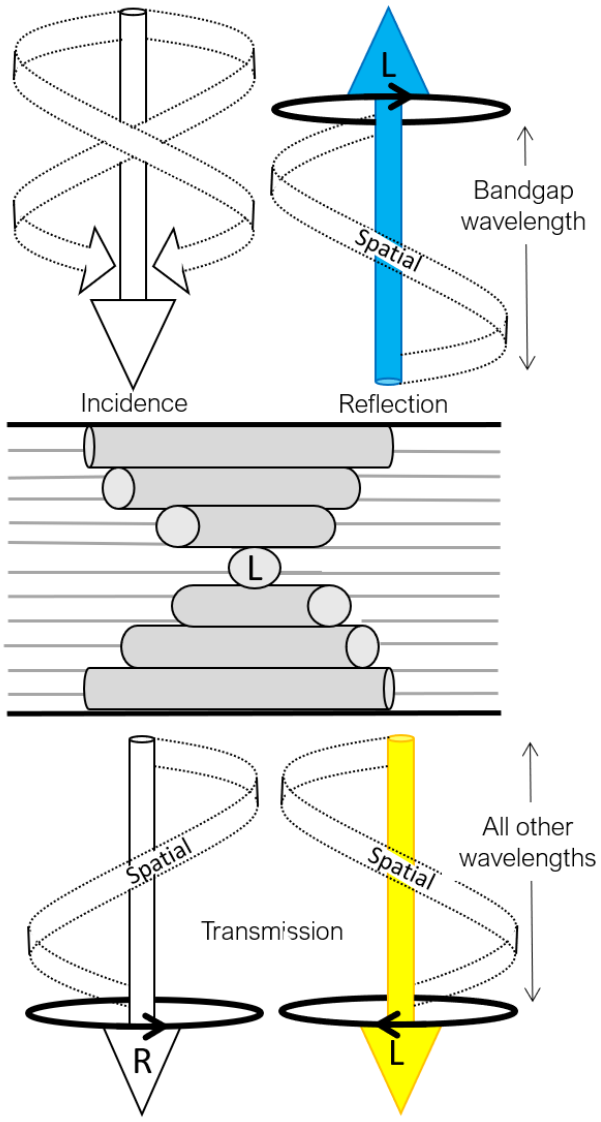

FIGURE 1.7: Schematic showing the reflection and transmission of circularly polarised light in a chiral material. The black loop arrows indicate the rotation of the electric vector at any point, which is opposite to the spatial orientation of the field. In order to understand this difference, consider the way that a gel is deformed by inserting a metal corkscrew by either twisting or pushing it in. A circular polarised wave propagates in the electric field analogous to the pushing rather than twisting case.

1.3 Pigment and Structural Colour

The analysis in this chapter has demonstrated how periodic nanostructures in otherwise transparent material generate brightly coloured reflection. Structurally coloured materials remain semi-transparent as indicated by the portion of light that passes through the film in figure 1.7, because the relationship between the periodicity and reflected wavelength makes them generally angular-dependent and wavelength-selective.

Pigment appearance, in comparison, occurs as pigments absorb some parts of the visible spectrum, scattering other wavelengths. Scattering occurs over the entire angular range and all the other colours are absorbed by the pigmented material. A cartoon in figure 1.8 shows the difference in white light reflection between structural and pigmented material.

The semi-transparency of structurally coloured material means its colouration is observed in combination with other light reflected from material underneath it. The illumination and reflection environment in which a structurally coloured material is seen is therefore important to the impression of the reflected colour. A bright background reflects light back through the structurally coloured material changing the overall visible spectrum.

Addition of an absorption pigment, or combination of the structure with a pigmented or very high refractive index material through which light cannot propagate, can be used to make the structurally coloured material opaque. In some cases, this role is fulfilled by one of the periodic refractive index contrast materials itself. [35]

The mechanism of structural colour is to separate incident light into different wavelengths in different directions. If a white scattering background is placed in the background, then all the light eventually comes back in reflection with a scattered angle, destroying the structural colour effect. For this reason structurally coloured materials must be imaged in front of a dark absorbing background, which is a commonplace practise. [36] Nevertheless, without understanding how the background contributes to the visual impression of the material, discrimination of the potential for application of a novel material is limited.

An example of the importance of background colour in understanding the visual impact of the structural colour is shown in figure 1.8 C. Although the image shows a blue-green reflective multilayer film, which reflects the same colours in front of both backgrounds, its semitransparency means the overall impression of the film is very different depending on background. A dark background makes the multilayer film appear brightly coloured, while the bright background makes the colour of the film appear indistinct and pearlescent.

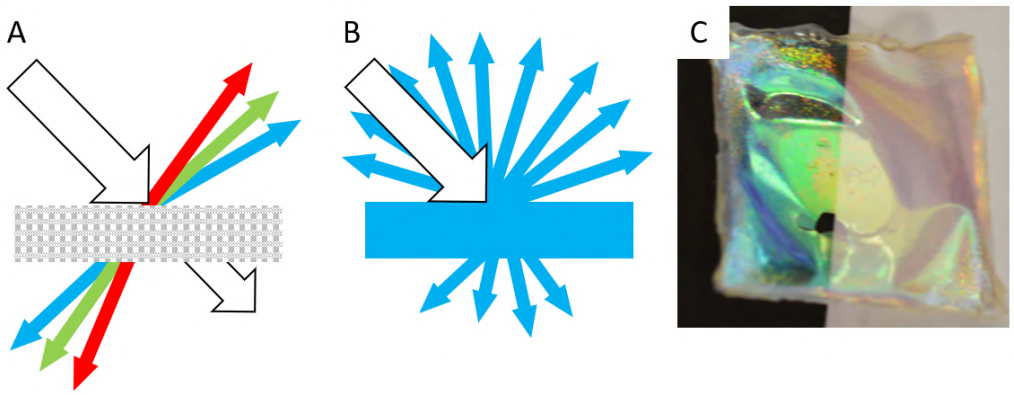

FIGURE 1.8: Cartoons comparing the qualitative response of A. Structurally coloured material and B. Pigmented material to incident white light. The light redistribution does not correspond to a real material but are intended to show the angular and spectral distribution of reflected light in either case. C. A structurally coloured multilayer film (width approximately 2 cm) on a white/black split background. Tilted planes show the effect of angular dependence on reflection.

1.4 Unit Conventions

This thesis uses 'um' to denote a micron or 10^{-6} metre wherever possible in the text and on figures rather than the traditional 'μm'. This is intended to make it easier for readers.

1.5 Experimental Methods

An introduction to the microscopy, analysis and numerical modelling techniques used in every chapter of this thesis is given here. Later chapters include short experimental sections outlining additional techniques where applicable.

Photographs were taken with a DSLR (Nikon D3200) camera. Photographs are used to illustrate visible appearance and exposure settings and adjustment were set accordingly.

1.5.1 Microscopy

Optical Microscopy

Two customised microscopes were used for the micro-spectroscopy in the following chapters. For transmission microscopy and all small samples, the reflection microscope (Zeiss, Axio Scope A.1) was mounted with an electronic $x-y$ stage (Prior H1P4AAXA1, Prior Scientific Instruments Ltd.) above a transmission microscope base with an independent light source. For measuring the cells on the living plant,

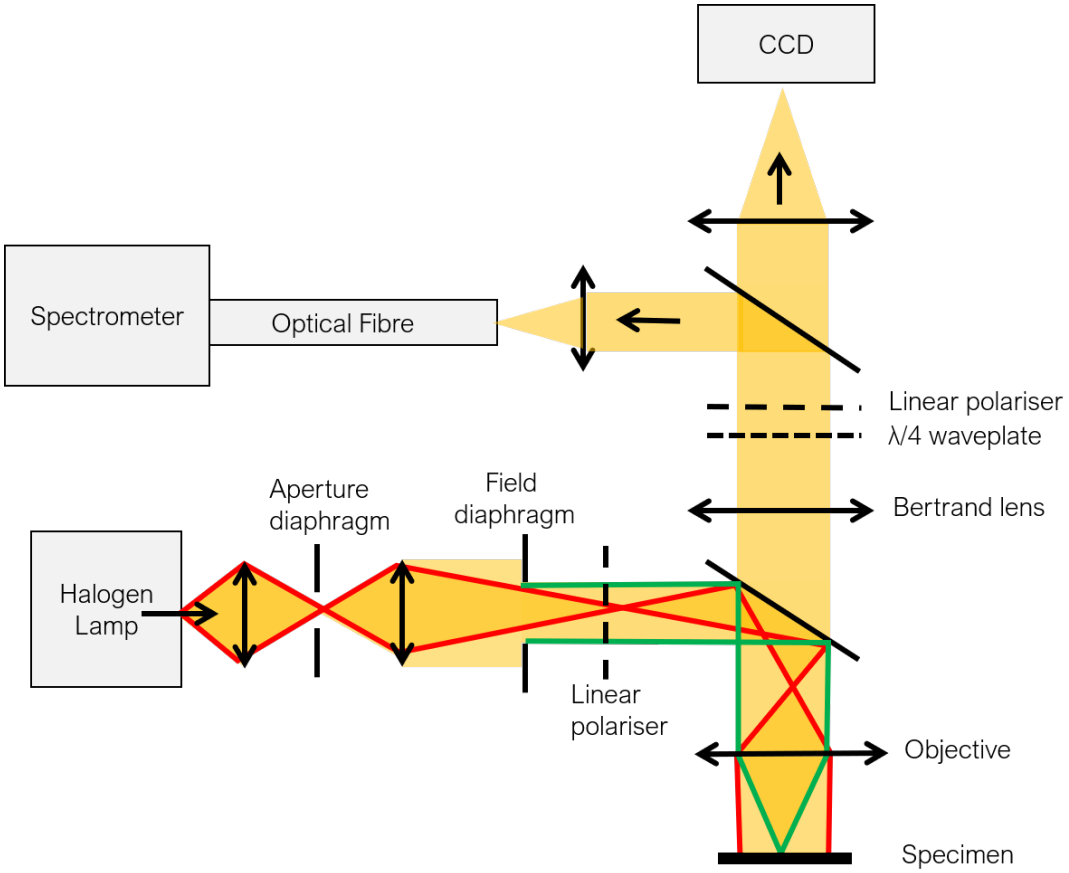

FIGURE 1.9: Schematic of a Koehler illumination microscope. Koehler illumination places the lamp and the specimen in inverse focal planes, avoiding the overlaying of the image of the lamp and the image of the specimen. The red and green lines indicate the light path of different light rays. Double ended arrows indicate lenses, single ended arrows indicate the direction of light propagation. Light propagates from the halogen lamp down onto the specimen, is reflected and passes through to the spectrometer and CCD. This image was designed with reference to Zeiss manufacturer's microscope instructions.

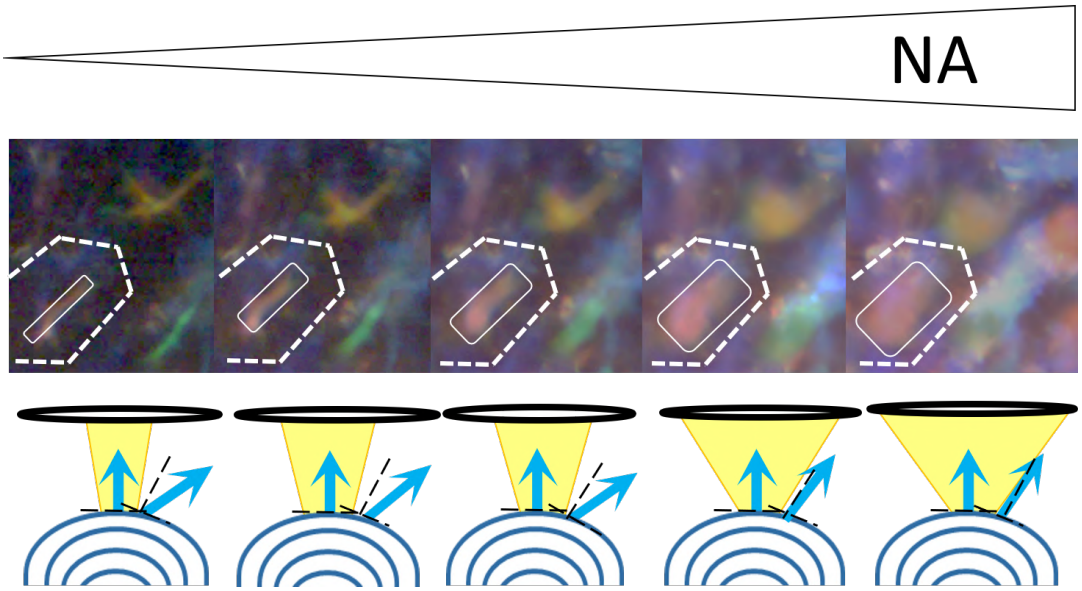

FIGURE 1.10: These photographs show the same area five times illuminated by an increasing numerical aperture width between 5 and 37° left to right. A dotted white line indicates the outer contour of the cell and the solid white oblong outlines the shape and size of the reflection spot on the red cell. Yellow and green neighbouring cells are also seen. The schematic series below shows the effect of increasing maximum incidence angle on a curved multilayer. The black ellipse represents the unchanging collection objective aperture. As the maximum angular incidence increases, more light is collected by the aperture from a larger area on top of the cell.

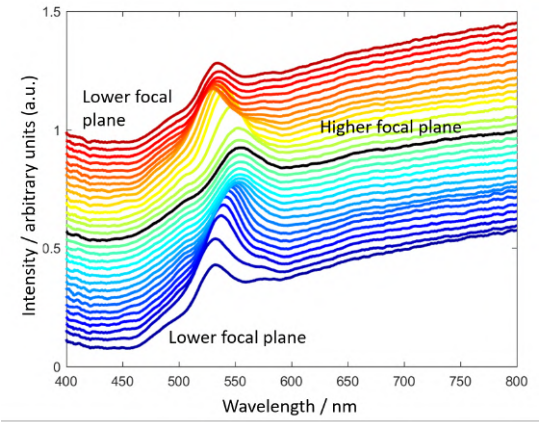

FIGURE 1.11: This plot shows a single location measured thirty times as the focal depth moves from the lowest focal plane in which the spot is visible (dark blue line), to the highest (black line) and back again (dark red line). The change in focal depth changes the location of the peak wavelength measured by about 20 nm, with the highest focal plane imaging the most red-shifted peak.

the microscope head (Zeiss Vario scope A.1) was mounted on a Zeiss column base which has a potential sample height of 38 cm.

Unless otherwise stated the microscope was configured for Koehler illumination, as in figure 1.9. All the components were aligned on the optical axis. For reflection measurements, the microscope was illuminated with a halogen lamp (Hal 100), passing through the numerical aperture. The field aperture was loosely constricted so that the edges of the aperture were visible on the image captured by the CCD (Thorlabs DCC3240C or IDS UI-3580LE-C-HQ). The CCD was accessed by ThorCam/ uEye Cockpit user interface software. The objective lenses used were Zeiss EC Epiplan Apochromat for 10, 20, 50, 100x magnification, having numerical apertures of 0.3, 0.6, 0.95, 0.95 respectively, or alternatively a 5x magnification Epiplan Neofluar objective lens, NA = 0.13.

Exposure time, gain and contrast have been enhanced where necessary to demonstrate the lower limit of optical reflection.

Numerical Aperture For bright field measurement, unless otherwise stated, the numerical aperture was narrowly constricted to allow approximately $\pm 5^{o}$ angular variation from the optical axis. This very restricted angular range was chosen to decrease the angular range as far as possible whilst maintaining enough incident light to resolve the peak in the spectral profile. Constricting the angular range decreases the size of the spot reflected from the cells, as shown in figure 1.10. This effect is caused by the curvature of the cell wall which makes the visible reflected spot dependent on the angular incidence. Constricting the size of the reflected spot is beneficial because it reduces the effect of overlapping reflections from other cells being accidentally included, and improves the focusing accuracy. Decreasing the angular range of incident light also simplifies the assumptions in the multilayer model, making it more accurate.

Spectral Measurement Spectra were recorded by coupling the focused light into a centrally aligned optical fibre (Avantes or OceanOptics 50 - 600 um internal diameter) attached to a spectrometer (Avantes AvaSpec-HS2048). The recorded spectrum was visualised live using a MATLAB interface. Recorded spectra had a subtracted background and were normalised with respect to full intensity reflection from a silver mirror (Thorlabs, PF10-03-P01 25.4 mm) with relevant optical components in place. The integration time was chosen to ensure a high enough intensity was recorded to see the profile of the spectrum clearly. Characteristic spectra are shown in figure 1.12 with a Gaussian fit applied. Raw and normalised spectra were saved for each measurement.

The microscope was focused manually. As shown in figure 1.11, defocusing introduces a difference of $\pm$ 20 nm although the peak remains identifiable. Photos of the

cells show a very good consistency of focus for all the cells indicating that this is not a major source of error. However, focusing on light reflected from structurally coloured material does in some instances represent a challenge in itself due to the way in which the light is reflected from a volume rather than a plane. There is a significant change in the defocused spectrum which shows also a decrease in the intensity of the peak when the change in the peak wavelength is $\pm$ 12 nm. This strong variation point therefore appears to be a good estimate of maximum error in peak identification.

Linear Polarisation Polarisation filters were used in some instances, where stated. For crossed and parallel polarisations, two linear polarisers were inserted as indicated in figure 1.9. The incident light polariser (Zeiss 427710-9000 hand rotated) was set parallel or orthogonal to the upper linear polariser (Thorlabs 25 mm wire grid polariser) which was rotated by a motorised controller (Thorlabs TDC001) interfaced by APT software. The reference spectrum was taken in parallel polarisation configuration.

Polarisation filtered images and spectra are referred to as 'cross polarised' or 'parallel polarised' to indicate where reflected light was collected using these configurations of linear polarisation filters.

Circular Polarisation For measurements taken in left or right circular polarised light, the incident linear polariser was not inserted as above and unpolarised light was incident on the sample. An additional quarter waveplate (Thorlabs 25 mm) was mounted below the output linear polariser, also controlled independently by motorised controller / APT software as in linear polarisation measurement.

Polarisation filtered images and spectra are referred to as left or right circular polarised to indicate that the measurement was taken using circular polarisation filters in either configuration. Light may also be referred to as being in the left or right circularly polarised 'channel', indicating the polarisation mode that is passed by the left or right circular polarisation configuration. For the definition of handedness of each circular polarisation, figures 1.4 1.5 and 1.7 may be referred to.

As discussed in section 1.2, circularly polarised light of one handedness is equivalent to a superposition of two orthogonal linear polarisations. Therefore, polarisation filters are used to compare either cross and parallel polarised reflection or left and right circularly polarised reflections.

K-Space K-space measurements were done by inserting a Bertrand lens (Zeiss, 453671-0000-000) as in figure 1.9. This allows the image conjugate plane to be

viewed, thereby imaging the light reflected from the specimen according to its angular distribution. Structurally coloured materials are often iridescent meaning the reflected wavelengths have an angular dependence. This information, although frequently clear by eye, is impossible to capture using bright-field imaging which illuminates and collects light normal to the surface.

Dark-Field Dark field microscopy illuminates the sample only with high angular incidence light, and collects all scattered light. Due to the very low illumination intensity from cutting out the low-angularly incident beam and the need to pass high-angled light to the specimen, the numerical and field of view diaphragms were both maximally dilated unless otherwise stated. Incident light in this case was at about 37º. Dark field imaging is used to emphasise light reflected from off-optical axis structures. This light is not captured by restricted numerical aperture bright field imaging because the high angle light is eliminated. Moreover, even with a dilated aperture, the high intensity of the normal reflection tends to dominate in bright field imaging, justifying the use of dark field illumination to distinguish the contribution from tilted interfaces.

Water Immersion Water immersion objective lenses used were Zeiss W N- Achroplan 10x and 40x magnification. Fresh DI water was pipetted onto the lens tip and then the adhered droplet was brought into contact with the sample for focusing and imaging. Spectra were referenced in water-immersion configuration. Water immersion is a technique used to reduce the reflected light from smooth upper surface refractive index contrast.

Transmission Transmission optical microscopy is not often used in this thesis because most of the structures investigated are structurally coloured in reflection. When transmission illumination is used, light from a halogen lamp (Hal 100) was passed optionally through a linear polariser (Zeiss A1 polariser D 427706) and focused through a condenser (Zeiss 424225-9001) onto the sample from below. Light collection was via the same method as for reflection.

Electron Microscopy

Scanning Electron Microscopy (SEM) Two different ordinary Scanning electron microscopes were used: in the Cambridge Nanoscience Centre (LEO GEMINI 1530VP FEG-SEM) and in the Department of Chemistry (Zeiss Leo Gemini 1530VP system). Prior to imaging, the sample was mounted on double-sided carbon tape on a metal SEM sample stub and then plasma coated with a 10 nm thick Au, Au/Pd, or

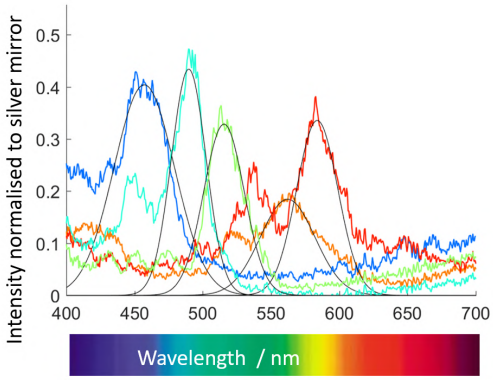

FIGURE 1.12: Spectra with a background removed and normalised by the total spectral reflection from a mirror are recorded. The curves correspond to coloured peaks, indicated by the spectrum image underneath the corresponding wavelengths. The peaks may be smoothed to remove noise, and fitted using Gaussian peaks. However, single Gaussian peaks do not always accurately represent true peak profiles.

Pt/Pd layer to make the surface conductive. The sample was imaged in a low vacuum chamber generally at 3.00kV except where very strong charging was visible, when the voltage was reduced to 1.5kV. Imaging was carried out with the beam at normal incidence.

Cryo-SEM The customised cryo-SEM system (FEI Varios 460 microscope with Quorum PP3010T cryo-SEM preparation and transfer system) at the Cambridge Advanced Imaging Centre (CAIC) was used to image fresh, hydrated specimens. The sample was prepared by insertion into a specially-adapted metal stub and held in place by slightly viscous carbon glue (Colloidal graphite (Aquadag) AGG303).

The sample was frozen by sudden immersion in liquid ethane cooled in a -196°C liquid nitrogen bath. The rapid infiltration of ethane flash freezes the cell contents without the growth of ice crystals, causing minimal disturbance to the cell contents. The sample was then transferred to a nitrogen-cooled vacuum chamber at -175°C and 10^{-5} Pa. A horizontal blade was used to fracture off the top part of the sample with a flat horizontal break, and the chamber temperature was raised to -145°C for five minutes to drive off surface ice through sublimation. The horizontal blade was placed a couple of millimetres above the surface to remove surface water by condensation onto the blade. The sample was then sputter-coated with gold for 60 seconds at 20mA to give it a conductive surface. This coating was on the order of 1 nm thick.

Resin Embedding and Transmission Electron Microscopy (TEM) TEM images are included, this work was done by collaborators Dr Paula Rudall, Dr Edwige

Moyroud and Dr Yu Ogawa. The method is included here for completeness. Samples were fixed in 3% phosphate buffered glutaraldehyde followed by 1% osmium tetroxide. Fixed samples were taken through a graded ethanol and LR White resin series prior to embedding. They were cut using a microtome (Reichert-Jung Ultracut), mounted on copper grids and stained (uranyl acetate and lead citrate) before being imaged in TEM (Hitachi H-7650 / AMT XR41 digital camera). Where indicated, the resin embedded sample faces from which the TEM sections were cut were also imaged using SEM as above.

1.5.2 Spectral Data Analysis

The methods used for analysis of the spectra are detailed in each of the sections treating developmental data in the subsequent chapters. Slightly different measurement strategies in each observation series necessitate different methods for isolating and analysing the structural colour component. However general methods for analysing the structurally coloured peak in chapters 3 and 4 are detailed here.

After the subtraction of the scattered background, the peaks were analysed. The data was smoothed using a moving average filter over 20 points, equivalent to 11 nm, in order to reduce noise. Smoothing introduces a slight uncertainty in the peak measurement, although this is smaller than the ± 6 nm identified as a maximal error due to focusing uncertainty.

Peak Identification

The peak boundary minima were identified and a MATLAB function was used to identify the peak's characteristics. Two models were used to do this, a single peak Gaussian fit and the simpler findpeaks, which identifies local maxima.

The Gaussian fit has the benefit of resilience to noise, as it should better fit a spectrum on the basis of its whole shape. However, the Gaussian model for the spectral peak is unrealistic because a structural colour peak should not in the real system conform to a Gaussian peak. Expecting a complicated asymmetric spectral profile with multiple peaks means that we are required to assess the importance of what characteristic of the spectrum is being considered here.

A comparison of the two methods of peak measurement showed that there was no difference in the trends measured. A comparison showed no bias to longer or shorter wavelengths between the two methods, with a standard deviation of 6 nm in the difference. The Gaussian fit tended to underestimate the peak intensity, because it failed to model narrow, sharp peaks within a wider envelope. Although each analysis gives a slightly different value for the intensity and peak wavelength for each spectral peak, the differences are small and there is no overall trend.

The findpeaks function was chosen over the Gaussian fit as the most appropriate measure. In seeking to characterise the growth of structural colour peaks in nature, the peaks are assumed to result from non-uniform multilayers. The varying pitches and interference from multiple typical lengthscales are therefore important, as are the changes undergone during that time. Although it is not possible to predict the exact material architecture given the limited data available, trends in the profile asymmetry witnessed in the case of multiple cells could be instructive in understanding material development. Therefore the apparently more simplistic measure of the local maximum is appropriate.

Each of the spectra were processed using the method described above. The identification of each peak were manually checked to ensure that the algorithm correctly identified the most prominent peak and not for example an erroneous noise signal. Peaks identified in spectra where the size of the peak were smaller than the level of noise were removed from the dataset. The spectra were also cross-checked with the photos to remove any measurements which were the result of a misidentification, misfocusing or misorientation of the target cell.

Trend Fitting

In order to understand the trends observed in the data as a function of time, a linear mixed effects model is used. This is a statistical model which fits a linear trend to the data set, according to a 'fixed effect' - time, the predictor variable. The model also takes account of the 'random effect' - each cell's identity, the categorical variable. This allows for an analysis of the time-dependence of each individual set of cells.

The mixed effect model fitting procedure evaluates two models:

$$\lambda \sim 1 + t + (1|cell) + (t|cell)$$
$$\lambda \sim 1 + t + (1 + t|cell)$$

where t is time, λ is the dependent variable, and *cell* is the categorical variable. Comparison of the two models indicates the influence of the extra parameter in the second equation, which correlates the intercept and the gradient for each category.

This fitting procedure is implemented using MATLAB, and the goodness of fit discussed in the text. The influence of the random variables is ignored, because the overall trend is the correlation of interest.

1.5.3 Numerical Model

The optical analysis of the fruit cells was complemented by a model using a transfer matrix method following Berreman, as detailed in 1.2.3. This technique produces a simulated reflection spectrum from an input multilayer material pitch profile. The code was developed by Bonan Zhu to model a helicoidal birefringent material and was previously demonstrated to well describe artificial photonic CNC films. [37]

A brief overview of the numerical model and a description of its use is given here.

Ideal Helicoid Model and Parameters

From early SEM images, initial values of the multilayer were taken and a related uniform multilayer was identified. This multilayer is modelled as a CNC helicoidal multilayer with 20 layers with a uniform pitch of 150 nm, n = 1.58/1.52 without additional absorption within or outside of the material, and white light incident at 0 degree normal. The reflection spectrum from this uniform multilayer was modelled and is shown in 1.13, plot A. The method produces a modelled intensity as a proportion of one circular polarisation of light, which is half the total intensity of unpolarised light.

Each of the parameters in the model was varied individually and are demonstrated in 1.13 and 1.14. Each parameter in the model is discussed below. The use of a CNC helicoid ignores the existence of other molecules and the differences between microfibrils and crystals.

Average Refractive Index A variation in refractive index might occur through the inclusion of an isotropic additional molecule, a change in the density of the cellulose microfibrils, or another difference in the characteristics of the microfibrils. The refractive index of *Pollia* microfibrils has not been directly measured and might differ slightly with respect to previously reported values of microfibrils.

Figure 1.13 B shows a difference in peak wavelength over the extreme range of refractive indices of 20 nm, with the higher refractive index giving a longer reflected wavelength, and slightly lower intensity. The higher refractive index increases the effective wavelength of light, which is why a longer wavelength is reflected.

The degree of variation was chosen to keep the average refractive indices within the range of realistic biological refractive indices. The range includes values extracted from published literature, $n_e = 1.586, n_o = 1.524$ [38] and $n_e = 1.603, n_o = 1.523$. [39] Neither of these measurements were made on a composite cellulose material,

but instead on free particles, and may therefore be inaccurate for the fruit material. The literature values are plotted in figure 1.15 to demonstrate the effect of choosing $n_e = 1.586, n_o = 1.524$. This value was taken to be more relevant as it was taken for structurally coloured helicoidal cellulose, rather than a microfibril from an unrelated, non-helicoidal and non-structurally-coloured material. [38]

Angle of Incidence The angle of incidence (and therefore reflection) is modelled and the results of incoming angle variation shown in figure 1.13 C & D. We understand from this numerical model that although a difference of incident angle of $\pm$ 5^o has a negligible effect on the wavelength and intensity of the reflected peak, a more substantial difference, of 37^o decreases the peak wavelength by 30 nm.

As described in the optical experimental section, during observation the numerical aperture of incident light was controlled and constricted to the minimal practicable value in the experimental measurement, and estimated to be $\pm$ the order of 5^o. As indicated in figure 1.10, it is expected that only structures with local planes normal to the optical axis reflect light back to the objective. The assumption is taken therefore, that a negligible range of angular incidence for modelling matches the experimental technique.

Pitch The pitch variation in the multilayer is shown in figure 1.14, A. Pitch is a key parameter defining the maximum wavelength. The pitch of the material might change for numerous reasons during growth, including the expulsion or inclusion of additional molecules, such as water or lignification. This might be expected given the transition undergone by the fruit. Notably in a self-assembling suspension such as CNC film, the pitch of the helicoidal assembly is seen to decrease during the assembly time. [38] This occurs as the particles are drawn closer together, gradually forcing the liquid matrix out. Self-assembly is not the only physical mechanism which could be responsible for a changing material pitch during growth, which might occur due to dehydration, enzyme activity or other molecular infiltration.

Absorption Unlike pigmentary reflection, absorption of light is not a necessary component of an ideal structurally coloured material. However in real material, light may be absorbed. This is included in the model using a complex refractive index, which dissipates part of the incident light. The cellulose material will be shown to be mostly transparent (see figure 2.8), making a small imaginary component likely. A variation of the complex part of the refractive index is shown in 1.14 image B. This absorption accounts for the structural colour material dissipation. The effect of absorption by other pigments in the material surrounding the multilayer

further compounds the intensity decrement with an additional fraction of the intensity lost.

Degree of Birefringence The degree of birefringence is varied in figure 1.14 C. An increase in the birefringence of the system increases the intensity of the reflected peak, without changing the wavelength of the peak. In a helicoidal system with no birefringence, there is no reflection. A difference in the real values of birefringence from the estimated values would be expected in the case of greater or lesser isotropy. Birefringence is the difference between the two optical axes of the material, so an increased difference in the optical anisotropy increases the birefringence.

Boundary Refractive Indices A final two refractive indices are of importance in the analysis of the material, that is the refractive indices of the materials directly above and below the multilayer. These variations were modelled and produce no difference in the resultant spectrum within the resolution of the numerical model. Both results are identical with 1.13 A.

Number of Pitch repeats An increasing number of pitches in the multilayer are modelled in 1.14 D. The more pitches are included, the larger the peak reflection is. The effect is consistent with each addition from a very low number of pitches. The maximum wavelength is not changed by an increasing number of pitches of identical length. The number of pitches is expected to increase in the cell wall material during growth because the general cell wall development model outlined in 3.1.2 describes microfibrils being extruded continuously from the membrane and laid down on the cell wall in layers, building up a periodic pitch profile. For the avoidance of doubt, a 'layer' in the multilayer model corresponds to one pitch.

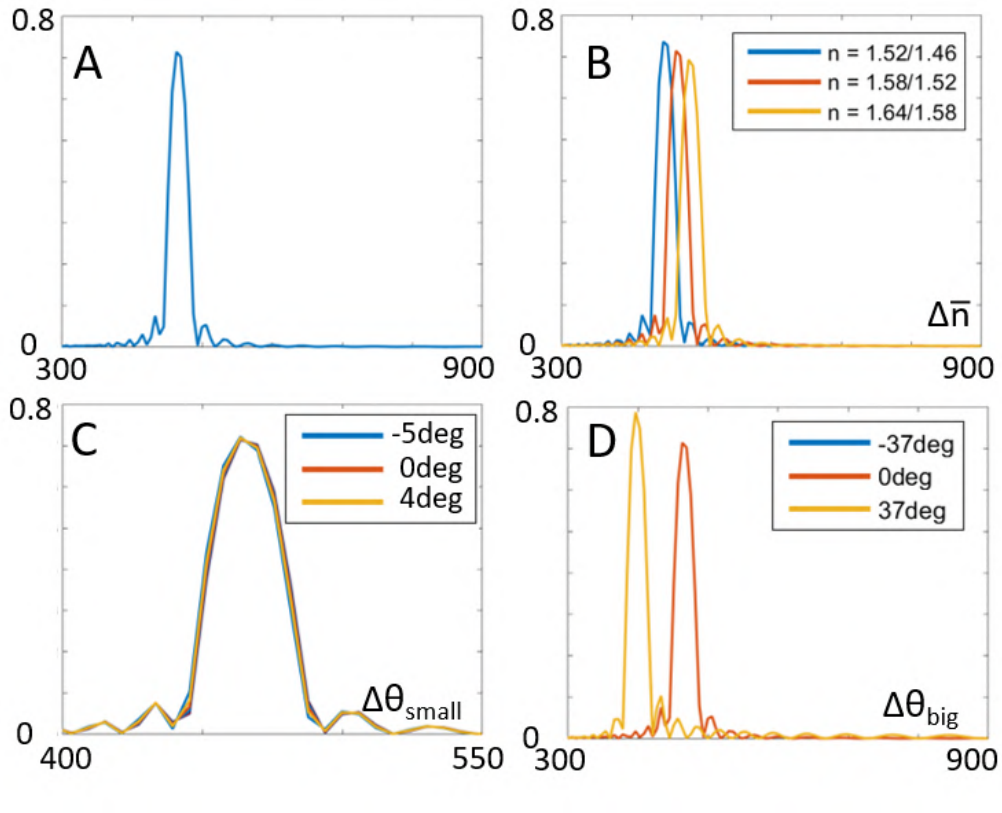

FIGURE 1.13: Different parameters are changed one at a time on a perfect uniform multilayer model. The original spectrum with 0 degree incidence, 20 layers, 150 nm pitch, n = 1.58/1.52 and no imaginary part, is shown in plot A. B shows a change in average refractive index, with the birefringence constant. C-D show a variation in incident angle, small angle variation as used experimentally is shown in plot C. X axis is wavelength / nm, Y axis is intensity as a proportion of left circularly polarised light.

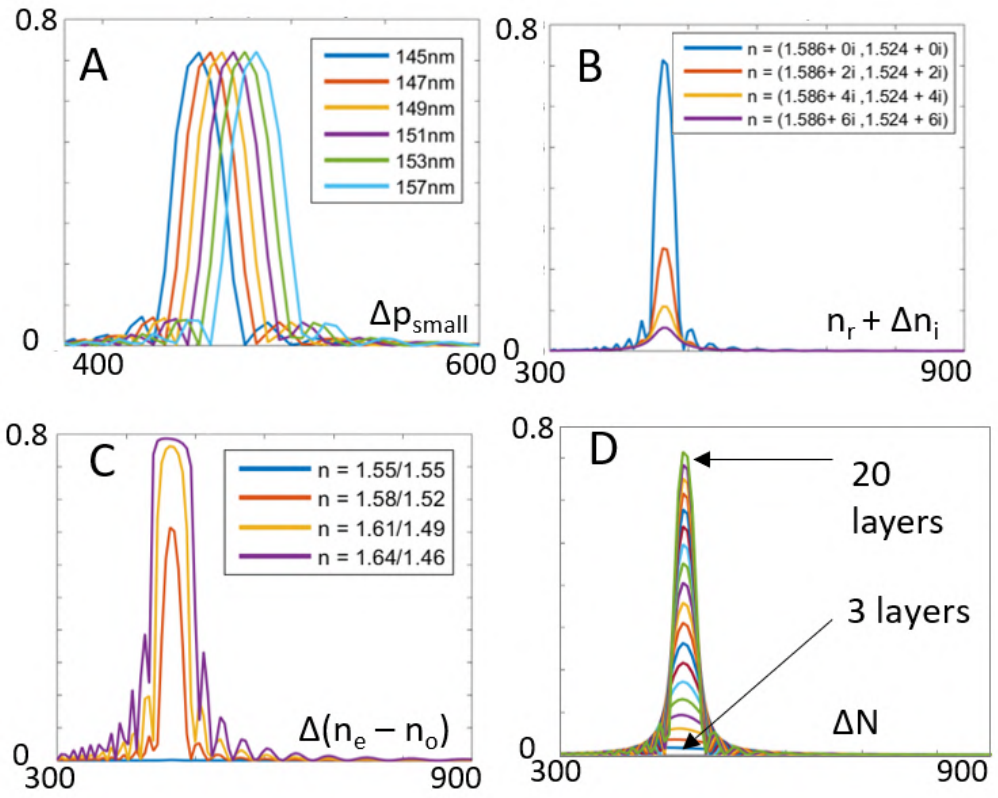

FIGURE 1.14: Different parameters are changed one at a time. The original spectrum, 0 degree incidence, 20 layers, 150 nm pitch, n = 1.58/1.52 no imaginary part, is shown in 1.13 plot A. In this figure, plot A shows a change in pitch length. B shows a change in the imaginary part of the refractive index. C shows a difference in the relative difference between the two orthogonal refractive indices n_e and n_o. D shows an increasing number of profile layers, between 1 and 20 showing increasing intensity. X axis is wavelength / nm, Y axis is intensity as a proportion of left circularly polarised light.

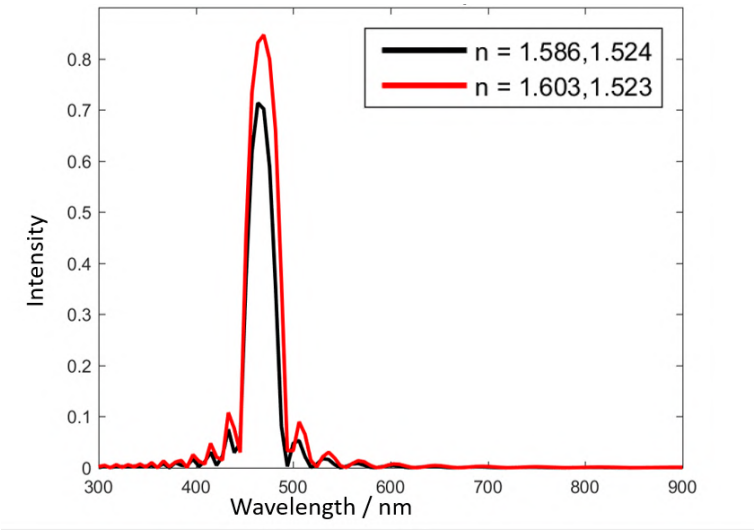

FIGURE 1.15: This plot compares the two values of cellulose birefringent refractive indices found in scientific literature, in order to compare the effect of choosing one over the other. [38] [39] For this plot a 0 imaginary part of the refractive index is assumed.

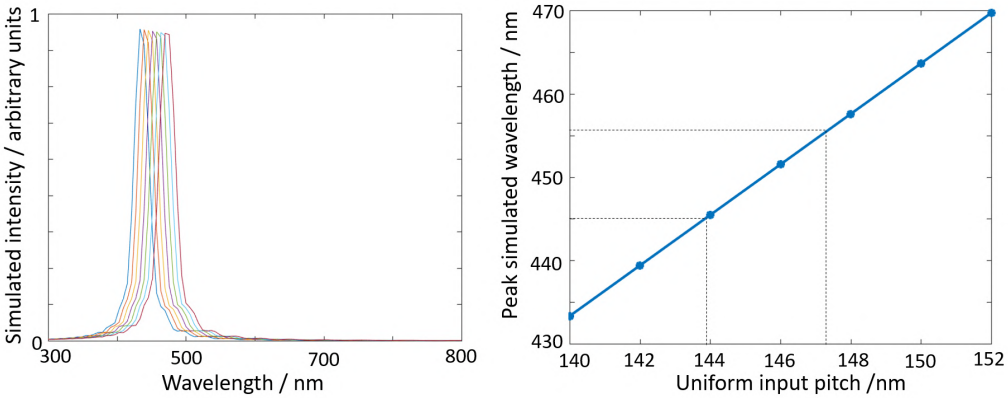

FIGURE 1.16: The left hand plot shows a number of peaks modelled using different realistic pitch lengths. The right hand side plots the pitch length against the peak wavelength of the modelled spectra. This correlation is linear.

Analysis of Cross-sectional Profile of Pitches From Electron Microscopy Images

In order to apply the numerical model to real materials, electron microscope images of cross-sections through fruits were analysed to produce a profile of pitches. An error of at least $\pm 10\%$ and sometimes as much as 30% in the lengths measured is predicted for biological TEM analysis due to the use of resin-embedding and dehydration in electron microscopy sample preparation. [40] This is dependent on the material and preparation procedure. Analysis of resin-embedded materials is however valuable, because of the controlled orthogonal cross-section that can be cut into embedded samples. Profiles were also taken from SEM images where a controlled orthogonal cross-section was achieved. This was possible on microtomed resin-embedded samples as in TEM. It was also possible in some orthogonally cut cryo-frozen samples. This profile measurement is used as a starting point for modelling to compare with the observed optical measurements.

Figure 1.17 shows the procedure for extracting a profile using image analysis software ImageJ [41] via the distribution FIJI. [42] The analysis of images is done by measuring the periodicity of the intensity of the average pixels across the cholesteric axis on the electron microscope images, as illustrated in figure 1.17.

The modelled optical reflectance from a material defined by measurements extracted in this way is shown in figure 1.18 plot A. The variations in the model parameters from figures 1.13 and 1.14 were then applied to the same profile to demonstrate how modification of the electron microscope image data within realistic parameters would be expected to change an experimentally measured profile. The same variations in the peak characteristics modelled for the ideal case are observed for the experimentally measured profile.

This cross-sectional profile, described in terms of a series of pitches is referred to as the 'pitch profile'.

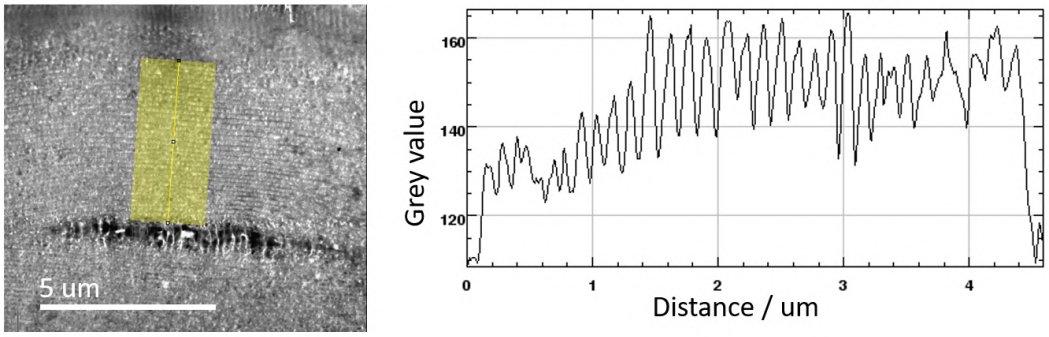

FIGURE 1.17: The left hand image shows a thick section of *Pollia* cell wall imaged in TEM (by Dr Paula Rudall) and measured in ImageJ. The profile on the right is the intensity along th elength of the yellow line on the right hand image, averaged over the pixels over the line's width . Electron brightness is dependent on microfibrillar orientation, the oscillations on the plot therefore allow the measurement of the pitches in the material.

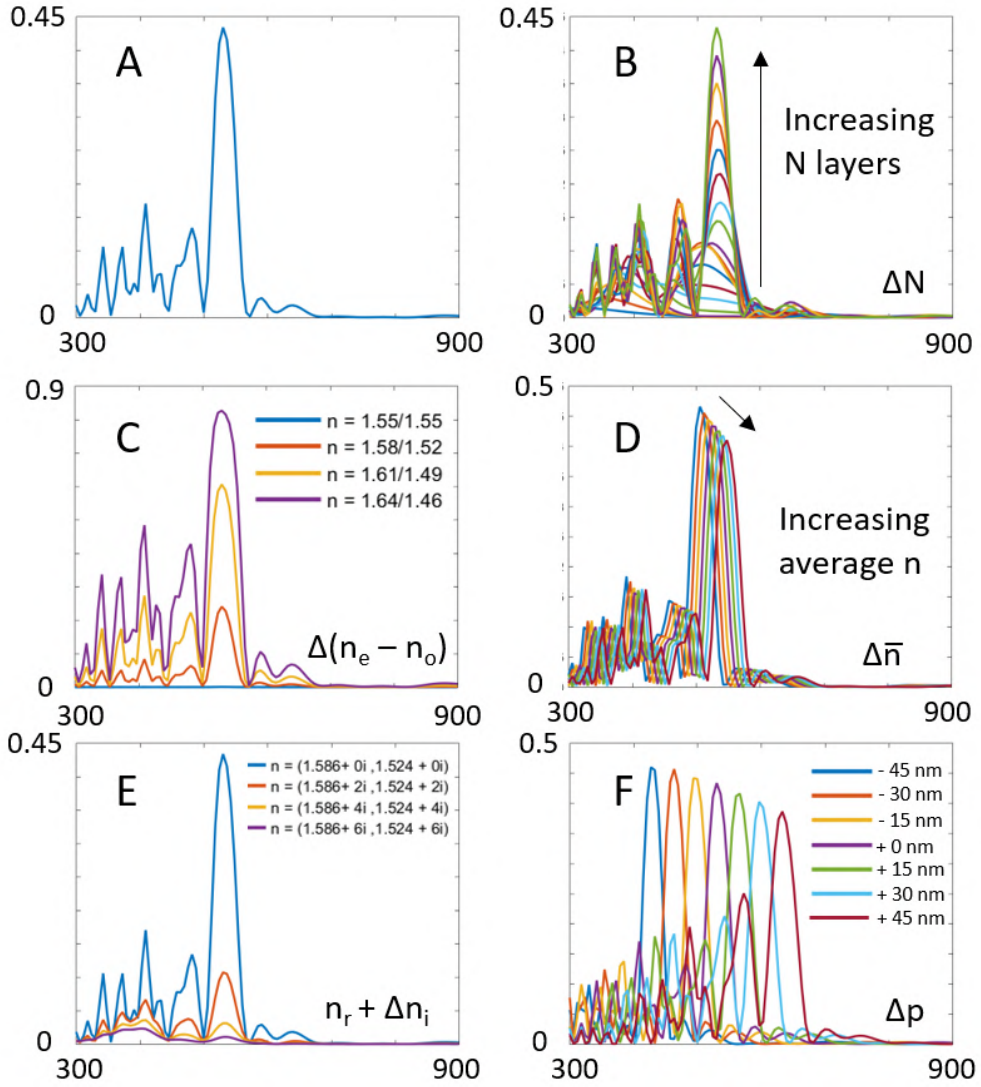

FIGURE 1.18: A pitch profile was extracted from a real SEM image, and used to model a 'realistic peak'. The parameters of the model were varied as before in figures 1.13 and 1.14. Plot A shows the initial parametrisation as before: 0 degree incidence, n = 1.58/1.52 + 0i. Plot B shows a gradual increase in the number of layers from 0 to the full measured profile, 40 layers. C shows an increase in the imaginary component of the refractive indices. D shows a change in the average refractive indices with a constant birefringence. E shows a variation in the difference between the two refractive indices in the plane. F shows expansion and contraction of the pitch lengths while keeping the variation the same. The X axis is wavelength / nm, Y axis is intensity, as a proportion of left circularly polarised light.

Variation and Averaging

A key difference between the numerical model and experimental reflection peak so far is that the model peak is produced from just one pitch profile. In order to accurately model an experimentally measured spectrum, a number of varied profiles must be averaged. Analysing the degree of averaging and variation is important in order to properly model an experimental spectral profile.

The cell wall multilayer is not very thick, with fewer than 40 layers. The cell pitch profile has a high degree of variation within the low number of layers. The variation of the pitch length is independent of depth within the multilayer, unlike in a chirped multilayer or other pattern. [43]

Unrelated profiles with pitch variation within the same distribution cannot be averaged to produce a realistic profile because of the low number of layers. Variation within one cell is smaller than the variation between cells. Therefore pitch profiles are averaged with additional profiles adapted from the original by a small variation.

Any randomly chosen optical measurement and electron microscope cross-section will therefore also not be comparable with one another. The obstacle of optically analysing and then finding and cross-sectioning the same cell in SEM makes the comparison of a single optical profile and its own pitch cross-section in SEM impractical. Artificial profiles with the distribution of variation within characteristic standard deviation of the cell wall are therefore generated in order to model experimental measurements. Characteristic standard deviation was measured from electron microscopy images to be between 20 and 40 nm, this is therefore the range within which artificial pitch profiles are generated.

Pitch Variation In order to understand the role of variation in the construction of a single pitch profile, profiles with pitches distributed around the same mean, but with increasing standard deviation were generated. The optical reflection from these pitch profiles was modelled for each case and the spectral intensity profile is shown as a a heatmap in figure 1.19.

The characteristics of the peaks in this plot were assessed and plotted for each value with increasing standard deviation in figure 1.20. From this we see that an increased standard deviation reduces the intensity and prominence of the primary peak (A & D), makes the primary peak wavelength variable (B), makes the peak slightly wider in general (C) and above 15 nm increases the number of individual peaks in the profile (E).

In order to choose a reasonable standard deviation for artificially generated pitch profiles, variation in electron microscopy images was measured and the modelled optical responses compared to experimental data.

Averaging The average variation of the pitch lengths within one cell was assessed in order to understand the appropriate degree of averaging to be included in the model. The collection spot of the optical fibre was 30 um wide, however, in practice the light was collected from a smaller area than that, corresponding to the width of the reflection spot which is the low-angle central region of the upper cell wall.

Profiles were measured over the full extent of the cell cross-section for several cells in order to characterise the intracell variation of the pitch. Across the full distance of the top of each cell, the mean difference over the cell was found to be 9 $\pm$5 nm. Averages were therefore made over variants on the input profile of standard deviation 10 nm in order to get a reasonable indication of variation in the spectrum reflected from a single cell.

Intensity The intensity result from the model was much higher than is recorded from experimental measurements. There are a number of good reasons for this. The real case includes additional cell wall material beyond pure cellulose crystallites and there is a layer of cuticle on top of the reflecting cell material. The geometry of the cell is curved and not perfectly ellipsoidal, making the reflection-spot irregular and often not covering the entire collection spot. The measured intensity was found to be on average for comparable cases about 5 times less intense than the modelled intensity. This is therefore taken as a rough estimate to make the modelled brightness scale roughly comparable for all modelled intensities unless stated.

It is assumed that the light intensity is better modelled as a fraction of the profile produced by reasonable parameters rather than the identification of parameters which will produce a light intensity to match the experimental data. This assumption has been thoroughly considered. As has been discussed in this section, there are many reasons for which reflection intensity may be reduced in a multilayer model, for example an increased imaginary component in the refractive index, a decreased refractive index contrast, or much lower numbers of layers than apparent.

Given the lack of knowledge about the material of the structurally coloured cell walls modelled in this thesis, these parameters undoubtedly play a role, however estimating the extent of that role for each of the different components is considered to be over-parametrisation producing unrealistic conclusions. The parameters used are therefore those associated with the helicoidal multilayer for which the model has proved itself effective. The model is used to identify qualitative rather than quantitative results.

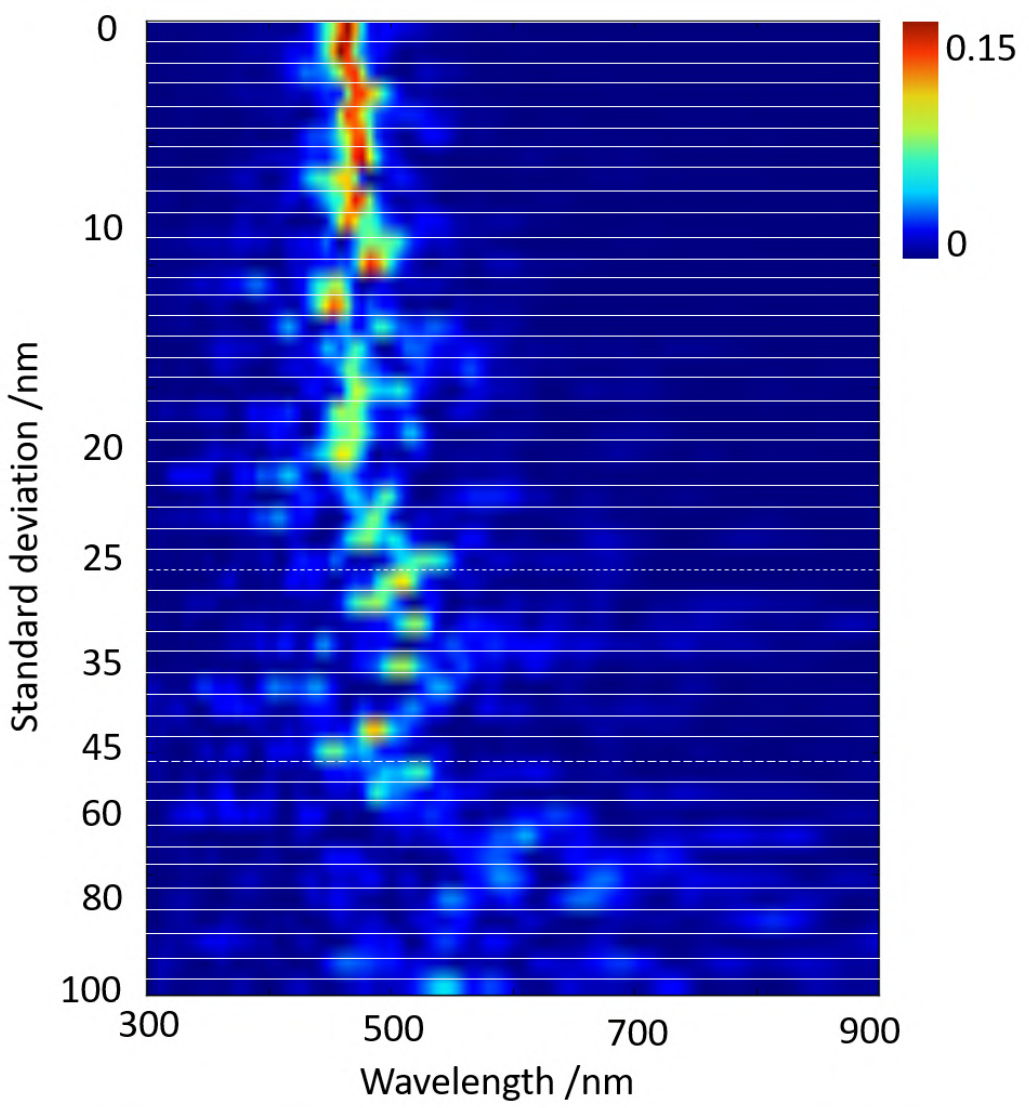

FIGURE 1.19: A number of profiles were generated with twenty layers, an average pitch length of 150 nm and a variable standard deviation. The heat map shows the intensity spectrum modelled for each profile.

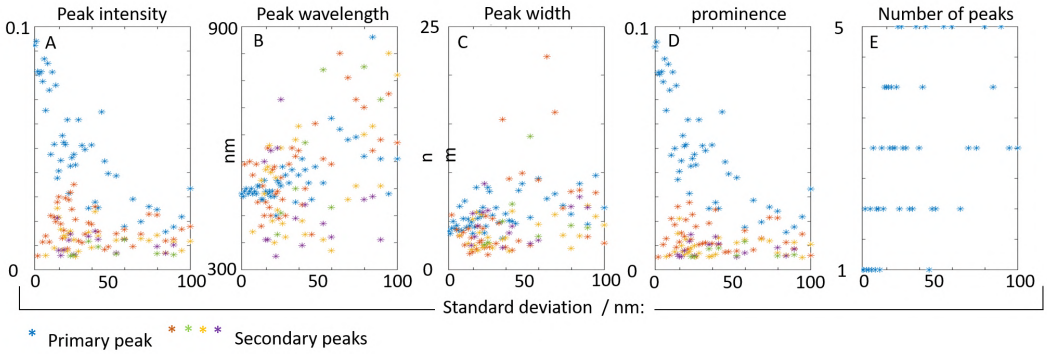

FIGURE 1.20: The peaks generated in 1.19 were analysed and the key features plotted. A. Peak Intensity. B. Peak wavelength. C. Peak width. D. Peak prominence. E. Number of peaks. Peaks were categorised in terms of relative intensity (1st is the most intense). A and D show that increasing variation correlates with decreasing intensity and prominence for the primary peak. Peak wavelength also varies from the value produced by the uniform profile as the standard deviation increases.

Chapter 2

Structural Colours in the Genus *Pollia*

2.1 Introduction to Biological Structural Colour

2.1.1 Structural Colour

Photonic crystals are responsible for the most brilliant and intriguing colours in the natural world, from peacock feathers [44] to squid skin, [45] vervet monkeys and baboons, [46] copepods, [47] weevils, [48] bacterial colonies, [49] marine worms, [50] viruses, [51] limpet shells, [52] butterflies, [53] and beetles, [54] as well as in non-biological structures like opals [55] and the rock labradorite. [56]

The distinctive nature of these colours, particularly their iridescent and metallic appearance has been known for a long time, and attempts to understand the effects pre-date Hooke [57] who used optical microscopy in its infancy to try to understand the role of structure.

The development of electron microscopy in the second half of the twentieth and into the twenty-first century has been the key to discovering the complex range of nanostructures in nature responsible for structural colour. Electron microscopes probe materials on lengthscales smaller than visible light which is necessary to understand the physical structures involved. The use of this experimental technique, combined with the electromagnetic and crystallographic theories described in the first part of this chapter have brought the field of structural colour to maturity.

Their endless fascination has provoked many reviews. [58] [59] [60] [15] [61] There are still after a century of work, [62] significant numbers of new structural colour tissues and species [63] being reported in contemporary scientific literature, as well as reports disentangling the effect of pigments and structures in natural colouration. [64] The subject has generated a wide interest due to the interdisciplinary ways in which it is approached. From a biological perspective, the reports pose the question of how these structures develop. In physical optics and engineering, current

research is also attempting to recreate mimetic materials that capture the optical effects in nature for artificial materials, in some cases taking direct inspiration from nature.

2.1.2 Structural Colours in Plants

Photonic crystals in plants and algae are far less well-studied than structural colour in other organisms [65], although a fast increasing number of unrelated species have been shown to make use of the phenomenon. In this section I give a brief overview of three different types of structures reported: diffraction gratings, multilayers, and helicoidal multilayers. Three dimensional photonic crystals are much rarer, although an example has recently been reported in the brown algae *Cystoseira tamariscifolia* which has an opaline iridosome containing highly-ordered lipid vesicles. [66]

Many of the species reported reflect blue colours which it has been suggested is in part due to the difficulty of achieving blue colouration via pigmentation. [67] [68] A particularly prominent group of structurally coloured plants are tropical understory species, living at ground level in rainforests and exposed to extreme light and shade they frequently display an ultraviolet or blue structural colour. [69] This characteristic is sufficiently widespread that it appears to have an adaptive benefit in this environment. For the majority of the structurally coloured plants, no definitive ecological-adaptive function has been demonstrated, although a number of proposals have been made. A notable exception are the diffraction grating species described in section 2.1.2.

Diffraction Gratings

Flower petals have been shown to display directional-reflection optical effects in their outer epidermis such as flat, mirror-like cells, which in one species acts in combination with pigments to mimic its female pollinator. [70] [71] The use of directional reflection has also been measured in buttercups. [72]

Although these examples of directional reflection rely on structural effects for enhancement, the colours are primarily pigmentary. Structural colour has however also been reported from flower petals as the result of striations in the outer cuticular layer acting as an independent diffraction grating. [73] [74]

Last year, we reported the existence of disordered diffraction gratings on a wide range of flower petals, and showed that these were responsible for a 'blue halo', an broad angular-dependent blue reflection. A blue halo effect was reproduced on artificial flower models and it was demonstrated that this enhanced bee foraging efficiency in a lab environment. [67] Figure 2.1 shows some data from this work,

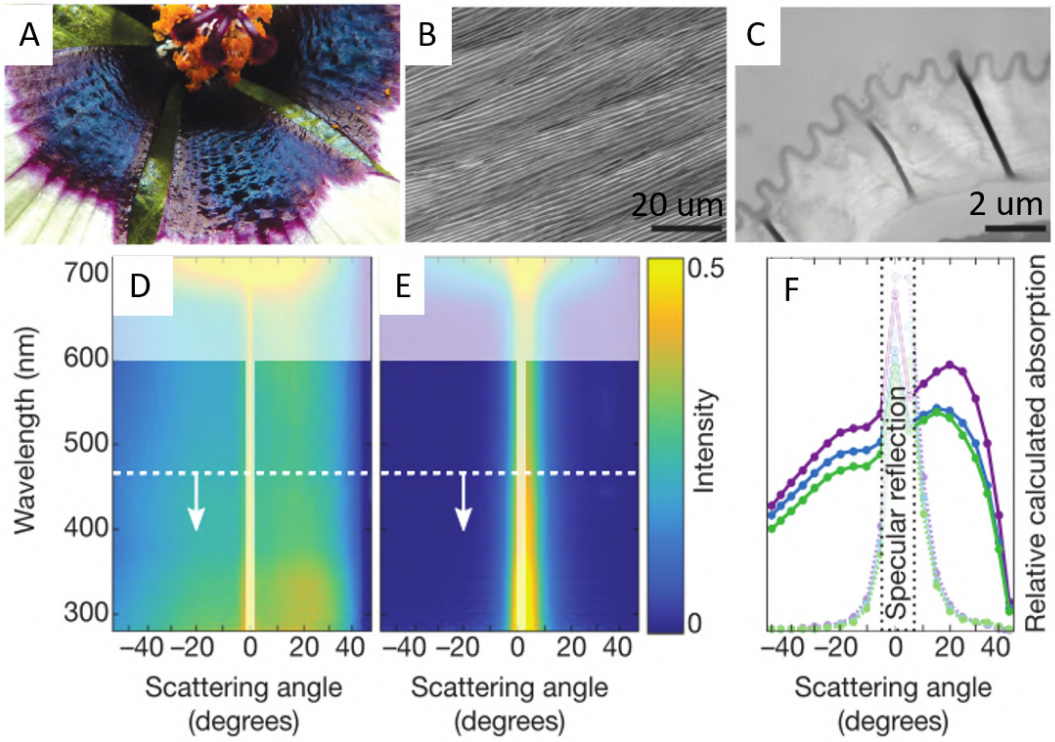

FIGURE 2.1: Figure adapted from material published in [67]. *Hibiscus trionum* A. photo showing iridescence. B. SEM of striations on the cell epidermal cuticle. C. TEM of a cross-section through the striations. D. Angular reflection from the petal illuminated at 45° perpendicular to the striations. E. Angular reflection from the petal illuminated at 45° parallel to the striations. F. Reflection data from D (bright lines) and E (pale lines) weighted with respect to bee eye photoreceptors in UV, blue and green. A-C were taken by coworkers, D- F were measured by the author.

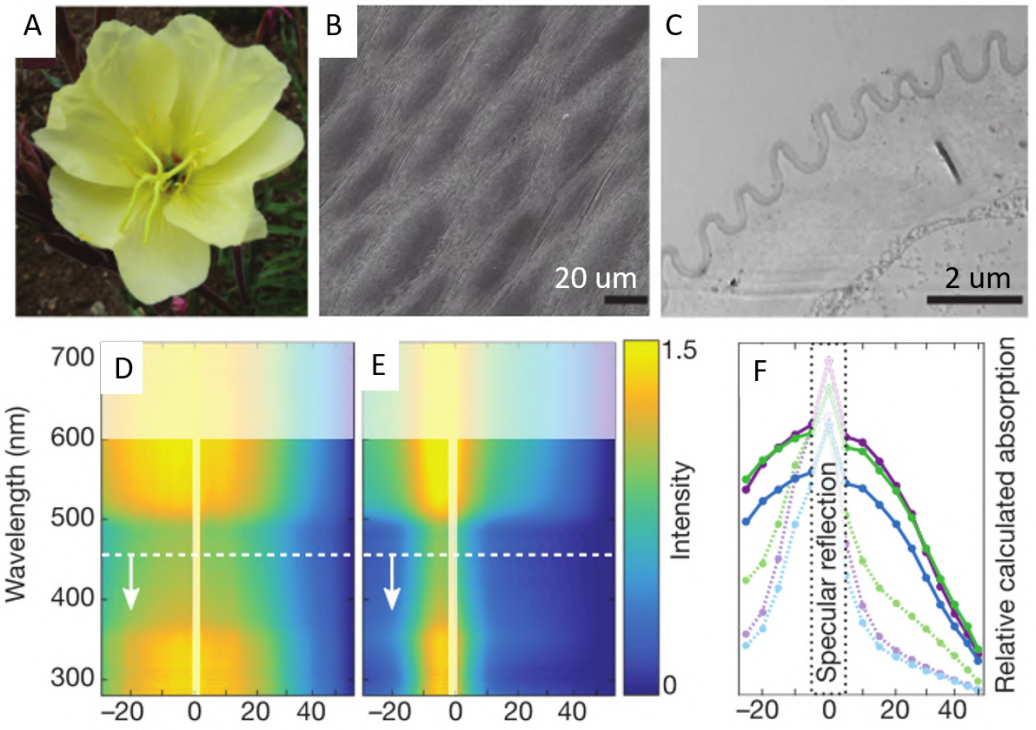

FIGURE 2.2: Figure adapted from material published in [67]. *Oenothera stricta* A. Photo. B. SEM of striations on the cell epidermal cuticle. C. TEM of a cross-section through the striations. D. Angular reflection from the petal illuminated at 30° perpendicular to the striations. E. Angular reflection from the petal illuminated at 30° parallel to the striations. F. Reflection data from D (bright lines) and E (pale lines) weighted with respect to bee eye photoreceptors in UV, blue and green. A-C were taken by coworkers, D- F were measured by the author.

demonstrating a visible iridescent colouration (A), and the diffraction grating structure from which it originates (B and C). The light reflected from the structure in directions perpendicular (D) and parallel (E) to the striations are shown and compared (F) in order to demonstrate the measurable blue halo on the flower of the *Hibiscus trionum*.

The optical analysis of surface diffraction gratings is not described in this thesis, but is extensively covered elsewhere. Analysis of the disordered gratings modelling the floral striations was done using Finite Difference Time Domain (FDTD) analysis, in order to understand the effect of disorder on the diffraction, demonstrating that disordered gratings produce a blue halo.

Highly angular-dependent 'perfect' iridescence makes object recognition worse for bumblebees, [75] unlike disordered floral iridescence which apparently make use of the enhanced colouration of diffraction effects whilst retaining a consistent appearance by a specifically blue and wide-angle reflection . [76]

The interplay between pigment and diffraction grating colour has been investigated, although not definitively described. The relative brightness of iridescent and pigmentary effects were shown to be important in the visibility of objects to bees. [77] The visibility of grating-derived colouration is also important for our own ability to distinguish it, and is particularly visible on dark petals or parts of petals. [78] Less obvious to our eyes are cases where iridescent grating-derived colours are overlaid on brightly reflecting pigments. However, the subtle effect may still be measured and generally observed. [67]

Data presented in figure 2.2 and 2.1 were published [67] showing that the effect of the disordered diffraction grating is to introduce an angular dependent (shimmery) blue halo on the petal. The additional reflection from the petal due to yellow pigmentation makes the colouration less spectacular in the *Oenothera* than in *Hibiscus* to the human eye. Although difficult to capture by camera, the petals in the study do appear to have a blue sheen in bright obliquely incident light.

Multilayers

The majority of the structural colours reported in plants, other than petal striations, originate from multilayer reflection, theoretical analysis of which was described in section 1.1.1.

Dielectric photonic multilayers can be made from any contrasting refractive index materials. Primary locations for the multilayers are in adapted chloroplasts, in adapted cells or cellular vesicles, or in the cell wall.

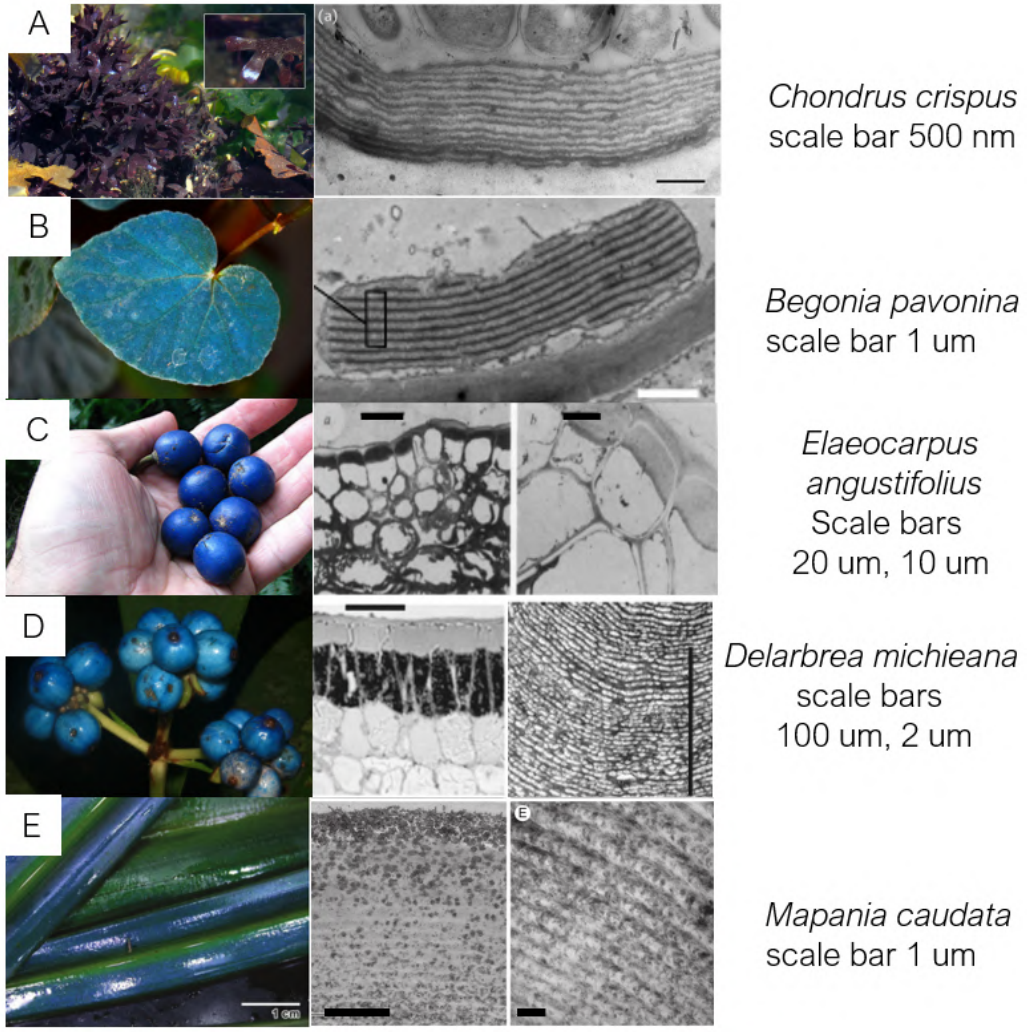

FIGURE 2.3: Some examples of blue structurally coloured plants alongside SEM / TEM images showing nanostructure A. [79] *Chondrus crispus*, B. [80] *Begonia pavonina*, C. [81] *Elaeocarpus angustifolius*, D. [82] *Delarbria michieana*, E. [83] *Mapania caudata*

Cuticle A plant-related species displaying blue iridescence is a red alga *Chondrus crispus* or Irish moss which was shown to generate the blue iridescence from a layered cuticle on its surface. It is shown in figure 2.3 A. [79] Although not a land plant, this alga is included to demonstrate the variety of materials used by photosynthesising organisms to produce structural colour.

Adapted Chloroplasts A mechanism apparently shared by *Phyllagathis rotundiflora*, [84] *Trichomanes elegans*, [85] *Teratophyllum rotundifoliatum*, [86] *Selaginella erythropus* [87] and *Begonia pavonina* (figure 2.3, B) is the adaptation of chloroplasts within the cells so that the functional thylakoid layers have a spacing on an optical wavelength scale, reflecting from within the leaf cells. This has also been shown in *B. pavonina* to improve photosynthetic efficiency by enhancing the quantum yield by 5-10% in low light conditions, [80] suggesting an adaptive advantage conferred by the

structural colour and inspiring design for improved energy harvesting. [88]

Unidentified Materials Two fruits with striking blue colouration have been reported, and structures in their epidermal cells identified as the potentially the origin of the colour. The materials in the structures and their precise optical effect have not in either case been clarified. These are included to highlight the frontiers and limitations in understanding of structural colour in fruits.

Elaeocarpus angustifolius is reported [81] as having a thick iridosome comprising the top third of the epidermal cell, as shown in figure 2.3 C. Although the layered structure has been identified as being partly composed of cellulose fibrils, the contrast media has not been identified. The images presented in the report identify two apparently different structures.

A second fruit with a similar structural colour mechanism was identified by the same author, *Delarbrea michieana*, see figure 2.3, D. The mechanism described [82] is constructive interference from the thick iridosomes beneath the cell wall. Again, the layering is identified as cellulose, but the other 'bubbly' layer material is not identified. No polarisation of the reflected light was reported.

As well as unconfirmed structures in fruits, the leaves of *Selaginella willdenowii* and *Selaginella uncinata* use a very small number of Bragg-condition conforming multilayers on the outside of the epidermal cells [89] [69] although the material composition has not been described.

Helicoidal Cellulose Multilayers

A further group of species reflect structurally coloured light from multilayers composed of helicoidal cellulose in their cell walls. *Lindsaea lucida*, *Diplazium tomentosum* [84] and *Danaea nodosa* [85] all have much thickened cell walls containing around thirty layers of helicoidal cellulose, and have angular-dependent blue reflection. Although in *D. nodosa* the authors describe layers of alternating electron-opaque and electron-transparent material [85], the images indicate that the layering may in fact be from a helicoidal cell wall. The spectra reflected from these plants are predicted to conform to the description given in the optical theory section, and reflect one circular polarisation at a specific wavelength in agreement with its observed pitch. However, in the reports the measurements were not made.

Mapania caudata shows a variation on a similar structure, [83] a thickened helicoidal cellulose cell wall was reported containing 'entrained' silica granules that accumulate at uniform positions within the helicoids. The silica is reported to play a part in the structural colour reflected from the leaves because no colour was reflected when

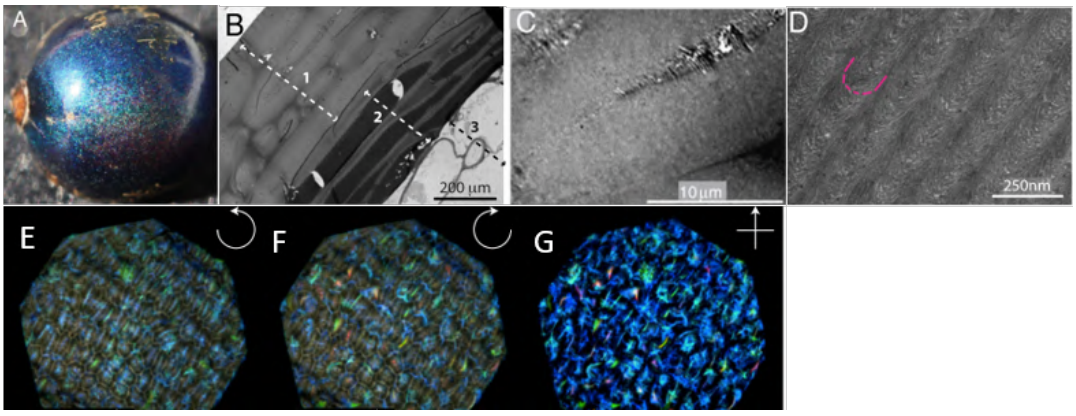

FIGURE 2.4: *Pollia condensata* A. photo B - D. SEM micrographs showing helicoidal multilayer material. E-G Optical microscope images of the same area in E. left circular polarisation, and F. Right circular polarisation. G. Between crossed polarisers, i.e. a superposition of left and right circular polarisations. All reproduced from [92].

the silica was removed, however, no mechanism for this is suggested, and the reflected light is circularly polarised, indicating that it originates from the helicoidal structure rather than the silica granules.

Finally, two fruits from distantly related genera also exploit thick helicoidal multilayer cellulose in their cell walls to reflect bright structural colour. The structurally coloured cell walls are extremely thickened in both *Margaritaria nobilis* [90] [91] and *Pollia condensata* [92] leaving almost no internal cavity and cell contents. The structures of both fruits were established by Dr Silvia Vignolini, who supervised this thesis, and coworkers. This thesis is based on their work, specifically on *Pollia*. An image of *Margaritaria nobilis* is shown in figure 2.9. Another related species *Margaritaria discoidea* also has fruits with a translucent outer shell which looks an iridescent blue when hydrated (unpublished). This species grows in some of the same regions as *Pollia condensata* - between Senegal, Ethiopia and Zimbabwe. [93]

Previous Work on *Pollia condensata*

The fruit of *Pollia condensata* is about 4-5 mm in diameter and better understood as a colourful capsule or seed case, made up of a hard dry spherical epicarp containing, in each of the fruits examined, 18 tightly packed seeds in six segments. It is a bright metallic blue colour, with a glittery 'pixelated' appearance. Although it contains a dark pigment, no evidence of blue pigmentation has been found via conventional extraction, [92] and all the colour reflected from the fruit is due to structurally coloured cell walls. Unlike the other structurally coloured plant tissue introduced so far, the fruit retains its colour indefinitely under moderate dry conditions, due to the fruit's dehydration as it matures.

The outer cells of the epicarp have extremely thick cell walls, which grow thick enough to take up the entirety of the cell space. The cell walls are made of a very regular helicoidal cellulose stack, like the materials discussed in 3.1.1, with a periodic pitch of approximately 150 nm, creating a thick photonic crystal chiral multilayer fulfilling the 'helicoidal Bragg' reflection condition. Several layers of structurally coloured cells are visible using a TEM cross-section. They have underneath them also a few layers of pigmented cells filled with brown tannin which serve as an absorber to enhance the visibility of the structural colour. With an optical microscope, multiple layers of reflecting cells are visible from different focal depths. Particularly distinctive is the microscopic appearance of the cells whose curved shape reflects light back normally only from the central perpendicular part of the cell wall, appearing as a bright stripe or spot in the middle of the cell as seen from above.

Perhaps the most interesting thing about *P. condensata* is that different cells reflect different handedness of circularly polarised light. No other helicoidally reflecting structure has been reported with both circular polarisations reflected in one material, whether in plants with optically reflecting cellulose, or any other structurally coloured material. Other helicoidal structurally-coloured material reflects only left handed circular polarised light, indicating a left handed chiral material structure (see figure 1.7). It is surprising and intriguing therefore to find a mix of both handednesses in one fruit tissue.

2.2 *Pollia condensata* Experimental Results

2.2.1 Experimental Approach

In section 2.1.2 the fruit of *Pollia condensata* was introduced via the work published in [92], (see figure 2.4). The rest of this chapter presents novel experimental results from a thorough study of *P. condensata*, the species described in the original paper, and a number of related species, which are compared in the later sections.

First, work on *P. condensata* is presented. Specimens of the fruit were analysed in order to describe the anatomy of the epicarp tissue. The optical response was then analysed in polarisation-selective microscopy. Spectral responses from large numbers of *P. condensata* cells were measured in order to understand the distribution of cell colouration across the spectral range and polarisation. The unusual polarisation characteristics were surveyed over hundreds of cells on multiple fruits in order to understand their spectral characteristics.

The analysis of the fruits was designed in order to characterise the unusual polarisation and optical geometry effects previously observed in the fruit and to determine the extent of their occurrence within fruits of this species, and for the purpose of

FIGURE 2.5: *P. condensata* fruit with a piece of the epicarp broken off to reveal the tightly packed seeds. The glittery cell reflections are visible. Stripe areas of increased purple and white reflection are indicated.

comparing with other species. Additionally, this full description is intended to establish the subject of the following chapters in which the biological material in these fruits is assessed during fruit development.

2.2.2 Fruit Anatomy

As mentioned above, the *Pollia condensata* fruit is comprised of a hard, dry epicarp (outermost layer) packed with typically 18 tightly-packed but unattached seeds, visible in the photo in figure 2.5, around a central column. Previous research [92] demonstrated that colours reflected from specimens that were decades old remained bright and vibrant, due to the durability of the multilayer material.

The epicarp is brittle - a scanning electron microscope (SEM) image of the broken epicarp in cross-section is shown in figure 2.6, A. The epicarp shows 4-5 layers of helicoidal, structurally coloured cells above 3-4 layers of flattened pigmented cells, and a lower layer of very flat softer brown cells on the internal surface of the epicarp.

Closer magnification of the broken structurally coloured cells in SEM show clearly visible layers within the cell wall, image B, whose broken edges form characteristic fan ridges, image C. This pattern is the hallmark of helicoidal architecture broken perpendicular to the layer plane and visualised using SEM. This is the correlate indication in orthogonal cross-section SEM of the Bouligand arcs reported in the Transmission Electron Microscope (TEM) images in figure 2.4. They can also be seen in self-assembled helicoidal cellulose nanocrystal (CNC) film which will be introduced in chapter 6 figure 6.2.

The iridescent cells are imaged in optical microscopy cross-section in image 2.6 D and are shown to be non colour-reflective in cross-section.

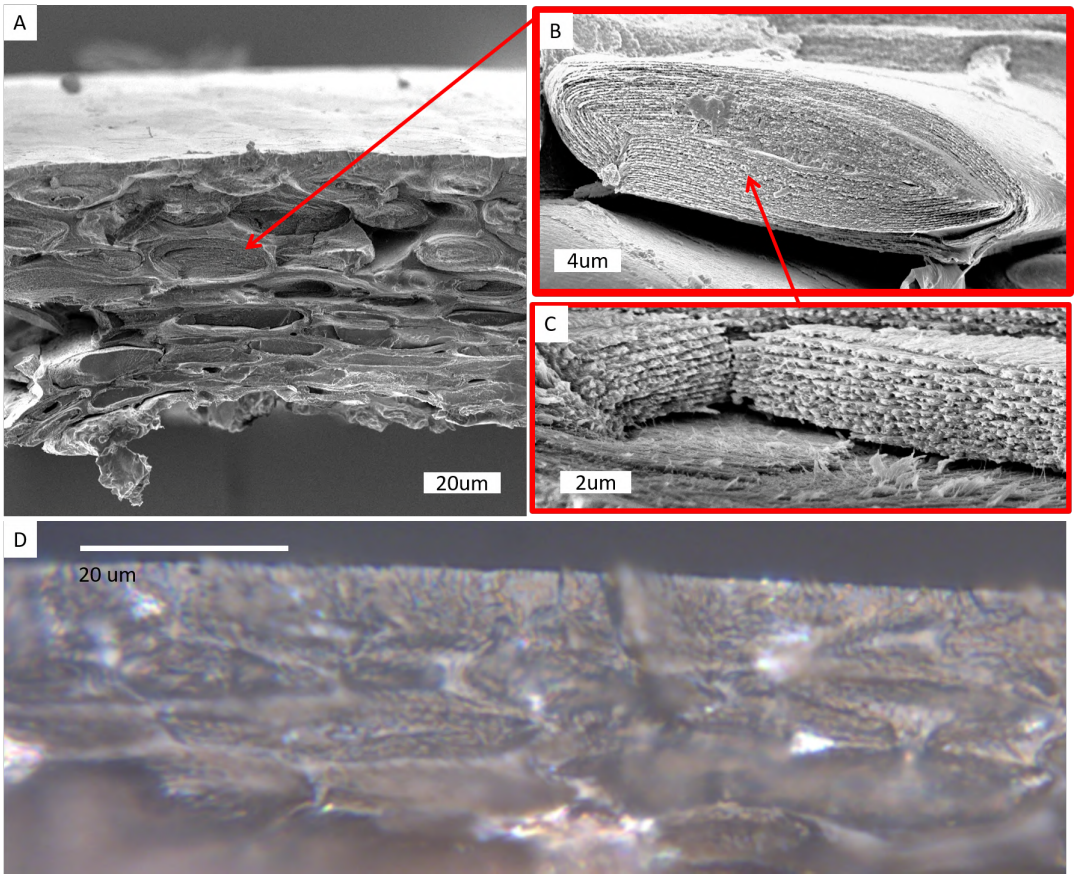

FIGURE 2.6: A,B,C: SEM images of broken *P. condensata* cross sections through *A. the whole epicarp B. a single structurally coloured cell C. an area of cell wall exposing arced fans. D is an optical microscope image through the top part of P. condensata epicarp, some individual cells are visible.*

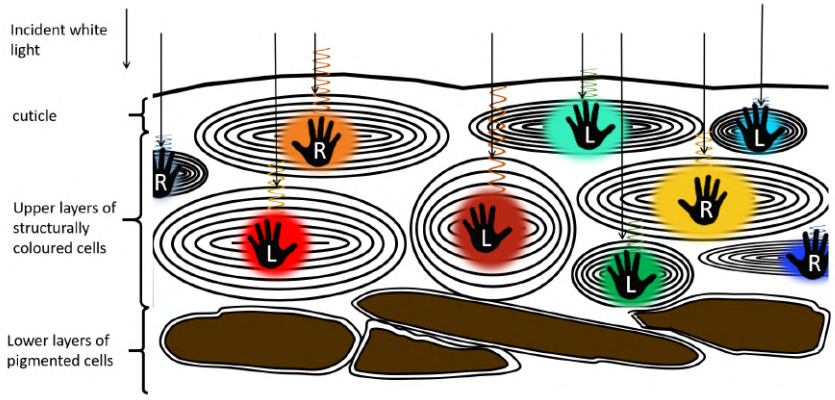

FIGURE 2.7: A labelled schematic indicating the structure of *P. condensata* cross-section which has several layers of entirely filled structurally coloured cells. Each of the cells reflects a different colour in either right or left handed circularly polarised light. Light that is not reflected is absorbed by the pigmented cells underneath.

The schematic in 2.7 is a simple cartoon of the epicarp cross-section. The incident light does not interact with the cells other than a single handedness of a particular band of the spectrum corresponding to the cells' pitch. This means that reflections from multiple cells at different depths of the epicarp may be observed from a location on the surface. This is a simplified model which ignores biological materials such as pectin which binds individual cells into a coherent tissue. However, the outer part of the epicarp, containing only structurally coloured cells, may be isolated by manually scratching off the pigmented cells, (see figure 2.8) and appears clear, indicating no other absorbing pigments within the multilayer cell slab. This combination of a clear and structurally coloured outer layer in contact with a pigmented absorbing layer is analogous to the structure that gives *Margaritaria nobilis* its intense colour [91]. In this case, the structurally coloured cell layer appears more transparent and much more closely bound to the pigmented layer, which in *M. nobilis* are detached entirely when the fruit dries, suppressing the colour visibility as shown in figure 2.9. [91]

2.2.3 Optical Response

Optical measurements of the epicarp were reported in the previous research, but are confirmed with additional observation here as a basis for the following results. The selective reflection from each cell of either right or left handed circularly polarised light is illustrated by the optical microscope image 2.10. The outlines of cells are indicated as guides, the cell edge contours being visible for surface cells, and the reflection of a spot of light inside each in either the left or right circular polarisation is shown. The spot of light is unusual with respect to the colouration of most biological plant cells because it does not fill the cell body. This effect is due to the curvature

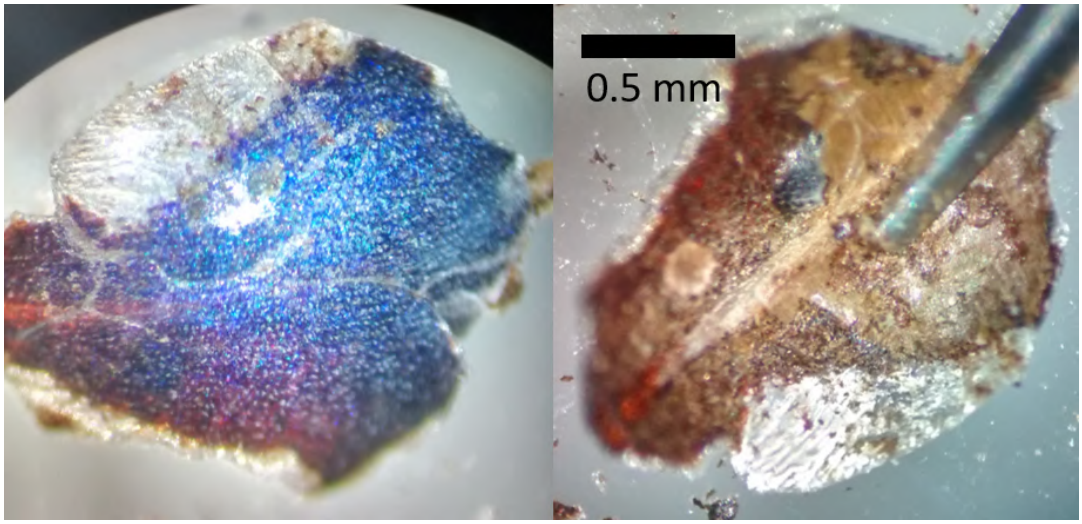

FIGURE 2.8: A part of *P. condensata* epicarp with a transparent area which has been manually scraped clear of pigmented cells from the underside. The left image shows the top of the epicarp as it appears on the fruit, the right hand image shows the underside. The structurally coloured cells from which spectra are measured are located in the transparent area, but they are not visible without the dark pigmented cells underneath.

FIGURE 2.9: Dry and fully hydrated *Margaritaria nobilis*. This structurally coloured fruit was discussed in section 2.1.2. It has structurally coloured cells similar to *Pollia* cells in the translucent outer shell, and when hydrated the shell is in contact with the dark inner fruit body and makes the fruit appear blue-green. [91]

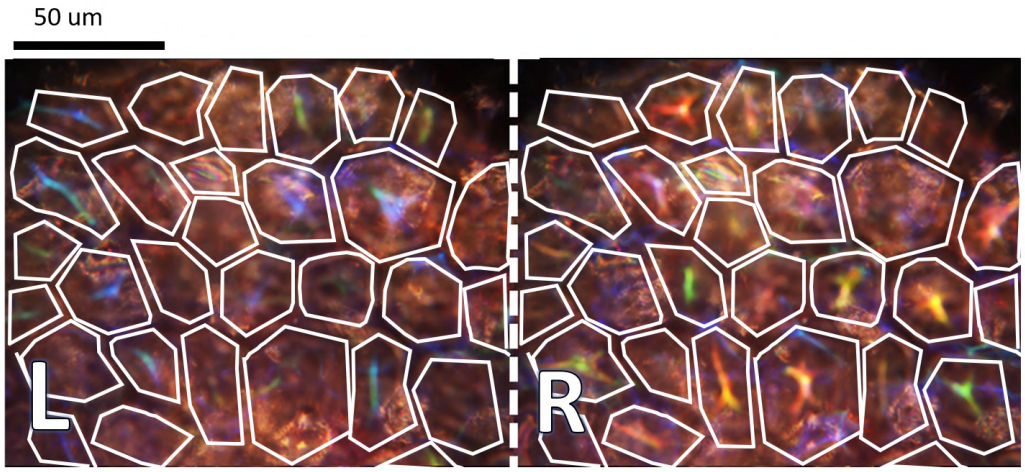

FIGURE 2.10: The same area of cells on *P. condensata* are imaged in left (L) and right (R) circular polarisation. Cells are indicated with a white dashed outline. Each of the cells reflects a colour in one handedness but not the other.

of the cells and the finite size of the numerical aperture, as previously illustrated in figure 1.10.

The distinctness of each reflected spot of light in the centre of the larger cell, and the different colours exhibited by each cell gives the 'pixelated' or glittery appearance described in [92] and clearly visible in 2.8 and 2.5.

2.2.4 Spectral Distribution

Prior work established the existence of reflective cells right and left handed chirality in the epicarp of the fruit, but did not demonstrate any distinction between the two types of cells. Here it's demonstrated that the two types of cells may be considered distinct populations due to different characteristic distributions.

Initially spectra from right and left handed chiral cells were measured separately from different areas of a fruit. A plot showing the distribution of the peak intensity and wavelength is shown in figure 2.11, A. Each peak is plotted using an image of the cell reflection spot it represents. The distribution of the left handed circular polarisation reflections is indicated with a triangle overlaid on the image and is blue shifted with respect to the right handed circular polarisation reflecting cells.

In 2.11 figure B, the peak intensity and wavelength of a large number of cell spectra is plotted, without indication of the handedness (in fact the vast majority of these spectra are from left handed cells). This second set of data was collected and plotted to understand whether pitches appeared grouped around characteristic wavelengths. Although the distribution in this set is not uniform, it is not the case that

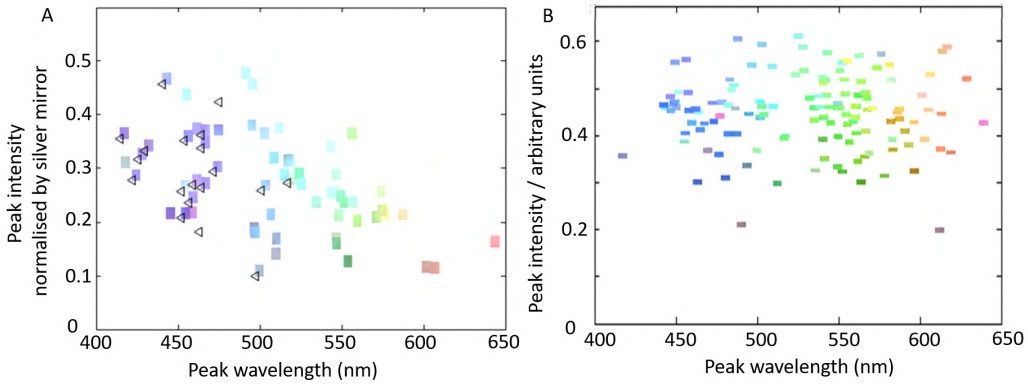

FIGURE 2.11: Two surveys of peak intensity of cells. Each point is indicated by an image of the area from which the spectrum was measured, demonstrating the range of colours reflected. In plot A left handed circular polarisation peaks are indicated by a black triangle. B shows a survey of cells without handedness indicated, although they are mostly left handed. Both surveys confirm the wide and continuous range of colours displayed by the fruits.

the cell colours are preferentially grouped round certain bandwidths. Cell colouration spans the spectral range.

2.2.5 Spatial Distribution

Measurement of the fruit showed that right and left handed cells are not evenly distributed with different areas being dominated by a non-exclusive tendency towards one of the handednesses. The predominance of red-shifted spectra reflected from right handed cells means the location of a high density of right handed cells can be identified by eye.

Inspection of the fruit in figure 2.5 establishes that its epicarp is sectioned by six stripes. These stripes are either whitish or reddish, in the figure, the top and bottom of the fruit have a visible whitish stripe, and a red stripe goes around the centre of the fruit. These coloured stripes, visible by eye, are where right handed cell majority areas may be found.

This conclusion was reached using a very large scale survey on multiple fruits. A spatial survey on a single fruit is presented in figure 2.12. The spectra from 9 areas are divided in two different ways along (front middle and back of the fruit) and across (inner, outer and between) the stripe axes.

At nine separate locations on each fruit an area was identified in the field of view without a polarisation filter and every cell's spectrum recorded from within this area. This approach was taken in order to avoid bias to brightly reflecting cells or one polarisation over another. Each area included 20-30 cells. Histograms in figure

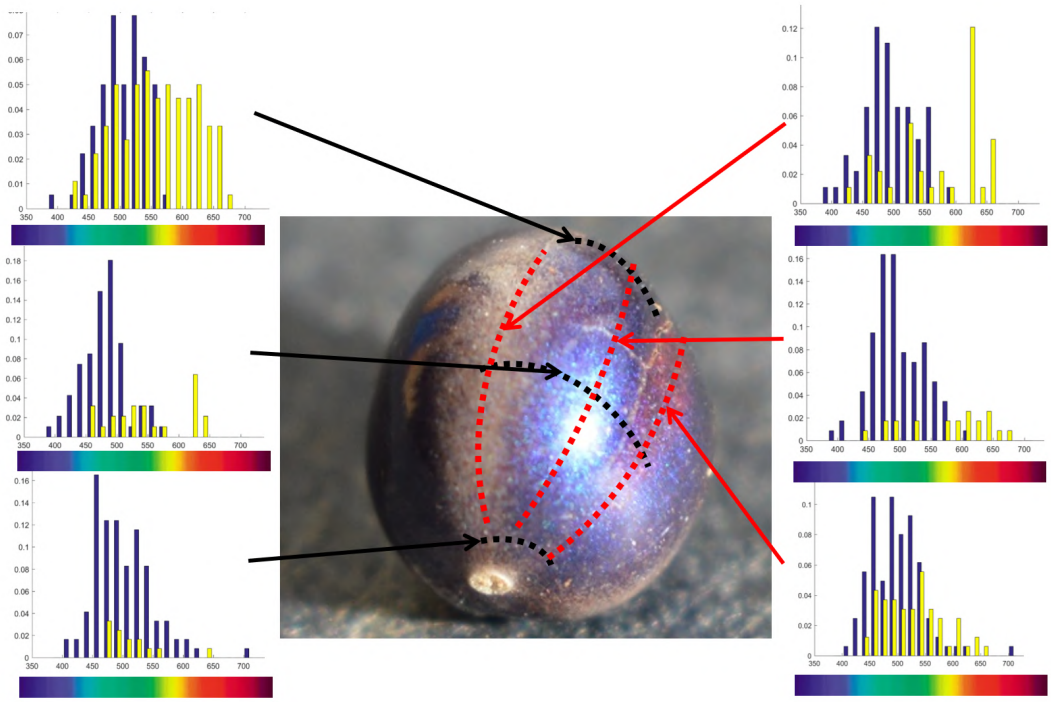

FIGURE 2.12: The spectra and handedness of the cells on the fruit are analysed on the reddish and whiteish stripes separately, and the area in between, and also on the cells at the front, middle and back of the fruit. Histograms are used to demonstrate the relative proportions of left (navy bars) and right (yellow bars) at each wavelength for each area. The dominance of left and right cells is very localised. In this fruit the highest proportion of right handed cells are at the back, and in the septum stripe. They are generally seen to be red-shifted. The same analysis was carried out on other fruits, which are included in the appendix. Generally, proportionally more right handed cells were found in the stripes, but otherwise there was no general rule found.

2.12 show the relative numbers of cells in both handednesses across the spectral range. Distributions are compared on different plots for spatial regions across and in parallel to the stripe areas.

The different locations in the histograms show very clear differences, with the vast majority of right handed cells appearing at the back of the fruit where it was detached from the plant, and with a distinct red shift, although overlapping with the spectral distribution of left handed cells. The right handed cells are also more common in the all stripes, than in the area between them. There are in this instance a few right handed cells not located on a stripe, and they also show a redshift with respect to left handed cells in the same area.

This survey was reproduced on three further fruits which are included in appendix 7.5. 200-250 cells on each fruit were measured. Although they showed a similarly strong spatial variation within each fruit, there was not a consistent general distribution across the fruits measured. Right handed cells were consistently identified with red-biased cell colours. The stripes are visible because of the increased proportion of red and yellow cells, and examining the stripes is therefore a reliable way to find right circular polarisation dominated areas. However, the right handed cells were not consistently distributed at the back or front of the fruit between different specimens, and there were many areas of the stripes where right handed cells were not present.

Colouration and Anatomy

The stripes correspond to structures inside the epicarp where thickened tough bands of tissue encircle the fruit. These bands are located over the boundaries between the seed segments. Three of the segments are located over the septa, tissues extending from the epicarp into the core of the fruit which separate the fruit cavity and the seeds into three equal lobes or locules. The other three bands are alternate with the septa stripes, and equidistant between them.

The fruit anatomy of *Pollia* species has not been previously described but elements are recognisable from studies of other *Commelinaceae*. [94] The existence of the three septa and locules each containing six seeds is consistent with the anatomy described in other fruits. The other set of stripes appear to correspond to the 'dorsal carpellary trace', or external vascular bundle connected to the central core at the two poles of the fruit.

The vascular tissues below the visible stripes are thicker and tougher than the brittle epicarp which may be broken off leaving just the tough connective tissue. An early-stage thickened tissue, including a cross-section through the vascular bundle, can be seen in an SEM image in chapter 4 figure 4.24. Another report of a *Commelinaceae* species, [95], demonstrated that vascular tissues develop from the earliest stages of

the flower's development, although they undergo significant growth after fertilisation and during development of the fruit. The stripes are referred to here as 'septa stripes'

Given the functional properties of the vascularised and connective tissues for the whole fruit, the occurrence of this distinct group of right handed cells predominantly in these regions could indicate that their development, structure or function is linked to that of the connective tissue. This may crucially provide an indication of the conditions under which the cells differentiate. Further examination using a biological and dissection approach to the association of right handed cells and vascular tissue during development is beyon dthe scope of this thesis which concentrates on the use of optical analysis as a tool. However, it is suggested that this would be a productive avenue of further research.

2.3 Comparison between Multiple Species in the *Pollia* Genus

The previous section focused on the spectral and polarisation range of *P. condensata* fruits in which structural colour had previously been described. The rest of this chapter is intended to contextualise the species and its unusual optical characteristics via comparison with other related species. The optical response of other members of the genus has not previously been described

This observation allows us to understand the ways in which related species exploit nanostructure for structural colour in different configurations. Analysis allows us to relate the fruits' different visual appearances with the structurally coloured material responsible. This gives us insight both into the biological material as a malleable starting point for variation in visual appearance tool for species themselves, and also expands our understanding of the boundaries in structural colour variance. Finally, the variation in natural material can be assessed from a biomimetic perspective to extract principles and inspiration for colouration engineering.

In this section, three additional species are introduced and compared to *P. condensata*. The macroscopic and microscopic appearances of the fruits are presented and assessed. The polarisation and spectral distribution of the cells are assessed similarly to the approach taken in the case of *P. condensata*. The distribution is used to conclude the commonalities and unique polarisation characteristics of *P. condensata*.

2.3.1 Species Investigated

The genus *Pollia* is of the family Commelinaceae and has twenty-one distinct species named in the Kew Herbarium catalogue. These are found across the remaining

FIGURE 2.13: Photos of mature, and therefore dry A *P. hasskarlii*, B. *P. japonica* C. *P. thyrsiflora*, D. *P. condensata*. The fruits are very durable and these specimens are years old, although not distinguishable from newly grown fruits.

tropical and subtropical rainforests of Africa, Asia and Australia and include one American species. [96] These species commonly make up a significant part of the ecosystem in many rainforests' understory flora. [97] [98] Suggested uses of *Pollia* reported by ethnobotanists are of the leaves in post-childbirth treatment [99] and as a stimulant [100] and of the fruits for the treatment of back-ache. [101]

Three species in the genus in addition to *P. condensata* are analysed here in order to compare them. These species, *P. japonica*, *P. thyrsiflora* and *P. hasskarlii* all inhabit Japanese or south-east Asian tropical rainforests, rather than the central African habitat of *P. condensata*. The four species' fruits are shown in figure 2.13 . *P. thyrsiflora* appears similar to *P. condensata*, although it is darker, smaller and more elongated in shape. *P. hasskarlii* is also very dark, and resembles these two. *P. japonica* has a very different appearance however, being slightly larger and with a matte grey-blue colour, unlike the very bright 'glittery' appearance of the *P. condensata*. The other species are markedly less colourful by eye, and with much less distinct vascular-associated stripes than the *P. condensata*, if any were visible at all.

2.3.2 Optical Response

The fruits were all imaged under an optical microscope between parallel and crossed polarisers, as shown in figure 2.14. Although there are evidently differences in the appearance of the fruits' epicarp using parallel polarisers, it is only with crossed-polarisers that the difference is very distinct. *P. hasskarlii* and *P. japonica* (images A and B) show distinct colours reflected from the one layer of cells only, without reflection from underlying layers. The appearance of *P. hasskarlii* is more similar to *P. condensata* due to a single point of reflected light in the centre of the cell, rather than a reflection of a uniform colour from the entire cell. *P. thyrsiflora* shares with *P. condensata* several layers of cells contributing to its reflection, but each cell is much less clearly defined, as the reflections from cells are not in discrete stripes or spots but more diffuse. The three other species appear more uniformly coloured than *P. condensata*.

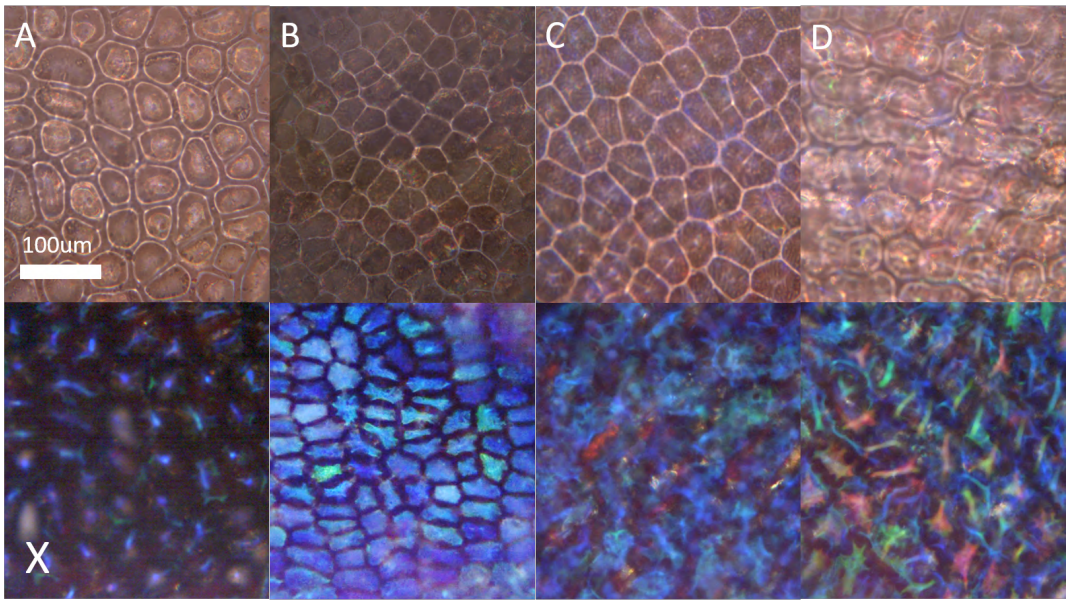

FIGURE 2.14: Microscope images of each of the four fruits in 2.13. The top row shows the parallel polarised image, the bottom row shows the crossed-polarisers image, where only the structural colour is visible. A *P. hasskarlii*, B. *P. japonica* C. *P. thyrsiflora*, D. *P. condensata*

All of the fruits are characterised by hard dry epicarps with a non-bleaching colour and circular polarisation reflection, indicating optically that their colour shares with *P. condensata* a structural origin.

2.3.3 Cell Wall Architecture

The shared structural mechanism is confirmed by the SEM images in figure 2.15, in which the outer cells of the epicarp show the distinctive layered cellulose described earlier. The optical characteristics of each species are also explained by correlation with SEM images of their structure. *P. hasskarlii* and *P. japonica* have only one layer of structurally coloured cells above the pigment layer, which is why in 2.14 only one layer of cell reflections is seen. *P. hasskarlii* cells are distinctly curved, like the *P. condensata*, correlated with the point-like reflection of light from within each cell boundary, whilst *P. thyrsiflora* has very flat and wide cells which accounts for the more diffuse reflections, which are not well-defined spots determined by the numerical aperture dilation.

2.3.4 Spectral Distribution

All the species were imaged in left and right circular polarisations in order to verify that the colouration was reflected by the helicoidal structure observed in the cells. Left and right handed circular polarisation images of the same locations are shown

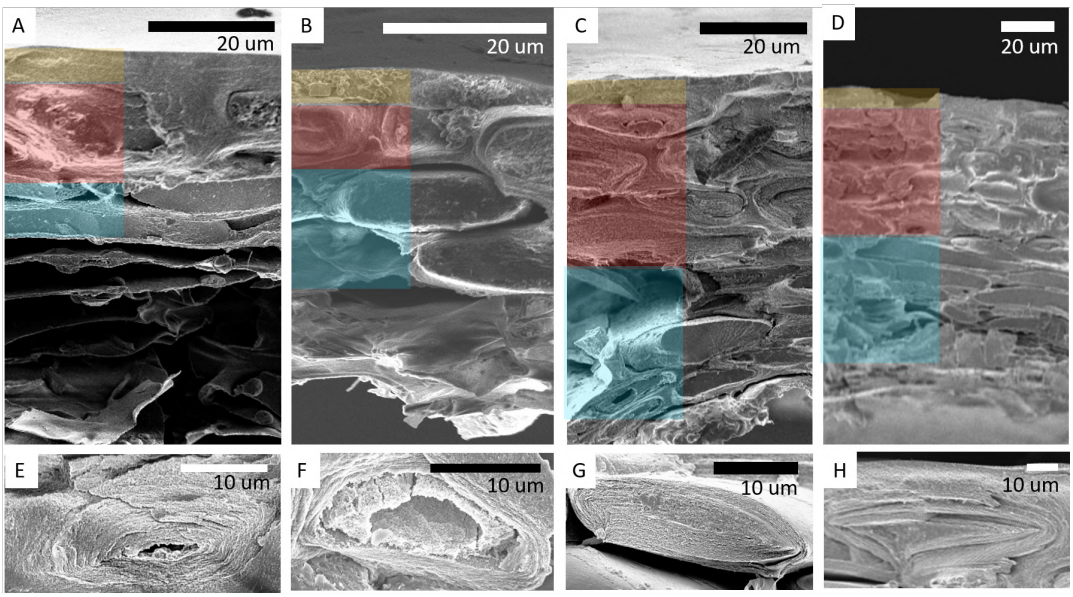

FIGURE 2.15: SEM images of the cross-section through the four different species. A *P. hasskarlii*, B. *P. japonica* C. *P. thyrsiflora*, D. *P. condensata*. The top row shows the entire endocarp cross-section with different regions indicated in shaded bands: cuticle (yellow band), structurally coloured (red band) and pigmented cells (blue band) indicated. The bottom row of images shows a single characteristic cell from each species.

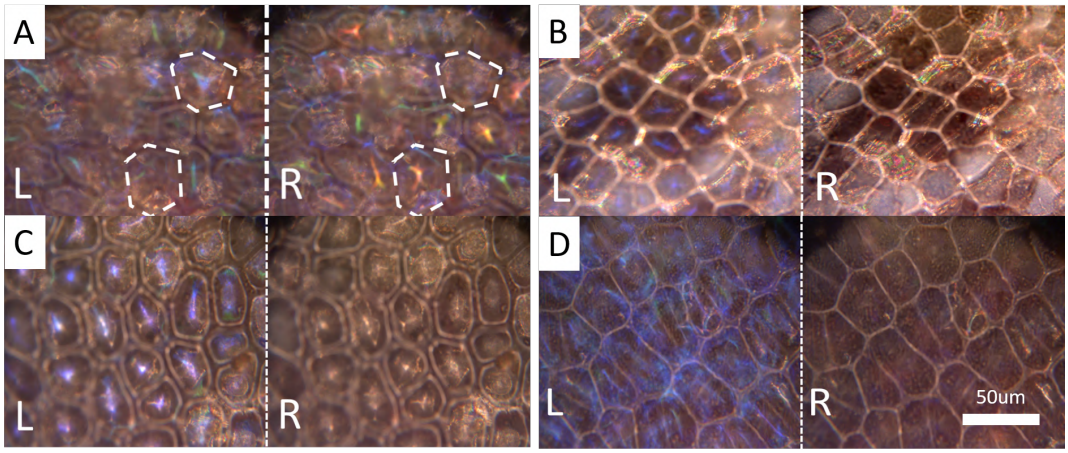

FIGURE 2.16: A. *P. condensata*, B. *P. japonica* C. *P. hasskarlii*, D. *P. thyrsiflora*. Each image shows the left and right handed circular polarised microscopic images. Only *P. condensata* shows any colour in the right handed circular polarisation.

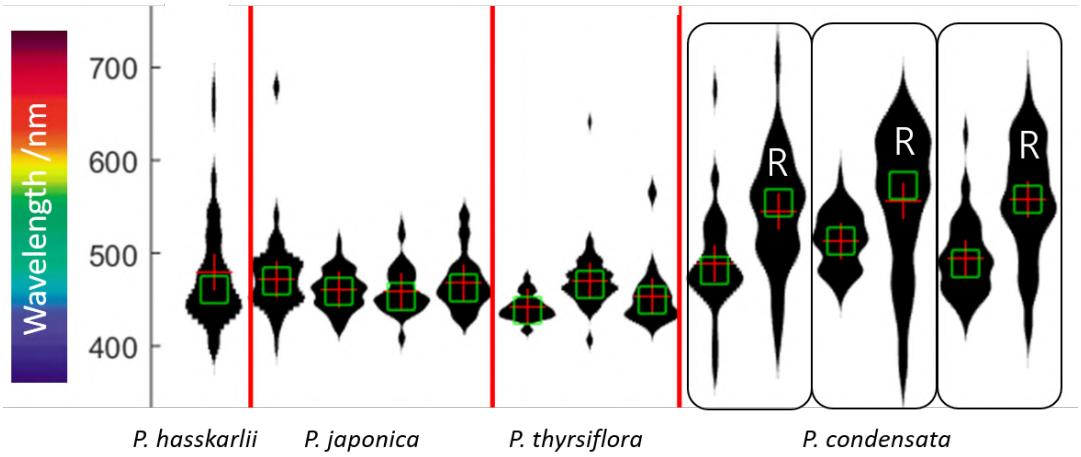

FIGURE 2.17: Histograms of spectral distributions from each of the different species. Each 'violin' represents cells from a single fruit, except for *P. condensata* where a single fruit is represented by two histograms, one for the left and one for the right circular polarisation, indicated by 'R'. For each species. Cells represented by the histograms are *P. hasskarlii*:90 *P. japonica*:140 *P. thyrsiflora*:60 *P. condensata*:300

in 2.16. The three other species were demonstrated to reflect only in left handed circular polarisation, unlike *P. condensata* which reflects left and right handed circularly polarised light from different cells.

In order to understand the differentiation of structures in different species of the *Pollia* genus, a spectral survey was taken of each species, by choosing several areas at different positions on a fruit at random and recording the wavelengths of the reflection peak of every cell in the area. The reflection peak wavelength of each spectrum was recorded and analysed as described in the experimental section and plotted as a violin histogram. The results are shown in figure 2.17. The width of the 'violin' for each point on the y axis corresponds to the number of cells found with that peak wavelength.

Each individual violin body (arranged and labelled along the x axis) corresponds to an individual fruit specimen, except in the case of the *P. condensata* fruits, where pairs of peaks are used to represent the two separate datasets from cells which reflect both left and right handed circular polarisation.

Further to the asymmetrical chirality distinction between *P. condensata* and the other species, the histograms and associated mean (red cross) and mode (green box) values demonstrate distinctive differences in the ambi-chiral species. The right handed cells, following indications in figure 2.11, are shown to have a strongly differentiated average peak wavelength with respect to the left, and a much extended range of peak values. Interestingly, the left handed cells in *P. condensata* also show a red shift and increased variation with respect to the species with only left handed cells.

2.3.5 Conclusion and Discussion

Of the examined species in the *Pollia* genus, and of all helicoidal cellulose tissues *P. condensata* remains the only reported one with both right and left circular polarisation reflecting structures. The genus does however share the unusual structural colouration of the outer epicarp cells. The optical effect of thickened cell walls that act as multilayers is different, both by eye and microscopically, in each species, and this is accounted for by geometric differences in the species' cells and cell layers.

As no phylogeny exists for this genus, the relationship between each of the species is unknown. The structural colour mechanism is shared between species spread over a wide geographical range although other anatomical characteristics are differentiated. The adaptive function of the structural colour is unknown, as is the relationship of the traits evolution in each of the species.

The *P. condensata* fruits are shown to have a greater range of spectral distribution of peak wavelengths. The mean peak wavelength of the left handed cells in *P. condensata* is redshifted by 30 nm with respect to the other three species whose mean wavelength is 466 nm. The right handed cells have a mean wavelength redshift of 85 nm.

These large differentiations observed across a very large number of cells demonstrate the distinctive characteristics of *P. condensata* and of the right handed cells. The direct link of structural colour spectra with the material in the cell wall indicates that there is difference in the material structure of the cell walls of both the right handed and left handed cells in *P. condensata*, although to different extents.

The large range of different colours reflected in *P. condensata* may have a different adaptation function or accidental or vestigial origin. However, the correlation with the right handed material provokes a hypothesis of a link between the material properties or development process, the red-shift and helicoid chirality.

Some hypotheses about the relationship between the colour and handedness of the structurally coloured cells are discussed.

Additional Polymers

As discussed in [102], hemicellulose has been suggested to play a vital role in the development of helicoidal structure in cellulose. A more accurate and comprehensive picture of cell wall structure [103] than used in the model we have considered so far does incorporate many other branched polysaccharides which enmesh cellulose microfibrils, and the insertion of chiral molecules has been proposed in a very different system to give rise to right handed helices in bacterial cell walls. [104]

The increase in the pitch of the material may be associated with additional hemicellulose or other molecules, the physical size of which account for the redshift. In this case, it might be a by-product of the different chirality-control mechanism in the cell, or it might be a necessary component of right handed helicoid. The existence of right handed cells with peak wavelengths shorter than those reflected from left handed cells makes this hypothesis less attractive.

In order to understand whether an additional molecule is present in the cell walls of all *P. condensata* cells, or even in right handed and not left handed cells would require a full chemical analysis of the components. This is complicated by the fact that suitable candidates for an additional molecule would be expected to be very similar to molecules found regularly in cell walls. Chemical analysis is complicated by the fact that simply to separate the right and left handed cells from one another, or the helicoidal cells from the others in the epicarp presents a significant challenge, as the cells are solidly fixed to one another. However, this experiment is feasible using, for example, microscopic Raman spectrometry.

Growth Disruption

A different, although related, proposal for the physical differentiation of right handed cells is that the construction mechanism of the helicoids is disrupted or altered in order to produce the opposite chirality. As discussed in section 3.1.2, there is still significant debate about the way in which cell walls are created, however, mutation of the control of microtubule orientation or adaptation in the synthase rosettes should be considered as likely mechanisms by which a different orientation of helicoid could be produced. This disruption could additionally introduce extra molecules like hemicelluloses into the material, or alternatively might retain the same cellulose fibril density with a smaller interfibrillar angle or more randomly oriented fibrils.

This mechanism could be probed with the use of disruption to the mechanisms hypothesised to be responsible for cell wall fibrillar orientation. Tools which could be employed include genetic modification of synthesis molecules or cell scaffolding control, or using poisons known to affect cell walls to understand whether left and right cells are affected equally. Understanding all of these processes relies on a greater understanding of the cell wall development, which will be discussed in the next chapter.

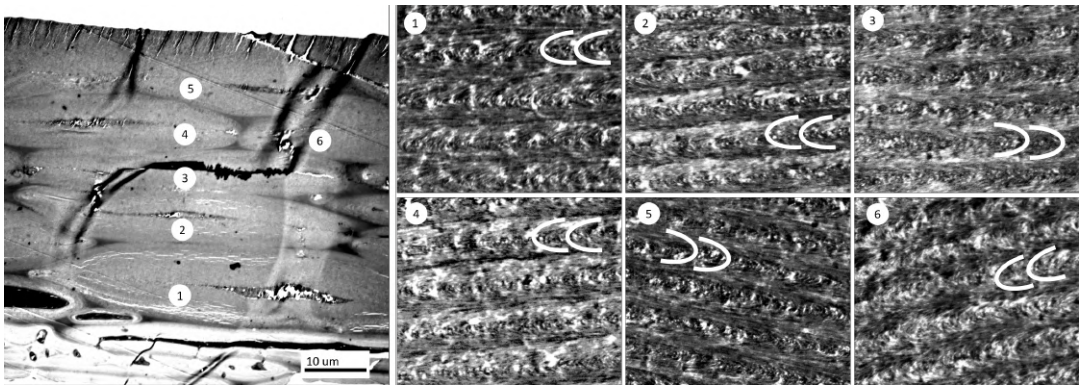

FIGURE 2.18: The large image on the left shows a cross section through the structurally coloured cells of *P. condensata* in a TEM cross-section by Tom Gregory. Numbers mark the locations at which the each of the higher magnification images were taken, corresponding to the label. Bouligand arcs are visible in each of the higher magnification images, and guidelines are used to indicate them in this figure. 1,2,4 and 6 share arc directions, and the opposite direction is seen in images 3 and 5.

Additional Polarisation Effect

There is a further possibility, that the reflection of right handed circular polarised light is not caused by right handed structures, but by multiple reflection and scattering of left handed circular polarised light from left handed chiral structures, or from these reflections passing through a waveplate, which occurs in the beetle *Plusiotis resplendens*. [105] However, as described earlier, the appearance of the *P. condensata* cells is very distinctive and an effect of the shape of the cell itself. A scattering or multiple reflection would be expected to cause a distortion in this appearance. In order to ensure that the measured light is directly reflected without secondary scattering, all measurements unless otherwise stated are taken from reflected spots which appear to be from the top layer of epicarpal cells. It should be noted that due to these cells' transparency, there is a possibility that a different reflective cell underneath may contribute part of the spectra recorded in this case, but every attempt was made to avoid this happening.

Additionally, a TEM cross-section by Tom Gregory who shown in 2.18 demonstrates alternating Bouligand arc directions observed in *P. condensata* cell cross-sections, indicating that there is a different chirality in adjacent cells.

2.4 Biological Context

The species in the *Pollia* genus are remarkably understudied, and therefore there exists a significant gap in our understanding of the biological and ecological context for the species and genus as a whole. Some smaller projects were instigated as part

of the work undertaken while producing this thesis in order to try to fill those gaps. These represent side projects whose conclusions do not fit into the larger themes of the work or the general conclusions. The ecology part was largely carried out by collaborators. However, they are included here in order to present as broad an approach as possible to the subject and to present the limits of current research into the biological significance of the species.

Ecology

Pollia condensata is widespread through remaining protected rainforests. Data are not available on the number of specimens, although it is included in a range of rainforest flora surveys. [106] [107] [108] [109] [110] [111] [112] [113] [114] The fruit's other names are nonexhaustively recorded in ethnobotanical studies and botanical translation : *litoto* (Bambenga), *pepepe* (Mbuti. This name is shared with at least two other species of understory plant also not considered useful.) [112] *ikangíla / makangíla / ikandíla / makandíla* (Kibira) and *kigenia* (Kibira - shared with red-fruited *Commelinaceae* species *Palisota ambigua*) [101] *endiki-uekeki* (Efe - meaning Forest Mouse eyelids)[115], *mlelevasi* (Hehe) [116]. These records generally characterise the plant as without use, game animals are reported to eat the leaves, [112] and mice to eat the fruits. [115]

The fruit was observed to be common in shaded high-canopy protected rainforests Kibale and Budongo National parks in Uganda and Kakamega National Park in Kenya. Fieldwork was carried out in collaboration with Dr Rebecca Karanja from Jomo Kenyatta University of Agriculture and Technology (JKUAT). The species was easily found because plants grow generally in large patches, found particularly on the edges of well-worn paths. These paths have plenty of human and animal traffic, and may also offer a clearing in the canopy overhead. The arrangement of leaves, as shown in figure 2.19 is also easily spotted as the large leaves fan out in a striking star shape, directing the eye to the central stem, where the flowers and fruits are found during the fruiting cycle.

Fieldwork in Kakamega Forest National Reserve in Kenya was carried out in September 2016 under permit from the Kenyan Forestry Service (KFS). Kakamega Forest is the only remaining part of the Guineo-Congolian rainforest in Kenya. [117] Our collaborators Dr Rebecca Karanja (JKUAT) and Wilberforce Okeka (KFS) carried out inspection of the presence of the species within the forest, the floral and fruiting cycle and surveys of the pollinating insects that visited the plants.

Identification of the growth of *P. condensata* was by a laying a line transect of 3.5 km along the open canopy sections of the forest, a photograph of a mature plant is shown in figure 2.19 showing the large star-like arrangement of the leaves around

FIGURE 2.19: Left: a photo of the star-like leaves of *P. condensata* growing in Kakamega Forest National Reserve. Right: A single flower open on an inflorescence, on a lab grown plant.

the central stem, where the fruit grows. 16 clusters of plants were found. The propagation was observed to be primarily through stolons and so clusters of plants were found together, in groups of 20 - 50. During the early fruiting season, only a few plants (1-5) per cluster were observed to bear fruits.

Assessment of the floral and fruiting cycle identified that the flowers emerged after 7-9 days of budding. An open flower is shown in figure 2.19. For observation of pollinator behaviour, 18 Camera traps were set, and additional species identification was done by insect netting. After pollination, the fruit maturation was observed to last around three months in the forest.

The pollination study was successful and demonstrated that the primary pollinating species visiting the plants were *Apis mellifera* or honeybees which accounted for 72% of visits to the flowers. A further 19% of visits were from other members of the *Apidae* family, and the rest from other bees. Pollination visits occurred predominantly before midday and in warm and wet conditions although no pollination visits were observed during rain.

Although a survey of the fruit-dispersers was attempted, it was not successful in capturing fruit dispersers. The only prior evidence on fruit consumption to our knowledge is the inclusion of *P. condensata* in a list of species consumed by baboons in Budongo forest, Uganda, [118] although the extent to which the fruits form part of the baboons' diet is not fully described. This identification of the fruit dispersers was supported by a single sighting by Wilberforce Okeka of a baboon picking the fruit but evidence was not recorded on camera.

Fossil Record

A full phylogeny of the species is missing, however, an apparently closely related species to *P. condensata* is recorded in archaeological work. [119] A huge number of specimens were uncovered of *Pollia tugenensis*, named for its location in the Tugen Hills, in a 12.2 million year old primary airfall tuff within the Ngorora formation, Baringo district, Kenya. Entire plants have been preserved, standing with minimal collapse, flattening or folding. The species show very little distinction from the extant *P. condensata*. All the specimens recovered during the research reported are held in the National Museums of Kenya (NMK), where they make up a significant proportion of the plant specimens held.

As part of research carried out towards this thesis, these specimens were all inspected carefully for signs of fruit-heads, six specimens were observed to have signs of partial or whole fruiting bodies preserved. The type specimen Box 80DE 10769 is shown in 2.20 and had a collapsed fruiting body, including fossilized epicarp material.

The fruiting bodies were measured with optical microscope spectroscopy for signs of having retained structural colour, which has been observed in other fossils. [120] The microscope used for this purpose was donated by Zeiss. [1] A fragment of this fruit epicarp is detached from the main body and this was borrowed from the museum under kind permission of the NMK, and imaged using SEM. The image is shown in 2.20. It confirms that the fossil has been formed through mineral crystallisation inside the cavity of the epicarp, and there is no prospect of a retention of structurally coloured material.

FIGURE 2.20: The photos show an extremely well preserved specimen of the extinct species, and half the epicarp of a fruit. The SEM image of the specimen in the bottom right hand corner shows flat planes characteristic of crystalline formation that has crystallised in the epicarp cavity.

Chapter 3

Development in *P. japonica*

In this chapter, current understanding of cell wall development is introduced. I then produce results from the direct observation of *Pollia japonica* fruit cell wall growth during maturation. The development is considered in three separate stages. The optical analysis is then compared with electron microscopy.

In order to use the structurally coloured cell wall material to give an insight into growth, the development of structural colour can be observed directly and compared to the physical model. This technique applies a physical and materials science understanding of light-material interaction to analyse and interpret a biological process. This chapter describes observation of *P. japonica* and discusses the challenges, methods and conclusions drawn about cell wall growth.

The results of this chapter are a description of the cell wall growth during fruit maturation. This is the first time that cell wall growth has been imaged during maturation without using staining, tagging or fluorescence techniques. This is in contrast to destructive sampling and the direct imaging of sub-wavelength structures, which is generally employed in similar studies.

I first present an introduction to the broader context of helicoidal cell walls and cell wall development.

3.1 Helicoidal Cell Walls and Development

3.1.1 Helicoids in Nature

The photonic helicoidal structure described in section 2.1.2 is responsible for only a tiny fraction of the photonic structures in nature, however, the architecture itself is very common. The discovery and analysis of helicoidal photonic crystals was made in the context of previous analysis of non-reflective helicoidal structures.

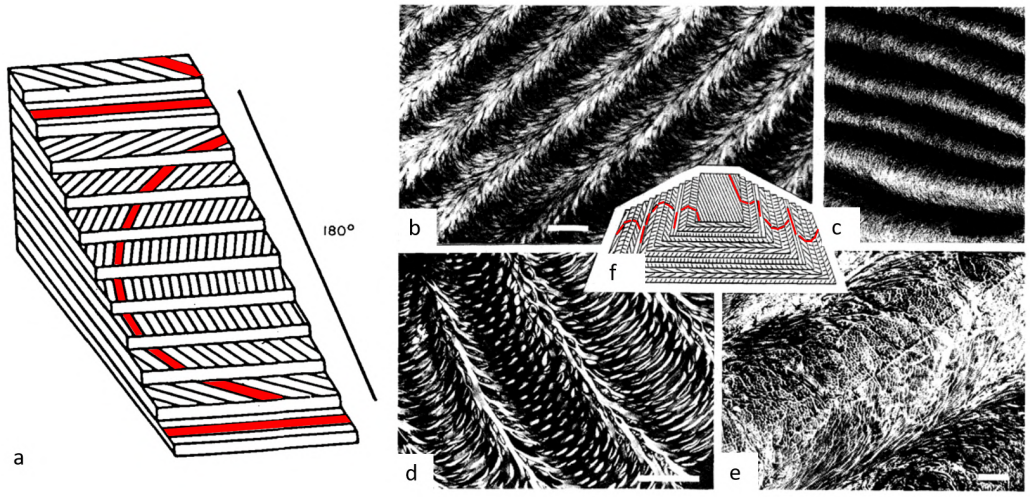

FIGURE 3.1: a. Construction of Bouligand arcs from a helicoidal stack of planes, adapted from [102]. b-f, collated by [121], b. Decalcified crab cuticle, bar = 2 um. c. Pear skin with polysaccharides visualised, bar=0.5 um. d. Collagen in dermal fish scales, bar = 40 um. e. Collagen in decalcified human bone, bar = 1 um. f. A diagram similar to a showing arc reversal with the opposite oblique section through the stack.

Non-photonic Helicoids

Helical plywood structures are extremely common in skeletal or protective extracellular tissues and cell walls [121] from human teeth [122] to crustacean 'claw' clubs [123] and fruit stone cells [124] where they contribute an enhanced isotropic toughness and energy dissipation through shear wave filtering, crack deflection and arrest. [125] These structures are on a larger scale than visibly-reflecting photonic crystals, but they share the same architecture.

The characteristic indication of a helicoidal geometry, the Bouligand arc [126] is used to identify occurrence of helicoidal architecture in tissue structures, normally through staining for transmission electron microscopy. Bouligand arc appearance, its mechanism and examples are shown in figure 3.1. Each plane in the Bouligand arc construction is in fact made up of layers of parallel fibrils, which makes it a natural extension of biological materials. [127]

Many biological materials are fibrillar. Prominent helicoidal composites are based on chitin,[128] collagen [129] and cellulose, [130] long chain biological molecules with a hierarchical fibre structure. Studies of chitin and collagen have demonstrated the existence of these phases on multiple scales, in fungus, bone, crustacean and beetles, however, for the remainder of this thesis we will be concerned with the occurrence of helicoidal architectures in cellulose.

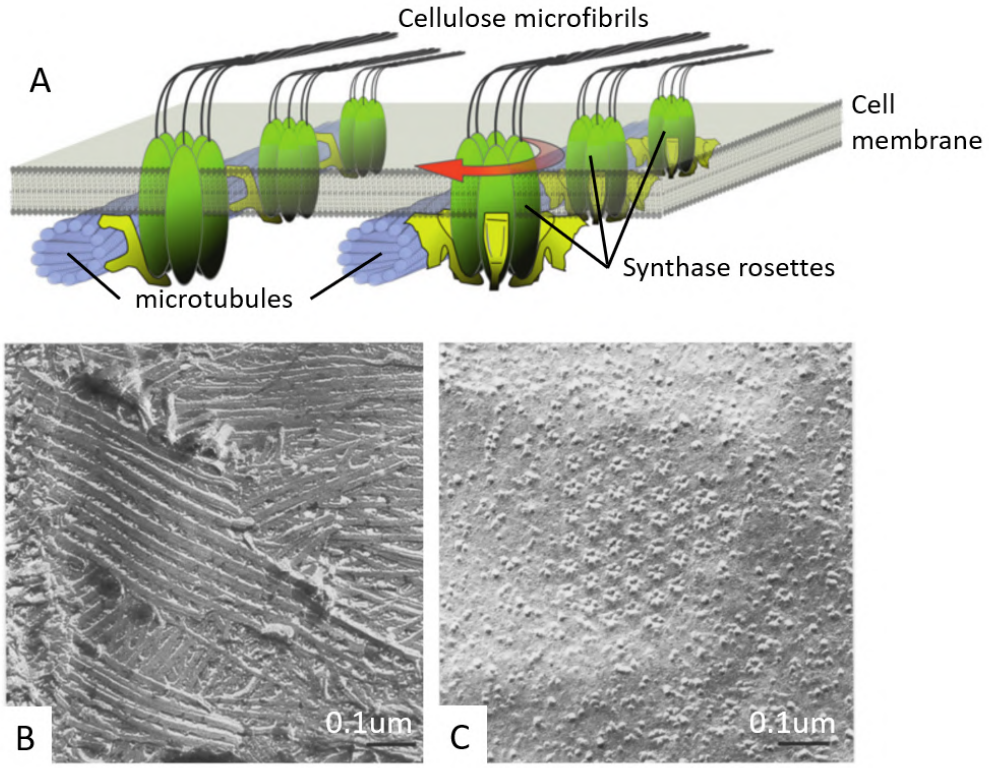

FIGURE 3.2: A. Schematic of cellulose extrusion from rosettes, reproduced from [138]. B. SEM micrograph of cellulose microfibrils at different angles in the cell wall of green algae *Closterium* C. Rosettes on the plasma membrane of the same algae. B& C Reproduced from [132].

3.1.2 Plant Cell Wall Assembly

Cellulose is the main component of cell walls, [131] it is a structural polysaccharide made from a long chain of the repeated monomer glucose, which is extruded from the external plasma membrane of the cell into the cell wall by groups of synthase molecules arranged in 'rosettes'. [132] The parallel synthesis of cellulose molecules creates hydrogen bonds between them, [133] forming polymorph *I* nanofibrils instead of the more energetically favourable polymorph *II* which forms in lab-crystallised cellulose. [134]

The rosettes are grouped together, as shown in figure 3.2 and travel around the surface of the cell membrane wrapping the continuously extruded fibrils around the cell. [135] [136] The arrangement of fibrils is adapted to the cell type and may be random, transverse, crossed, helical, helicoidal or a mix of these, the various orientations are shown in figure 3.3. [137]

In the helicoidal arrangement, each individual microfibril is arranged parallel to one another in stacked planes, the orientation of each plane offset by a few degrees from the one below.

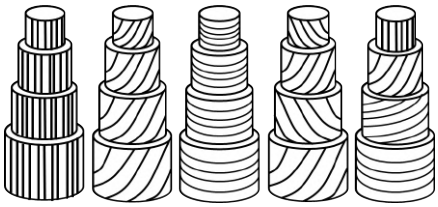

FIGURE 3.3: Schematic showing the different possible orientations of cellulose microfibrils in cylindrical cell walls, the furthest right demonstrates helicoidal layering.

Microtubule-directed Assembly

The mechanism by which the relative orientation of the microfibrils in the cell wall is controlled is a subject of debate. Studies have demonstrated the importance of numerous different factors in the assembly, and the interaction and relative importance of these different mechanisms remains to be fully determined.

Control of the fibril deposition by microtubules has been the focus of significant research and has yielded important results. The microtubule mechanism proposes that synthase rosettes travel on the plasma membrane along microtubules within the cell cytoplasm, and the microfibrils are laid down in place onto the solid cell wall. [139]

The research on this point is extremely extensive, and beyond the scope of this thesis. A few characteristic results are given here. Previous work on the growth of cell walls has relied on fluorescent tagging of cellulose synthase proteins in transgenic *Arabidopsis thaliana*, a well known model species, and visualisation using laser stimulation of molecules in living cells in a confocal optical microscope. The technique gives high definition images and has demonstrated in fine detail the colocation of cellulose synthases and microtubules [141] as shown in figure 3.4, L,M,N. Moreover, drugs which reduce the function of microtubules have been shown to reduce the degree of orientation in microfibrils, see 3.4 A-D vs E-H. [140]. However, in this study, total poisoning of the microtubules did not stop the microfibrils from orienting in a similar pattern to the case of fully functioning microtubules, images I-K. These results indicate that the relationship between microtubules and fibrillar orientation is complicated.

Microtubules are thought to have many roles in plant cells. For example genetic modification of microtubule control genes has been demonstrated to change the chirality of the entire stem of Arabidopsis seedlings causing the whole plant to twist. [143] Their multiplicity of roles makes the correlation between microtubule and microfibril alignment less clearly direct.

Genetic modification and poisoning have demonstrated a correlation of microtubule loss and changes in chirality or cell shape. [138] These techniques have been used to argue for microtubule dominance in fibril orientation, although they fail to answer

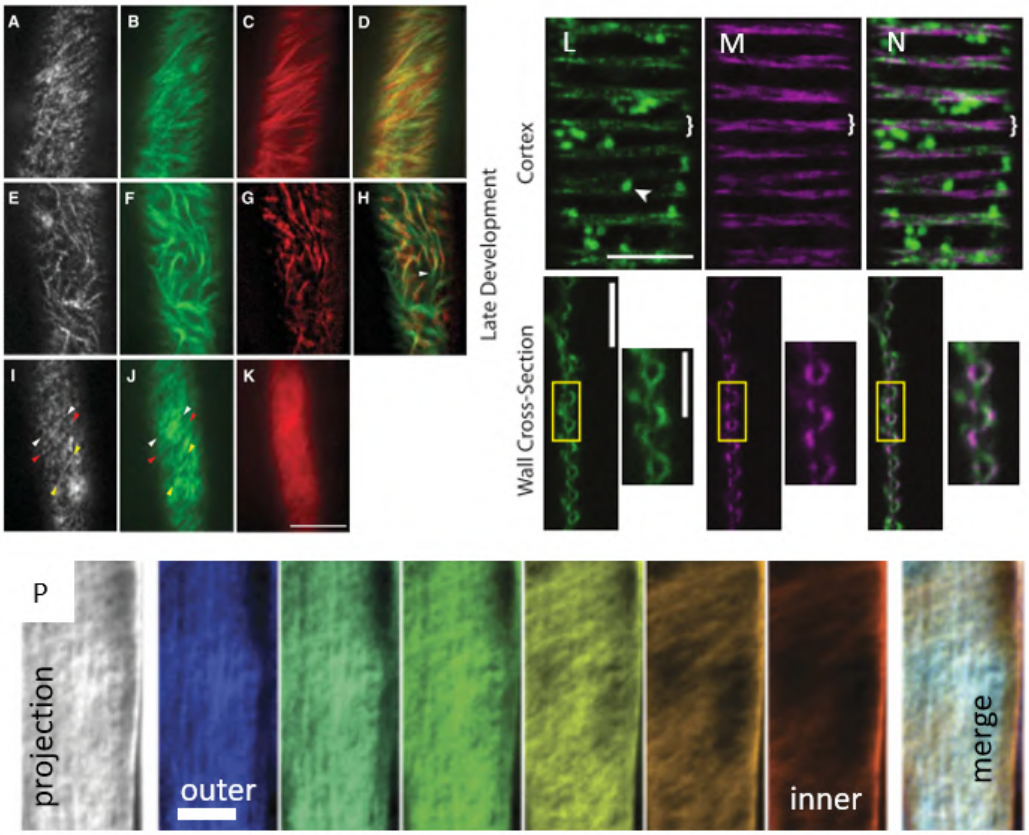

FIGURE 3.4: A-N are two different studies using fluorescence confocal microscopy in living *Arabidopsis* cells with tagged proteins. A-K: Grey and green are YFP::CESA6 on cellulase synthases, Red is CFP:TUA1 tagged to microtubules. L-N: Green is cellulase synthases labelled with YFP::CESA7, purple is microtubules labelled with RFP::TUB6. A-D show normal growth, E-H show treatment with a drug causing loss of microtubule organisation, I-K show more intense poisoning, although there is near complete loss of microtubule structure (K), arrows indicated a retention of organised cellulose synthase tracks, better than the semi-poisoned state. Reproduced from [140] L-M show the very strong association between cellulose and microfibrils, especially in the wall cross-section. Reproduced from [141] All scale bars 10 um.
P shows sections of Arabidopsis cell walls at increasing depths of 200 nm, showing the cellulose fibrils stained with S4B. [142]

some outstanding questions. The feasibility of experiments in which microtubules may be transgenically mutated, tagged and imaged has influenced the kinds of experiments and therefore mechanisms which are investigated for understanding cell wall growth.

An influence on cell wall orientation that has been proposed alongside microtubule control is reorientation within the cell wall after deposition. [103] At least in some instances cell wall fibrils are aligned in one direction and entirely reoriented during cell expansion. [142] Another proposal, taken from experiments in which the removal of microtubules was again demonstrated not to affect cellulose orientation, is that this orientation is defined by membrane streaming fluidity. [144] A further mechanism proposed is the existence of a 'scaffold molecule' outside of the cell membrane which is able to define the orientation of fibrils, and which interacts with microtubules. [145]

Given the huge variety of plant cells that exist, it seems likely there may be multiple different control mechanisms at work. However, it is clear that the microtubule hypothesis as it stands fails to account entirely for the existence of helicoidal morphologies in plant cell walls. An outstanding question remains on the control of the handedness of cell walls, for which no microtubule explanation has been given. [146] Microtubule models in some cases have ignored completely the striking fact that the vast majority of cellulose cell walls are left handed, [139] and instead assumed an equal likelihood of helicoid formation in each chirality.

Despite these lacks, some consensus has emerged with an increasing prominence given to research exploring the importance of biologically controlled microtubule effects. However, it is by no means a closed question [147] due to a 'lack of tools to connect the molecular and cellular scales in living cells'. [148]

The Role of Liquid Crystals in Biological Helicoid Development

Since the discovery of helicoidal materials in nature, analogies have been drawn between them and liquid crystals. This comparison is useful in describing the structures and optical properties of both materials, and it has also inspired the suggestion that solid crystalline helicoidal materials are the product of a 'solidified liquid crystal'. [149]

Subsequent to the first instance of this suggestion, it has been repeated many times, especially in work by Neville, [150] [151] [130] [152] [102] whose book *Biology of Fibrous Composites* [29] is a seminal and much-referenced text and whose contribution to the understanding of biological fibrous composites is enormous. What began as a tentative suggestion that beetle elytra may pass through a liquid crystalline phase

[149] [150] expanded into the same suggestion for plant tissues [151]. Neville continued to make the case for liquid crystalline phases through theoretically dismissing the capacity of microtubules to produce helicoids [152] and developing a model of self-assembly requiring the complex hemicellulose structure found in cell walls. [102]

Neville's suggestion is attractive because of its simplicity. Self-assembly in cells allows us to understand biological tissues as passive materials rather than living processes, and therefore promises a simple model and the possibility of reproducing it outside of the cell. The strong similarity between the solid and liquid helicoidal crystal is striking and seems to demand an explanation. Neville's suggestion has therefore often been reproduced in analysis of solid biological helicoids, with the justification of implication by morphological similarity. [124] [153] [154] [155] [156] This similarity extends beyond the helicoid pattern to defect morphologies that are common in both materials as well.

The idea has been further developed with an attempt to demonstrate the reassembly of extracted cell wall components, and the role of 'twisting molecules' in order to create the chiral architecture. [157] Other work has focused on true liquid crystal helicoids found in beetles [158] and in plants. [159] The example of a liquid crystalline phase in plants is in quince mucilage, an oriented cellulose fibril layer which may be swelled with water and has been shown to demonstrate truly liquid crystal behaviour.

Despite a lack of good evidence for a self-assembly process in the deposition of cellulose cell walls, the idea has become well known, and provoked contradictory responses directly addressing the hypothesis. Arguments against the suggestion have come in the form of a different preferred mechanism, like those discussed in the section 3.1.2. [144] [160] These arguments are unfortunately not well made because of the lack of ability of these other mechanisms to entirely describe the process themselves. Whilst the idea of a cell wall assembling in a cell just as a photonic crystal assembles in a Petri dish is fanciful, a role during wall assembly for these forces within a fluid cell boundary phase is not obviously untenable.

More compelling arguments point to the fibrillar materials themselves, and the impossibility of interpreting very long fibrils as being subject to the same forces as colloidal particles, which would be needed for self-assembly to take place. [137] This critical analysis also identifies strong constraints on the volume of material available for self-assembly and the spatial and temporal variation of the cell wall structure as inconsistent with a free liquid crystal phase. [161] A very brief phase of liquid phase orientation is instead suggested.

Unfortunately these differences between colloidal particles and fibrils have not been

addressed by proponents of the potential role of liquid crystalline assembly in biological materials. The in vitro use of a collagen colloid [162] and cellulose suspension [163] have both been suggested as indicative of a self assembly mechanism in vivo. Due to the lack of other evidence for or against the hypothesis the implicit direct analogy between the colloids and biological fibrils is not clearly supported or refuted.

As an open hypothesis requiring further research, the suggestion is harmless but it has been misinterpreted on multiple occasions. This comparison has been compounded by a further over-simplistic analogy. The different helicoidal materials, formed from chitin, collagen and cellulose again all share the same striking morphology. However, the biological tissues they form are very different. Unfortunately, the identification between the colloidal particles and biological fibrils, and between different materials holds back analysis of the differences between them. [121] [164] [165] [127]

The liquid-crystalline phase idea is also spread through an ambiguous use of phrasing like referring to solid helicoids as 'liquid crystal analogues'[147] and as having 'cholesteric liquid crystal organisation',[166] being the result of 'directed self-assembly',[147] and the analogy of liquid crystals as being 'relevant to cell wall ordering'. [167]

Unfortunately, the development of this idea without enough evidence has led to confused and erroneous claims that biological helicoid materials in general [128] or beetle elytra in particular [168] [169] have been demonstrated to be the result of a self-assembled liquid crystalline phase. These claims in well-respected reviews are troubling, because although the hypothesis has not been ruled out, it has not been demonstrated either. The sources cited to support the claims here are mostly based on in vitro collagen research. It is important that the short-hand assumptions about the role of liquid crystals are not allowed to pass unchallenged.

There are many difficulties in attempting to assess whether a liquid-crystalline phase exists inside helicoidal plant cell walls, and this report does not attempt to produce a description of the development mechanism in plant cell walls. However, it does attempt to investigate the cell wall development process itself, and to understand the characteristics of this growth. This is intended to contribute to our understanding of the physical changes that the material undergoes, and to provide evidence against which cell development theories ought to be compared.

Information about *Pollia* cell wall morphology may be gained directly by optical observation, due to the unusual scale of the cell wall which renders it structurally coloured. The report attempts to show that an understanding of the structural colour mechanism can be used as a tool in itself to understand the characteristics of material development in this case.

Studies on the Development of Structurally Coloured Biological Tissues

Material development in structurally coloured architectures has been very sparsely studied in comparison to the bulk of literature on the materials themselves. The research that has been carried out though has largely focused on unpicking the effects of passive material self-assembly and mechanical processes and active cellular control. [170]

Structural development in butterflies and moths [171] [172] and in birds [173] has been investigated. In these studies, the complex and varied structures in the tissues appeared to develop largely inside the cell. The periodic photonic crystal in several cases was itself the result of a passive self-assembly process such as spinodal decomposition, where the phase separation of a mixture according to its least energetic state creates a complex periodic pattern. However, this process did not occur in the bulk material of the precursor but was guided by a strongly confined geometry of cell vesicles and membranes. After defining the initial wet template, the self assembly via deposition on the scaffold, phase separation of the confined medium or mechanical buckling takes place. The cell then dies and dries to leave an air-filled cavity with a large refractive index contrast in a complex photonic pattern. Although much of the patterning is constrained by the parameters of passive self-assembly, it is by no means an undirected process. This has ramifications for attempts to mimic the tissue without biological mechanisms. Some conditions for the creation of structured materials both inside and outside of the cells in these systems remains undefined.

A closer system to the *Pollia*, although still formed of chitin, is the multilayer found in the elytra of the beetle *Gastrophysa viridula*. In this material, a continuous and very thick multilayer covers the outer cell layer. The study [174] on development of this material showed that the multilayer is made up of a very thick helicoidal chitin structure. Surprisingly, maturation of the structural colour is in two phases; first the helicoidal material is deposited, and then layers of melanin are deposited inside the structure which provides the refractive index contrast for the optical multilayer. The multilayer is formed from a phase contrast of melanised and non-melanised chitin, rather than a helicoidal structure, reflecting light under a standard Bragg condition, see figure 3.5.

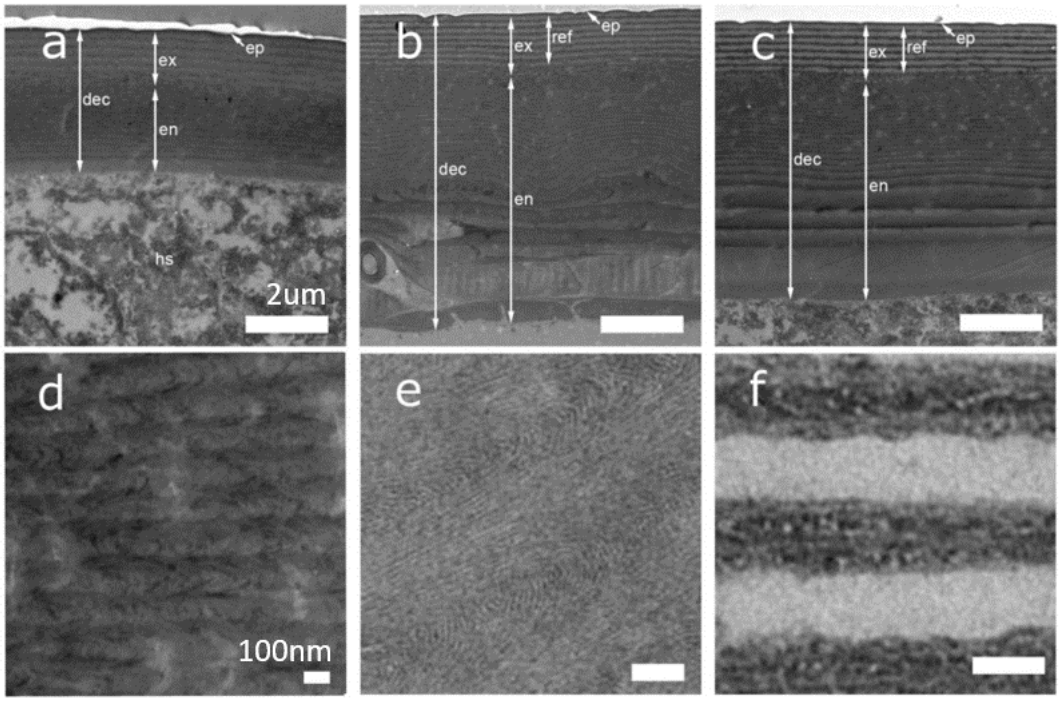

FIGURE 3.5: Reproduced from [174]. TEM sections of beetle elytra in young (a & d), maturing (b & e) and old (c & f) cuticle. Helicoids are visible in the high magnification images of young and thicker semi-mature cuticle, but not in the mature cuticle which shows melanised density contrast.

3.2 Experimental Procedure

3.2.1 Growing *P. japonica*

Cells were measured directly from living plants. All measurements were performed on mature fully grown specimens of *Pollia japonica*. The plant was grown at a stable warm room temperature in the University of Cambridge Department of Plant Sciences greenhouse at a variable humidity for 2 years. Plants were grown under glasshouse conditions at 23°C in Levingtons (UK) compost. During the growth period, plants received supplemental lighting from Osram 400 W high-pressure sodium lamps (Osram, Munich, Germany) on a 16 h : 8 h, light : dark photoperiod. The plant had previously fruited once in these conditions. The observation period recorded here is during July-August 2015. There were two plants which successfully flowered and then fruited. One plant was suitable for study due to its size and shape, the other was not subjected to microscope observation, but allowed to grow normally in the same conditions as a control. No differences were seen in the two specimens.

During the experiment, the plants were transferred to the PhD offices of the University of Cambridge Department of Chemistry. They were grown on the windowsill

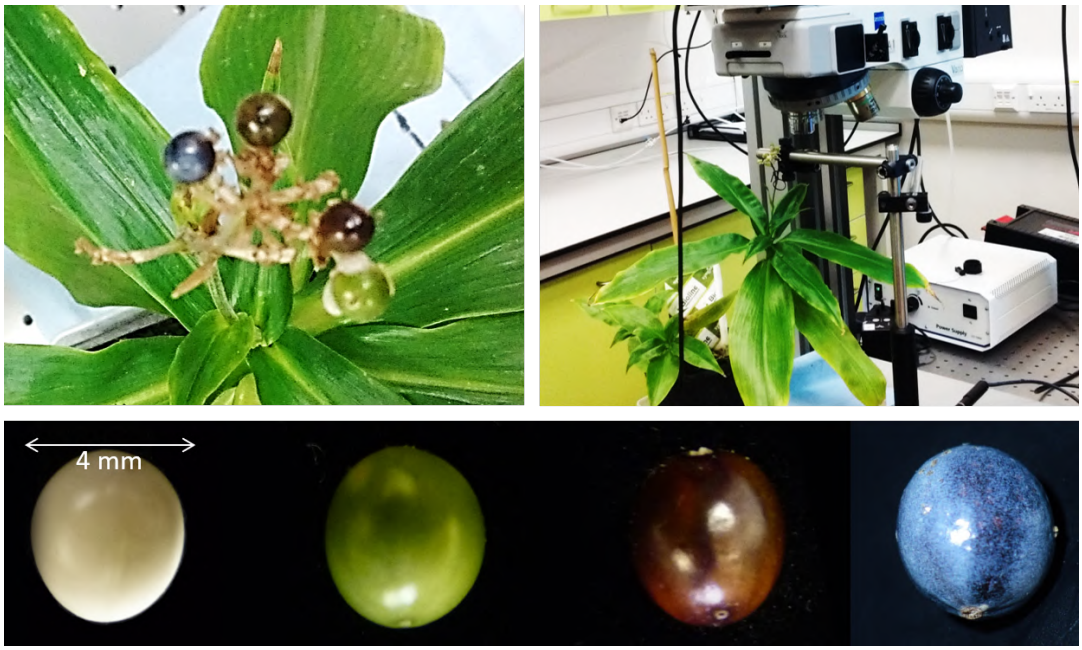

FIGURE 3.6: Above: all stages present on one plant & the whole plant in situ under the microscope. Below: each of the four stages. Photos of stages 1-3 by Dr Edwige Moyroud.

of a large north-facing window over the summer in an air-conditioned office kept at a temperature around 23°C, low/environmental humidity and watered regularly. The plants were approximately 50 cm tall.

The colour change of the macroscopic fruits had previously been observed by Dr Edwige Moyroud and photos of each of the four identified stages are presented in figure 3.6, lower panel. In the final stage the fruits in general have a matte light blue appearance, although they have a smooth reflective surface.

3.2.2 Fruit Cell Observation

Full description of the microscope techniques are given in section 1.5. To pursue the experiment, the plant was moved into the optical laboratory in the department, and top of the fruiting stem bent slightly and tied gently using a plasticised wire and Blu Tack to the support. The horizontal metal support was held by a vertical metal stand on a small x-y stage, see 3.6, top right. The plant and x-y frame were placed underneath a microscope, details of which are given in 1.5.1. The fruit was manipulated until the observation area was at the top, normal to the optical axis of the microscope objective lens, and then observed under 10x magnification. A low magnification was used in order to improve visualisation of each cell in its local environment for enhanced cell location and facilitation of movement between each cell sequentially to collect spectra. The instruments are detailed in section 1.5. The collection fibre had a 50 um core diameter, collecting from a spot of 30 um diameter.

The development may be described as occurring in four stages, as employed to characterise the macroscopic fruit change in figure 3.6: an initial pale white-green stage, a green stage, a brown stage and the final, mature blue stage. The observations took place over two sets of consecutive measurements, the first was of the initial white-pale green stage represented by the first photo in figure 3.6 and the top left hand image only in 3.7. The second set of measurements was made on a different fruit from the same plant and was of the later green→brown→blue stages. This was necessitated by heat damage to the first fruit. None of the observations included in the first series were taken after photo-damage. The damage was spatially confined and primarily of the lower pigmented cells, as shown in Appendix 7.5.

For the purposes of analysis and interpretation I have split the second observation series into two separate parts, 'part 2' which comprises the green-brown stages, and 'part 3' which is constituted by the transition from brown to blue, broadly the last three images in both figure 3.6 and all the other microscopic images in 3.7. Parts 2 and 3 are examined in sections 3.4 and 3.5.

A number of individual cells were chosen on the first day of observation, and subsequent measurements tracked the development of each of these individuals. The location and identity of the selected cells was recorded by creating a map of their appearance and relation to one another on each subsequent measurement, as demonstrated in figure 3.8. The changing appearance of the target cells necessitated frequent observation, in order to be able to re-find the same cells at each interval.

For the first series, 29 observation locations were identified, of which 20 showed the development of structurally coloured peaks. The other observation points were either badly located: falling on a cell wall rather than centre, lost: subsequent observations failed to locate the same point, or undeveloped: during the early stage that was the focus of this study, no structural colour was evident at these locations.

For the second study, 23 already reflecting cells were identified, of which 22 observation series were successful, and one cell location was lost and abandoned early on.

This experiment represents an ambitious and novel approach to development studies, due to the difficulty in re-measuring many cells over a long period without keeping them in place under the microscope, which was not possible. These cells changed their appearance, representing another challenge to re-identification. Furthermore, the cell contours and shapes were not always easily distinguished.

In order to resolve the difficulties associated with re-identification, an early attempt used an average spectrum collected from a randomly chosen set of cells each day. However, it was observed that variation between the cells, in their colouration but also in their growth stage, made this data incoherent.

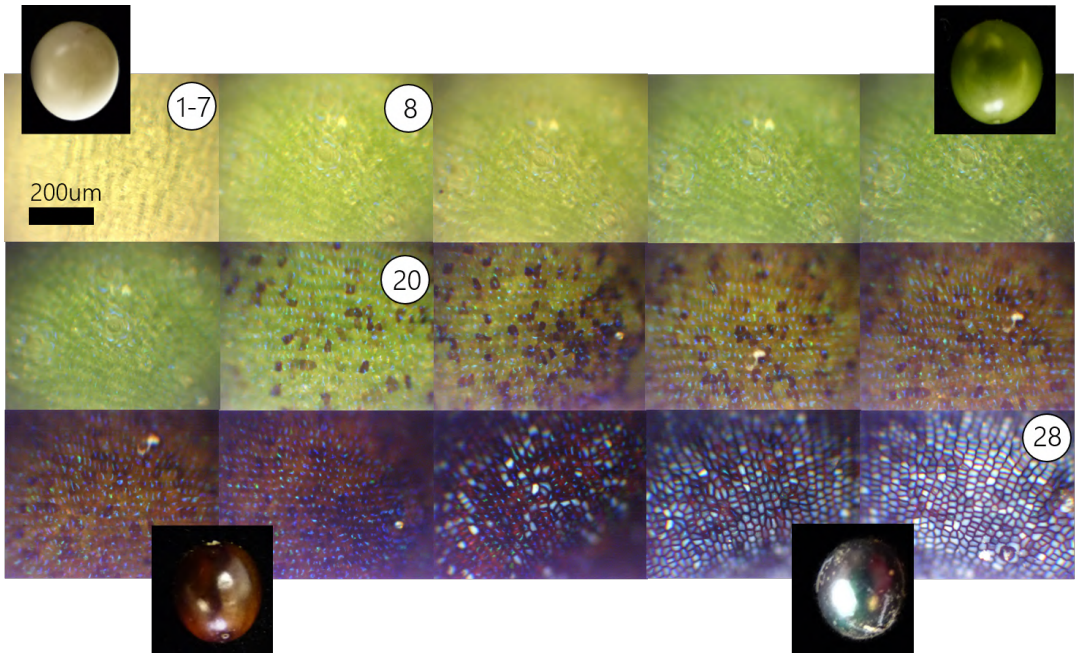

FIGURE 3.7: Images showing a large area of the fruit over the course of the maturation period. The image in the top left-hand corner is of the data set part 1, all others are part 2. The labels are the relative day of growth.

In order to observe changes in this biological tissue using an optical / materials science understanding of the material, changes in each individual cell material were considered separately. By retaining the cell identities, the experiment was controlled to measure only growth in specific cells.

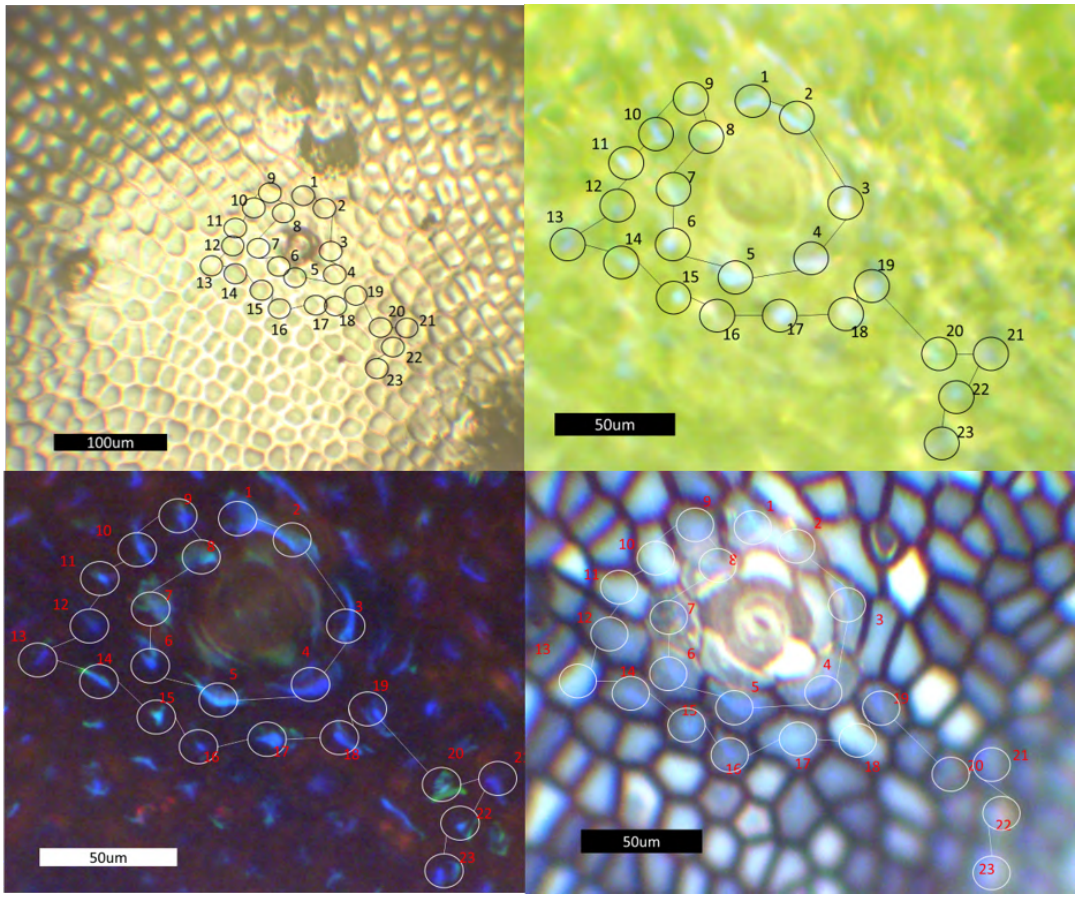

FIGURE 3.8: Optical microscope images of the cells measured in the part 2 growth series, at four points over the course of the study. The left-most image is taken between parallel polarisers, and the other three are between crossed polarisers in order to better show the reflected cell colouration.

3.2.3 Optical Measurements

Each observation of an individual cell was taken using a spectral measurement referenced to a mirror, and a near-simultaneous microscope photo. The details of instruments used are specified in section 1.5.1. Here I briefly compare different polarisation filter measurements using spectral peaks from *P. japonica* cells.

Figure 3.9 shows low magnification images normal to the surface of *P. japonica* in crossed (X), parallel (P), left (L), and right (R) circular polarisations for dry and water immersed objectives.

A significant amount of light is reflected from the smooth surface of the *P. japonica* cuticle. This light is reflected because of the refractive index contrast, and retains its incident polarisation. This reflection dominates the image in parallel (P1), left (L1) and right (R1) circular polarisation for the dry objective. Crossed polarisers cut this cuticle-reflected light, allowing reflection from within the cells to dominate the image (X1). This is effective to visualise scattering and circularly polarised reflections. In thecase where internal reflection from a cell is from an isotropic planar structure that is also suppressed.

Water immersion microscopy is detailed in section 1.5.1. The technique uses a water droplet to bridge the objective lens and the sample, so that the refractive index contrast is reduced, and the image is dominated by reflection from within the cell as in the case of crossed polarisers with a dry lens. The advantage of water immersion microscopy is that the reduction in cuticle glare may be combined with other polarisation filters, as all are effective in immersion for imaging reflection from within the cell (L2, R2, X2, P2).

Measurements comparing the use of left and right circular polarisation with crossed polarisation filters in water immersions are shown here to support the choice of polarisation measurement and analysis.

Left and right circular polarisation spectra measured in water immersion are shown as pairs on the same plot in figure 3.10 plot A, and the difference between the two profiles for the same data is shown in plot B. The use of this subtraction method allows pure structurally coloured spectra to be gauged. The characteristic peak is seen to be a single or double peak location below 550 nm.

L-R subtracted profiles are compared to crossed-polarisation measurements in figure 3.11 A. The peak wavelength was identified from each spectral profile individually, and the paired L-R and crossed peaks were compared to understand if any systematic bias was introduced in peak wavelength identification through the use the techniques with respect to each other. The results are plotted in plot B of the same figure, and no systematic bias was identified. A small random error was seen, with a standard deviation of 7.5 nm. Examination of the actual peaks observed in the two

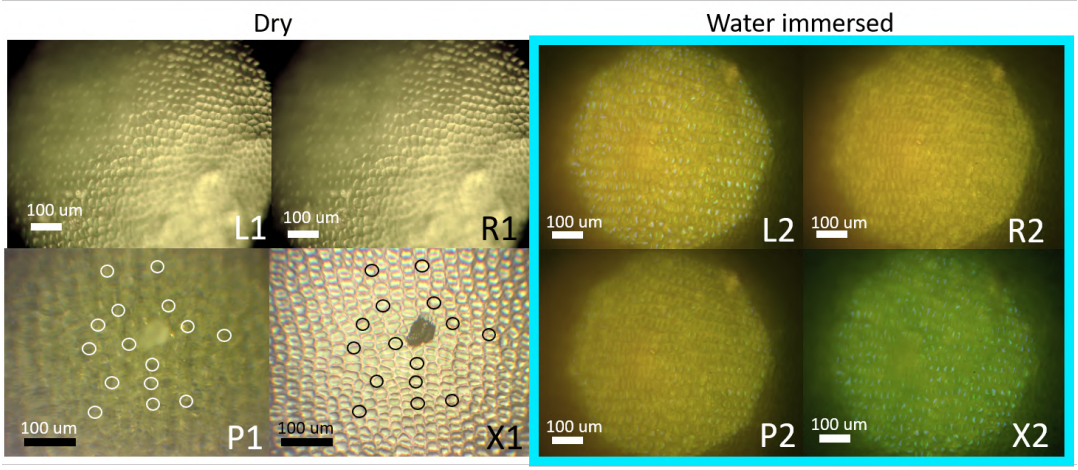

FIGURE 3.9: L1, R1, X1 and P1 are images of *P. japonica* using a standard (no water immersion) objective in left, right, crossed and parallel polarisation respectively. X1 and P1 show the same area, with the cells measured in the first experiment indicated. L1 and R1 show the same area which is also measured in the corresponding images with a water immersion objective L2, R2, X2, P2. These are filtered using left, right, crossed and parallel polarisations.

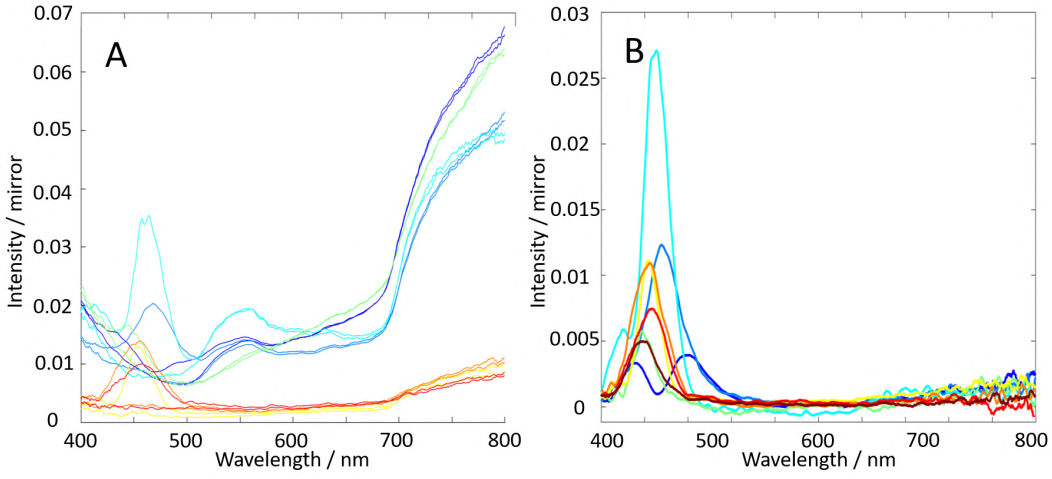

FIGURE 3.10: A. Left and right handed circular polarisation spectra measured at several intervals. B. The same data but the right spectrum has been subtracted from the left handed circular polarisation spectrum to reveal the purely structurally coloured peak. The noisy signal above at longer wavelengths is likely to be the result of reduced accuracy of the polarisation filters at wavelengths above 700 nm.

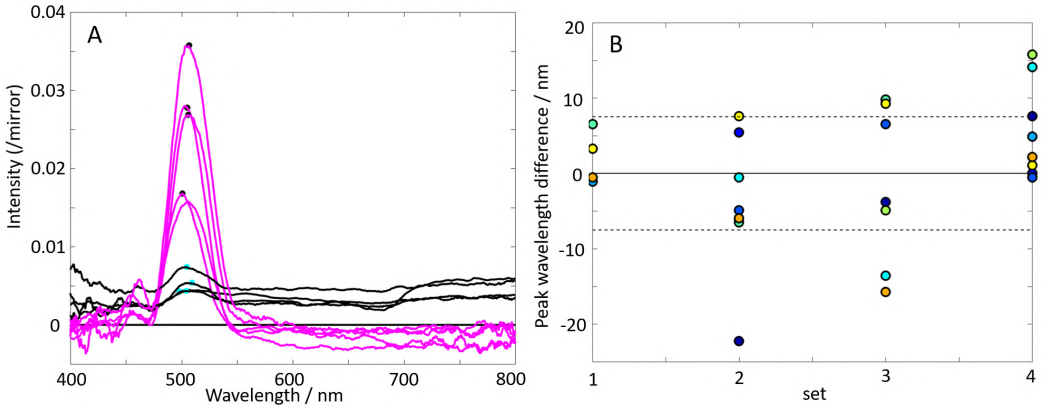

FIGURE 3.11: A. The structurally coloured peaks are identified in both the L-R subtracted profile (magenta), and the crossed-polarisers profile (black). B. Comparison on four occasions of the difference between the peak wavelengths identified in each method. The peak identified in crossed polarisation is subtracted from the L-R peak wavelength and the difference plotted

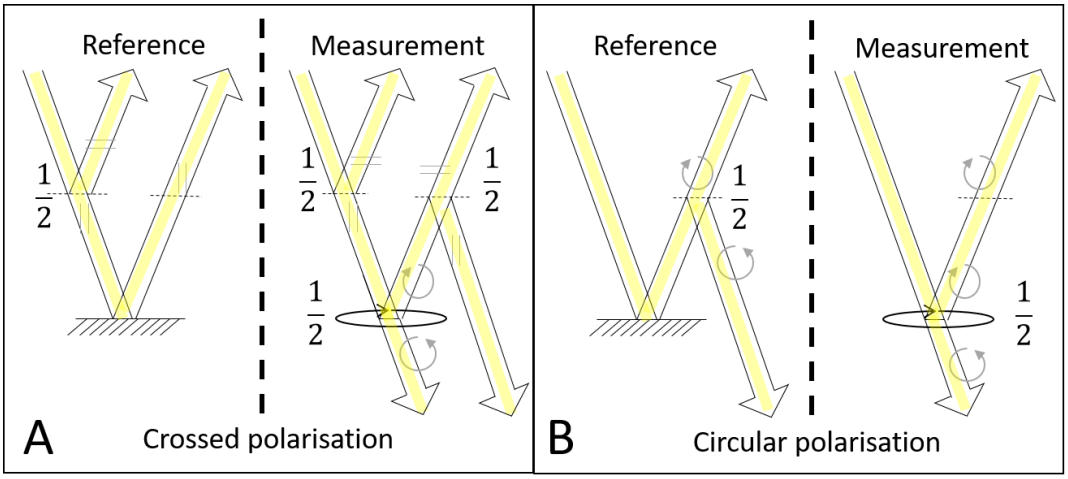

FIGURE 3.12: Schematic showing the ideal case of reference and circularly polarised reflection in crossed polarisation (A) and circular polarisation measurement (B). Fractions indicate where proportions of the light are lost by filters, which are indicated with dashed lines. A uses two filters, and B only one. The polarisation of light were it exists is indicated after each filter by curved arrows and parallel lines.

different polarisations showed that it was seen where the structural colour peak was very low, making it difficult to distinguish from noise and pigment scattering.

The intensity measured by the L-R method is more intense than the intensity measured by the crossed-polarisers method for the same spectrum. This is due to the use of different polarisers and references for the measurement. The schematic in figure 3.12 shows the references and measurements on ideal circularly reflecting samples. From this diagram, we can see that in an ideal system, the L-R spectrum measured should be four times more intense than the crossed-polariser method.

The two sets of peaks measured in crossed and circular polarisation in figure 3.11 were compared and it was found that the difference in magnitude of reflected intensity is 4.7. The additional light intensity is likely to be absorbed by the input linear polariser which is not present in the circular polarisation measurement and also acts as an absorber.

The degree of non-uniform scattering reflection from the surface cells of the fruit is very high and in order to use left and right handed circular polarisation filters, they must be used in water-immersion configuration. Water-immersion introduces significant experimental limitations due to the difficulty in maintaining a stable water bridge between the objective and sample. However, as described in 2, *P. japonica* reflects structural colour with only left handed circular polarisation, making it suitable for analysis with crossed polarisers in dry observation. This technique was adopted, and is used for the rest of this chapter. In order to produce a realistic reflection intensity comparable with circularly polarised measurement, intensities are reported with a x4 factor in this chapter and the next. This is likely to be an underestimation of the appropriate factor, due to the filter absorption.

3.3 First Stage Growth

First, I present growth observations, then I discuss processing of the data for analysis. I describe the changes observed and trends visible in the entire set of cells and propose an interpretation, which I illustrate by considering the particular case of individual cells.

3.3.1 Results

Optical Characterisation

The changes observed over the initial period are illustrated by the images in figure 3.13. This figure is intended to demonstrate that the fruit did not appear to change significantly during this time.

However, the same period measured using a spectrometer on each individual cell shows clear changes in the optical response. Figure 3.14 shows how the reflection spectrum of a typical cell changes during this time. The signal features two distinguishable component peaks. The broad humped peak above 500 nm is characteristic of chlorophyll reflection and the narrow peak below 500 nm corresponds to a structurally coloured blue spot emerging from the cell.

The plot shows all the measurements recorded in the first stage. The earliest measurements show no structural colour visible, transitioning slowly to the final stage where a blue peak is visible with 0.025 of total light intensity. The intensity of the higher wavelength broad scattered reflection peak also increases during this period.

Non-structural colour profile. Chlorophyll pigmentation in the *P. japonica*, its density, location and changes undergone during the studied are treated as a baseline reflection. Briefly, the chlorophyll spectral reflection is characterised by the absorption profile of chlorophyll which is shown in figure 3.15 and characterised by two sets of peaks in the blue and red regions. The green colour reflected by chlorophyll is the scattered green light that falls between the two absorption peaks and is not absorbed. An increase in the chlorophyll density or absorption increases the levels of light being absorbed at these wavelengths. There is also a small amount of light absorbed at wavelengths between the peaks, the intensity of the scattered light at green wavelengths is therefore also affected by the density of chlorophyll. However a more profound change occurs when brown pigments, absorbing strongly at green wavelengths, are introduced into the system. A full analysis of the relative importance of these pigments is not attempted here. I refer in the following work to the reflected 'chlorophyll spectrum' but it should be remembered that characterising the scattered light which is convoluted with the structurally coloured peak is a mixed scattering from tissue largely defined by the absorbance peaks of chlorophyll and other pigments.

Interpretation This peak clearly grows in intensity with no large change in its maximum wavelength. This initial result, although so far relatively uninterrogated is unprecedented. It should be recognised at this point that this series of measurements is a coherent, clearly well-defined set of spectra taken from individual cells over a long time span, and the growing spectral peak location appears to be unvarying.

Further discussion of the deconvolution of this spectrum from the non-structural colour baseline signal follows. The initial representation by this data of no change

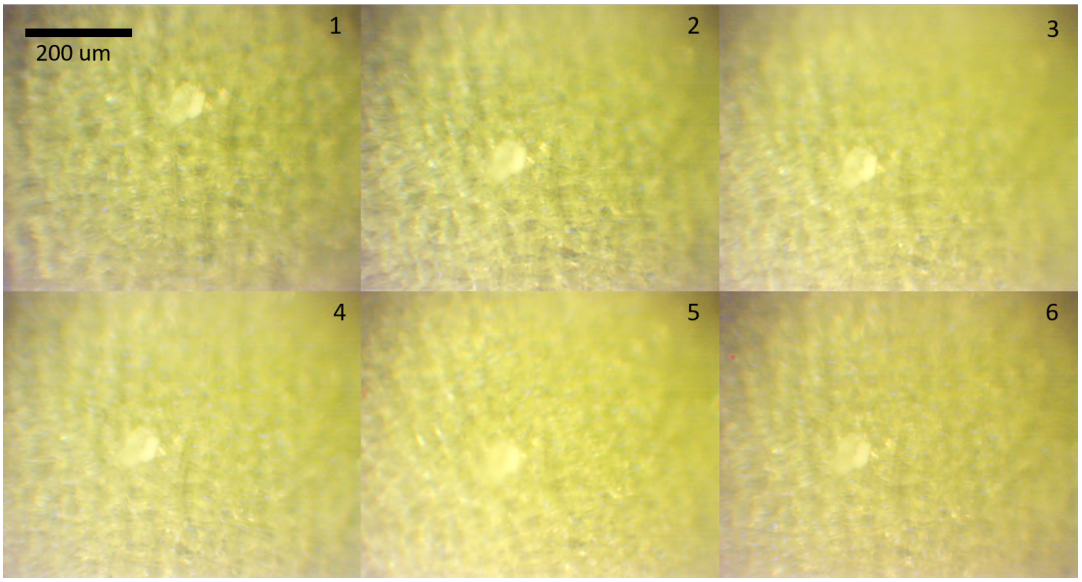

FIGURE 3.13: The entire target location without cells labelled, imaged at intervals over the observation period of five days.

is examined to understand its boundaries. However, the simplicity of this measurement should not detract from the strength of the message it conveys. These measurements place tight parameters on any peak wavelength change observed after further data processing.

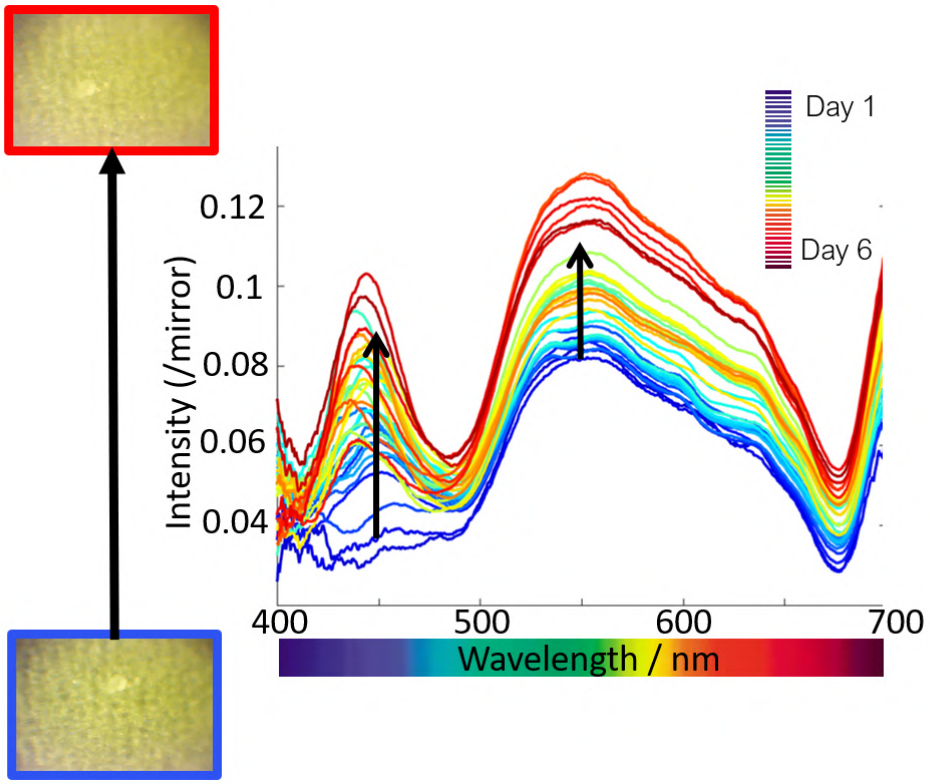

FIGURE 3.14: This plot shows all the spectra measured from one cell over the first week. The chronological order of the lines is shown by the plotted colour, with blue being the earliest plot through to the last in red. The inset images' border colours correspond to their respective line colours.

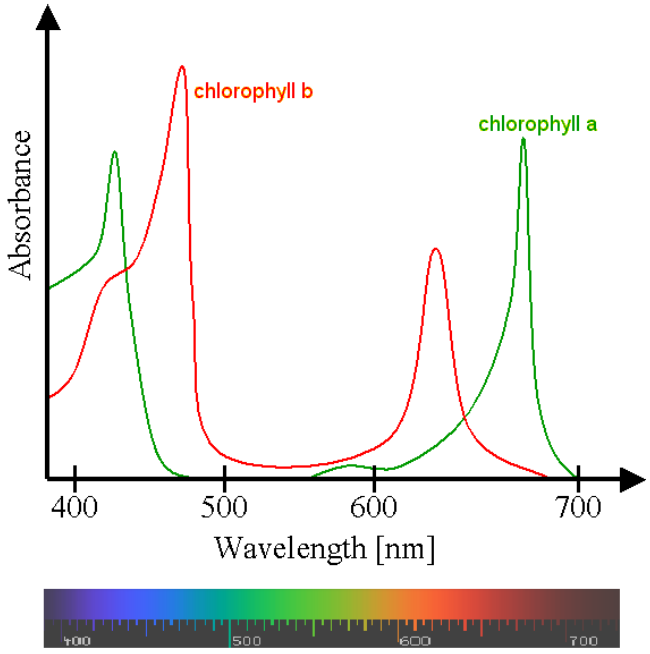

FIGURE 3.15: This figure shows the known absorption spectra for chlorophyll a and b. [175] The pigments and chlorophyll content and location in the *P. japonica* are not identified. This figure is reproduced from [176].

Control Data and Structural Colour Extraction

Figure 3.14 shows an increasing structural colour peak and an increase in the peak of light scattered from the cell below. Therefore the structural colour peak must be separated in order to understand the degree to which the peak characteristics can be accounted for by changes in the nanostructure.

The scattered chlorophyll-based profile did not change uniformly during the variation in its intensity. This required for each measured spectrum a control spectrum of approximately the same pigmentary age. Control cells were measured throughout the observation period. These were cells in which no structural colour peak was visible in any part of the spectrum throughout the study, due to being at the edge of a large and relatively underdeveloped cell. Each spectrum from the control cell was rescaled to the brightness of the target cell spectrum and then subtracted in order to leave the structurally coloured part.

The control spectra are shown in figure 3.16. The processing protocol is schematised in figure 3.17. The process does not work uniformly to give a pure structurally-coloured peak outcome as seen in the long-wavelength peak in a few outcome spectra of figure 3.17. Nevertheless it produced a good fit as judged by the flatness of the spectra over the area of the characteristic chlorophyll spectrum.

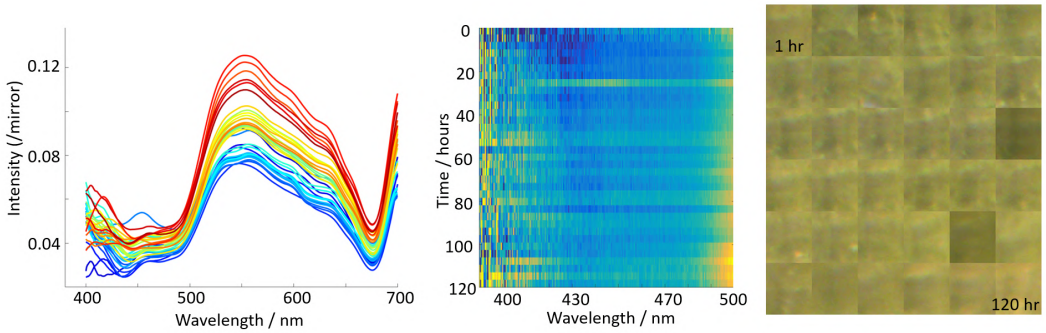

FIGURE 3.16: The control spectra reflected from an 'empty' i.e. non-structurally coloured cell area. The first plot shows all the spectra chronologically as before. The middle plot shows the same spectral information as a heat map with time increasing down the page. The right hand image is a montage of the cell at every observation time a spectrum was recorded. There is one erroneous measurement with a peak in the blue clearly visible, this was not included.

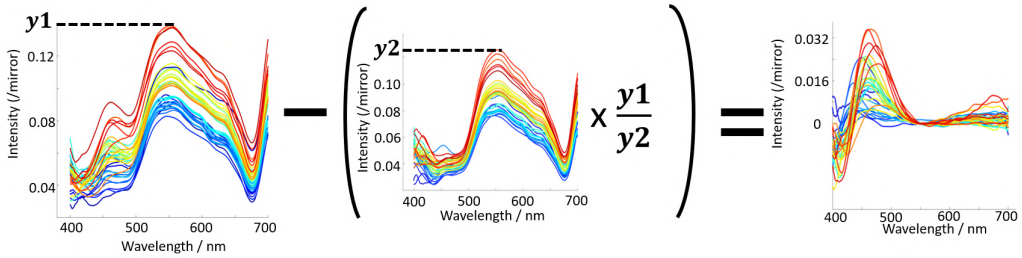

FIGURE 3.17: A schematic showing the process for removing the chlorophyll component of the spectrum from the original data by subtracting a pigment-only profile scaled to the intensity of the original cell's maximum chlorophyll spectrum, to give a peak-only plot. y1 and y2 are the respective intensities of the scattered light profiles.

3.3.2 Average Trends

After removing the control spectra, each of the measured peak intensities and wavelengths were identified and plotted.

The trends of each of the individual cells were modelled using a linear mixed effects (LME) model, as described in 1.5.2. Time is treated as the fixed effect, and each cell is treated as a random effect, in order to find a linear regression for the entire data set. The overall trend results are discussed for peak intensity and wavelength.

Peak Intensity

Figure 3.18 shows all of the measured peak intensity points plotted over time. A linear mixed effects regression model [177] combines the fixed time-dependent effects that are being modelled, with the random effect of each cell identity. The intercept and gradient for each cell trend are taken as independent variables by comparison of LME models with and without a correlation term.

Using the linear mixed effect model allows the influence of the random effect coefficients - the cell identities, to be treated separately, leaving the fixed effect elements of the characteristic model. The fit in this case gives an equation of $I = 0.01 + 0.003x$ with a very small p-value for the fixed effect gradient, being 3×10^{-9} and therefore confirming an increase in intensity by rejecting the null hypothesis.

Over 120 hours, the change is an increase in the intensity by 1.5% of the total incident left circular polarised light.

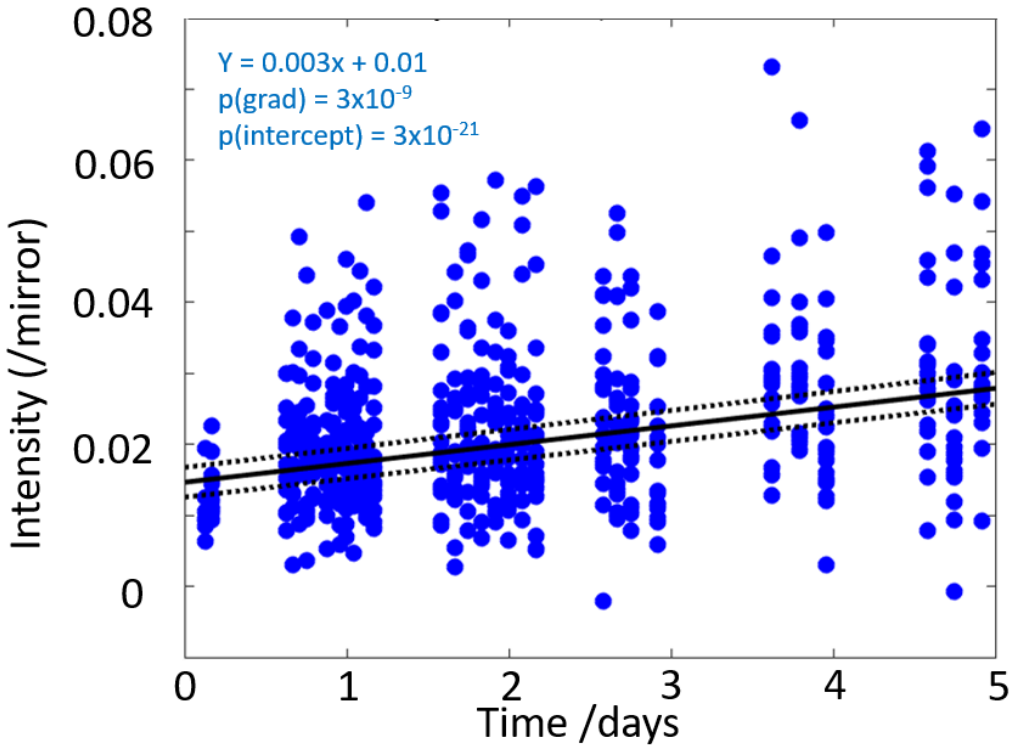

FIGURE 3.18: Peak intensity for every spectrum at hourly intervals over the observation period are plotted. All the spectral series are fitted using a linear mixed effects model, and the fixed effects average model plotted in the black line representing $y = 0.01 + 0.003x$ where y is intensity as a proportion of total incident light and x is time in days.

Peak Wavelength Trend

The linear mixed effects technique was also applied to the peak wavelength series. All the points and the linear mixed effects model are plotted in figure 3.19.

The best fit regression model in this case is $W = 452 + 0.1x$ which represents a very small change in the peak wavelength over 5 days of 0.5 nm, which is negligible, given estimated error. This is also supported by a large p-value indicating a failure of it to reject the null hypothesis, which is no change in this scenario.

The two linear mixed effects models in 1.5.2 were compared and a correlation between the initial peak wavelength and subsequent change in wavelength was not ruled out. However, the correlation term was not strong enough to prove this, and so the initial starting wavelength and subsequent change in wavelength were treated as independent. A graphical representation of this independence is shown in figure 3.20, in which no clear observation of correlation between peak wavelength and wavelength change is observed.

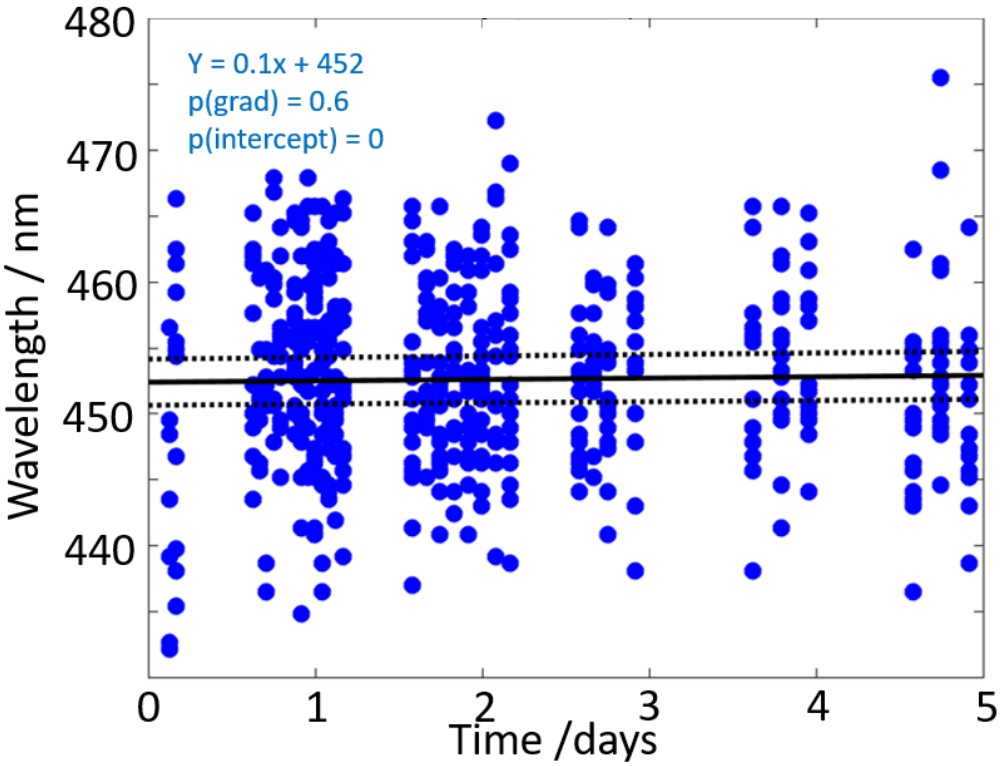

FIGURE 3.19: Peak wavelength for every spectrum at hourly intervals over the observation period are plotted. All the spectral series are fitted using a linear mixed effects model, and the fixed effects average model plotted in the black line representing $y = 452 + 0.1x$ where y is wavelength in nm and x is time in days. The model represents negligible change in the wavelength with time.

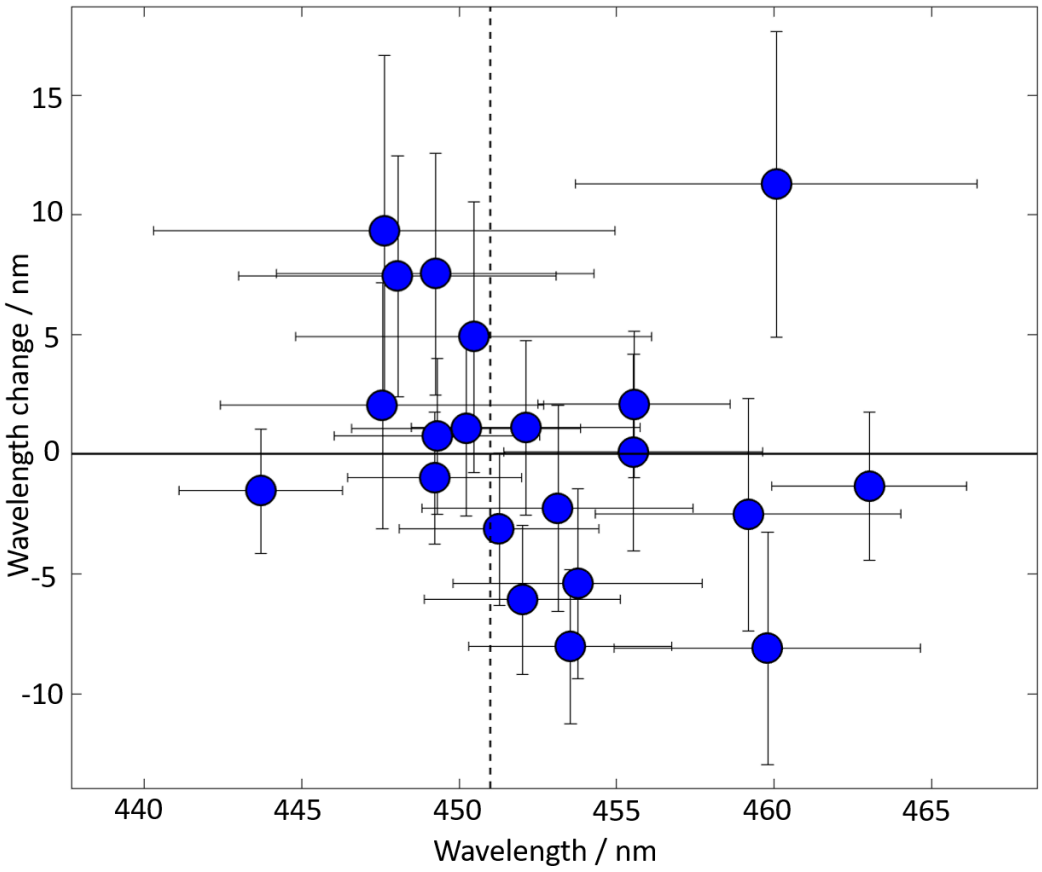

FIGURE 3.20: The change in wavelength in nm for each cell in the cohort is plotted against the average wavelength of the cell over the observation period. The standard deviations are plotted as the error bars. The points are fitted to a linear trend and the significance of this discussed in the text.

Trend Interpretation

The LME fits show that taking account for the differences in trends between cells, an overall dependence of the peak intensity and peak wavelength can be ascertained. The intensity is seen to increase over time, whilst the wavelength stays the same.

The change in spectral profiles confirms that development in the cell wall multilayer does occur during this stage of fruit growth. The interpretation of the change therefore provides information about the cell wall.

Comparison of the intensity and wavelength trends with the numerical model and parametrisation in section 1.5 is used to define the model for change in the cell wall multilayer. The lack of change in wavelength indicates that the pitch remains constant during development. This rules out a significant movement of the fibrils towards or away from each other during this phase.

In order to interpret the increase in intensity, the different parameter variations that induce an intensity change are considered. The increased brightness could be the result of an increasing birefringence in the fibrils of the cell wall, a decreasing imaginary component of the refractive index i.e. degree of absorption in the multilayer, or an increase in the number of pitch repeats present in the multilayer.

The explanation in terms of increasing birefringence is unrealistic because the birefringence of the initial material would have to be close to 0 to account for the earliest measurements. This would contradict a reasonable understanding of fibrillar cell wall material. The decreasing imaginary part of the refractive index would be a more acceptable account, although there is not an obvious material explanation for decreased absorption. A mechanism for the decrease in the absorption would be the expulsion of pigments or other molecules from the cell walls for example, perhaps into the body itself. This does not seem very likely.

The most straightforward explanation, that the number of layers in the multilayer increases during this time, is endorsed, requiring further evidence for confirmation. This explanation is consistent with previous understanding of cell wall biology and growth processes.

Individual Cell Trends

The individually tracked growth measurements mean that the data can be analysed also by considering each cell's development. Each of the cells in the set measured has a distinctive profile change in peak wavelength and intensity. Each of the cells' maturation profiles are not identical. This is a general observation coherent with the

spread of different wavelengths measured in chapter 2, and the variation observed in microscope images of the different cells.

Two cells' peak evolution are shown in figure 3.21 alongside the images of the cells. In order to characterise the change in the wavelength and the intensity of the cells during the maturation period, a comparison is made of the initial and final values of the fitted trend in the data. This is expressed as a total change in the peak wavelength in nanometres, and a change in the peak intensity.

Each of the cells in the cohort which developed colour is plotted in figure 3.22, eight measurement locations did not develop a coloured spot during observation. 50% confidence intervals are shown, some of which include 0 gradient in intensity.

A number of observations may be drawn from the overview plot in figure 3.22. The change in reflected peak wavelength over the time period is very small, in almost all cases amounting to a change of less than 10 nm. The peaks themselves generally have a full width half max of 20-50 nm, so this does not represent a change in location of the whole peak. By comparing this evolution to the calculated correlation of material pitch and reflected spectral peak from the numerical model, as shown in figure 1.16, a difference in 5 nm of the reflected peak corresponds to a material pitch change of approximately 1 nm.

Therefore, given the very small change in peak wavelength during the increase in the profile intensity, an additive interpretation is suggested. The peak wavelength change can be accounted for by a variation in the average pitch length, due to additional pitch repeats of the cell wall with different pitches. The additional pitch lengths do not vary with a systematic trend but fall within a characteristic distribution. This explanation maintains that the optical response is varied by a change in the average material properties due to cumulative addition, rather than a change in the extant material.

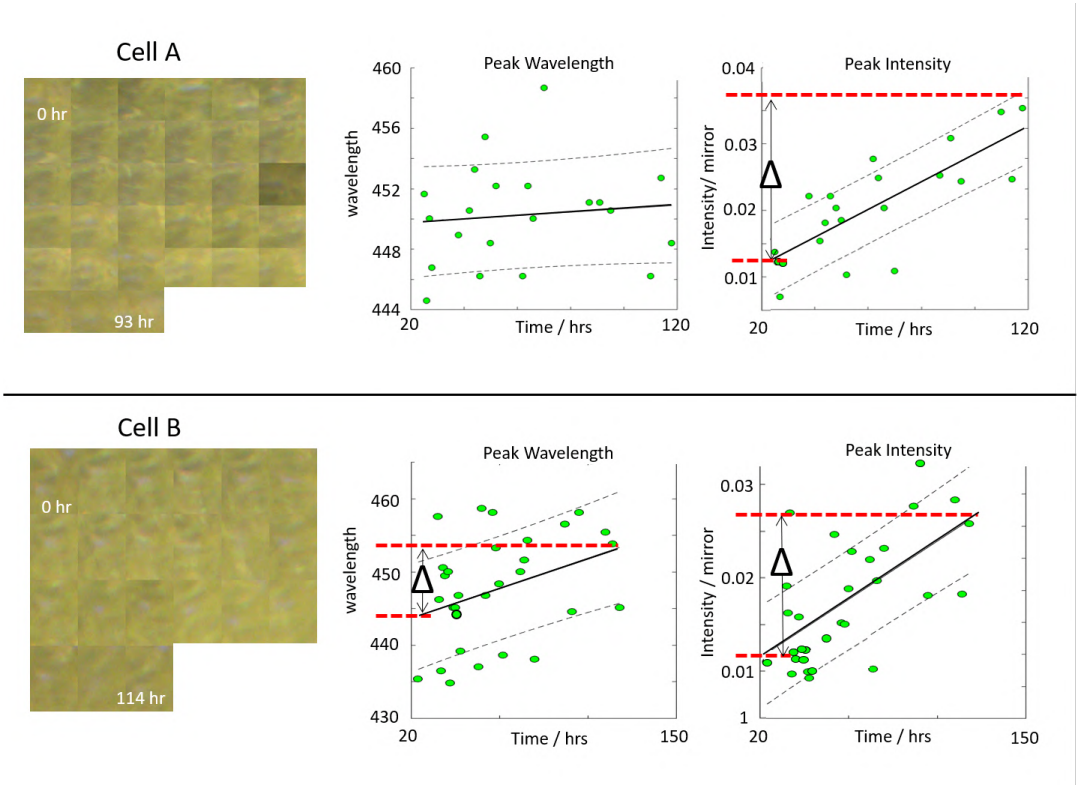

FIGURE 3.21: The change in peak wavelength and intensity are plotted for each of two cells A and B. Cell A shows an increase in peak intensity but not wavelength. Cell B shows a small increase in wavelength and a change in intensity. On the left hand side is a montage of each of the two cells over the observation period.

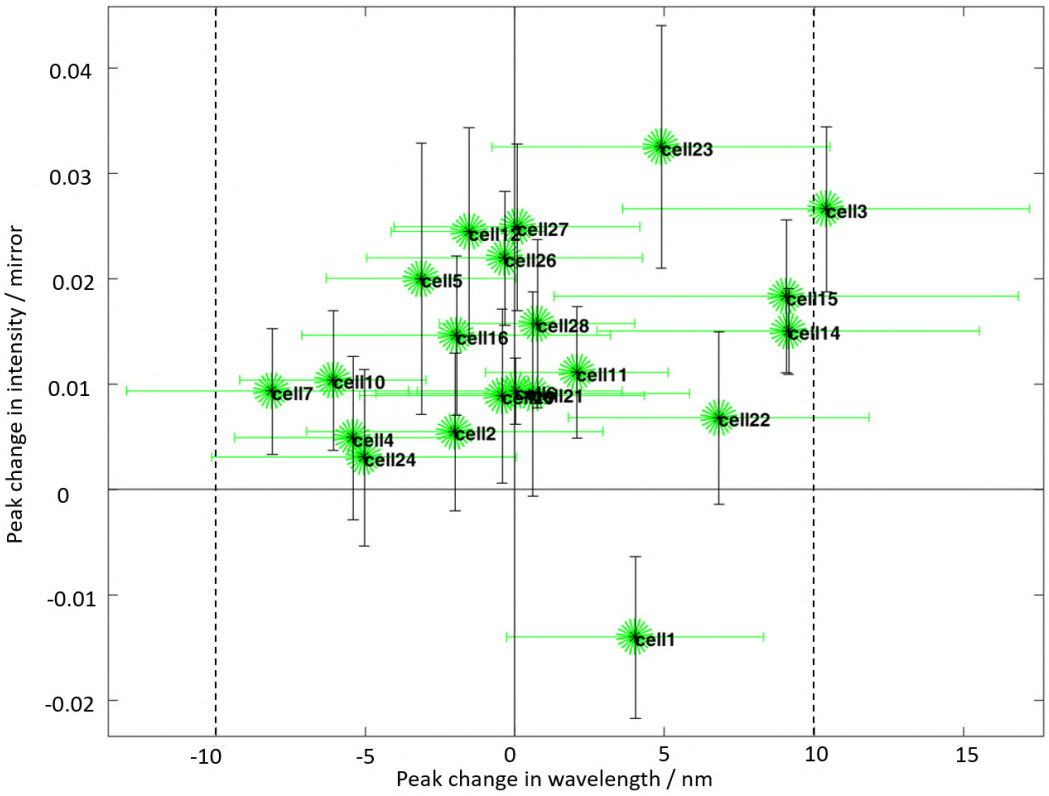

FIGURE 3.22: The overall changes over 120 hours in wavelength and intensity are plotted for each cell, with the 50% deviation shown. All the cells with measurable structural colour are plotted and labelled. Wavelength changes of ±10 nm are marked as guides to the eye.

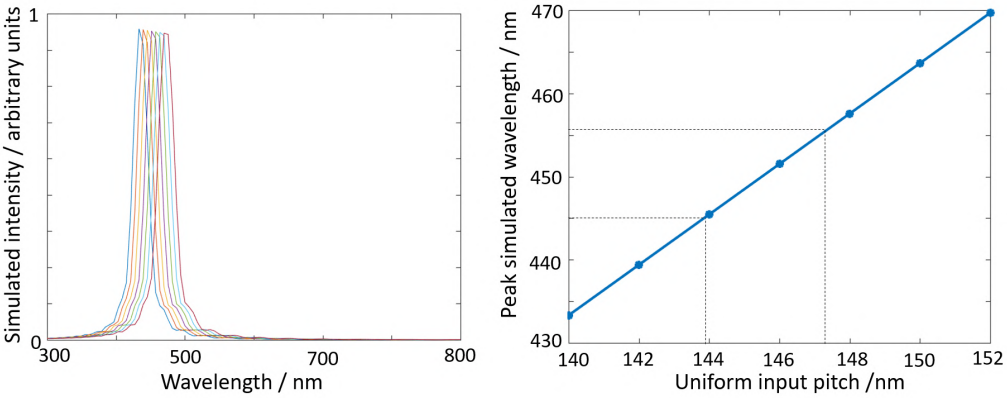

FIGURE 3.23: The plot on the left shows modelled optical peaks from a helicoidal multilayer reflector with a pitch varying at uniform intervals between 140 nm and 152 nm. The input pitches and corresponding model peak wavelength are plotted on the the right. The numerical model was discussed in section 1.5.3

.

3.3.3 Individual Cell: Increasing Intensity Reflection

In order to interpret the behaviours predicted by the analysis laid out above, individual cell behaviour is presented.

Figure 3.24 shows the photo montage of a cell with a marked increase in the intensity of the cell during observation, and no change in the wavelength over the time. The variation in measurements of the peak wavelength over 120 hours is ± 3.1 nm.

The removal of the chlorophyll signal has clearly been successful in this case, as demonstrated by the flat signal outside of the structural colour peak zone.

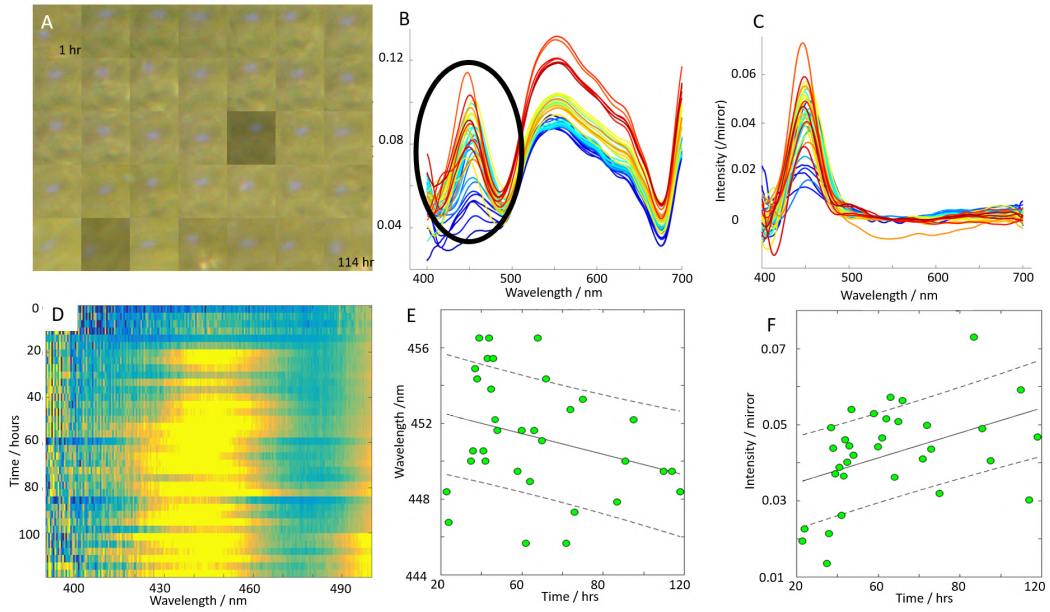

FIGURE 3.24: Different representations of a cell showing increase in intensity over time without significant change in the peak wavelength. A. Montage of optical microscope images of the cell. B. Unprocessed spectral series plotted chronologically in colours from blue (earliest) to red (latest). The wide characteristic chlorophyll profile is seen above 500 nm. The structural colour peak is circled. C. The processed spectra with control chlorophyll spectra removed. D. Heatmap showing the structural colour peaks represented in plot B. E & F. Identified peak wavelength and intensity plotted with respect to time.

3.4 Second Stage Growth

The second part of the study of *P. japonica* maturation was made on a subsequent observation series on a fruit located on the same stem as the original but that had not previously been exposed to focused light. The second fruit appeared to be further in the green stage than the first had been at the beginning of the first stage observation. The same cohort of 22 cells was measured on this fruit from the green stage through

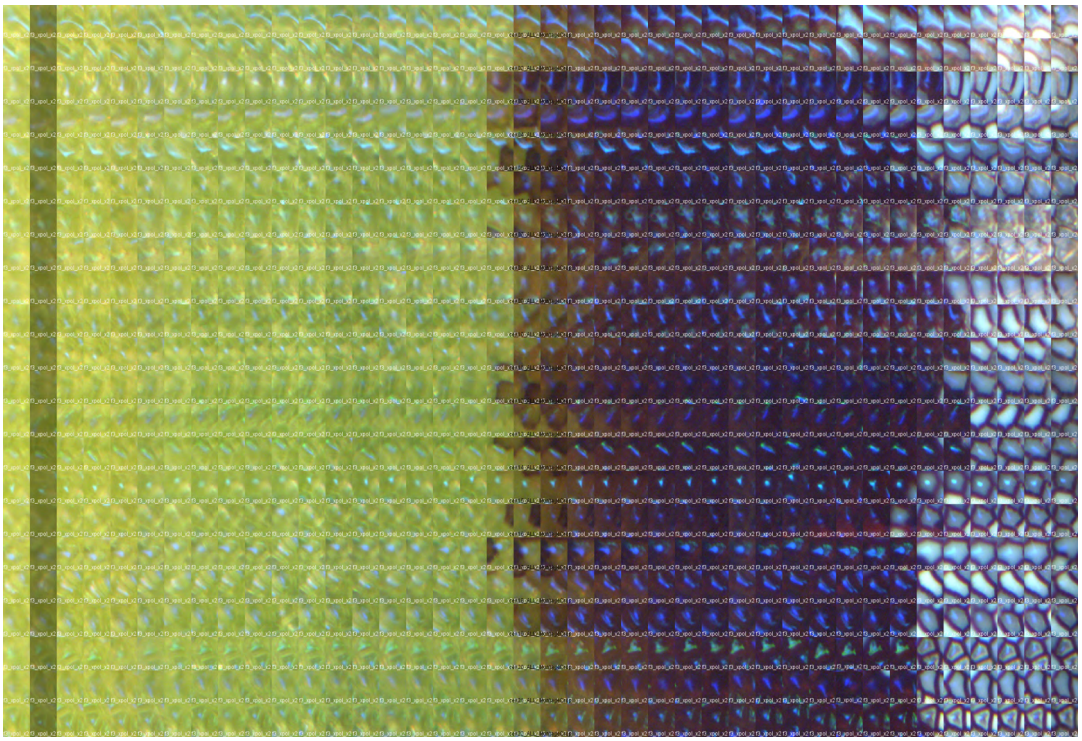

FIGURE 3.25: A montage showing a different cell in every row over the entire second observation period with time increasing left to right. The second column has a different exposure level and is dark. The three later stages can clearly be observed in the maturation period.

to full maturity as visible in figure 3.25. This transition is characterised by treating distinctly the green-brown transition, up to the end of the brown cell images in the montage, which took approximately 17 days, and the final transition from brown to blue, which occurred rapidly and is described in section 3.5.

3.4.1 Data and Processing

Optical Characterisation

The cells were chosen in order to be easily identifiable over a prolonged period, without the benefit of several observations a day, and were located around a stoma, as shown in figure 3.8. All the cells observed already featured a coloured reflection spot on initial observation, and were successfully monitored throughout the maturation period.

Data

A consistent peak profile transition pattern was observed in all the cells and a set of spectra from one cell simplified for clarity is shown in figure 3.26. The stage we consider here is the transition from the green framed inset image to the brown

framed image, and not the subsequent change which is discussed separately in section 3.5.

During this period, as visible in the spectral plot, the green scattered light peak grew, reached a maximum and decayed non-uniformly. The reduction in intensity of the reflected light was due to an increased presence of an absorbing pigment, which is seen in the gradual transition of the cell background to brown in figure 3.25. Full development of the broadband absorption pigment suppressed all non-structurally coloured light, exposing the target peak. This gives a purely structurally coloured profile and allows the pigment/structural mixed profile to be usefully compared to the purely structural peaks. From this comparison, it is observed that the peak wavelength after pigmentation was unchanged from its earlier apparent spectral location. This supports the analysis that extra scattered light does not change the apparent peak wavelength of the structurally coloured peak, even when measured from a mixed profile.

The non-structurally coloured spectral profile does however have a demonstrable impact on the structural colour peak intensity. Although the peak intensity of the structural colour appears to decrease over the observation time in this data set, this is because a significant amount of the light collected, even in the < 500 nm range, is due to the scattered profile contribution, which is decreasing. This is visible in the correlation between the observed impression from the microscope image which is dominated by the pigment contribution, and the peak intensity in the spectrum, see appendix 7.5, figure 6.

In the previous stage a control series was recorded which was used to deconvolute the structural and pigmentary components of the peaks. In this case, the peak profile was evaluated in terms of prominence. This measure, which takes the height of the peak only from its boundary minima is not the same as structural colour intensity because of the existence of non-flat pigment absorption profile below 500 nm. However, the contribution of absorption peaks in the short wavelength region is small, as seen in the control data in the first stage, see figure 3.16.

This was the best measure of the peak evolution as no control data was available for the second stage. The analysis of prominence as a measure gives a good understanding of the feature size and shape and the dominance of structural colour in the profile. It is not identical with intensity and should not be directly compared. The non-uniform change in the pigmentary contribution makes the use of a single scaled chlorophyll profile inaccurate, disaggregation attempts based on this method are included in appendix 7.5 figure 5.

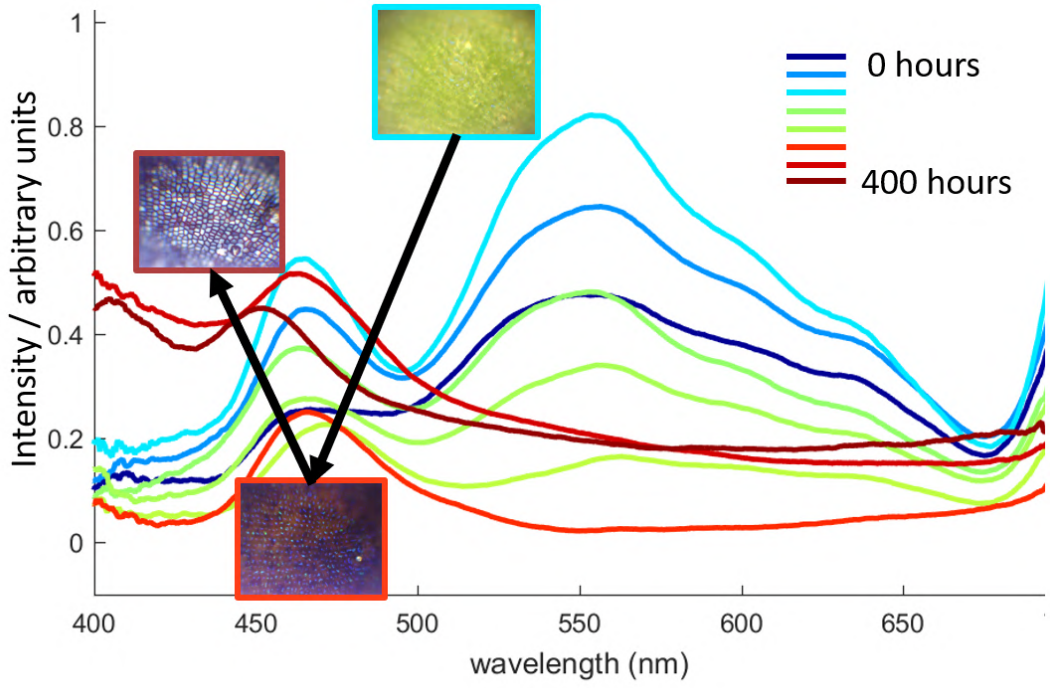

FIGURE 3.26: The plot shows a selection of characteristic spectra taken over the observation period, covering the green and brown stages and also the transition to the blue stage which will be considered in section 3.5. The inset images represent the appearance of the target cell area at three intervals. 400 hours corresponds to 17 days.

3.4.2 Trends

In order to understand the trend in peak characteristics during the second stage development, the peak wavelengths over time were fitted with a linear mixed effects model as discussed previously in 1.5.2 and used in the first study in 3.3.2. The confidence interval for the correlation between the intercept and the gradient included 0, indicating no correlation. The fitted model therefore models the intercept and gradient of the wavelength change as independent variables for each of the cells.

Peak Wavelength

The peak wavelengths are different for each cell but remain unchanged during the observation. The lack of a trend in the wavelength indicates no change in the cell wall pitch after having been laid down. This result is consistent with the result in the previous observation of stage one which also found that the cell wall material does not subsequently change pitch after development. The subtraction of the unabsorbed reflectance spectrum from the profile to expose the structural colour peak that was performed in the first section indicated that this did not significantly change the peak wavelength identified within its error. The no-change trend in the peak wavelength during this time is therefore taken to be robust.

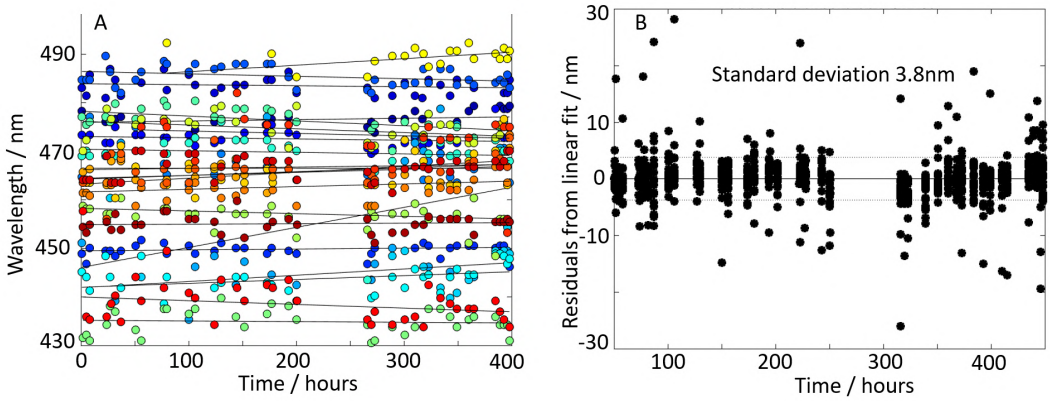

FIGURE 3.27: A. The peak wavelength of each cell over the time in hours is plotted for each cell alongside a linear fit. B. The residuals of the points from the linear fit for each cell are plotted. The points are fitted closely with small residuals showing a good approximation to linear fit. The standard deviation of the residuals are shown by dotted lines.

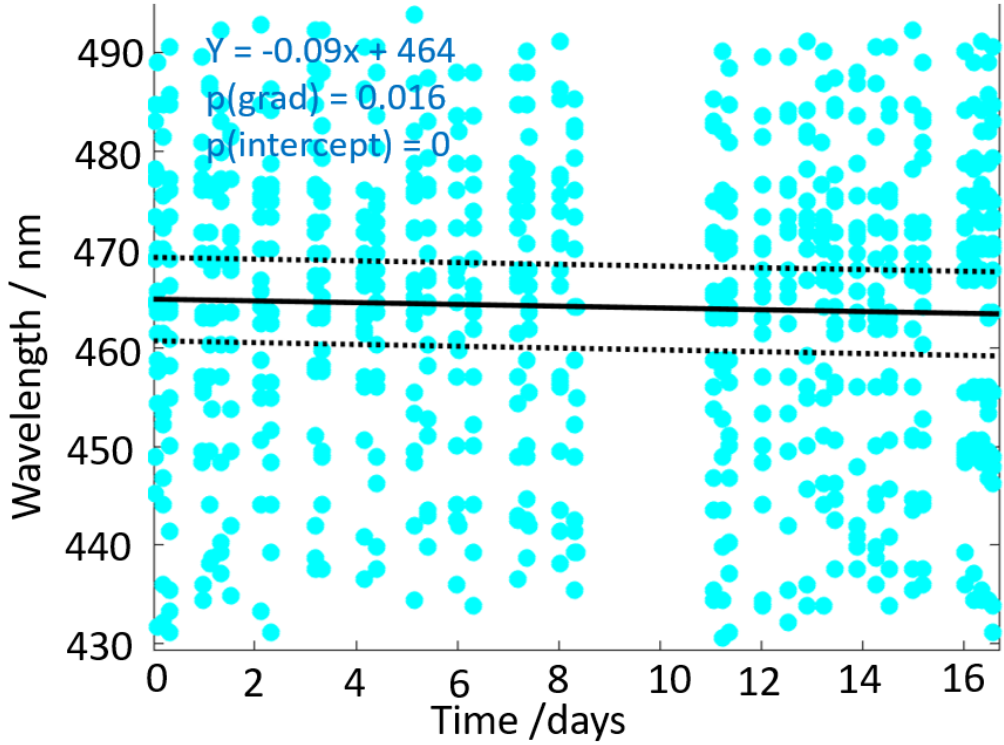

FIGURE 3.28: Each of the cell peak wavelengths are plotted over time as before, and a linear mixed effects model fitted showing a close to 0 gradient over 17 days.

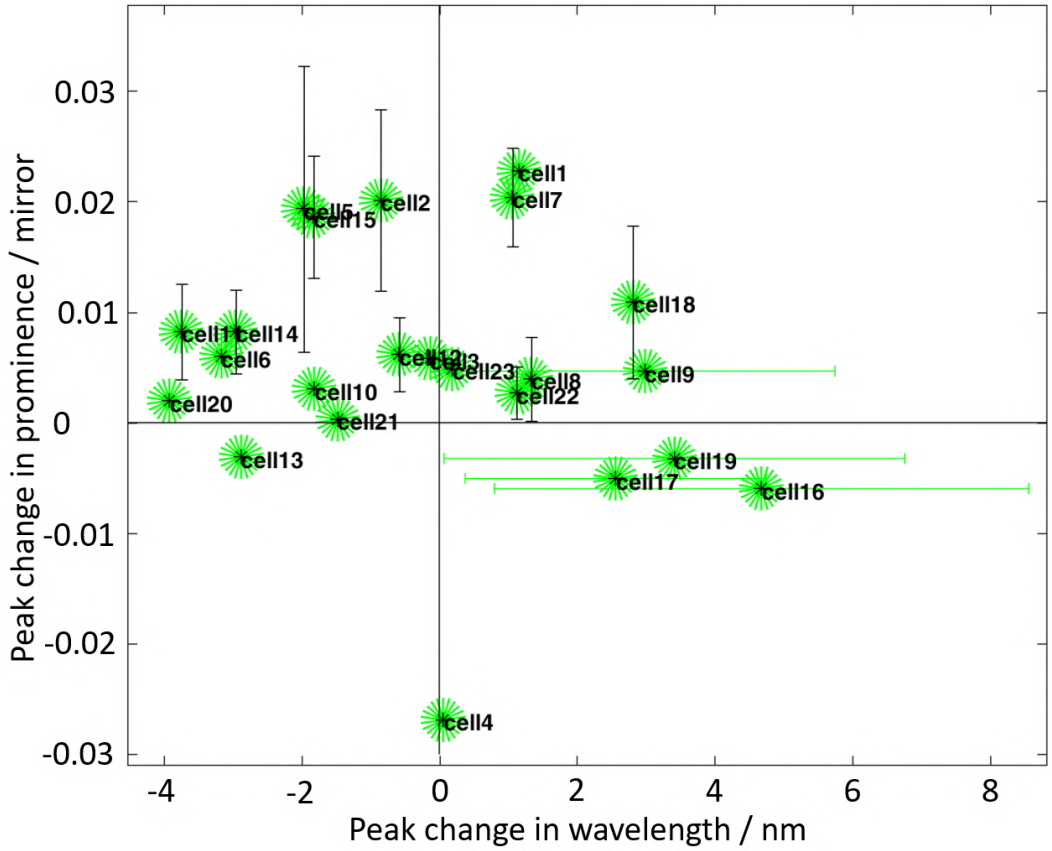

FIGURE 3.29: Each of the cells in the second cohort is plotted in terms of the overall change in prominence as a function of the overall change in wavelength. It should be noted that the time considered is four times longer than the observation period in the previous section. The 50% deviation intervals are indicated by error bars on both axes where the error bars do not include the 0 change.

These results were fitted with linear trends. Figure 3.27 shows the linear fits of each of the individual cells, and the resulting residuals. The overall degree of change over the observation period is plotted in figure 3.29, again confirming no change in the peak wavelength within errors.

The best fit by the linear mixed effects model is shown in figure 3.28. The plot shows a wide spread of average wavelengths for the cells, but for each cell a long-term constancy with very little change occurring over the 400 hour observation time. The gradient of the linear mixed effects model is -0.09 nm/ day, or an overall estimated change of -1.5 nm / day over 17 days. The very small confidence interval in this case does not include 0 gradient, and the p value is 0.016, which is very close to 0.01, a good indicator that the null hypothesis might be rejected in favour of the fitted gradient. Despite the fit being a good one in this case, I do not think that the evidence is sufficient, given the error to confidently conclude a very small decrease in peak wavelength over this very extended period.

Figure 3.29 shows each of the individual wavelength changes plotted on the x axis. Cells are distributed fairly evenly with both slight changes in peak wavelength. Error bars are shown for those cells whose 50% confidence interval does not include no change. The only peak wavelength changes for which this is true are cells whose peak wavelength increased by a very small proportion. This evidence, in opposition to the very small decrease described by the linear mixed effects plot indicates that no change is a better conclusion than either an increasing or decreasing average wavelength.

Peak Prominence

Figure 3.29 shows the prominence change in each of the cells plotted against the change in peak wavelength. The prominence is shown as a total change over the observation period. The spread of prominence changes show that there is a tendency towards increasing prominence.

A simple growth model expects that a multilayer increases then remains at a constant thickness. Cell transitions with either increasing or unchanging prominence are therefore consistent with this model. Ten cells showed an increase in the prominence of the peak, thirteen showed a change including 0 gradient within the 50% confidence interval. Of these, eight showed a slight increase in prominence, and five a slight decrease.

One cell showed a pronounced decrease in prominence of -0.025, although with significant error. This cell had a particularly high initial prominence, more than twice as large as each of the other cells. This cell was measured to have the clearest stability, i.e. the smallest peak wavelength gradient - the wavelength change measured

in this cell was 0.06 $\pm$1.3 nm. The cell was also one of the first to reach full maturity, indicating that the cell wall may have fully developed earlier in this cell. The decrease in prominence is therefore attributed to a decrease in the ease of measuring the cell wall material over time, due to the cell orientation and shape. Initially the cell may have been at a fortuitous angle for measurement, making it especially bright, and therefore an easy and conspicuous target. This bias seems a probable source of erroneous prominence decrease measurement.

3.4.3 Individual Cells

There is a clear standard behaviour apparent in many of these cells. The long time-period and large number of data points collected in this instance make the trend convincing across the cohort. Instances of cell development here are used to illustrate those transitions.

Increasing Prominence Cell

The cell in figure 3.30 is clearly and consistently identified, as shown in the montage. The cell reflection spot is brightly visible in the first instance, and remains a similar size and shape throughout measurement. The plots of peak wavelength and intensity in the figure show an increase in prominence of the structural peak, centred at 475 nm, although the intensity decreases during this time. The change in peak spectral wavelength over 400 hours is estimated as a decrease of 2 nm, smaller than the 50% confidence interval of the trend line of $\pm$3 nm. The prominence increase in this instance may be the result of an increased structural colour contribution. However, an effect of the declining contribution from the chlorophyll profile might also be responsible for the apparent increased prominence.

Stable Prominence Cell

Figure 3.31 shows a cell in which the cell reflection spot is again clearly visible from the initial observation. In the brown phase the bright blue dot appears to have slightly grown, showing areas of structurally coloured material over a greater area of the cell before the final transition to blue-grey (this final transition is treated in the next section). The trend again appears to show a change in wavelength well within an error of less than 3 nm spectral shift. The prominence of the peak also in this case appears entirely constant over the observation period, although the overall intensity decreases due to the decrease in the chlorophyll pigment contribution. If the prominence is taken as a proxy for intensity, this observed cell would be explained by a cell wall which has stopped thickening and developing before the beginning of the observation period, which undergoes no subsequent change.

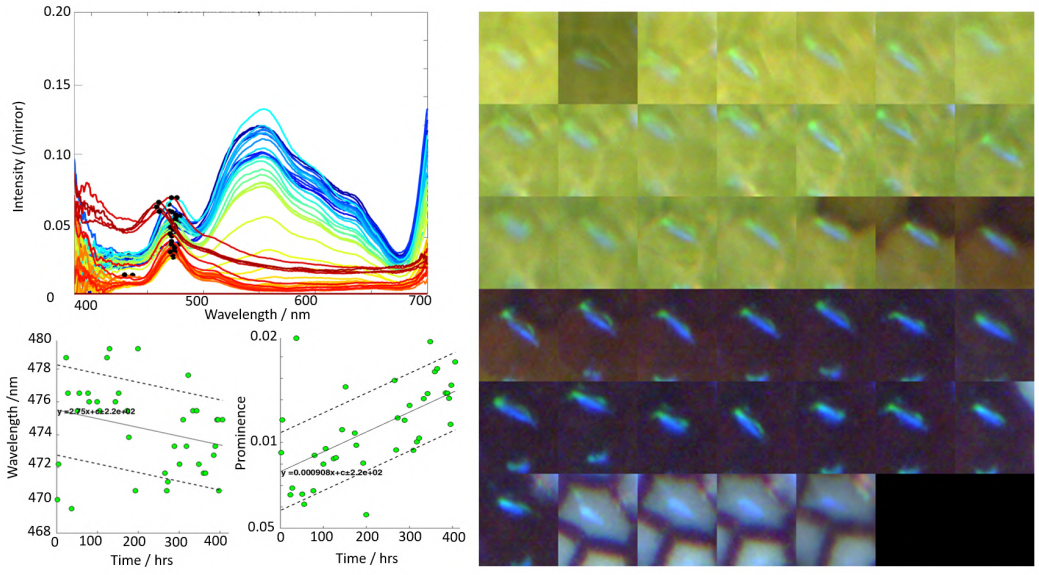

FIGURE 3.30: This case study shows a full spectral characterisation over time and the structurally coloured peak identified. The peak wavelength and prominence are plotted on the lower left-hand graphs. The montage on the right show the same cell at each of the observation intervals. This cell shows a clearly increasing prominence, and unmoving peak wavelength.

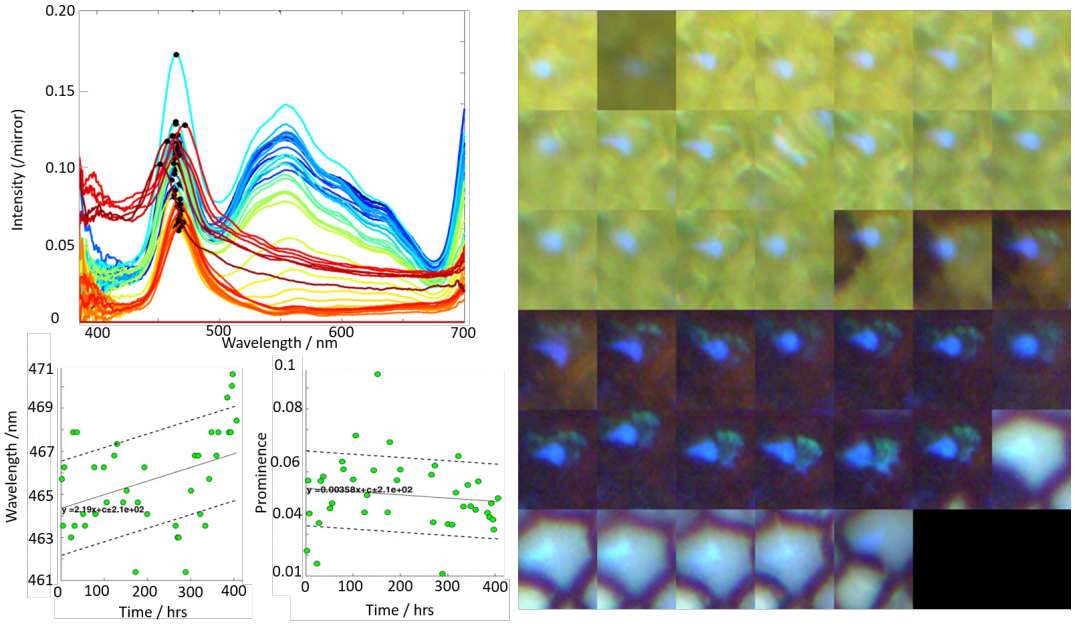

FIGURE 3.31: This case study shows a full spectral characterisation over time and the structurally coloured peak identified. The peak wavelength and prominence are plotted on the lower left-hand graphs. The montage on the right shows the same cell at each of the observation intervals. The cell shows an unchanging prominence, and borderline stable peak wavelength.

3.5 Part 3: Final Dehydration

The montage images in the previous section, for example figure 3.25, include the final transition from the brown phase through to the mature blue-grey appearance of the fully developed fruit. This final phase is of quite a different character to the previous development phase, it was unexpected and is undescribed in the literature on structurally coloured cells. The transition phenomenon is described and a mechanism suggested here.

3.5.1 Observation and Measurement

The final stage of the maturation of *P. japonica*, observed in the points after 400 hours in the plots of figure 3.32, is more dynamic than the previous stages. The change in visual appearance of the cells when observed was completed in a fraction of a second, as demonstrated in figure 3.33 which shows frames from a video captured of a fruit cell undergoing transition. The 25 fps frame rate was not high enough to observe significant intermediate appearance between the two stages.

The spectra and extracted peaks from consecutive observations are shown in figure 3.34. The spectral progression is notably less varied and shows a clearer evolution than in the previous scans. This may be due to the distinctive transition to the final phase, but it is also likely to be an improved observation due to the increase in the absorption pigment background which mops up stray light. Further factors making the measurement of the transition more homogeneous are the relatively short timeframe, and the clearer definition at maturity, with respect to its earlier stage.

Trends

After this dramatic transition, the reflected light intensity increases at every wavelength. The coloured peak is significantly wider after the cell transition, and has a peak wavelength around 10 nm shorter than the pre-transition peak, see figure 3.34. The light is subsequently reflected from the entire top surface area of the cell rather than a central coloured spot, although in most cells there remains a slightly brighter and more strongly coloured spot in the centre.

3.5.2 Explanation

The transition observed in this section is very different to the evolving growth that is the focus of the other measurements presented in this chapter. Interpretation of the distinct brown-blue transition specifically is given here.

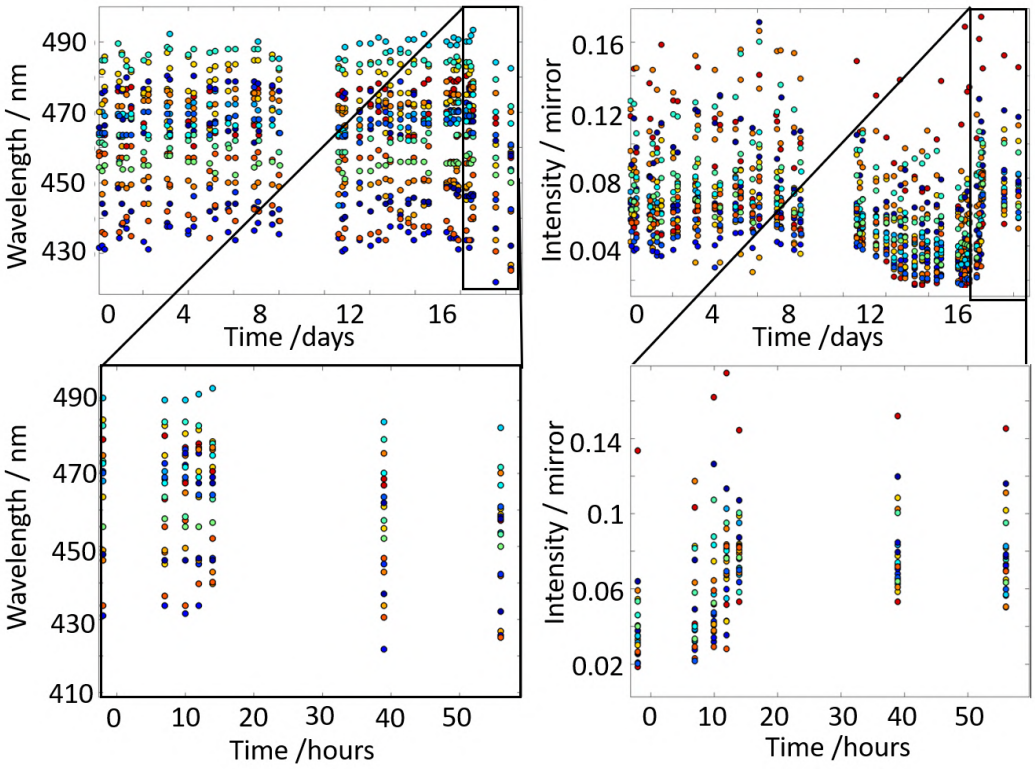

FIGURE 3.32: The final stage is considered here, represented by the lower pair of plots. Their relationship to the second observation period data is indicated by the boxes. The pigmentary contribution in the beginning of this stage is taken to be negligible and the intensity is therefore accurate without removing a pigmentary contribution.

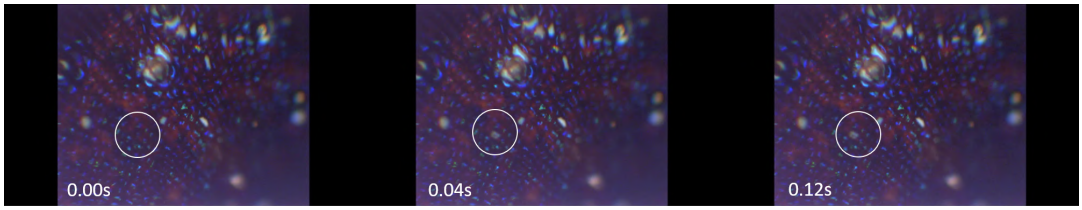

FIGURE 3.33: Frames of a video taken of the final transition occurring rapidly in a single cell, indicated by the white circle. The frame time is indicated on each image.

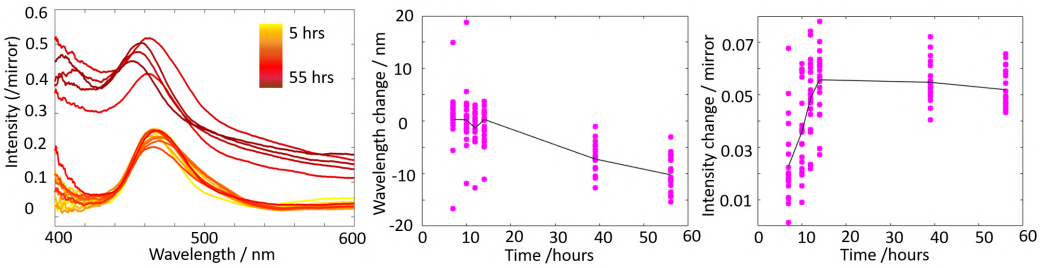

FIGURE 3.34: The left hand plot shows the transition over time of the spectra from one cell during the final transition. The middle and right-hand plots show the extracted peak wavelength and intensity respectively of all the cells measured over the final transition and the average values at each time, showing a clear decrease in peak wavelength, and increase in peak intensity.

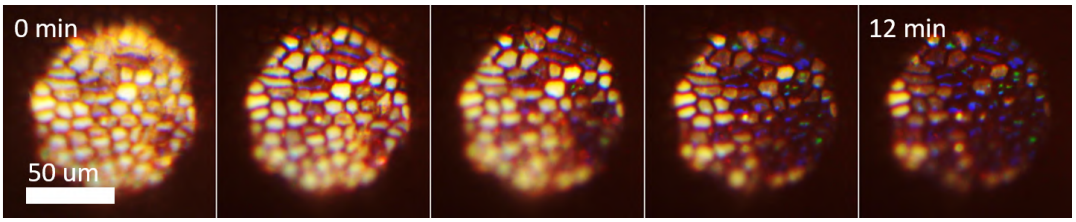

FIGURE 3.35: A series of microscope images taken at regular intervals over a period of 12 minutes while the cell area of a recently matured fruit is coated by a water droplet. The objective lens used was a water immersion lens. Over the period the cells rehydrate and their appearance returns to the 'brown stage' where a discrete spot of reflected light is visible in the centre of each cell.

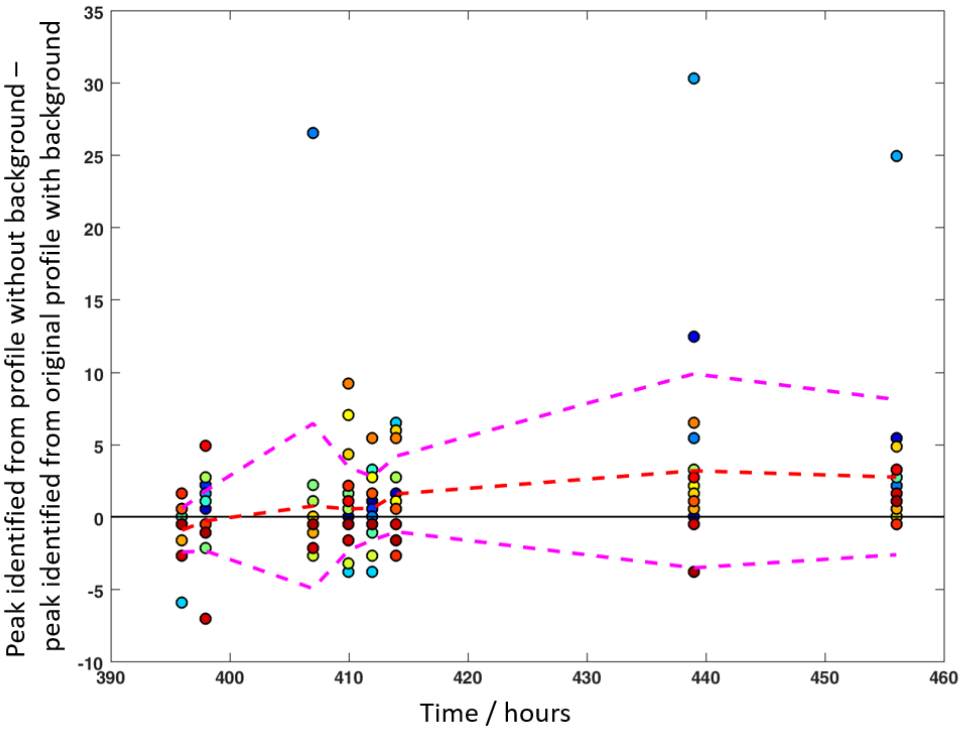

FIGURE 3.36: In order to understand the effect of the additional 'scattering background' in the blue stage, the peak data was de-trended, fitting an interpolated slope to the spectrum outside of the peak. This was then subtracted from the original spectrum and the peaks reidentified and peak wavelength identified. The difference between the 'detrended' data and the original data is shown here over the transition time, indicating that a small blueshift in the peak wavelength can be attributed to distortion by the underlying 'background' scattering spectrum.

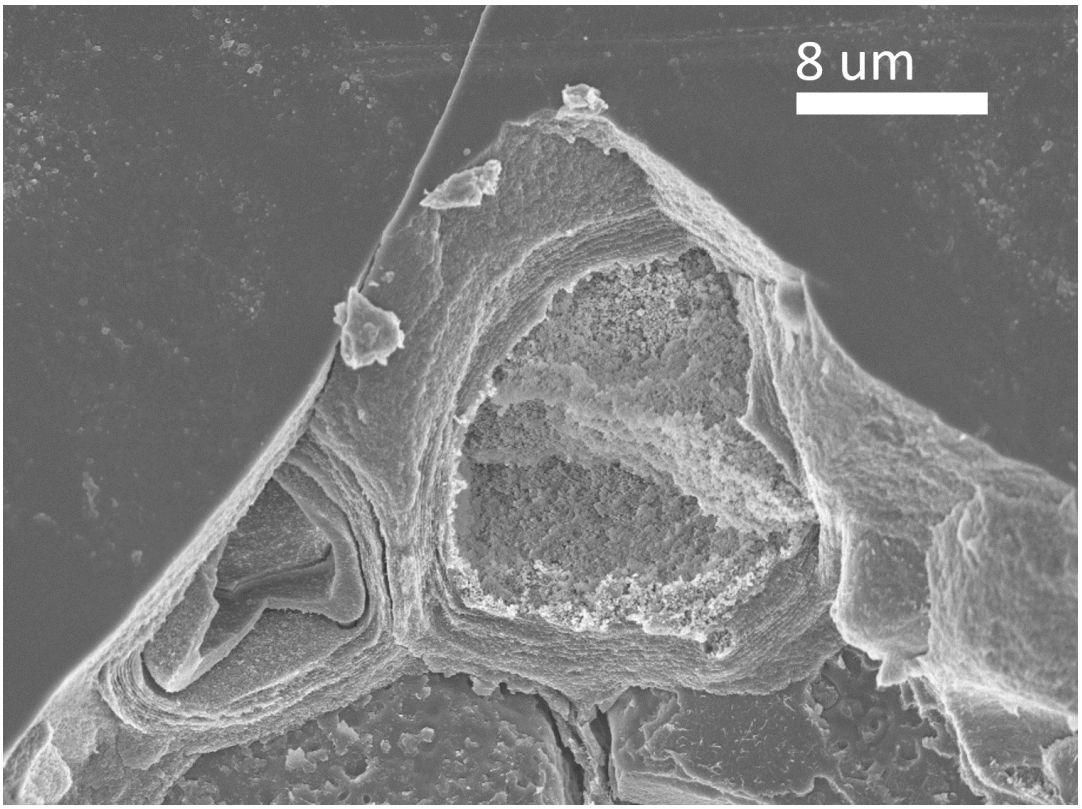

FIGURE 3.37: An SEM image showing two broken structurally coloured cells on the outer surface of the fruit epicarp, viewed from above. The right hand cell shows a number of pitches in the cell wall and a cell cavity full of a disordered scattering material. The left hand cell shows some material remaining in the cell dried to the cell edges and a cell cavity.

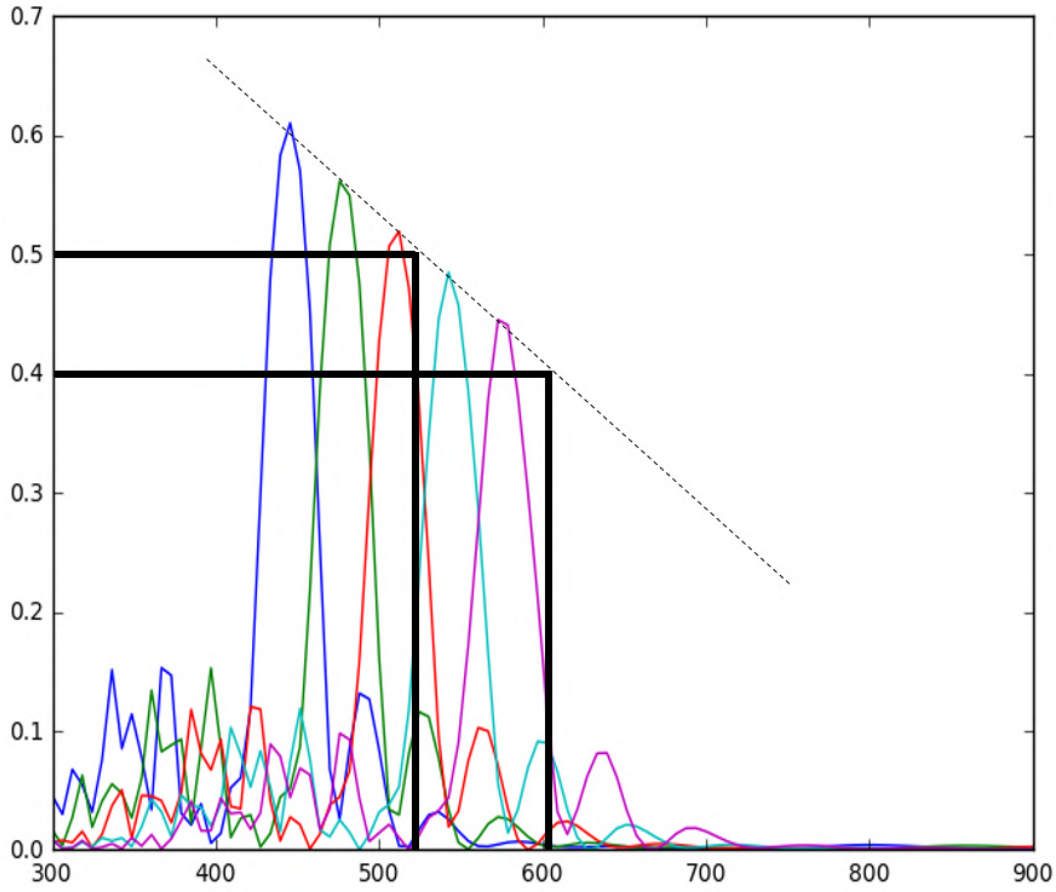

FIGURE 3.38: This shows a number of modelled peaks, as described in section 1.5.3, with a range of unrealistic average refractive indices, the difference between the ordinary and extraordinary axes in each plane remaining unchanged. The series shows a linear relationship between the refractive index and peak reflected wavelength according to the numerical model. A change in peak wavelength of 10 nm corresponds to a change in average refractive index of 0.013 $\pm$.001

Observation indicates that the transition may be the result of dehydration. Some instances of the cells undergoing the effect were triggered by the heat and light of the microscope, although in other cells it was spontaneous outside of microscope exposure and therefore confirmed not to be an artefact of observation. The fully mature fruits appear entirely dry, and retain their appearance after further drying. The cell transitions were temporarily halted when imaged in a water-immersion configuration. Furthermore, water immersion can be used to 'reverse' the process, producing the appearance of the earlier phase. The effect of re-wetting is visible in the frames in figure 3.35. The re-wetting process is much slower, taking several minutes whilst the drying transition occurs over fractions of a second.

In order to understand why physical drying causes the optical transition measured some alternative mechanisms are considered.

Unlike *P. condensata* and other species' cells, *P. japonica* cells have a large internal cavity at maturity, rather than being entirely constricted by the thickened cell walls. Some cells show apparent empty vacancies in the fully mature dry fruit, others have cavities filled with a porous disordered material which may be the dry remains of functional cell organelles, or a scattering-adapted material.

Spectral Change Analysis

Three candidates for the optical origin of the spectral changes are proposed:

- that the dehydration of the cell's internal cavity introduces an effective scattering body with a blue scattering profile, which biases the cell's multilayer-reflected spot to create a blue shift.
- that the dehydration occurs only in the cavity at the internal surface of the cell wall, creating an air gap which changes the refractive index contrast of the multilayer's lower surface and inducing a shift in the wavelength reflected.
- that the dehydration occurs at least partly in the cell wall, changing the average refractive index of the multilayer, and therefore the peak reflected wavelength.

The first hypothesis is examined by removing the background spectrum from the peak for each of the spectra during the transition, and re-identifying the peak wavelength. The difference between the peak wavelength for the peak identified with and without the background profile is shown in figure 3.36.

After the transition, the subtraction of the background from the peak profile induces a redshift in the peaks identified of around 5 nm, indicating that this difference can be attributed directly to a background trend which is reflected from the scattering internal contents of the cell.

The additional scattering background therefore appears to account at least partially for the blue-shift observed during the transition to the final mature stage. The origin of this scattering spectrum, which appears suddenly on dehydration, seems to be geometric optical scattering. The particles visible in the SEM images, as shown in figure 3.37 are several microns big, and therefore too large to contribute Rayleigh or Mie scattering.[178] However, further investigation of the nanostructure and material are needed to confirm this.

As demonstrated in figure 3.33 the most dramatic change in the cell appearance frequently occurs over a fraction of a second. This very sudden transition seems likely to be the effect of the entire internal cell membrane detaching and drying at once, rather than the necessarily much slower process of expulsion of individual water molecules from the cell wall. However, a change in the refractive index of the layer underneath the chiral multilayer results in a negligible change in the peak reflected, this result was not included in figure 1.13, because when both variations were plotted only one line was visible. This indicates that the change in peak wavelength does not result from the change in the lower boundary of the cell wall multilayer.

The last proposal, that the change in the peak wavelength is the result of a change in the refractive index of the multilayer could account partially for a slower blue-shift transition as water molecules diffuse from the helicoidal structure itself, increasing both the ordinary and extraordinary refractive indices equally. As shown in the numerical model in 3.38, an increase of the refractive index of around 0.013 ± 0.001 could account for the change in refractive index of 10 nm. A change in refractive index from dehydration could also affect the internal material of the outer cell walls if it is the result of a structural effect.

Conclusion

In conclusion, the final brown to blue transition is responsible for the very different appearance of *P. japonica* fruit with respect to the other species of *Pollia* presented in chapter 2. The difference is seen both macroscopically in the photos in figure 2.13 and the microscope images in 2.14. Prior to this transition, the microscopic appearance of the fruit much more closely resembles the other species.

The transition is caused by the introduction of a dehydrated interface at the internal edge of the mature, dehydrated cell wall. A strongly enhanced blue-biased scattering reflection profile is measured, in addition to the structurally coloured peak. This is the result of a scattering interaction with the material and cavity inside the cell.

The peak of the structural colour reflection is observed to blue-shift during this transition. This change is partly accounted for by the extra scattering profile, although

may be partially attributable to a change in average refractive index from dehydration.

In order to better understand the transition, the scattering material in the outer cells should be identified and characterised in terms of its optical reflection profile. This would permit the analysis of the interaction between the two effects, and therefore also clarify whether dehydration of the cell wall is also implicated in the transition.

3.6 SEM and Cross-sectioning

The subject of this chapter has been the development of the optical response of *P. japonica* cells during maturation, and the use of the multilayer model to understand the changes in the internal structure occurring during growth. This technique permits investigation without affecting the growth by cutting or killing the tissue which allows for a longitudinal study on individual cells.

A more traditional approach to understanding cell growth is employed here to complement the optical technique. Fruits were picked at different stages of growth and infiltrated with fixative TEM resin by Dr Edwige Moyroud. TEM images were taken of microtomed slices from the face of the fixed block by Dr Paula Rudall and are shown in figure 3.43. This was done in order to provide additional insight and a comparative technique to the novel optical characterisation demonstrated so far.

3.6.1 Technique

Sample Preparation

For the *P. japonica*, two approaches to scanning electron microscopy were used, in addition to TEM scans produced by a collaborator Dr Paula Rudall. The two techniques are compared in figure 3.40. The first technique simply used broken edge of fruit epicarp tissue, mounted at an oblique angle to the electron beam, giving a view of the broken cell cross-sections. As shown in the top images of the figure, this technique has the benefit of minimal preparation, and alteration of the fruit tissue, allowing close detail to be distinguished, and giving a good qualitative indication of the architecture of the cell wall and contents.

The second method involves the infiltration of the fruit tissue with fixative resin. This was done by Dr Edwige Moyroud. The sample was then microtomed to produce a uniform cross-section through the cell wall and contents. This was done primarily to prepare the samples for TEM, and was carried out by Dr Paula Rudall. This

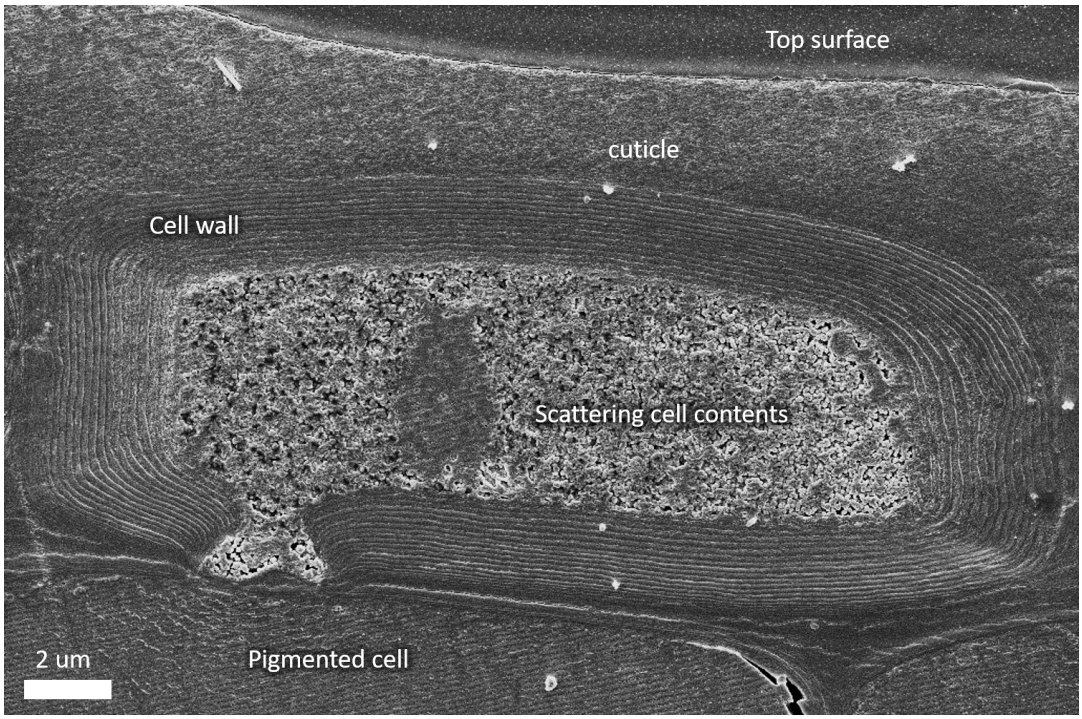

FIGURE 3.39: A labelled cross-section of a structurally coloured outer cell embedded in resin. The parallel lines visible in the patch in the middle of the scattering cell contents, and in the lower pigmented cell are an artefact of the sample embedding and cutting. The lines are perpendicular to the direction of cut by the microtome section and unrelated to the sample itself

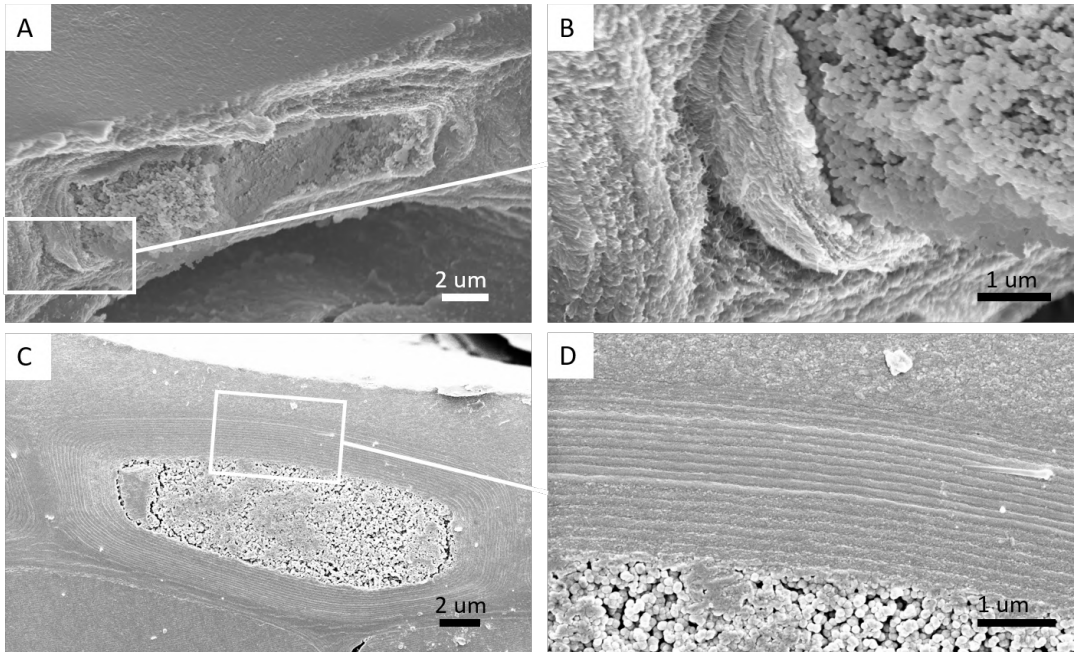

FIGURE 3.40: SEM images: A. Full cell cross-section B. Cell wall. Both imaged obliquely from a fractured unembedded sample. C. Full cell cross-section D. Cell wall. Both for a normal angle cross-section of the cell embedded in resin.

method has the benefit of producing clear uniform samples which can be measured to provide quantitative analysis of the material architecture, such as pitch which is subject to foreshortening in profiles not imaged orthogonal to the surface, and is therefore not possible to measure.

The embedded SEM technique is however very labour intensive, and difficult to create the larger and more varied samples which are easily accessible using uninfiltrated tissue. Therefore, the number of cells which can be inspected in this way are limited. The embedding resin and microtome blade also introduce a flattening artefact which makes the smallest fibrillar structures and textures of the cell impossible to measure. Furthermore, the embedding resin introduces a variability into the sample preparation procedure as different materials take up the material differently. In the embedded cell imaged below, it appears that the central cavity and its contents remain resin-free, indicating that the resin has not infiltrated all the way through the cell wall.

Development Study in SEM

3.6.2 Results

The SEM cross-section in figure 3.39 shows the labelled cell of a mature blue-stage *P. japonica*. The cell shares the thickened cell wall of the *P. condensata* but retains an

internal cavity, generally filled with what appears to be scattering material. This scattering material can also be seen in a non-embedded SEM imaged from a dry, broken fruit in figure 3.40 B, indicating that it is not an artefact of the treatment for resin embedding. The material inside the cell body was discussed in section 3.5.

In order to obtain quantitative measurements of the multilayer pitch at the different stages of the cell maturation, the resin-infiltrated cross-sections of all the cells visible in the prepared sample were measured using image analysis software (ImageJ) to extract their profile statistics.

The samples in the white and brown stages were not clear enough to extract profile measurements from the SEM images, but data from cells in the green (9 individual cells) and blue (13 individual cells) stage tissue samples were measured. A comparison of green and blue cell tissue is shown in figure 3.41. The profiles were used to model spectral responses, as shown in figure 3.42. The destructive technique means that the same cell could not be measured twice during development, and that therefore later-stage and earlier-stage cells are not directly related to each other. Averages were made of the modelled spectra and are presented in figure 3.42.

3.6.3 Analysis

Figure 3.41 shows SEM scans taken from the block face of microtomed resin-embedded fruit tissues prepared for TEM for green and blue stages of the fruit. Comparing the two cross-sections it is clear that they are very similar to one another. By eye the cell walls and cell contents appear comparable. The cell wall appears perhaps slightly thicker in the blue stage, and its boundary with the slightly thinner cuticle layer seems better defined. A comparison of all the cells visible in the two sample cross-sections confirm that the enhanced definition on the cuticle-wall boundary between the green and blue stages appears to be true generally for the two tissues.

Some important observations on the cross-section pitches are that there is no evidence of a systematically varying pitch width, such as the progressively lengthening or 'chirping' seen in some beetle species. [179] The layer pitches appear uniform all the way around the cell, although they clearly have a natural slight variation along each pitch.

TEM Images

Figure 3.43 shows thin TEM sections from the earliest, white, stage of development (A), the mid-stage green phase (B) and mature blue stage (C) in microtomed sections from the resin-embedded fruit tissue. A shows a cell wall with five distinct pitches

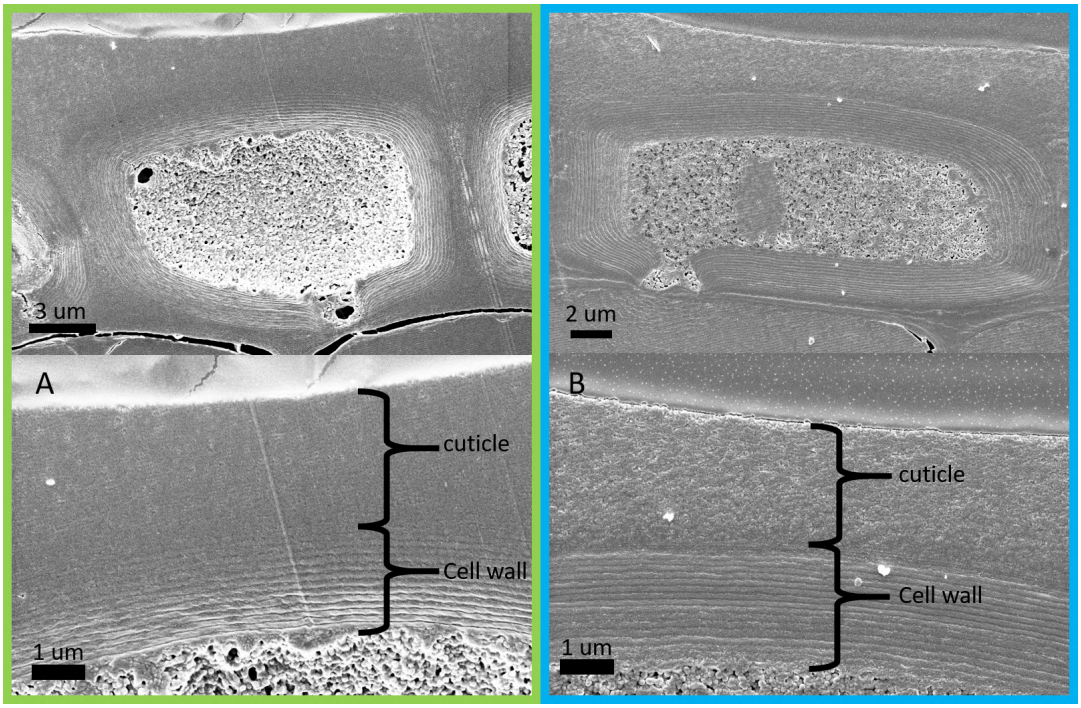

FIGURE 3.41: Cross-sections of the resin-embedded cell. A. green and B. blue fruits. The upper images show the entire cell, and the lower image just the outer cell wall and cuticle as indicated.

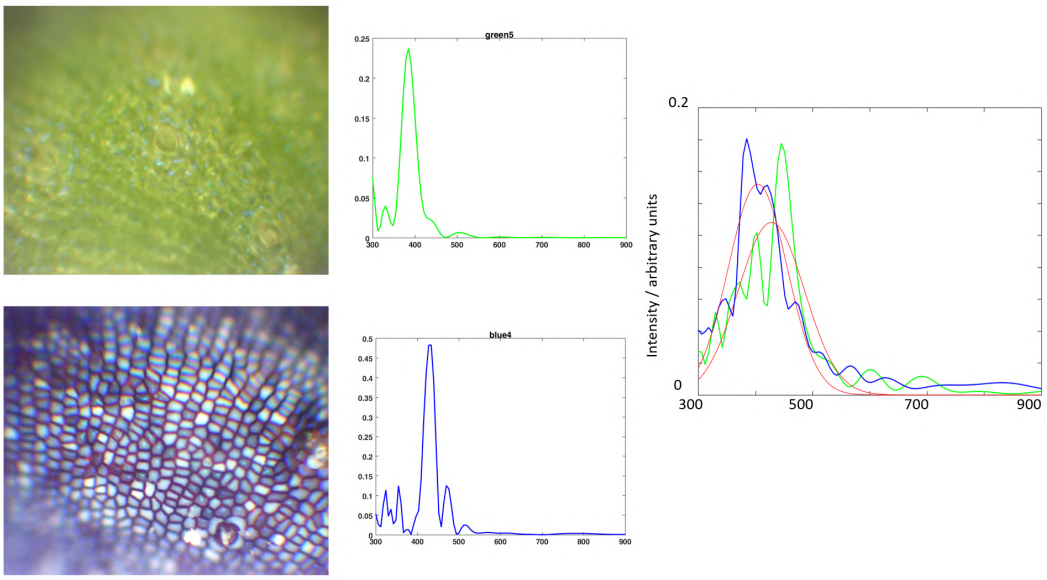

FIGURE 3.42: SEM images of resin-embedded cells like those in figure 3.41 were analysed to extract pitch profiles as described in section 1.5 for cells from the green and blue phases. The individual plots are of single constituent optical responses from modelling a single measured profile from each group. The combined plot shows the average profile over all of the SEMs measured in the blue and green sets, and a Gaussian fit for each shown in red.

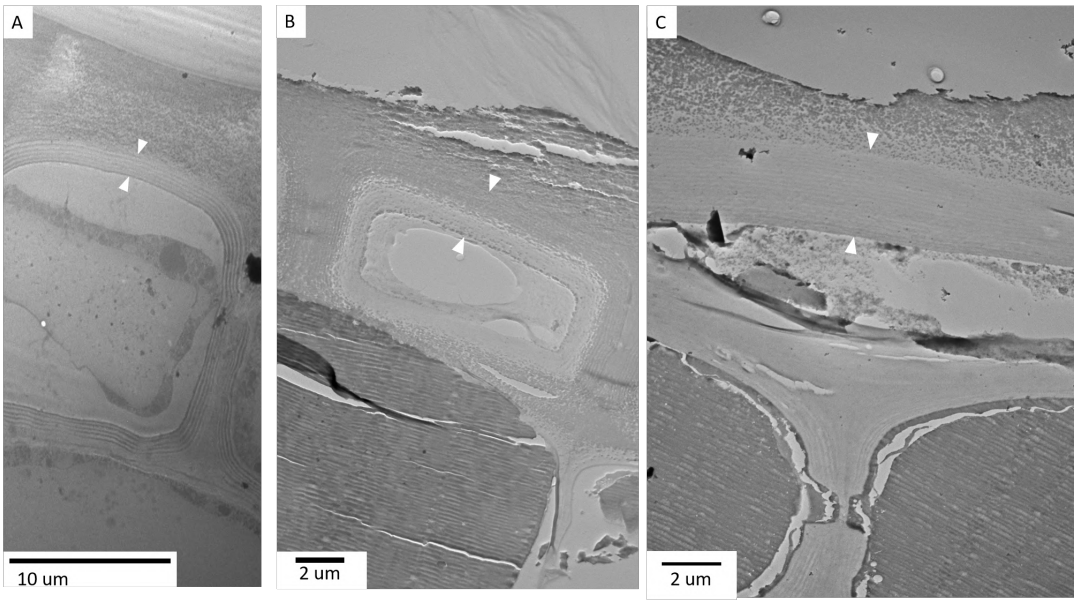

FIGURE 3.43: TEM images of the A. white stage B. green stage and C. blue stage of the fruit taken from microtomed sections of the fruit embedded in resin. The sample was prepared by Dr Edwige Moyroud and imaged by Dr Paula Rudall. White arrows indicate the external and internal edge of the upper cell wall in a surface-layer cell.

and a thickness of 1.2 ± 0.3 um, indicated by white arrows on the image. Also visible is evidence of the cytoplasmic material inside the cell. The pitch width is clearly visible. The blue and green stage section show a thicker cell wall of approximately 2.1 and 2.8 um respectively. The pitch profiles are not individually identifiable in the green stage TEM.

A significant limitation in using the TEM sections as evidence is the very few good quality scans that were obtained, making characterisation of variation between cells difficult.

Profiles from the TEM images in figure 3.43 were identified and used to numerically model optical responses which are shown in figure 3.44.

Analysis of SEM and TEM Profiles

SEM Figure 3.42 shows the collection of all cell profiles available from SEMs on the resin-embedded tissues, and the numerical model produced by taking the profile from each of the individual cells for both the blue and green fruits. An average of the spectral profiles is then taken and the two sets compared using a Gaussian fit.

As plotted on figure 3.45 measurements on the two sets of image profiles show a negligible difference in average pitch length between green and blue stages. Standard deviation of the pitch in one profile is $\pm$ 30 nm. The lack of difference between

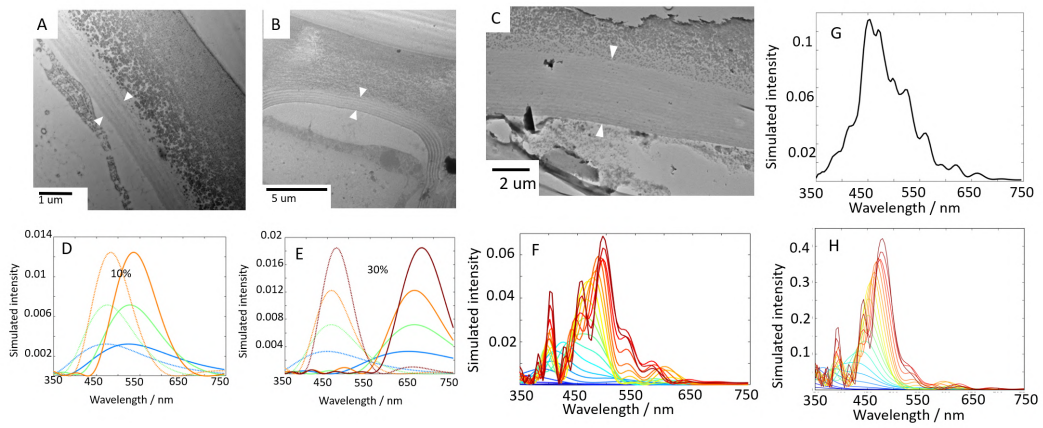

FIGURE 3.44: A, B, C. TEM by Dr Paula Rudall of fixed sections through white (A and B) and blue *P. japonica* cell wall. D, E, F. modelled responses from the profiles extracted from the cell wall cross-sections in A,B,C according to the technique in section 1.5. D and E show the modelled responses using the measured profiles with unbroken lines, and with dotted lines a model of the profile contracted by 10 or 30 % as labelled. G shows an average over 5 profiles within a standard variation of 15nm of the original profile. H shows a plot of the measured profile with 70% variation. For plots where multiple profiles are shown, each line represents the addition of another single pitch in the material profile, with the darkest blue line representing one pitch, through to the maximum width of material in red.

green and blue stages is consistent with the observations previously described in this chapter.

One result of the image analysis of the SEM profiles is shown on the right hand plot in figure 3.45. An increase in the number of pitch repeats in the cell wall was observed between the green and the blue stage. This implies that there is still some growth ongoing in the cell wall after the green stage.

This agrees with the model that a large proportion of the growth occurs in the early stages, although later stages provide some extra cell wall growth.

Numerical models of the blue and green cell wall profiles do not show an increase in the simulated intensity for the thicker cell wall profiles, as shown in figure 3.45. This is because of the configuration of the varying pitches within each multilayer, which is responsible for the intensity of the primary peaks. Because the cells imaged in the blue and green stages are different, a thicker cell wall in this particular group does not imply a more intense reflection. This shows the value of continuous monitoring of cells on an individual basis, and observation of the entire cell reflection profile.

TEM The optical responses modelled in figure 3.44 are significantly different to those taken generated from the SEM profiles in figure 3.42.

The pitches identified in the white stage images A and B generate peak wavelengths significantly longer than those observed in either mature fruits in chapter 2 or in the immature cells observed in this chapter. This inconsistency might be explained by swelling and distortion implicated in the resin-fixing, microtoming and imaging process. A piece of evidence in favour of this hypothesis is the strong variation between the two white profiles measured. A decrease of 10% and 30% respectively of the pitches measured is shown to generate peaks of a similar wavelength to that observed optically. 10 to 30% fall within a generally tolerated length variance in TEM image analysis, [40] so this seems a likely explanation.

The pitch profile measured from image C in figure 3.44 corresponds to the plot in image F. The peak wavelength reflected in this case is a realistic one, being within the range of mature cell peak reflections. However the cell shape is at odds with the simple, narrow and single peaks identified in optical measurement and in the SEM-profile-derived models shown previously. Plot G shows an average of the profile over a standard deviation of 10 nm, commensurate with variation measured over one cell's profile. The peak is seen to be much wider than those observed in *P. japonica* cells.

One possible interpretation is that, if this numerical model is accurate, it may be that the measurement and peak extraction of the structurally coloured peak from the *P. japonica* fruit is insufficiently sensitive to measure the secondary peaks, which are perhaps absorbed, or overlap with pigmented fluctuations in the background spectrum. The whole peak which is apparently identified, is therefore in fact only the peak reflected above a threshold background intensity. This is a possible explanation.

Another possibility is that distortion in the TEM images introduces an additional variation in the pitch profiles, which is an artefact of imaging rather than a feature of the fruit tissue. The microtome sections in these images are extremely thin and feature many artefacts such as folding, tearing and compression from the microtome blade action. This possibility is used to suggest an alternative analysis of the profile identified in figure 3.44 plot H. Here the profile's variation from the mean is reduced by 30% from the observed value of around 30 nm. This profile is a much more familiar with respect to the characteristic peaks measured optically.

Another factor that impacts our ability to extract meaningful measurements of the pitch variation from the TEM image is that the image has a pixel dimension across the multilayer direction of 15 nm. The line width over which the profile is averaged is much larger than this, reducing the limit somewhat, however it is important to observe that the image itself is not accurate within this limit. As presented in the introduction to the model, a change of just 3 nm in the input pitch of a uniform multilayer is responsible for a change of 10 nm in the peak wavelength. Moreover, the pitch variation, which as described here, is very important to the profile shape. The

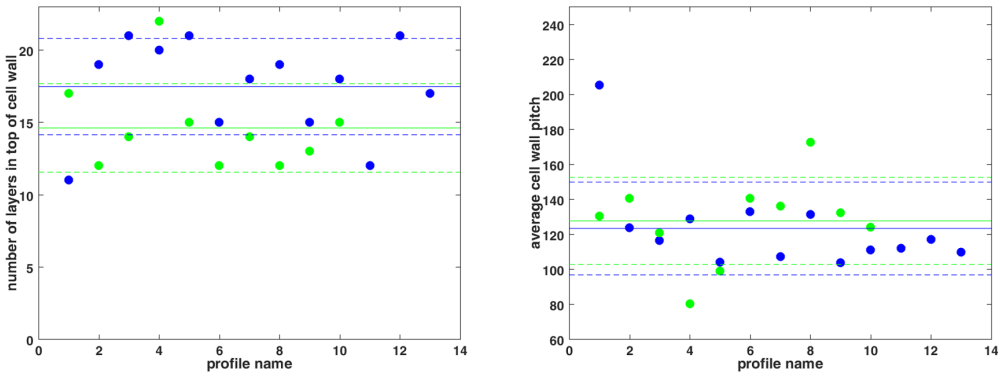

FIGURE 3.45: Profiles measured from the electron microscope images showed these distributions. The blue profiles had a higher average number of pitch repeats in the cell wall by an average of three pitches, or 17%. Due to the distributions of the pitches in the profiles however, this did not increase the intensity of the modelled peaks, as seen in the figure 3.42.

70% variation used in plot H, gives a relative secondary peak intensity and distribution much closer to characteristic experimental profiles than the variation measured from the electron microscopy images. This reduction in variation corresponds to a change in 10 nm in the standard deviation, less than the resolution of the TEM image.

This second explanation, that the TEM imaging process introduces an additional variation which is not present in the fruit is preferred because the imaging and peak extraction process is held to be accurate. Furthermore, the observation of the blue peak reflected from the nearly mature cells in the brown stage, when background pigments remove the need to further process the data, do not reveal cell profiles with more complicated spectra. Modelling in relation to the optical measurements actually observed is further discussed in section 3.7.3.

Limitations of Electron Microscopy

A number of limitations are present in the method for extracting and modelling the profile. The imaging of the embedded tissues presents some potential problems, the cut may not, despite best efforts, be exactly orthogonal to the surface, introducing a systematic elongation of the pitch estimation in the affected sample. The cut also causes some clear damage to the cross-section, blurring the boundaries of each individual pitch.

The most likely two candidates for introduction of error into the attempt to characterise the fruit tissue profile are the low number of samples given the biological variation expected, and the use of an embedding matrix in sample preparation.

The biological variation within the tissue means that for only 10 or 13 scans, the numbers used in the two tissues here, the average spectrum is likely to be unable to represent a larger number of cells. This makes it difficult to compare two sets of cells. The optical method gets around this problem by measuring the same cell over an extended period, ensuring that it is reasonable to compare the spectra.

The use of resin for embedding samples for electron microscopy and microtoming is widely recognised to introduce a significant expansion or shrinkage in a given biological tissue. Studies into the shrinkage and expansion errors induced by preparation for electron microscopy show a huge range caused by a combination of multiple factors. [40] The process of processing for TEM involves fixation, dehydration and embedding, each of which has been demonstrated to have a different effect depending on the tissue. Different scale distortion has been seen again in critical point- and freeze- drying. The scale of these artefacts were measured to exhibit a full range of the various processes from a 73% shrinkage to 61% expansion. There was also variation associated with different dimensions in cells. The majority of the reports [180] on biological tissues are on mammalian cells rather than plant cells. The latter, due to their rigid cell wall, should be expected to have a significantly reduced distortion effect. Plant cells included in the review however showed 30% shrinkage due to osmosis.

A further barrier to applying results found in previous studies on the effects of sample preparation to our case is that studies have generally been limited to a multicellular tissue scale. In understanding the changes in cellulose cell walls, only part of the cell is relevant. The ability to understand true distortion at smaller scales has been limited by microscopy techniques. For structures smaller than the resolution of optical microscopes, only comparative length distortion between different sample preparation methods can be measured.

Even assuming that cell wall material is significantly less subject by expansion and shrinkage than cell volumes, the degree of volume change seen in cells implies that cell walls are likely to be affected. A change in cell volume of 30% is likely to cause a substantial impaction or distension.

In addition, the distortion introduced to microtomed sections both parallel and perpendicular to the direction of cut have been shown to be up to 17% in resin-embedded mammalian tissues. [181]

The difference in the bonding, hydration or materials of *P. japonica* tissue between the green and blue stage might be expected to introduce a different shrinkage or expansion in the two different tissues that therefore could obscure a real change. However, given no contradiction in the optical and electron microscopy evidence that the pitch remains unchanged during maturation, it should be assumed that the specimen preparation does not introduce a different expansion or contraction of the tissues. In order to verify this, fruits picked at the same stages of growth should be

imaged and compared after preparation both with and without resin-embedding. Our ability to do this is limited by access to fresh fruits at different growth stages, and the difficulties in imaging fresh wet tissues in SEM without inducing further damage.

3.7 Conclusions

3.7.1 Reflected Intensity & Cell Wall Thickness

The optical measurements indicated that a large part of the growth occurred in the earliest stage during the white - green transition, average intensity grew by 1.4±0.5% of total illumination to an average 2.7% (see figure 3.18).

The intensity changes in the second part of the observation were difficult to analyse due to significant changes in the chlorophyll spectrum and limitations in the experiment. For this reason an estimate of the peak intensity change over this period is not attempted. However, the final intensity of the purely structural coloured peak after 400 hours, (before the addition of the scattering profile in the blue stage), was on average 4±2% of total illumination.

This puts the structurally coloured intensity of the cells at the end of the brown stage at a very similar intensity reflection as the cells at the beginning of the green stage. Caution should be exercised in comparing the intensity in the two studies, because they were measured from different sets of cells. However, the appearance of the structurally coloured reflection spot does not appear to change much through the green and brown stages, supporting the idea that the most significant period of cell wall thickening is during the earliest part of the green stage.

The electron microscope images of cell profiles confirmed that a significant proportion of the cell wall is indeed laid down in the earliest part of the white-green stage, although additional layers appear to be developed in later stages. A low number of pitches were shown in a scan of the white earliest stage by Dr Paula Rudall, figure 3.43.

3.7.2 Reflected Wavelength & Cell Wall Morphology

The optical measurements of the cells over maturation showed some variation in cell spectra over time, but no systematic peak wavelength shift between the earlier and later stages. The change in the peak wavelength is proposed to result from cumulative additional cell wall pitches within a consistent distribution.

The measurement of the SEM profiles from the electron microscope images was consistent with the analysis of the optical data. There is no systematic change in

the width of the pitches within the profile and the blue and green profile averages showed a negligible difference.

The cell reflection peaks were numerically modelled and it was shown that the change in wavelength and intensity could be described using a model of the cell wall as a helicoidal cellulose material with a gradually increasing number of pitches and pitch differences falling within a realistic normal distribution.

3.7.3 Interpretation

It is proposed that instead of a role for a reorienting self-assembly mechanism, the cell wall is laid down in place.

This is consistent with the rosette- model of cell wall fibrillar deposition as described in the first chapter. The theory that the cell wall is built up layer by layer, rather than assembling from a prior volume of existing cell wall material looks much more supported by this evidence.

The second stage of data, when considered in conjunction with the first, indicates that after initially being laid down in place, there is little further change in the cell walls of *P. japonica* even over a long maturation period of 17 days. The wavelength of the structurally coloured material is extremely consistent. The intensity of the light reflected may grow partially, but it does not change dramatically.

This study therefore suggests that the important temporal period for cellular growth in this species is the white-green first stage. The second stage data also supports the claim made after the first stage analysis that the cell wall is not formed from a change in a bulk material but rather, once created, the cell wall has a fixed architecture.

Numerical Model

Figure 3.46 shows a model of the growth in the well-characterised cell above, created according to the method described in section 1.5.3 by identifying a characteristic standard deviation and mean and producing a number of artificial profiles which may then be matched to the optical target. The model plots a new model response for each additional pitch added to the pitch profile, simulating cell wall development through increasing layers from the inside of the cell.

A numerical model in plot B is matched to the experimental observation of a single cell series shown in plot A of the same figure. The use of random profile generation and matching to the target response is not meant to indicate that this process reproduces the profile in the original cell which is responsible for the optical signature. This is clearly impossibly unlikely given the reliance of the optical profile on each of the randomly distributed pitches within the material. The model is used instead to

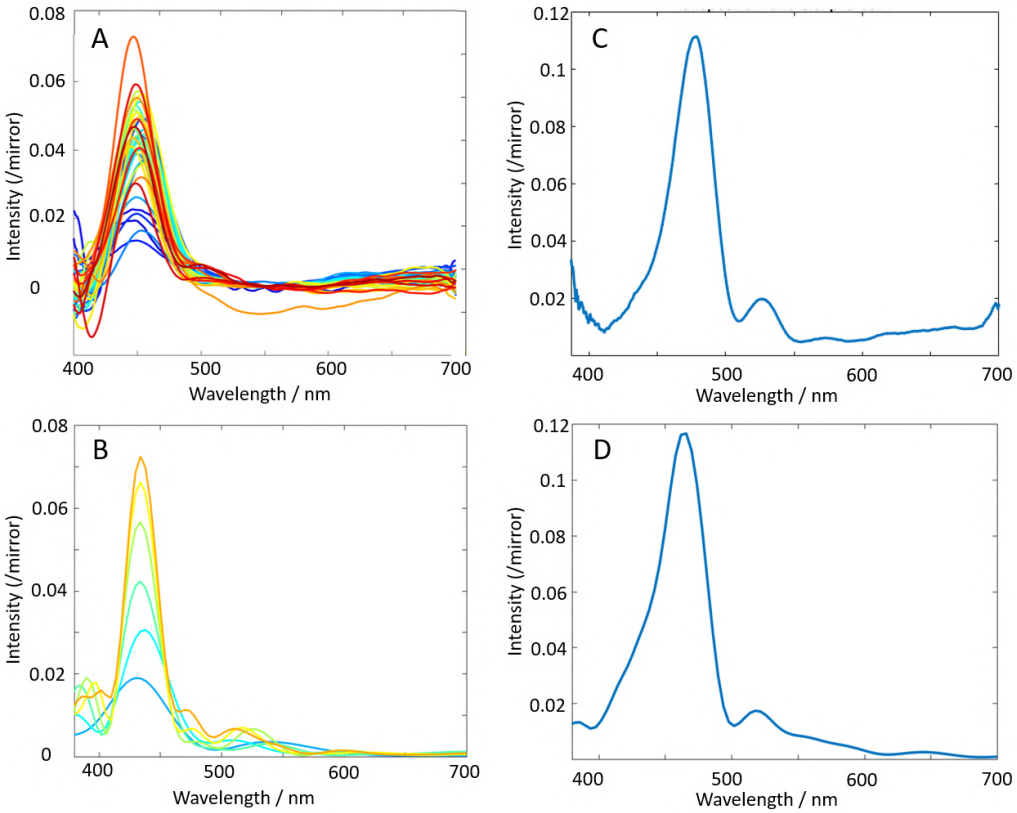

FIGURE 3.46: A. Development series measured from one cell of *P. japonica* over the first observation period, i.e. 6 days. The scans are plotted after chlorophyll signal subtraction. The earliest scan is plotted in blue. B. The model demonstrates increasing intensity with increasing numbers of pitch repeats. Each consecutive line represents the addition of two more pitches to the profile. The model uses averages over 5 profiles with a standard deviation of 10 nm. C. Experimental profile of the scattering-free final spectrum for one cell in the brown stage, immediately prior to transition to the final blue stage from the second observation series. D. A model of a similar peak averaged on five profiles with a standard deviation of 20 nm.

illustrate the theoretical principles which have been invoked to explain the observed development. That is the increase in reflected intensity at constant wavelength by an increase in the number of cell wall pitch repeats. The successful correspondence of realistic parameters for the numerical model with experimental data is taken as a positive evidence that the theory is consistent with the model of the cell wall as a multilayer.

Plot C in the same figure shows the 'full maturity' profile measured from a cell at a late point of the brown stage just before the final sudden change to blue fully mature appearance. The spectrum is therefore straightforwardly measured without further processing. It is taken to be a true spectral profile from the mature cell multilayer without additional scattering effects. The intensity of the profile measured is only slightly greater than that measured at the end of the growth profile recorded in the first observation series, as represented in plot A. Spectra in A and C are from different cells, and therefore do not represent the direct continuation of the development process in one single cell. However, the growth profile that is concluded from observation of the two series is that the majority of the growth occurs in the green stage and that the intensity of the structural colour peak after growth in the green stage should correspond to the final structural colour intensity, as observed here in this comparison.

The plot in D of figure 3.46 is another model generated via the use of random pitch variation profiles, this time with 20 pitches and averaged over a set of similar profiles with a standard deviation of 15nm.

Making the further assumption that the numerical model is accurate for the cell wall, the conclusion for the cell wall growth rate in the initial growth period early in the white-green phase is that the cell wall in this case increases by 12 pitches in 114 hours, a rate of approximately 2.5 pitches or 0.4 um thickness / day. The growth rate after this early stage is predicted to be strongly reduced, but is not estimated here.

Numerical model limitations are discussed in section 1.5 and this result is taken to be an estimate.

3.7.4 Conclusions on *P. japonica*

Pollia japonica's appearance is due to structural colour in a single outer cell layer in which a thickened cell wall acts as a multilayer reflector for visible light. The fruit transitions through four rough stages during growth, changing from a whitish to bright green, to a brown and finally a mature pale blue. The cells reflect a bright blue spot from the cell centre which grows more intense during the white-green stage and then remains fairly unchanged throughout the green-brown transition which occurs due to pigments beneath the structurally coloured cell wall. The final transition

occurs through dehydration of the structurally coloured cells which contain a light scattering material. This changes the reflection of the outer cell from a discrete bright narrow band spot to a scattered reflection from the whole cell.

The growth of the cell wall happens by a gradual process of building up the pitches which are laid down in their permanent configuration.

The study was intended to understand how the cell wall growth occurs in *P. japonica*, and whether during the development of its very thick cell walls, there was a change in pitch. The results show conclusively that there no change in pitch occurs during the growth of the cell wall, or during the maturation of the fruit after that. The optical analysis confirms that development of the pitch profile is gradual and permanent. This conclusion is made for periodic pitch in the cell wall, rather than for the much narrower microfibrillar cellulose layers which build up to produce them. The conclusion is extended to the cellulose layers on the basis that the periodicity of this material does not imply discrete and alternating materials as in isotropic multilayers, but is formed from a continuous helicoidal pattern.

3.7.5 Assessment of the Optical Technique

The optical technique employed, along with the model of the cell wall as a cellulosic multilayer worked very well to identify the structural colour peak and its characteristics to a good level of accuracy. The method of repeated optical measurement is laborious as it requires regular and frequent measurements during maturation. This could be improved by additional automation, for example automatic spectral measurements after initialisation.

The optical measurements compare favourably with a destructive electron microscopy technique in which fruits are picked at different stages, sectioned and imaged using scanning electron microscopy. The optical technique provides considerable insight that is not possible with the electron microscopy technique due to its ability to track one particular tissue. However, the use of electron microscopy provides direct confirmation of the conclusions drawn from the optical analysis technique, without which the findings would be less confidently established.

3.7.6 Experimental Limitations

Structural Colour Peak Isolation

The limitations in this experiment are largely around isolation of the structural coloured peak from the other scattered light in the system. In the first observation series, crossed polariser measurement was used and a control cell measured to subtract an approximation of the background reflection. This choice was necessitated

by the very low intensity of the structural colour target signal itself relative to the bright reflection profile from the cuticle surface.

The second set of observations is limited by the lack of a chlorophyll control profile. A good sense of the peak intensity is gained by the measurement of peak prominence, but a non-structural colour control profile would enhance the accuracy of this intensity measurement. A control profile would only be possible up to the brown stage as there is no non-structurally coloured area in the blue stage.

Experimental Challenges

Further limitations are caused by the difficulty in reproducing the same measurement of each cell on each observation. Due to a slight off-centring of the fibre collection location, the cell position was sometimes slightly off-centred in order to capture the spectrum of the cell. This was checked both by the visible location of the cell in the microscope image, but also by the peak appearance in the spectrometer. The cells show a good reproducibility of location both between different cells and between different observations but they are not perfect. Where observations resulted from a cell misalignment evident in the recorded image, they were not included in the data set but due to the difficulty in distinguishing the cell features especially in the early stages, this may not have always been possible.

This error was minimised by the use of many measurements over the observation period, allowing an error tolerance to nevertheless show an overall trend for each cell. In fact inspecting the recorded images, there is a very strong consistency in the placement of the cell reflection spots, and for this reason the overall trend is taken to be a good measure of the cells' true reflection intensity. An additional challenge is represented by the different angular orientation of the cell at different measurements, although the exact reproduction of the original orientation was attempted every time.

A further limitation is the sensitivity of the plant to light. The use of very frequent measurement contributed to the early cell death by overexposure to intense light that ended the first set of observations. This introduces the problem of comparison between the first and second series of observations which are on unrelated cells. The plant's health must also be considered during the observation period and it was therefore moved to be exposed to natural light between measurements which were carried out in a windowless optics lab.

Measurement

Finally, the size of the fibre with respect to the size of the cells and cell features introduces another limitation. The cell reflection spots were in general smaller than the

size of the collection spot in at least one dimension. This means that the size of the cell reflection also plays a role in the intensity level recorded. The cell reflections are generally also irregularly shaped and have diffuse and intense parts. The shape of the reflection is due to the geometrical shape of the cell wall. The problem of measuring a true intensity from an individual cell which gives insight into the widths of the cell wall pitches is a fundamental problem in the case of a growing cellular system.

Growth of cells during the observation period reorients and exposes differing areas of the cell wall multilayer, changing the area of the reflection spot. In order to overcome this limitation, a higher magnification objective lens should be used to ensure that the fibre collection zone is small relative to the reflection spot. This poses problems in itself as it limits the intensity of the light available for collection further, and makes it much more difficult to measure multiple cells by making movement between cells less simply navigated. It is also likely that the effect cannot be totally eliminated due to the narrow and irregular shape of many of the reflection spots. An attempt could also be made to assess the area of the collection spot that contained the reflecting material, however this poses yet more problems in assessing this quantity.

3.7.7 Outlook

The measurements on the growth of the *P. japonica* have indicated an unexpectedly early growth period, and demonstrated that there is no significant change in the wavelength during cell wall growth. There was no general trend in the cell peak spectra although there was some indication that some of the cells undergo a small variation in the peak wavelength during growth, and this was explained as resulting from the cell wall layer pitch variation. The observation of the intensity of the multilayer reflection presented a number of challenges, and was not properly characterised during the second part of the observation which covered the later stages.

Future work implementing an enhanced control and precision in following the cell spectra could give a much better measurement of the cell wall growth during every stage. There are clear experimental parameters which could be improved to significantly enhance the accuracy of the measurement. This improved precision would enable the identification of the growth rate beyond a linear trend. The value in this would be to demonstrate the limits of the technique, and gain an understanding of variable growth rates.

As discussed in section 3.5, an improved understanding of the mature cells' spectral profile could be achieved by an analysis of the composition and structure of the

scattering cell contents. Understanding and modelling the interaction of extraneous scattered light with the multilayer would be informative. This would provide a useful outlook on understanding the characterisation of other multilayer materials. Currently the exploitation of artificial structural colour for pigmentation is limited by an understanding of how to control the directionality of structurally coloured micro-components, and understanding and taking inspiration from this natural system could indicate a productive blueprint for alternative pigments.

This study has demonstrated clear analysis of cell development from an optical / materials science perspective. Demonstration that results obtained on this species can be transferred to non-structurally coloured cell wall growth requires further comparison of the material and biological characteristics of both systems.

A biological approach could also be applied to understanding the cell wall growth, and to complement the current study, by using growth rate inhibitors, microtubule poisons and different environmental conditions. As discussed at the beginning of this chapter, these traditional biological methods have been applied to the study of *Arabidopsis*, and might be extended to *P. japonica*.

Chapter 4

Development in *P. condensata*

The previous chapter investigated the development of optical response in the maturing cell walls of *P. japonica* using a cellulose optical multilayer as a model. This maturation study demonstrated that the cell wall material's growth could be observed via the interaction of light with the material structure.

The cell wall in *P. japonica* is considerably thickened with respect to standard cell walls. However, thick cell walls are not unknown in common plants, for example the outer epidermal cells of *Arabidopsis* seedlings, which have thicker walls than others in the same plant and are around 1 micron thick,[182] - a roughly comparable thickness to the 2 um cell walls in *P. japonica* (see figure 3.39).

As discussed in chapter 2, *P. condensata* displays significant dissimilarities to the cells in *P. japonica*. These are in the form of the visual appearance of the fruit, both macroscopically and in microscopy, the numbers of cells, the cell shape, the range of spectral peaks and therefore structural dimensions, the cell wall thickness, lack of a cell cavity and the handedness of the cellulose helicoids.

These characteristics differentiate *P. condensata* from *P. japonica* with which it shares a common mechanism for visible light reflection, and also from other plant cells. The extension of the development study to investigate *P. condensata* is intended to understand whether the extra differences observed in the fruit follow the same developmental behaviour as *p. japonica*. The observation of an alternative pattern during growth where the cell wall cavity is nearly eliminated, and the cell wall material has a unique chirality, would indicate the point of differentiation in these characteristics. Otherwise, a similar or identical growth pattern would indicate that the spatial development of the cell walls remains the same for these characteristics and explanation of their unusual morphology should be developed in accordance with that observation.

A similar experiment to that reported in the previous chapter was devised in order to perform this investigation. Observation of a large number of cells' growth during a maturation period was carried out in order to understand the growth and similarities between the two species.

4.1 Methodology and Experimental Design

The plant was grown in a centrally heated office at 23°C on a north-facing window sill. Several plants grew successfully from a single shoot and stolon system. Figure 4.1 shows an early image of the young shoot (A) and a later image of multiple mature plants (B) connected by stolons. Each plant produced flowers, shown in 4.1 C and then fruits, flowering and fruiting on every plant, even when very small and with negligible root system. During flowering, the flowers were brushed with a small paint brush on each carpel in order to encourage pollination and fruit development. The growth of fruits in this species took a lot longer than the *P. japonica* which happened over the course of one month. Instead, this species took more than two months for unripe fruits to develop past the early green stage. The progression of subsequent maturing stages in the fruit is shown in 4.1 E- H, and can be characterised similarly to those observed in *P. japonica*. Further discussion of flowering and growth of the plant in its natural habitat was presented in section 2.4.

The earliest stages of the plant cell wall growth were shown in the *P. japonica* study to be implicated in structural colour formation. The period of earliest spectral visibility is also the most sensitive to developmental change, making it the most informative period over which to measure. This was used to inform the observation period for *P. condensata*. Fruits were measured therefore over the earliest period that they were accessible by cutting away parts of the fleshy sepals. During the observation period their macroscopic appearance appeared the same pale green. Several patches of cells were measured on adjacent fruits and each patch appeared to be at slightly different stages of maturity, as visible in the microscope images of the cells, within the white/pale-green stage.

In *P. condensata*, the closely packed infructescence is very stiff and central to the entire plant and the stem, unlike in the case of *P. japonica* where the fruits are separated and form on the ends of individual extended flexible pedicels. In order to measure fruits, the entire stem had to be bent and fixed to a moving stage underneath the microscope objective, limiting the accessibility of fruits and cells. The same observation procedure was followed as previously. The fruit-head in place under the microscope objective is shown in figure 4.1 D. Spectra were taken in left and right handed circular polarisation (using a quarter wave plate and rotating wire-grid polariser) in order to distinguish circular peaks of opposite handedness from different cells.

The appearance of the fruit through different filtered polarisations is shown in figure 4.2. A number of coloured cells are indicated in the dashed circle. The central image shows the unfiltered reflection, in which, like the parallel-polarised image P, the coloured reflections from the cells are barely visible. The left and right handed circularly polarised images L and R show the coloured reflection as well as the outline

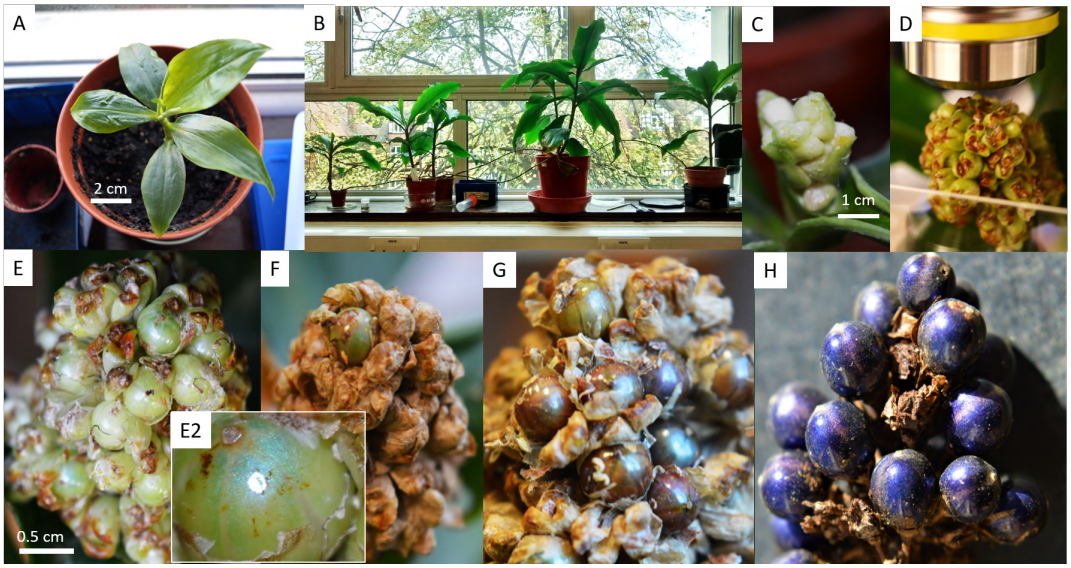

FIGURE 4.1: A series of photos of the *P. condensata* plants in different stages of maturity: A. A young shoot. B. The mature plant C. Budding/ flowering from the inflorescence. D. Fruit-head at an early stage in place under the microscope objective. E. The pale green earliest stage with sepals cut away from the fruits. F. Green stage with sepals in place but dried up. Inset image E2. a close up of the immature fruit in the green stage with blue 'shimmer' appearance reflected from the camera flash. G. Dark red-brown stage H. Mature dry fruit head on a dead stem from a different plant.

and surface of the cells. The brightly coloured reflection is clearly visible although the outlines of the cells are not.

Water-immersion microscopy was attempted and found to be unsuitable due to the close proximity of sepals and other fruits which wicked water and prevented stable bridging via water droplet of the specimen and objective lens. Although both the left and right circularly polarised images contain a significant component of non-structurally-reflected light from the top surface of the cuticle, the use of both filters in combination allows the structural reflection to be extracted. This is possible because unlike in *P. japonica* in the previous chapter, scattering from pigments does not occur in the top layer of the epidermis where the target cells are. Pigmented cells are located much lower in the epidermis, under as many as 5 layers of structurally coloured cells. A schematic of this organisation was shown in chapter 2 figure 2.7.

An additional complication in this fruit however, is the existence of multiple layers of cells. In some instances, this means that multiple reflections are measured simultaneously from different layers, although where possible this was avoided. Where two cells of different handednesses are measured at once, subtraction of one handedness from the other does not give the accurate spectrum profile. However, the cells were disentangled in these cases by treating the cell reflections of different handednesses separately.

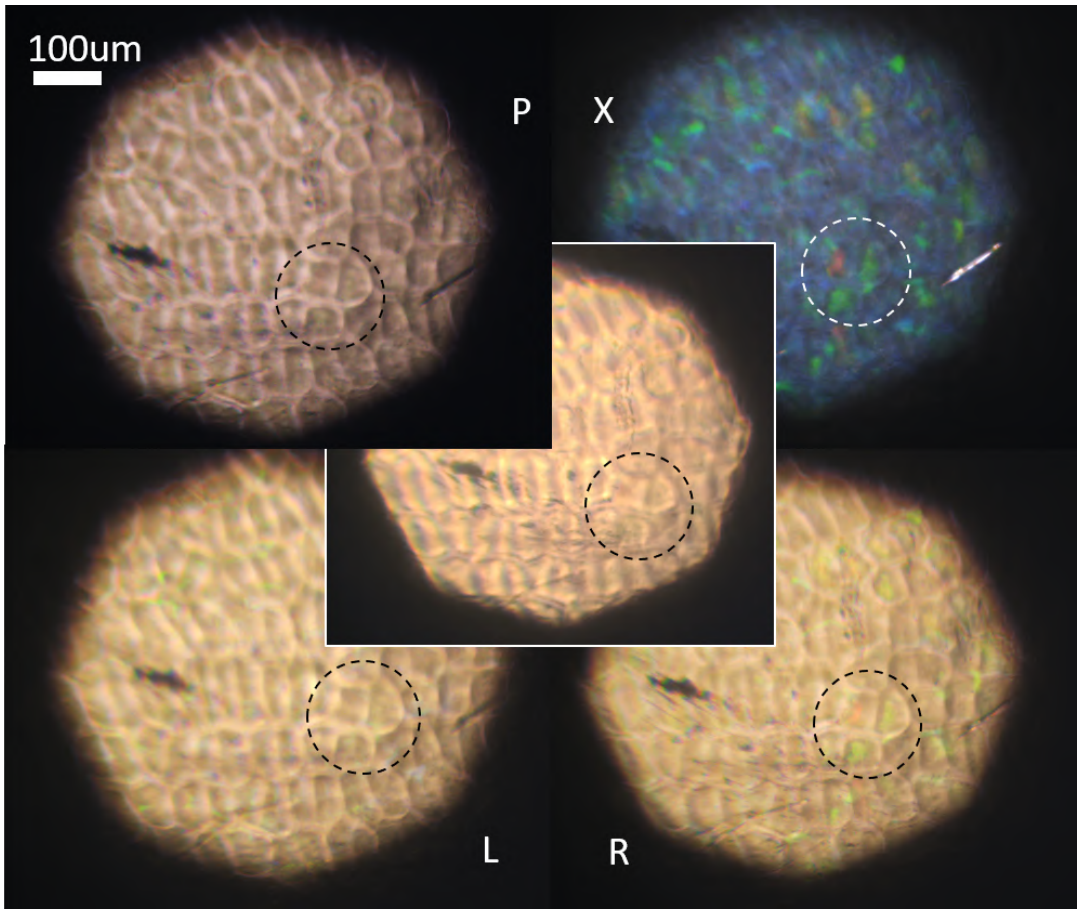

FIGURE 4.2: Visibility of features in *P. condensata* under different filters. P: parallel polarised reflection. X: cross polarised reflection. L: left handed circular polarisation. R: right handed circular polarisation. Central image: no polarisation filters. The same area is circled in each image.

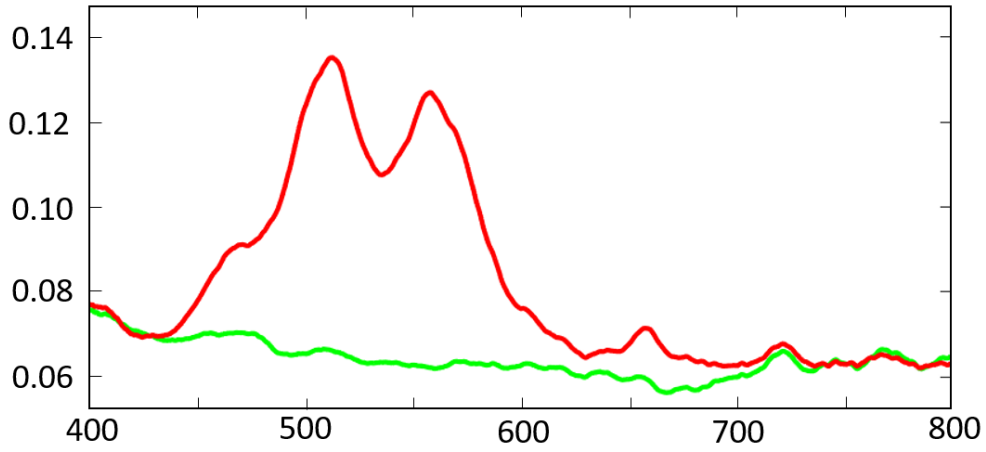

FIGURE 4.3: Spectra in left (green) and right (red) circular polarisation channels are compared. This spectrum is taken from a right handed cell.

A double peaked spectral profile from a cell reflection spot is shown in figure 4.3 in left (green) and right (red) circular polarisation to demonstrate the two separate measured spectra before subtraction. In this case, the reflection is from a right handed cell, and there is no contribution in the left handed circular polarisation. Even without using subtraction of the two circular polarisations, the lack of pigment contribution makes the structurally coloured peak very easy to identify.

4.1.1 Cell Cohorts

Four areas on four different fruits of the same infructescence were observed over periods of between 11 and 32 days. 67 individual cells were followed for some duration of this period, of which 41 cells were used in the analysis. Cell observation was judged successful when it produced a coherent series in which a structurally coloured peak was repeatedly identified over an extended period, and matched with a microscope photograph of a well defined cell for each spectrum.

Each of the four areas at the beginning and end of the observation period is shown in figure 4.4. The cells were chosen in order to get a representative spread of cells from the early stages of growth.

- Eight cells were initially identified in the first area, shown in image i. On initial identification they were already reflecting a large and brightly coloured spot, they represent a group of cells later in development. Four additional cells were added from this area much later than the first group. However, measurement of three of these was abandoned due to difficulty in re-identification and they were not included. Measurement for one cell from the original eight was also abandoned due to lack of certain identification.

- Cells shown in image ii were chosen from an area with a very dense mixed population of right and left cells. Ten cells of each handedness that already displayed colour were chosen. Again, as the cells already displayed some colour, the stage of development is judged to be slightly advanced. However a significant degree of change was seen in the cells and their surroundings during the time. The area was situated very close to the calyx and the surface was not flat. Six right handed cells were not used because of doubts about the cell identification as a surface layer cell.

- Cells shown in image iii were chosen when no colour was observable in the region. 29 cells were chosen, again from an area near the fruit calyx. All cells were directly adjacent to one another. Cells 17 to 25 were not used because this row was right next to the calyx, where they were overshadowed or distorted, making measurement difficult, and very little colour was measured. This can be seen in figure 4.4. Five other cells in this group were abandoned due to indistinct identification.

- Nine cells were chosen in image iv. These cells were large, flat and on a flat and undisrupted area of the fruit, similarly to area i. They were also chosen when no coloured reflection was evident in the region, making this the earliest observable structural colour in the development of the fruit. One cell from this group was not included due to lack of proper identification.

Figures 4.5 and 4.6 show montages of the target cells during the observation period. The image tags i-iv correspond to figure 4.4. It can be seen immediately that the bright coloured cells in montages i and ii demonstrate a consistent appearance over the period. The areas in which very little or no colour was initially measured are shown in montages iii and iv, and the development of colour in these cells is demonstrated.

During the development observation, many of the cells surrounding those in which colour was present from the start also developed coloured peaks. Due to the multiple layers of structurally coloured cells observed in the species, unlike *P. japonica*, some of these cells reflected through the same location as the target cells. This complicated the analysis of these peaks as the spectra could not be identified simply by finding the difference between the two circular polarisations. The subtraction technique remained useful for identifying the very low reflection intensity of the structural colour peaks in the earlier stages (figure 4.6, images iii and iv). The two sets of cells are therefore separated in this analysis into two sets. The first set is the single profile cells, in which the subtraction technique was used. The second set is the multiple reflection cells, in which subtraction was not used, but the target cell spectrum was identified by comparison of the microscope photograph and the left and right circular polarised spectra. Crudely this distinction also works to separate out the earlier stage in which very few coloured reflections are present, and the later

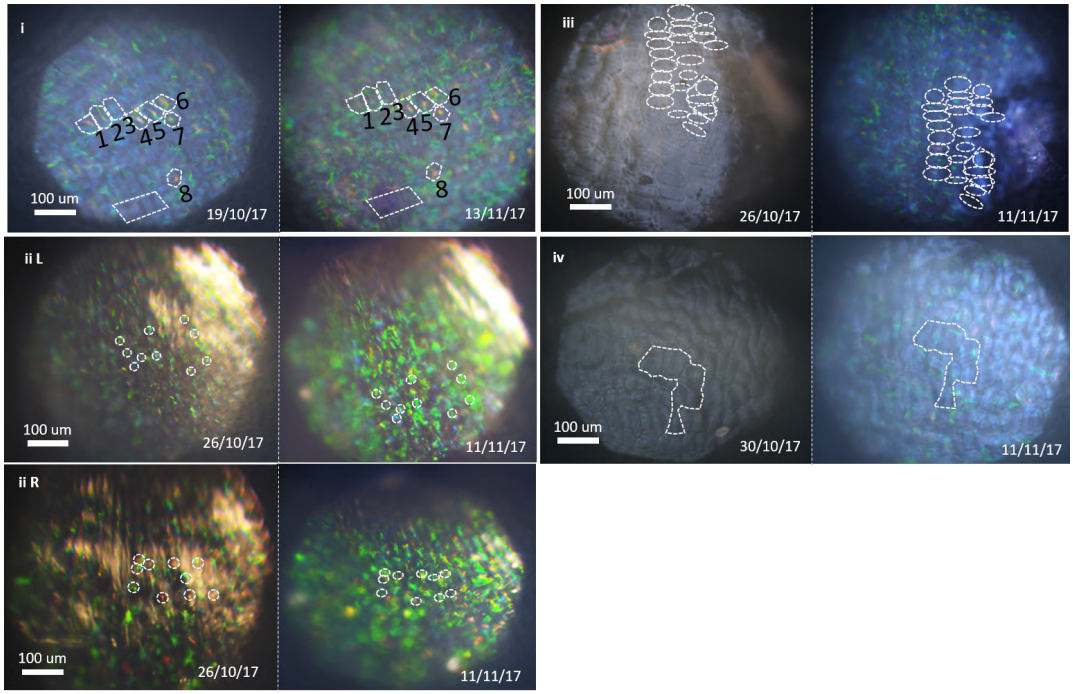

FIGURE 4.4: The four fruit areas studied. Area i: Large spots of bright colour already reflected from early on. iiL and iiR. Small spots of bright colour, ten cells chosen in left and right circular polarisation respectively. iii. No colour visible initially, 25 adjacent cells identified, some of which did not develop visible reflection. iv. No colour visible initially, 9 cells chosen, 8 of which developed well-characterised coloured reflection spots during the observation. i, iii and iv are shown in crossed polarisation to highlight the changes in cell colouration. The iiL and iiR image pairs are shown in left and right circular polarisation respectively. All initially identified cells are indicated with white outlines. Many of the cells were no longer feasible for observation after some days of maturation, as is visible in the images - for example those on the right-hand column of cells in set iii.

stage in which the tissue contains reflections from cells at multiple levels at many locations.

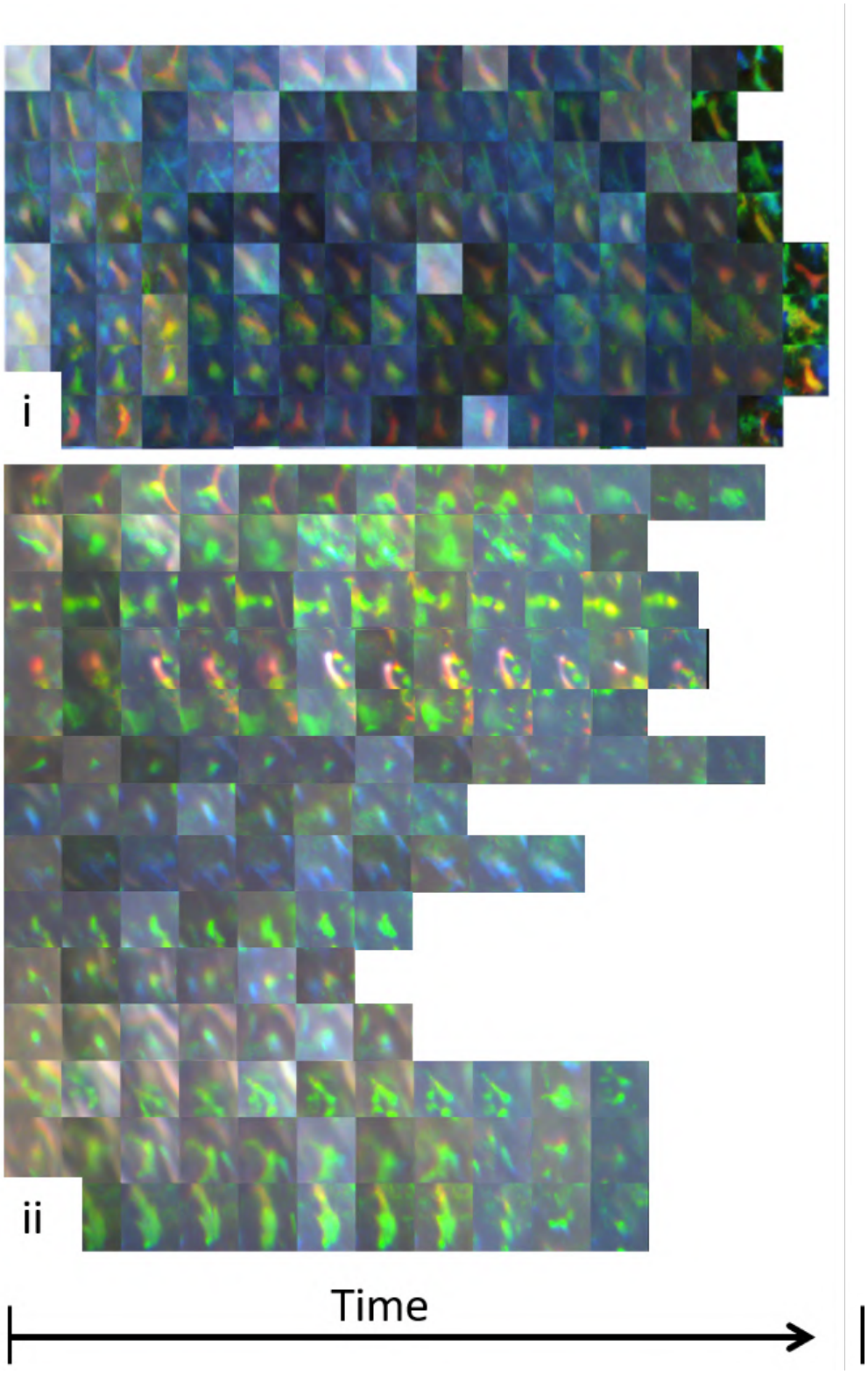

FIGURE 4.5: With 4.6, montages of each of the target cells in the study. Each row corresponds to one cell, repeatedly imaged every one or two days over the observation period with time increasing from left to right. The labels on each section correspond to those on the areas in figure 4.4 from which they are taken. i, is taken in crossed-polarisation, ii is in the appropriate circular polarisation, left or right, corresponding to the handedness of each cell, due to the higher density of reflection in this area where the epicarp is thicker.

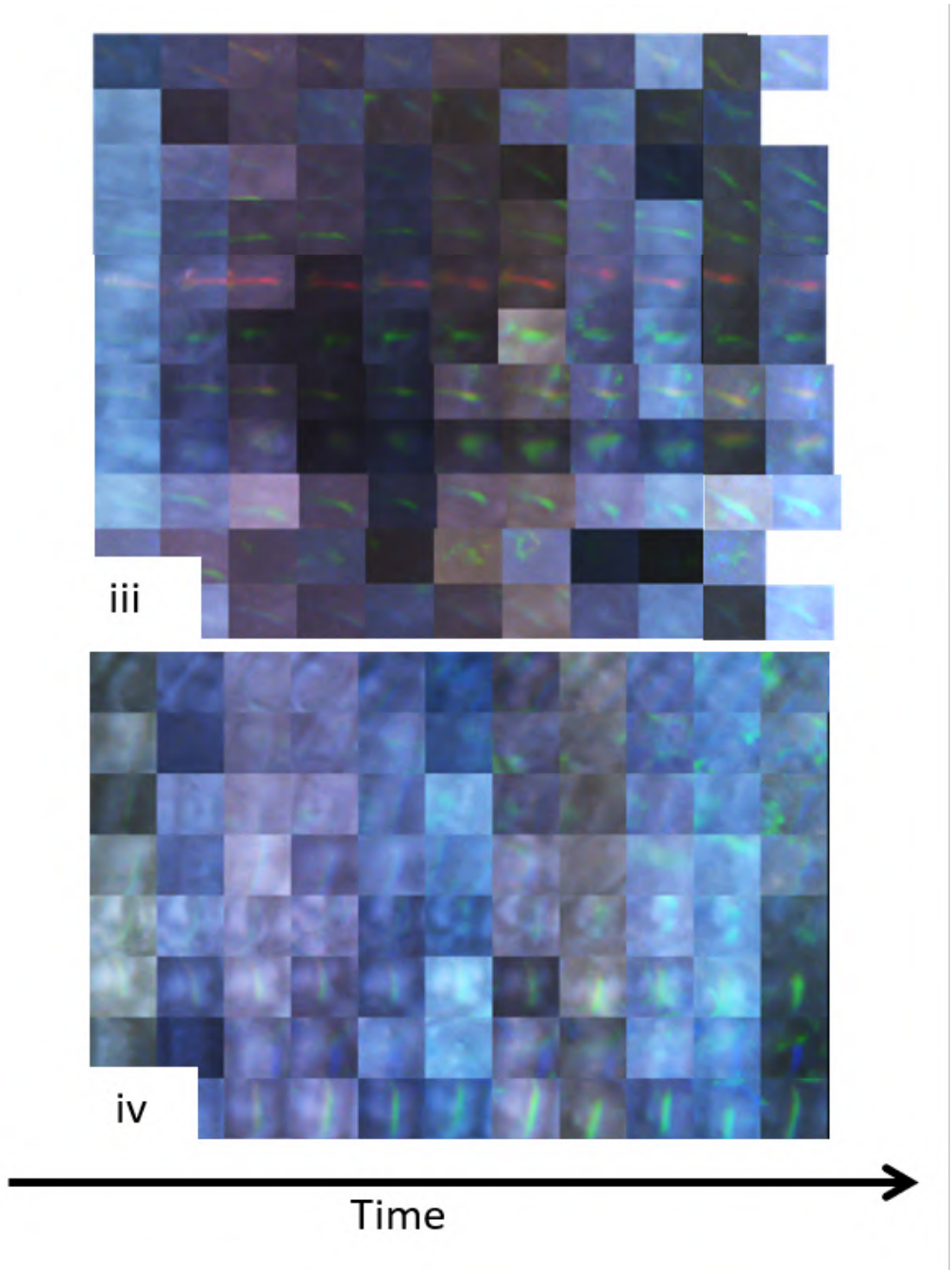

FIGURE 4.6: With 4.5, montages of each of the target cells in the study. Each row corresponds to one cell, repeatedly imaged every one or two days over the observation period with time increasing from left to right. The labels on each section correspond to those on the areas in figure 4.4 from which they are taken. Both sets are taken in crossed-polarisation.

4.2 Isolated peaks - Early Development

4.2.1 Trends

This section analyses the development of peaks which are isolated, that is locations from which the reflection from just one cell is recorded. This is evident in the microscope images of the individual cells and in the spectral profiles.

All cells identified fulfilling these criteria were left handed. This is consistent with the earlier observation that right handed cells are more common in the fruit stripes, where there is a greater thickness of cell tissue, and therefore greater likelihood of multiple reflections being measured.

Figure 4.7 shows heatmaps demonstrating the evolution of these individual peaks through time. These plots make it clear that a single and consistently identified peak is found across each set of scans, and the technique has been successful in measuring a well characterised optical response from each of the cells throughout the observation period.

Each of the spectra were matched with the microscope photo and then the peak characterised by identification of its peak intensity and wavelength. The evolution of these two quantities is shown in figure 4.8 for each of the cells. The progressions were fitted with a linear mixed effects model, as previously used in section 3.3.2 and discussed in section 1.5.2. The resultant linear fits are shown in figure 4.8 along with the intervals which show 50% confidence of both the gradient and intercept independently.

Intensity

Analysis of the linear fit for the cells' peak intensity in figure 4.8, plot A shows that for these there is a small but clearly increasing intensity. The change in intensity per day for the first 8- 10 days is 10% of the initially measured average peak, and the p-value for the gradient fit is 0.0003, suggesting a very good fit. The 95% confidence interval for the intensity gradient does not include 0.

The cells were taken from the areas in figures 4.4 and 4.6 labelled iii and iv. Each of the cells in these areas was chosen without evidence of a coloured reflection spot. That these measurements are the earliest possible observations of the multilayer reflection is responsible for their very low intensity. The growth in intensity measured in the spectra is consistent with the visible appearance of colour during the observation period from an initial non-coloured appearance.

Although some of the cells chosen without colour developed into right circular polarisation -reflecting cells, there were not a large number, and none without a left

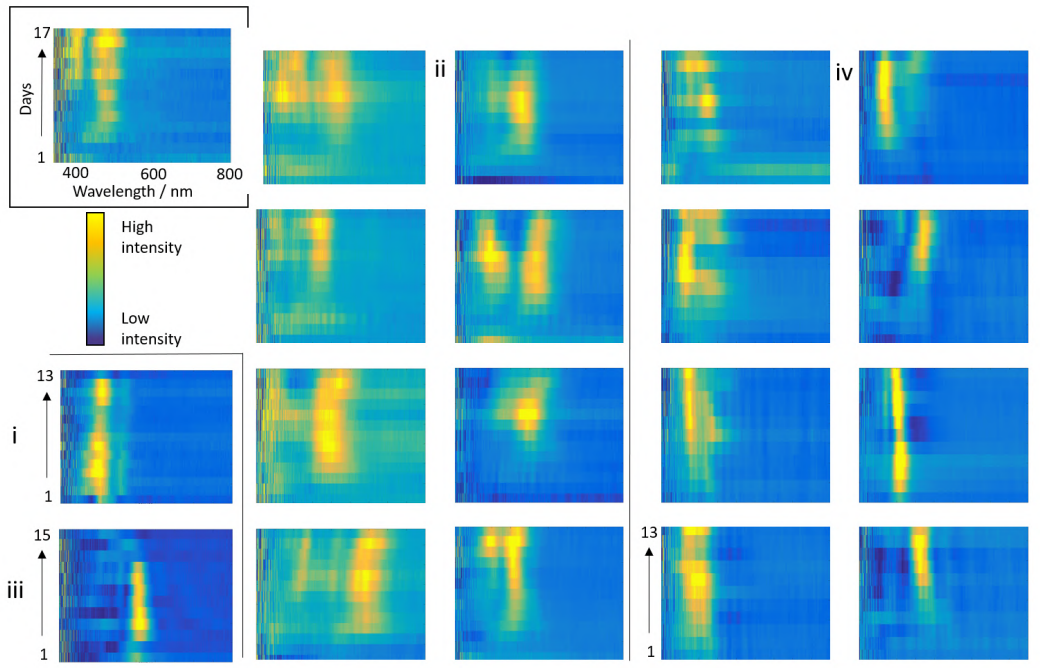

FIGURE 4.7: Each of the isolated peaks identified from the cell areas ii and iv, shown in figures 4.4, 4.5 and 4.6 are shown here as heat maps of the intensity difference between left and right circular polarisation ie. purely structural colour.

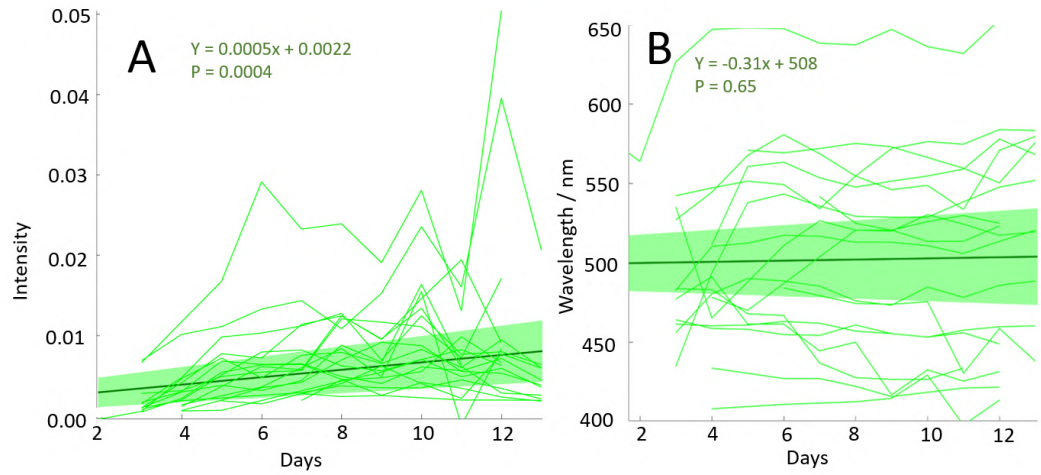

FIGURE 4.8: A. Peak intensity change over time. B. Wavelength changes for the same cell peaks over the same time. In both plots all the cell progressions are plotted with connecting lines. The linear fits are shown with straight lines and shading to indicate the 50% interval for the gradient and intercept.

circularly polarised reflection measured from underlying cells. Therefore, this section deals only with left handed circular polarisation reflecting cells ('left handed cells').

Wavelength

Analysis of the change in wavelength during the period of increasing intensity showed no change in wavelength. Comparison of the temporal heatmaps in figure 4.7 and the individual cell evolutions plotted in the plot B of figure 4.8 shows that some cells do appear to show evidence of a gradual change in peak wavelength, either redshifting or blueshifting, or in some cases undergoing partial shift in both directions. The trends observed by taking the linear fit demonstrate that there is a range of possible best fit gradients including the 0 gradient, and the P-value is very large, much larger than any imaginable statistical threshold to be a good indication of reasonable grounds to reject the null hypothesis. There is therefore no evidence to suggest a consistent shift in the material pitch during growth.

4.2.2 Individual Trends

Nineteen cells, largely from series ii and iv are summarised in the plots in figure 4.8. Each cell may also be treated individually by plotting the linear fit of its evolution in intensity and wavelength over time. This was done, and the overall change in the wavelength and intensity plotted in figure 4.9. The error bars show the 50% gradient deviations.

From the plot in figure 4.9, the majority of cells are seen to have an increasing intensity, consistent with the general trend found from the linear fit model. There are close to equal numbers of cells and degrees of change observed in increasing and decreasing wavelength.

The change in intensity for the different cells indicates the degree to which the multilayer appears to be thickening during this process. The very low intensity of reflection overall that is observed for each of these cells, due to the early period of maturation that is observed makes the intensity change appear minor. However, there is a well-defined change which may be associated with increasing multilayer thickness.

Although it has been shown that the average change for the group is zero, for individual cells, the spread of changes in the peak wavelength is between increase and decrease of 60 nm. This is much greater than the changes observed in the previous chapter in which a change of 10 nm was characteristic of the wavelength changes during maturation in *P. japonica*.

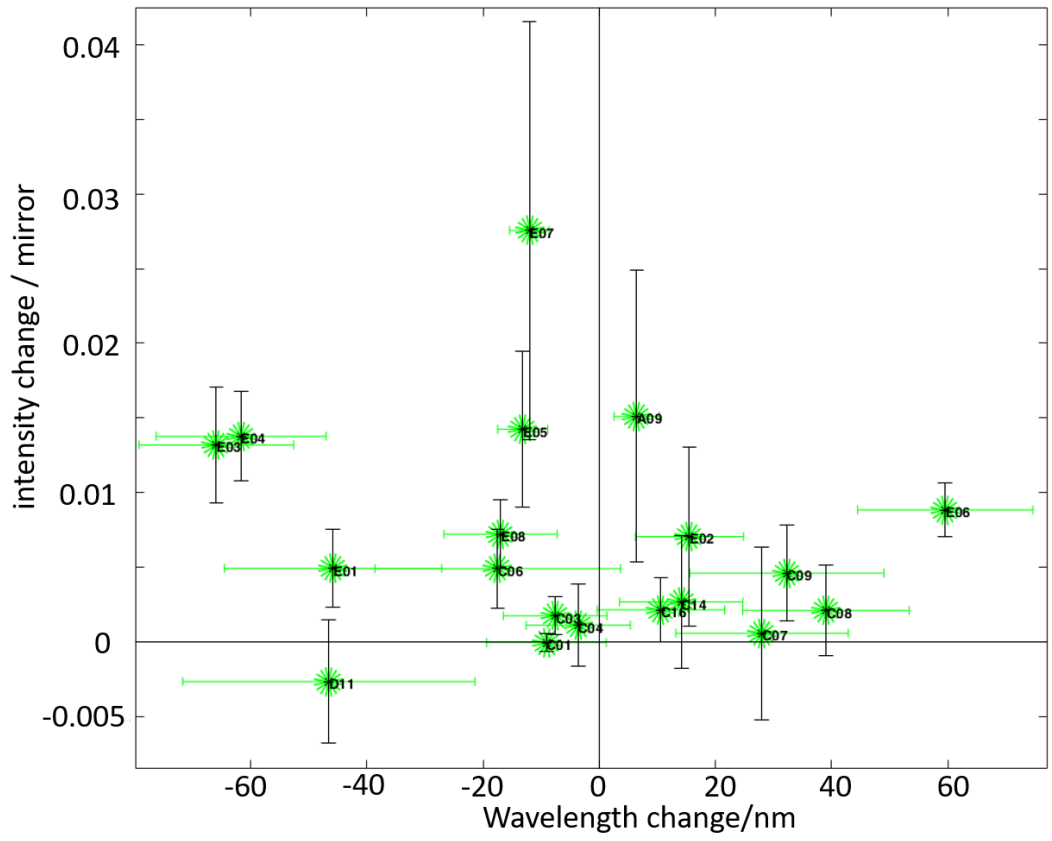

FIGURE 4.9: Plot of change in wavelength vs. change in intensity. Each cell is plotted with error bars indicating 50% confidence intervals round the gradient for each cell.

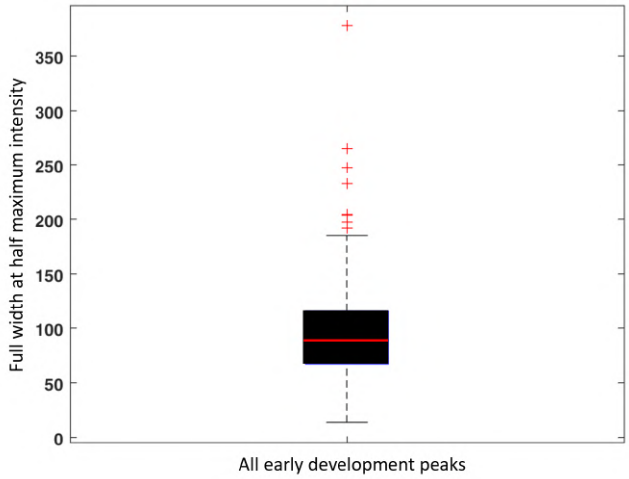

FIGURE 4.10: Peak width average and range for all cell peaks. The median value is indicated with a red horizontal line. The top and bottom of the box shown the 25th and 75th percentiles, and the whiskers indicate the range. Outliers are in the upper 0.05 percentile of the distribution modelled as normal. The modal width across the observation period was measured to be 93±36 nm.

The spread of changes in wavelength and intensity across the left and right cells does not indicate any other correlation which defines a distinct population of increasing or decreasing wavelength cells. In order to understand the potential explanations for the individual changing peak wavelengths within cells, the changes are compared to the width of peak profiles. The range of widths observed in peak profiles is shown in figure 4.10. The average full width of the peak at half maximum intensity is measured across the temporal range to be 60 - 120 nm. Changes of peak wavelength of up to 60 nm must therefore be assessed in the light of a much greater peak width, and an increasing intensity.

Inspection of individual trends indicates that the change in peak wavelength occurs in these cells predominantly within the peak profile width, and may, as in *P. japonica* analysed in chapter 3, be accounted for by an increasing thickness in the multilayer with a varying pitch profile adding to the cumulative reflection. The lack of consistent change in these cells is noted as an indication that the cumulative addition of multilayer pitches does not follow a trend such as increasingly narrower or broader pitches with change in the layer depth.

4.2.3 Example

The trends identified in the changes in intensity and wavelength of all the cells are exemplified in the cell in figure 4.11, cell 'E08' as identified within the upper left quadrant of figure 4.9.

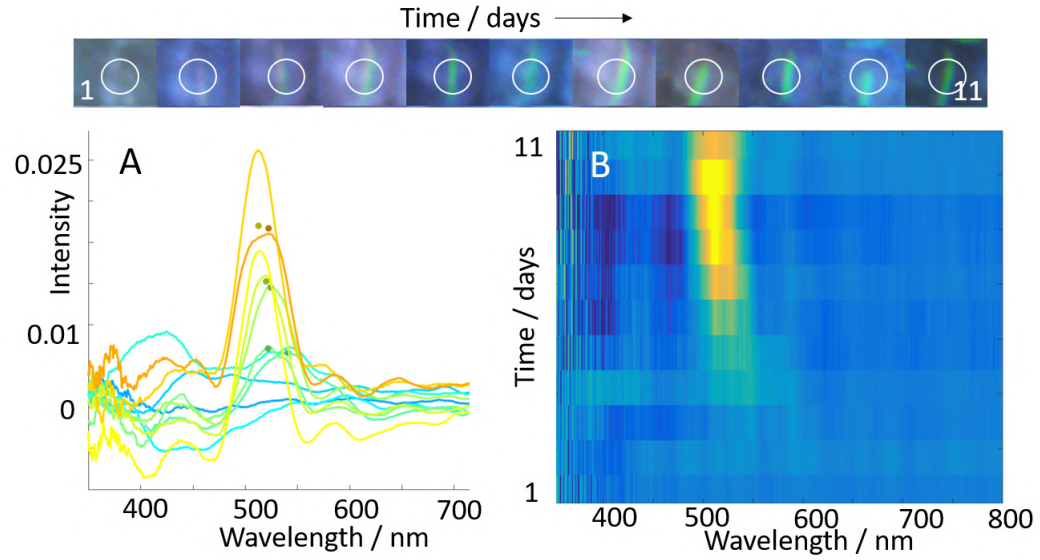

FIGURE 4.11: Cell labelled E08 in figure 4.9. Photo montage at the top showing progression. The white circle indicates the approximate size and location of the fibre collection spot. Its spectra are plotted below. A. Left - right difference offset. B. Heatmap showing transition of the peak over time.

The cell undergoes an increase in intensity, and also a decrease in peak wavelength during the observation time. The change in wavelength can, as before, be explained by a cumulative increase in the lower wavelength proportion of the peak, with increasing multilayer thickness.

The cell measurements present a number of challenges. In the cases where no colour is seen, the appropriate location measurement is defined by looking at the cell wall outline and taking the central spot. However, colour does not always develop symmetrically in the cell centre, or uniformly. When the cell starts to appear coloured, the coloured reflection spot is measured, and the same location reidentified on each repeated measurement. The reflection spot shape and size observed is not always uniform during growth. Although the cells were seen to have a generally uniform colouration, a very small shift in the tilt of the multilayer, either due reflection from the edge of the multilayer, or changes in cell shape causing tilt would be expected to introduce a slight change in peak wavelength. Due to the extremely low intensity reflection, as seen both in the spectral profiles and the microscope images, it is not always immediately clear whether the initial colour observed is the coloured reflection spot from the target cell, or colour reflected from underlying cells. This is much clearer once the reflection colouration is established after several more days growth. In some cases however the additional increase in reflection from a cell underneath was recognised to dominate inextricably the reflection of the target cell, again introducing an error.

Added to these issues were problems of tilt introduced by repositioning the plant for

every measurement, and recognising the same cell location over an extended period of significant change.

Each cell series of spectra and microscope photos were cross-checked and compared to data in each time series to assess the reproducibility of the measurement. Measurements where significant error was introduced by the complexity of the response as described above were removed from the data set. This made some cell sets too short to properly analyse and they were abandoned.

4.3 Adjacent Cell Spectra

As discussed in the experimental methods of this chapter, a number of cells were chosen although they already displayed a brightly coloured reflection spot similarly to the right handed cells in the first part of this chapter. These cells are clearly in a later stage of their development than the left handed cells treated previously in this chapter.

During the measurement of many of these cells, other reflections of the opposite handedness were also included. These reflections are from cells in different planes but the same location. The observation of reflectance peaks in both left and right circular polarisation makes analysis by subtraction of one spectrum from the other impossible. Treating the two polarisations separately is important in order to measure the target cell.

Inspecting the optical microscope images in developing cells, the location of the chlorophyll pigmentation appears not to be in the outer cell layer as it was in *P. japonica*. The background contribution from the chlorophyll absorption spectrum is significantly decreased, making the analysis of the structural colour peak relatively uncomplicated. However, the degree of overall light intensity in the profile is variable, so the spectra were normalised by the intensity of light at 680 nm.

4.3.1 Trends

Only the target cell, which had been identified at the surface of the fruit, was included in the general trend, in order to make sure the analysis focused on a well-characterised simple single reflection. Two sets of cells were separately measured. The first, set i in figures 4.4 and 4.5 were significantly bigger, more brightly reflecting and more clearly defined than the second set, which is shown in set iii in the two figures. The larger area of reflection, cell area and bright, better defined reflection spots are again taken as evidence to suggest that these cells may be at a later stage of development than the smaller, less bright set.

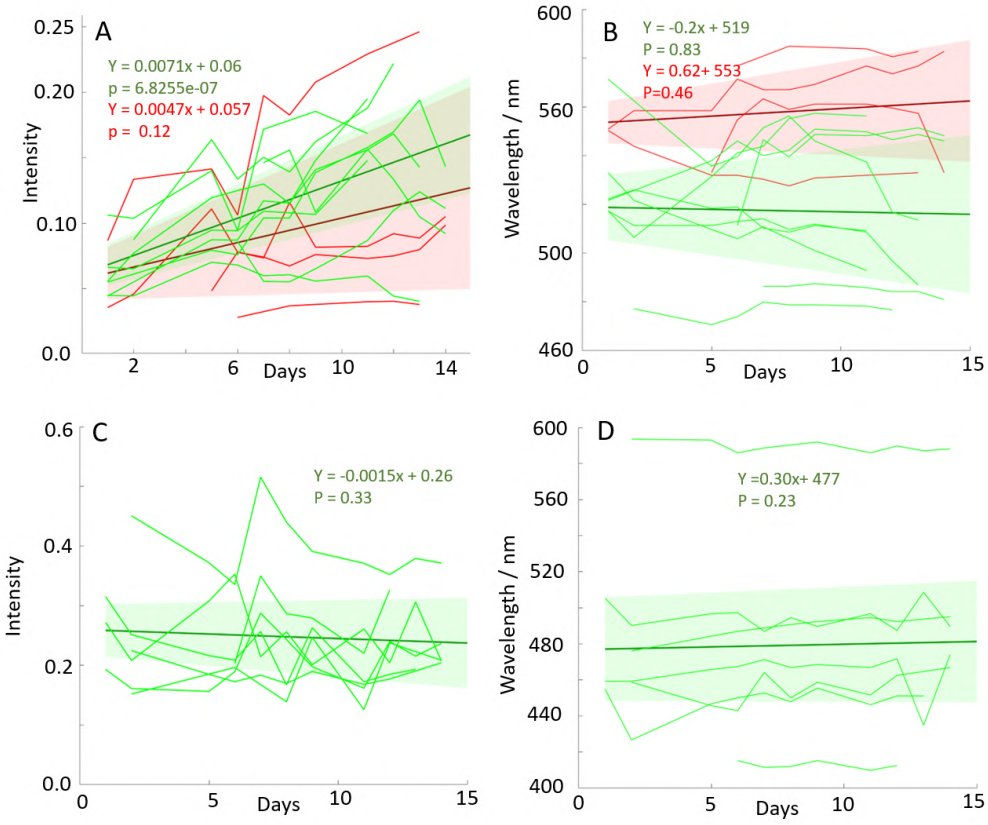

FIGURE 4.12: Plots of intensity (A and C) and wavelength (B and D) changes over a two week observation period for two sets of cells. Each of the cell progressions is plotted as a line joining measurement points. The linear mixed effects best fit is plotted in the heavier dark line. The shaded area represents $\pm$ 50% confidence intervals for both intercept and gradient of the line. Left handed cells are plotted in green, and right handed cells are plotted in red. The lower plots are of a cell cohort which did not include any right handed cells. The cell group plotted in A and B are area (ii) in figures 4.4 and 4.5. In the same figures, the cell group plotted in C and D are labelled (i).

The two sets are shown independently in figure 4.12. Plots A and B show the development of the earlier, less mature set (labelled 'iii' in earlier figures) which was initially chosen to include left and right circular polarisation reflecting cells. Plots C and D show the 'older set' (labelled 'i' in earlier figures) with brighter, better defined peaks.

Intensity

Plots A and C in figure 4.12 show the intensity change over two weeks for the set of younger (plot A) and older (plot C) cells respectively.

Plot A shows cells of both handednesses. There is a strong increase in the intensity of the peak observed in the left handed cells in this cohort from the increasing gradient of the linear fit, which was carried out using the linear mixed effects model as before. The p-value indicates very high confidence in this fit.

The right handed cells also show substantial evidence of increasing intensity, although the p-value is not low enough to outright reject the zero-growth model. Looking at the individual progressions both on this plot, which may also be compared with the plot in figure 4.13, the majority of the cells exhibit increasing intensity.

Plot C shows the intensity measurements from the already well developed cells. This set of cells only included left circular polarisation reflecting cells. These cells are notable for their bright colour and large reflection spots, which were significantly further developed than other adjacent cells in the same area of the fruit at the beginning of the observation period, as seen in figure 4.4. Plot C shows that the intensity measured for the cells over the observation was consistent, with some measurement error and did not increase (or decrease) over the time for most of the cells. This is taken as evidence that many of the cell walls were not increasing in thickness during this time. The study of these cells therefore represents a period subsequent to the initial growth of the cells, although the fruit at this time was still green, and surrounding cells in the same area showed significant change in the intensity of their reflection.

It is reasonable to assume that cells go through phases of different growth rates as the development progresses. It is also reasonable that the maturation phase and therefore growth rate between cells on different fruits at any time may differ.

Wavelength

Plot B shows the peak wavelength progression of the same cells in right and left handed circular polarisation. The trends, which are indicated with the line of best fit

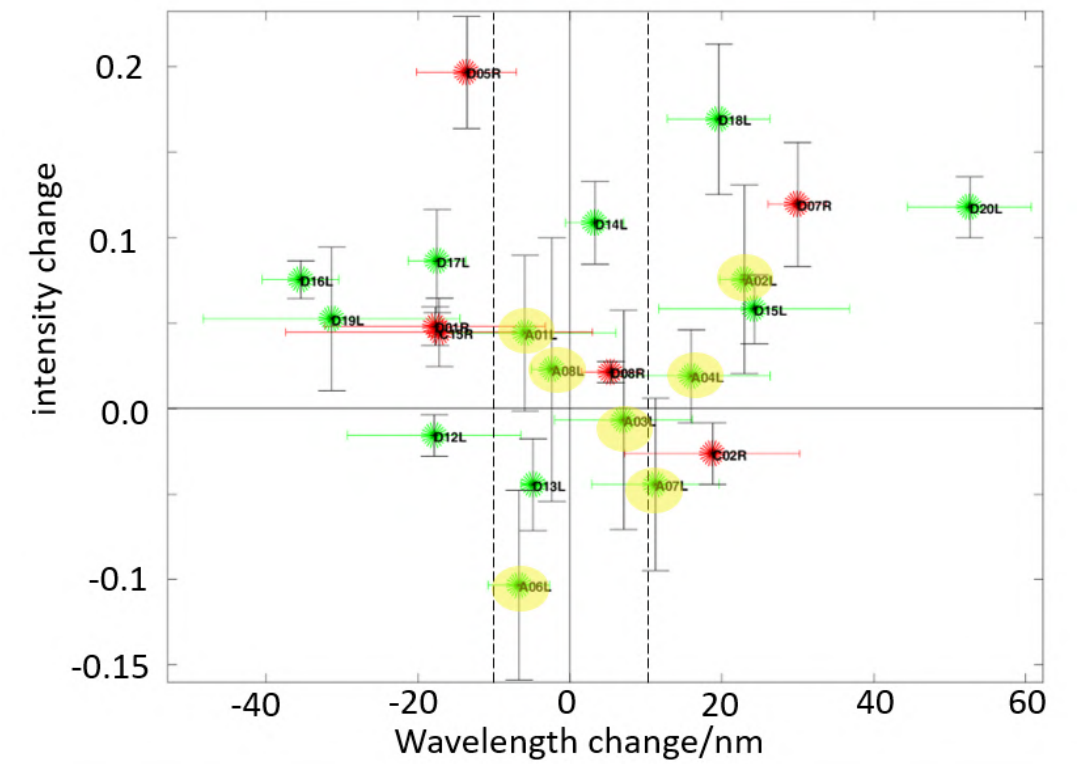

FIGURE 4.13: Each of the cells plotted in figure 4.12 is labelled according to the overall change in wavelength and intensity in this figure. The error bars in both directions represent the 50% confidence interval. Left handed cells are plotted in green and right handed cells in red. The more developed set of cells which have an average zero intensity gradient have a yellow tag. The 0 change intensity and ± 10 nm wavelength changes are indicated with black lines.

and 50% confidence intervals in intercept and gradient fitting coefficients contained within the shaded area, indicate that no overall change occurs in the peak wavelength of either the left or the right handed cells. Importantly, although as before the right handed cells are seen to have a longer average wavelength than the left handed cells, there is no significant difference in the wavelength evolution, which for both peaks is seen overall to be no change.

The evolution of the peak wavelength in plot D, which shows the later developed cells shows even greater stasis in the peak wavelength measured. The 50% gradient range includes the 0 gradient, and is very severely constrained to a 50% gradient interval more than four times smaller than that of the cells in plot B. The lack of change in the wavelength during stable intensity indicates that there is not further reorientation of the internal distances between the stable number of pitch repeats.

4.3.2 Individuals

Each of the overall changes for the individual cells measured is plotted in figure 4.13. The plot shows the two sets of cells:

- Set iv - the younger set, in which 12 showed increasing intensity, and 3 showed a decrease.
- Set i, (marked in yellow) of which one showed an increase, one a decrease and 5 showed no overall change.

Again there is a moderate change in wavelength observed in many of the cells, with no overall bias. The largest changes in the wavelength are observed for cells with the greatest intensity increase, while none of the cells with a stable or decreasing intensity has an observed change in peak wavelength greater than ± 10 nm, which as discussed earlier is within the peak identification error of these broad peaks.

4.3.3 Example

Two cells are presented in order to understand the changes observed.

Figure 4.14 shows a cell with increasing intensity and wavelength. Both the right circular polarisation target spectrum and the left circular polarisation non-target spectrum are shown in plots A and B, in which the offset is designed to demonstrate the changing wavelength over time. The target spectrum refers to that of the surface layer cell, which is identified, in focus and visible. The other spectrum belongs to an out of focus underlying cell, and is not characterised. They are also both shown in plot D. Photos of the measured area in both left and right circular polarisation are shown in the photo montage C. The two distinct reflections are observed to overlap

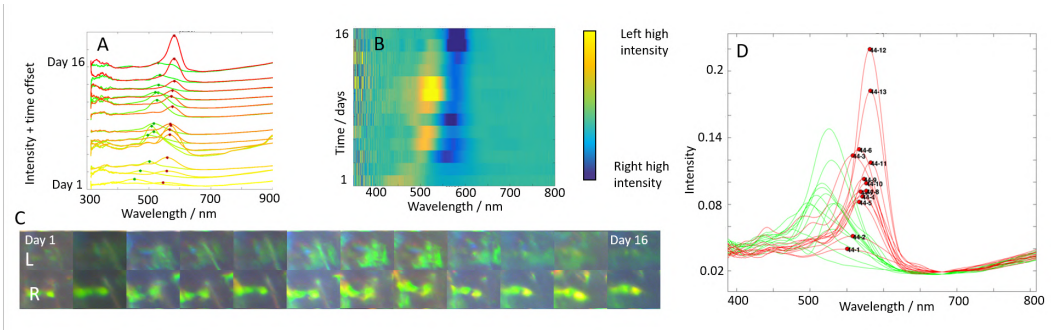

FIGURE 4.14: Example cell A. Right and left handed circular polarisation spectra are plotted with decreasing yellow colouration corresponding to increasing time, and a temporal offset. The two peaks for each spectral pair are seen, along with the identified peak. B. A heat plot showing the same spectral features with time increasing up the page. C. A montage in left (top row) and right (bottom row) of the identified cell over the 16 day period. D. Both left and right circular polarisation intensity plots for each observation plotted on the same axis. The right handed circular polarisation spectral peaks, which correspond to the surface-layer target cell are labelled.

in terms of location, although they remain distinct in the peaks and appearance of the reflection.

Looking at the progression in the target spectra of right circular polarisation, it is clear that some red-shift is seen in the peak wavelength, but that the change is consistent with a cumulative average difference rather than alteration of existing reflection.

Some of the cells in the study show more sudden changes in peak wavelength than the very shallow gradient generally observed. This is the case when multiple peaks are observed within a single spectral profile, and the growth of one relative to the other shifts the peak wavelength.

Wavelength change has been described in this thesis as the result of a shift in the average pitch length in the cell wall multilayer structure, by addition of layer rotations with different pitches. The existence of multiple peaks is also the result of inhomogeneity in pitch length, as explored in section 1.5. The transition between multiple peaks therefore should not be differentiated from the general trend of peak wavelength change.

In one cell, which is not included in figures 4.12 and 4.13, this effect was observed to occur over a long range. It was not included in the average trends, because the tracked behaviour was markedly different to the other cells, and therefore introduced a non-realistic skew to the average. The cell is presented in figure 4.15. The peak wavelength was seen in this case to jump by nearly -100 nm which is a much greater distance than other observed transitions. Inspecting the spectra over the

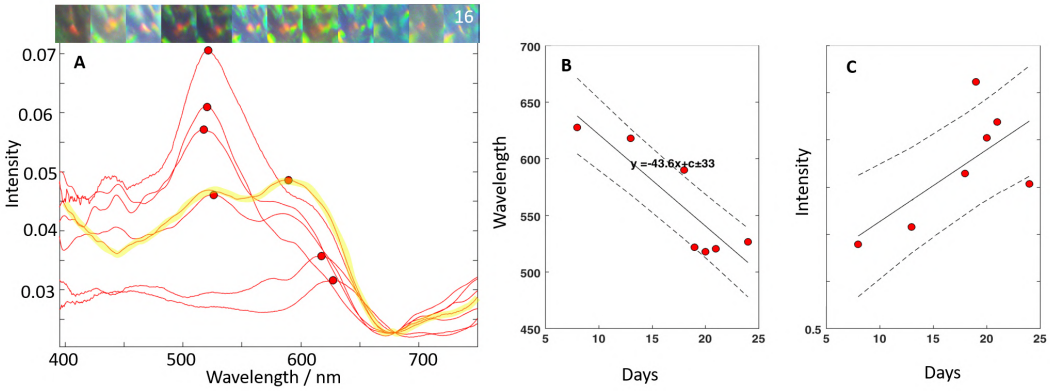

FIGURE 4.15: Example cell. A. Plot of each of the spectra measured in the observation series and their peaks identified. The spectral profile corresponding to the transition between from the higher dominant peak wavelength to the lower wavelength is indicated with a yellow line. The spectra were taken in right circular polarisation. Above, a photo montage of the cell over the observation period, taken in right circular polarisation. B. The peaks wavelengths identified in A plotted according to the observation time, and a line of best fit used to link them. Two distinct dominant wavelengths are observed. C. A plot of the intensities of the same peaks over time and their line of best fit. The intensity scale is arbitrary. The dashed lines indicate the $\pm$ 95% confidence intervals of the fitting lines.

transition,in figure 4.15 plot A the jump is seen to occur between two distinct peaks with a large difference in peak wavelength.

It is possible that this change in wavelength is actually the result of a combination of another underlying cell's reflection spectrum with the target cell's. In this case, due to the same handedness of polarisation, the two spectral profiles cannot be unpicked. This seems a likely explanation, especially given the photo montage of the cell above plot A which shows the persistence of a red reflection spot, but also the inclusion of a number of other colours.

4.4 Comparison of Development Series on both Species

All the trends observed in *P. condensata* cells studied are combined in figure 4.16.

The intensity range for the *P. condensata* cells in the second half of this chapter, as in figure 4.12 is approximately five times more intense than the intensities shown in the first part of this chapter, in figure 4.8. This is largely because the cells are generally large and bright and significantly more developed than the previous sets.

A small contribution to the enhanced intensity in this set of measurements with respect to the previous is a small portion of non-structural reflection that is included in

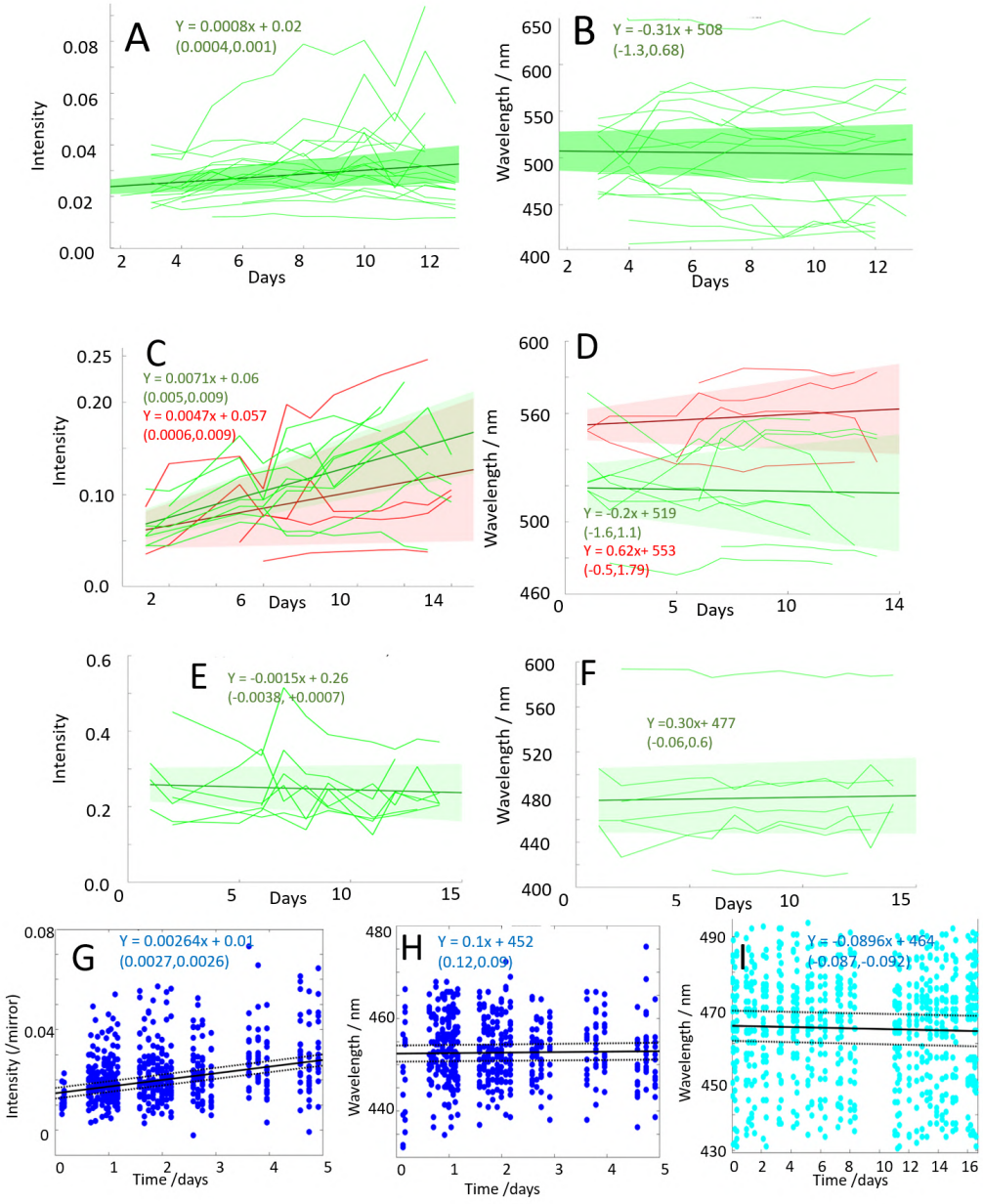

FIGURE 4.16: Collected graphs of overall and individual cell changes for each set of *Pollia* cells are reproduced for comparison. Green indicates left handed cells and red indicates right handed. *P. japonica* plots are reproduced in blue. A and B represent the intensity and wavelength of the same cells as analysed in figure 4.8, but without using the subtraction of right and left circular polarised spectra and the intensities are therefore directly comparable with the other plots. C and D represent quantities for the set of initially coloured cells with some growth in intensity still apparent. E and F show the peak values for cells that are no longer undergoing increase in intensity. G and H represent values for the early stage *P. japonica* and I represents the wavelength progression for the late stage.

the measurement due to the impossibility of extracting the structural peak by subtracting the left and right circular polarisations. The effect of pigmented scattering in this fruit is much less prominent than in the *P. japonica* because of the separated locations of the structurally reflecting and pigmented or chlorophyll-containing cells. The background signal is therefore effectively removed by taking account of the overall background level. However, a small portion remains and contributes to the measured peak. The data from figure 4.8 is reanalysed without this subtraction and plotted in figure 4.16 for comparison with the more developed *P. condensata* cells. This adds approximately an extra 0.06 to the overall intensity.

In all the cell sets analysed wavelengths are not seen to change consistently in the red or blue direction, although individual cells undergo some change in the peak wavelength. This is explained by the use of a model of progressively accumulated pitch repeats with a significant variation in pitch.

The same model is proposed for the two species. Gradient trends in intensity and wavelength with $\pm 50\%$ confidence intervals are plotted in figure 4.17. Red (right), green (left) and blue (*P. japonica*) are used to plot the sets of cells with a confirmed increasing intensity, and cyan (left) for the *P. condensata* cells without a measured increase.

Inspecting the distribution of cell wavelength changes, the variation in *P. condensata* is significantly more extended than *P. japonica*, seen in the length of the $\pm 50\%$ error bars. There was no difference seen between left and right cells beyond the reaffirmation of the finding in chapter 2 that right handed cells have a longer average wavelength than left handed cells. Although the average of the right handed cells is redshifted compared to the left handed cells, the 50% error includes both the 0 gradient and the average for the other handedness, in both cases.

I suggest that the larger variation in the wavelength changes observed in the *P. condensata* peaks is associated with the wider spread of peak wavelengths seen in chapter 2. Each cell contains within it a greater variation of pitches, making the peaks more convoluted, and as the cell wall develops, resulting in a bigger change in the location of the peak wavelength reflected. The greater sensitivity to structural colour in the measurement of these cells, due to the lower pigment contribution and use of the circular polarisation subtraction technique means that a comparison of the two studies cannot be used to support this conclusion.

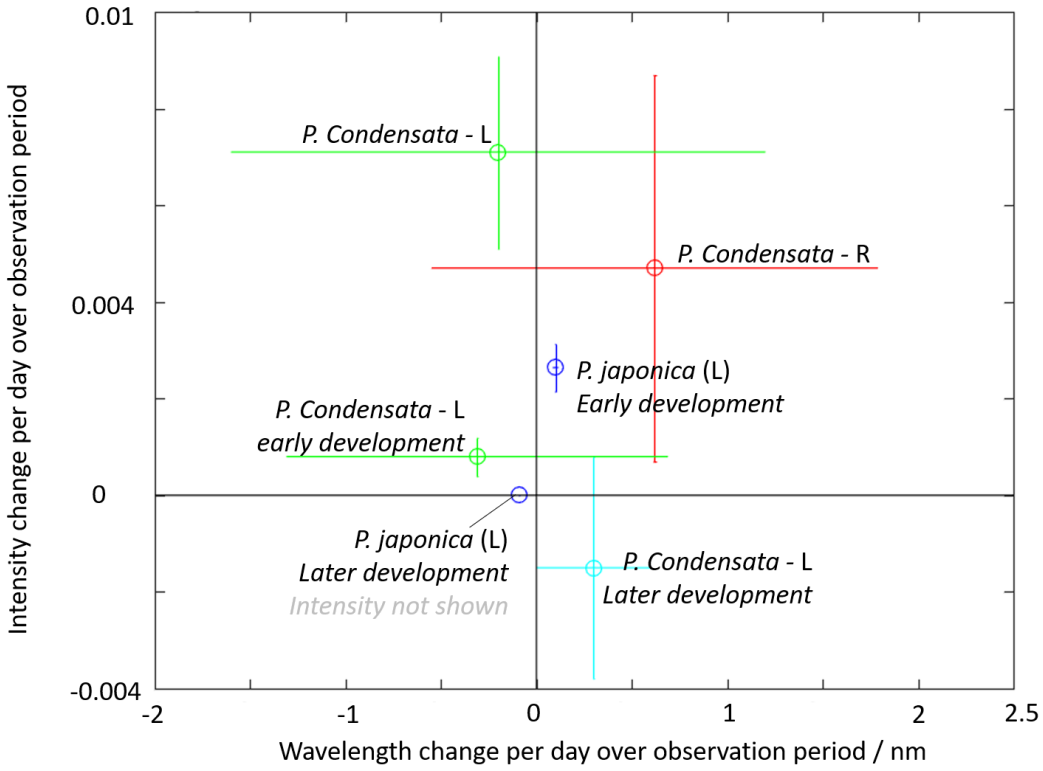

FIGURE 4.17: Overall gradient trends and their 50% bounds for average intensity and wavelength changes measured. The variation in the lengths of time and sizes of the data sets, and the measurement techniques should be considered when making direct comparisons.

4.5 Limitations

Some error is observed in the measurement of peak intensity, as is evident in the random error from the linear fits, in both growing and non-growing stages. This occurs because of difficulty in making the observation conditions such as angle of illumination on the cell body consistent. Nevertheless, growth is measured and demonstrated here in the earlier cells, the experiment is judged to remain tolerant to the experimental error.

Significantly fewer right handed cells are measured than left handed cells, making general conclusions about the right handed cells with regards to the left difficult to make. This is due to the uneven distribution of left and right handed cells discussed in chapter 2, and the limited range of choice for cell measurement areas introduced by the shape and orientation of the fruits with respect to the plant and each other, as discussed in the experimental introduction to this chapter.

A very low intensity in the cell reflection is measured in the single peak measurement of this section. This is due to the observation of the very earliest stages of measurable structurally coloured reflection from the cells, which necessarily meant the peaks were extremely small. It is the introduction of left and right circular polarisation filters which permits the measurement of this very low signal.

It is also concluded that in some cases the reflections measured may include other cell spectra as well and this does not affect the conclusions drawn.

Direct quantitative comparison between the *P. condensata* and the previously observed *P. japonica* is limited by the differences in the two systems, particularly the different epicarp architectures and the very different time-scales over which the fruits mature. This study indicates that in both cases, early growth in intensity of the cell wall reflection occurs without a change in the peak wavelength. This corresponds to increasing numbers of helicoid pitches without pitch change.

4.6 Electron Microscopy

4.6.1 TEM and Numerical model

TEM images were taken of a microtomed section from a resin-embedded mature fruit, which is shown in figure 4.18. The top half of an external *P. condensata* cell wall is shown in image A. Numerical modelling of the profile taken from the TEM is shown in B in a series of profiles with progressively increasing numbers of pitch repeats. As before, the variation over a single cell is accounted for by averaging over five similar profiles with a standard deviation from the TEM profile of 10 nm. This is shown in plot C. One of the cells measured which showed no intensity increase over

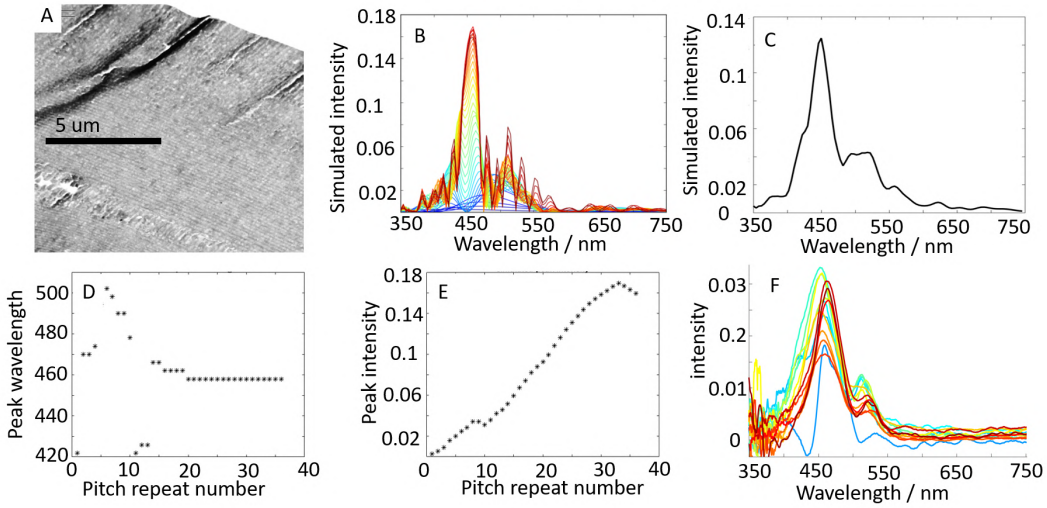

FIGURE 4.18: A. TEM section of the top half of a surface cell of *P. condensata* by Dr Paula Rudall. B. Model of additional pitches of the profile measured from A, according to the modelling method in section 1.5. C. Model of the extracted profile over five profiles with standard deviation of 10 nm from the original. D and E. Plots of peak wavelength and intensity with increasing number of pitch repeats. F. Experimental profiles of a cell peak series measurement in which no intensity growth was observed for comparison.

the observation period is shown in plot F, in order to demonstrate that the modelled profile shows a profile shape similar to those observed in the study - a low number of peaks with a similar width.

Plots D and E show the change in peak wavelength and intensity as pitches are accumulated. Notably, there is significant change in the pitch repeats. The peak intensity of the numerical model also does not increase uniformly over the series of increasing number of pitches in the profile.

The pixel dimension across the multilayer, and therefore theoretical limit on the resolution of the TEM image, and therefore the pitch variation accuracy is 20 nm. This impact of this is reduced by averaging across each pitch over a length of 1-2 um, however, given the fundamental limit of the resolution, it seems likely that some significant limit on measurement of the variation remains.

4.6.2 SEM Techniques

Electron microscopy was used to complement the optical analysis. Cryo-electron microscopy was used as an invaluable tool to draw further insights from the developmental stages of the young *P. condensata* cells in the white/pale green and red/brown stages, when the cells of the epicarp are hydrated, unlike the SEM images previously presented on the mature *P. condensata* fruits, which are entirely dry.

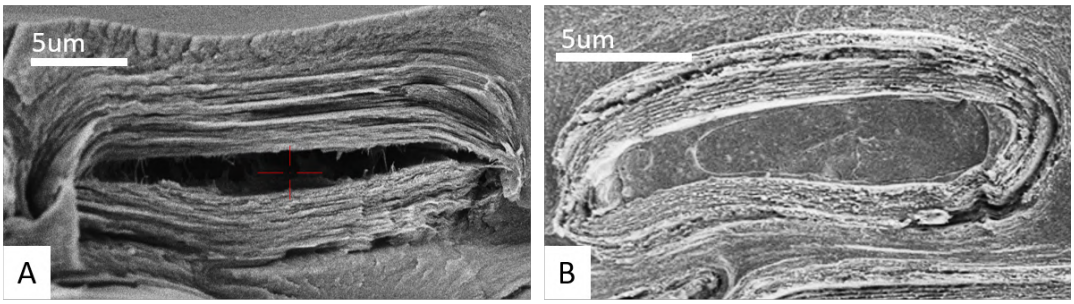

FIGURE 4.19: A. Room-temperature SEM image of an immature (white/green stage) *P. condensata* fruit. B. cryo-SEM image of a cell from the same specimen showing better retention of lifelike cell features.

For preparation of the sample for cryo-SEM, a fragment was prepared as described in section 1.5.1 by flash freezing.

In order to illustrate the importance of the use of cryo-SEM, figure 4.19 shows a comparison between a normal SEM image of a dehydrated young *P. condensata* surface layer cell, image A, and a similar surface cell at the same stage imaged via cryo-SEM, image B. The difference between the two is clear. The cryo-image (B) allows for the visualisation of a hydrated cell with substantial liquid cell-contents, including the outline of some cell organelles. Image A, in contrast shows a hole where the cell contents have dried, without an indication of its original size. Furthermore, the cell wall and cuticle appear to have crumpled through dehydration. Finally, the use of the controlled freeze-fracture blade in the cryo-SEM gives a large, clean cross-section with good cell visibility.

4.6.3 Epicarp Dimensions

The epicarp cross-section of the *P. condensata* fruit at three stages are compared in figure 4.20. A, C and E show cross-sections through the entire epicarp. B, D and E show a single cell from each of the cross-sections.

Coloured bars on the images indicate the relative proportions of cuticle (yellow), structurally coloured cells (red) and pigmented or fleshy cells (blue). Over each subsequent stage the overall width of the epicarp decreases from a difference of 50% between the first and second stage and by a further 40% decrease between the brown and blue stages. The proportions of the different cell layer sections also change, with the structurally coloured area taking up a progressively greater fraction of the overall width over time. As can be observed later in figure 4.24, there is considerable variation of the epicarp thickness depending on the location on the fruit, but the thick hydrated cell layer in the white/ green phase is characteristic.

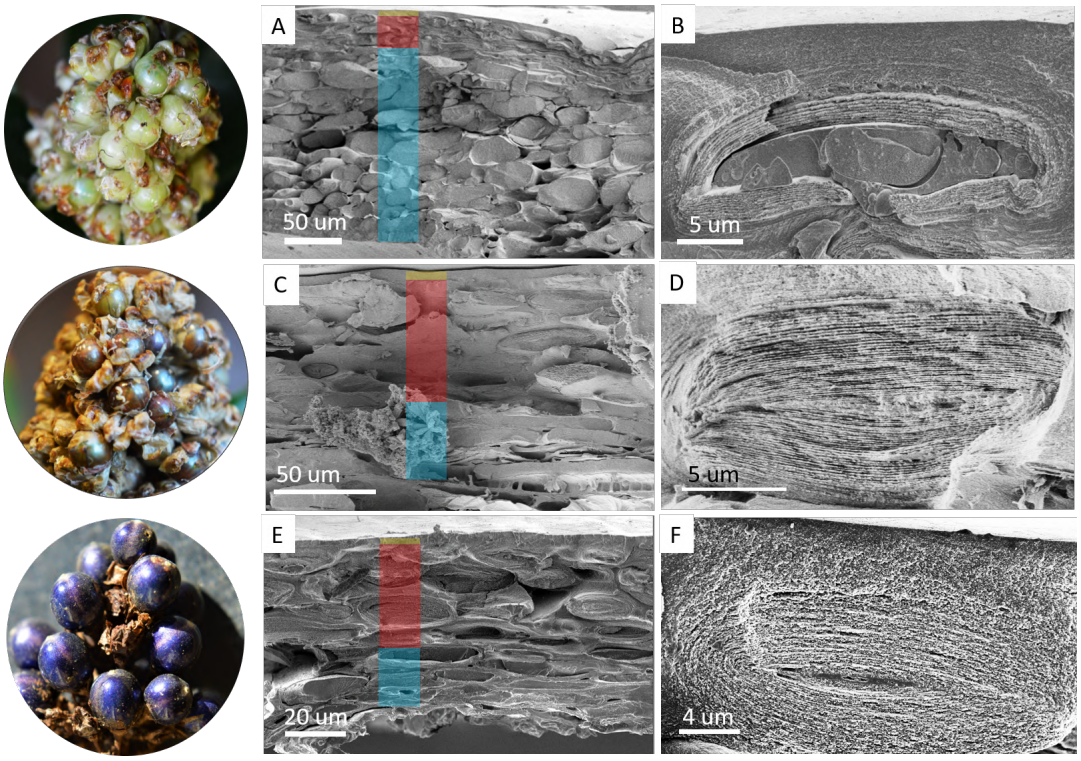

FIGURE 4.20: Electron microscope images corresponding to samples at three stages: the white/green earliest stage, top row, images A and B. The reddish-brown stage, middle row, images C and D. Mature blue stage, bottom row, images E and F. A-D were taken using cryo-SEM, E and F were taken on fully dried material using room-temperature SEM. Images A, C and E include bars indicating the relative proportional thickness of cuticle (yellow), structurally coloured cells (red), and pigmented or fleshy hydrated cells (blue).

The individual cells undergo a considerable change between the white/green stage in which a thickened cell wall is visible, but surrounding a significant volume of liquid cell contents. In the brown section, the cell volume is almost entirely composed of cell wall material. Very few differences are visible between the brown and blue cell examples.

4.6.4 Cell dimensions

Measurements on SEM images are presented in figure 4.21. A different area of the white/green fruit sample is shown in the image A, arrows indicate the two width dimensions - length in the horizontal plane parallel to the epicarp surface, and thickness measured in the vertical plane, or perpendicular to the epicarp surface.

Inspection of the white/green epicarp cross-section shows that the majority of the thickness across the tissue is composed of tiers of large volume cells in the central section. Measurement and comparison of the two immature phases of fruit growth bears this out in plot B of figure 4.21. In the white/green fruit, these fleshy middle

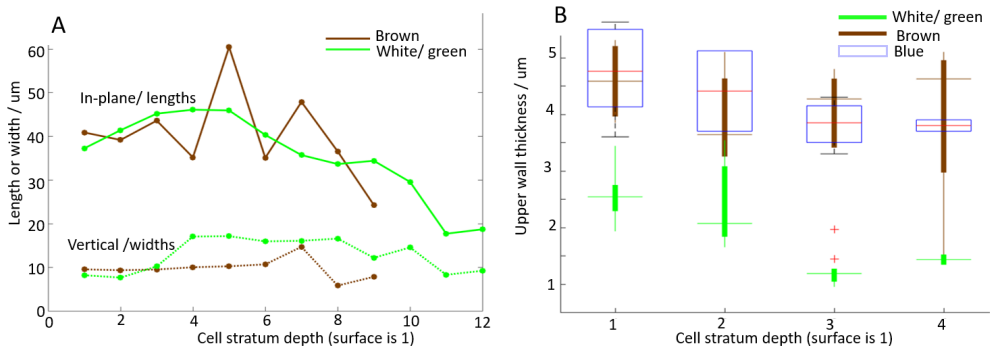

FIGURE 4.21: A. Average lengths and widths (dotted line) of cells from white/green and brown stages. The distances are plotted against cell depth in terms of layer number. B. Box plots representing the range and mean upper wall thicknesses for 28 early green cells, 26 brown cells and 14 blue cells.

cells have a larger average horizontal width and vertical thickness than cells at the top and bottom of the epicarp.

In the plot of cell dimensions of the brown phase fruit on plot B, it is seen that the fleshy middle cells lose their much thicker vertical dimension, which in the white/green phase is a clear transition in the fourth layer. The horizontal plane dimension remains on average the same, and fewer pitches of cells are measured.

The thicknesses of the structurally coloured walls were measured for a number of cells from the same set of data. A summary of the lengths measured for upper cell wall thickness are shown in box and whisker plots in C of figure 4.21. The average thickness of the walls measured in the early white/green phase was demonstrated to be significantly less than those of cells in the brown cell tissue. Measurement of the mature blue fruit's upper cell wall thicknesses are plotted alongside the other two averages and are seen to overlap significantly with the brown fruit cells.

Demonstration that the structurally coloured cells' reflective cell wall tissue is fully developed before the brown stage confirms the result observed using optical analysis in this chapter from which I concluded that structural colour development occurs during the green stage.

4.6.5 Variant Cell Shape

Entire cell shape has not been an important factor in modelling the cell wall architecture of this study. This is because of the limited central region of the cell wall which is the effective reflecting surface. However, optical and electron microscopy indicates that a range of cell shapes beyond simple ellipsoidal structures are present

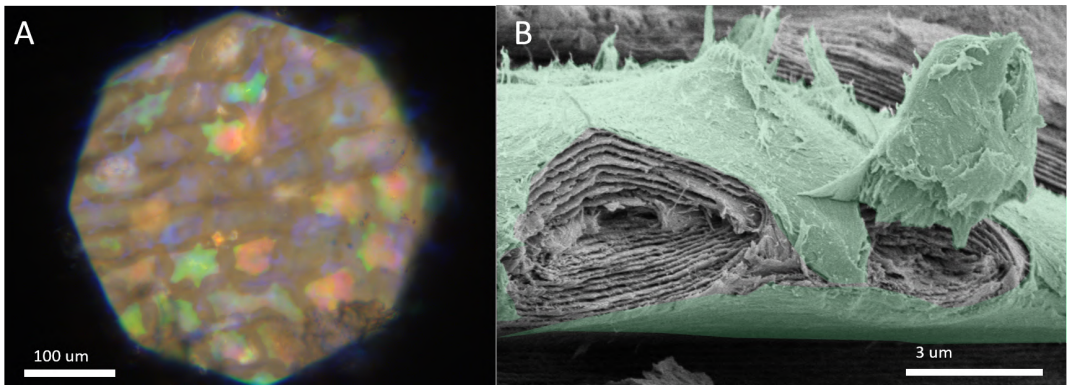

FIGURE 4.22: A. Microscope image with a large numerical aperture, showing the multilobed pavement cell reflection. B. False-colour cryo-SEM (brown stage) showing an exposed cell exterior with two broken lobes.

in *P. condensata* epicarp, some variations in the cell morphology is discussed briefly here.

Low numerical aperture means that only a small area on the upper cell wall is the effective reflecting region. However, use of a large numerical aperture for microscopy, as shown in figure 4.22 A, can be used to collect reflected light from the cell surface over a greater area. In this image the cells are shown to have multiple lobes from the central body. These cell shapes are common in plants and are called pavement cells. [183] The morphology is confirmed by electron microscopy. A false colour SEM image (B) of a broken cell at the fracture surface, shows where pavement cell lobes have been broken off. These fractures expose the ordered cell wall periodic pitch structure inside, parallel with the curved top surface of the cell and therefore not reflecting light in low numerical aperture microscopy.

The layering in the cell wall appears to be continuous between the body and the lobes from the SEM image. The increased angle of these layers to the normal of the surface means that light is not collected from them in low numerical aperture microscopy. The optical microscope image of pavement cells shows that in some cases the lobes reflect a different colour to the cell body. Potential reasons for this may be a change in the pitch length between the different areas of the cell wall, or the effect of the higher angle of incidence and reflection.

4.6.6 Macroscopic Blue Appearance

An issue that has been unaddressed in this chapter is the overall appearance of the *P. condensata* fruit. The subject of the development study has been the outer cells of the fruit which may be comprehensively characterised, and as demonstrated in chapter 2 both by microscope images and spectral survey, the species shows a wide range of different colours reflected from these cells. Although under strong light a

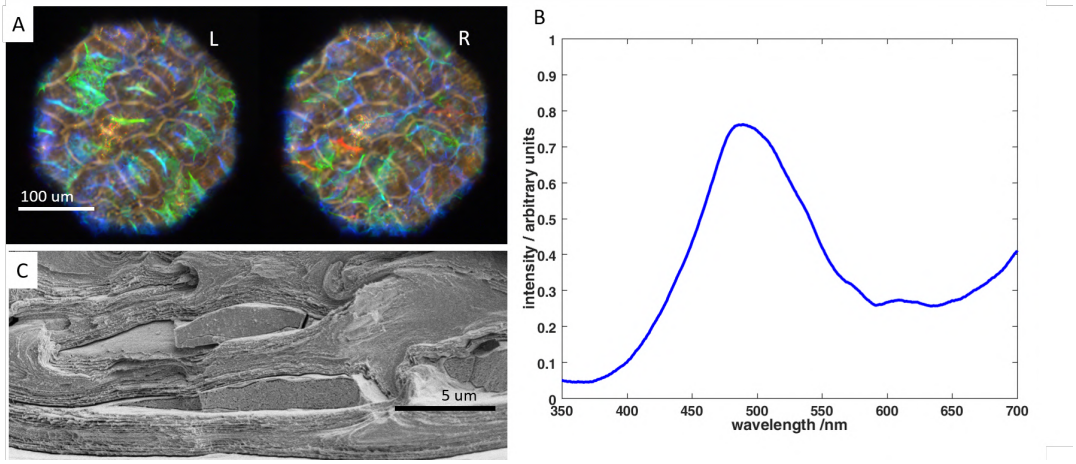

FIGURE 4.23: A. Microscope image of the same area in left and right circular polarisation showing a diffuse blue background reflection in both handednesses. Images of patterns in the blue reflection are slightly different. B. An averaged intensity plot of reflection over a large area of *P. condensata* cells. C. Cryo-SEM image (brown stage) of highly flattened and irregularly shaped cells found in the lower layers of structurally coloured cells.

rich depth of 'pointillist' and varied colours can be made out, the fruits appear to be predominantly blue-reflecting. An average spectrum taken over a large area of hundreds of cells is shown in figure 4.23, and is a broad blue peak.

In microscopic analysis, a significant amount of blue reflection is seen from below the top target layer of cells. Blue reflection is seen in both circular polarisations, as shown in figure 4.23 A, although the potential for multiple reflections and passing through birefringent material make it difficult to define the original reflecting structure.

4.6.7 Lower Layer Flattened Cells

There are many layers of cells in *P. condensata* fruit epicarp, as has been discussed. In addition to cells similar to those on the surface layer, highly flattened, wide area cells were also observed in electron microscopy, like those in figure 4.23 C. These make up a flattened and gap-filling material, and appear to be collapsed cells with thinner walls than the upper layers. Due to their depth, it is not demonstrated that these cells are reflective, but their cell walls appear similar to those in cells above.

In order to understand the overall appearance of the *P. condensata* epicarp analysis of the lower layers of cells, potentially including these flat shapes, should be considered.

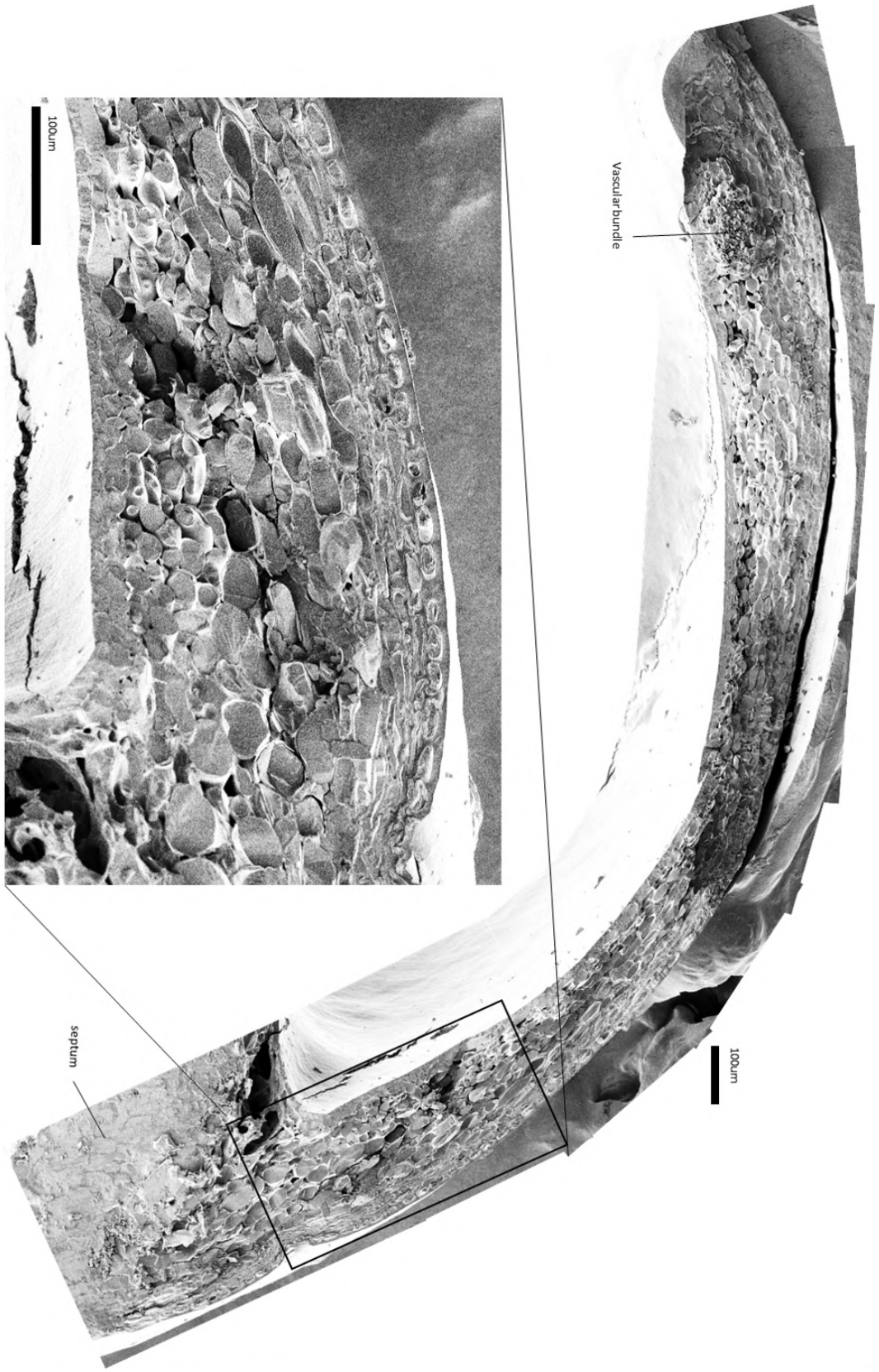

FIGURE 4.24: A large stitched image of the white/green sample imaged using cryo-SEM, showing over 1/6 of the total fruit cross-section, between a septum and midrib.

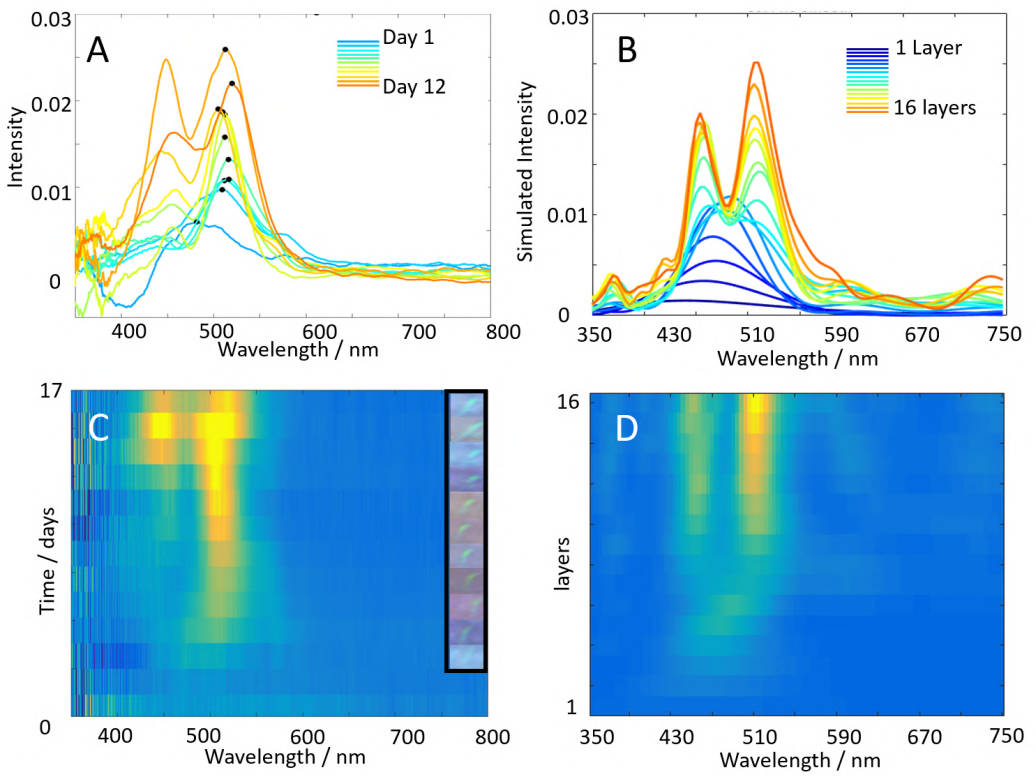

FIGURE 4.25: A. Experimental set of left-right polarisation profiles for one single cell over 12 days where a peak is identified and plotted. B. A numerical model demonstrating a similar shape and growth pattern, each plot represents an additional pitch from one to 16 repeats. C. Heatmap of the spectra in A with inset microscope images of the cell over the period. The pitch profile has a standard deviation of 40 nm. D. The profiles in B plotted as a heatmap.

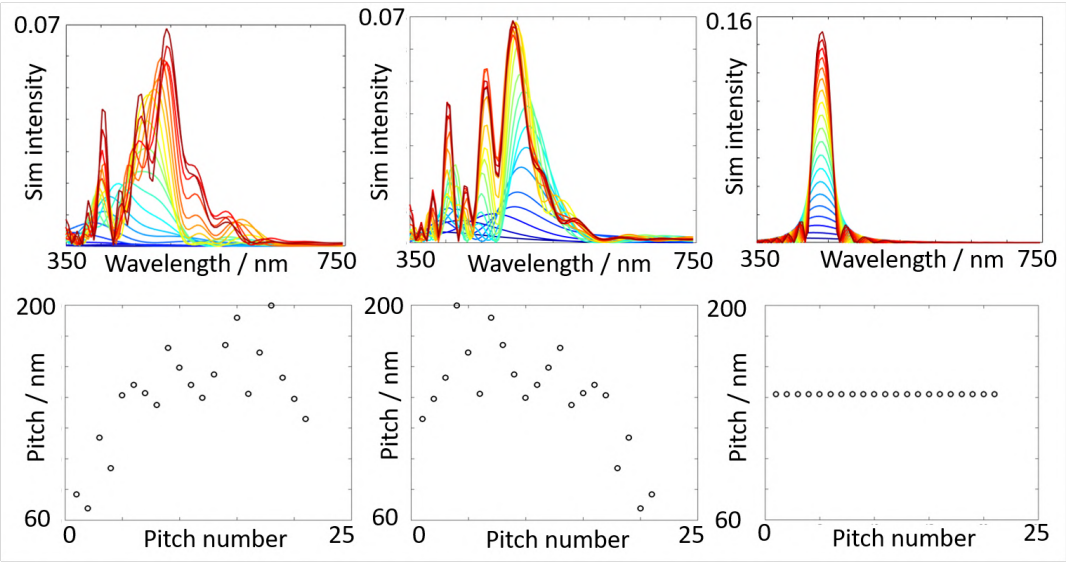

FIGURE 4.26: Above: the modelled optical profile of (left to right) a roughly chirped multilayer, the inverse of the same multilayer, and a uniform multilayer. Below: the pitch profile for each case from 1 the uppermost pitch, to 21, the lowest and last added pitch.

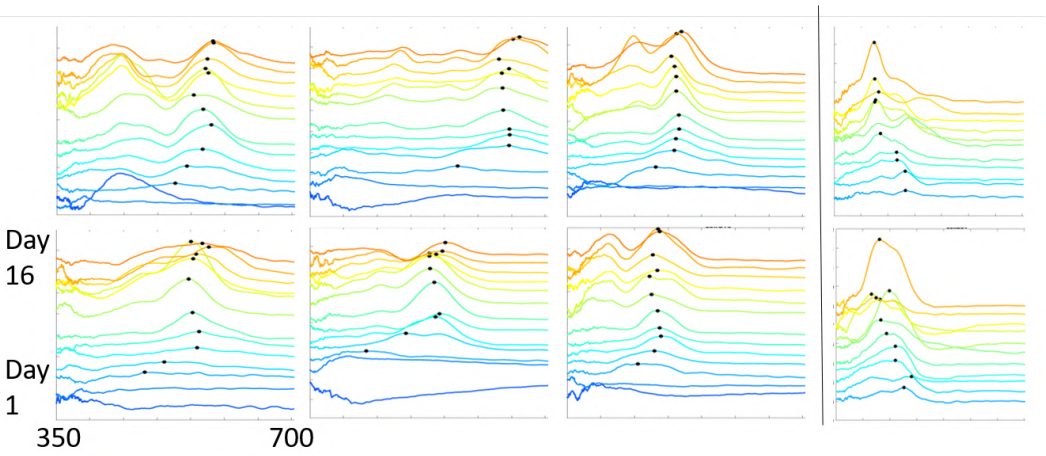

FIGURE 4.27: Offset intensity plots of each *P. condensata* cell from the groups which were measured at the earliest stages of growth and showed a wavelength change in the earliest stages of peak formation. Another six cells showed no peak wavelength change. Noticeable is a shift towards the longer wavelength peaks after the first couple of plotted profiles.

4.6.8 Spectral Response Modelling

The optical response was modelled numerically to show that the behaviour observed in cells growing in *P. condensata* can be predicted with a gradual addition helicoidal multilayer model. The fit was found by taking a range of randomly generated pitch profiles and matching the target peak. The optical response was then modelled for a pitch profile with each pitch added one by one. The result is shown in figure 4.25 A pitch profile was found with standard deviation of 36 nm and mean 159 nm over five similar profiles. A sixteen-pitch profile is shown in figure 4.25 plots B and D. Although a larger number of layers and cell wall pitches is observed in fully mature *P. condensata* cells, these measurements are taken from the earliest stages at which structural colour is visible. A lower number of pitches is therefore taken to be realistic.

Only one circular polarisation is considered, this is therefore comparable to the optical measurements which are referenced to one polarisation. A challenge in matching the modelling with the optical measurement is that the intensity of the numerical model is set at an arbitrary 20% of its modelled intensity. This was taken as a rough estimate of discrepancy between the average intensity of mature cells of both *P. japonica* and *P. condensata* and modelled intensities taken from TEM profiles of mature cells from both species. The decision is justified by the consideration that plant cell walls are far from an ideal system and this is a reasonably large proportion and matches the experimentally observed intensity. Considerations such as a difference in the birefringent refractive index for the real material were considered in chapter

1 and alone cannot account for the difference between measured and modelled intensity. Significantly for the analysis of immature cells, the numerical model may be considered to be approximately calibrated to the intensity of a mature cell. Given the approximation, the use of intensity alone is however not enough to justify identification of the exact number of pitches in the model profile matching experimental data.

This figure is compared with the average values for the upper cell wall width in figure 4.21. The average upper cell wall for external cells in the green stage are seen to be 2.5 um. Estimating the number of pitches in a cell wall this thick, either using the average measured profile by TEM of 165 nm, or the mean pitch in this numerical model of 159 nm, gives an estimate for the cell thickness of 15 to 16 pitch repeats. Whilst the sample from which these cells were measured was approximately the same age as the imaged sample, the cells have some variation, and there is no reason to assume that this cell is well characterised by the average. The coincidence in this case conveys a misleading level of accuracy. However, the number of pitch repeats in the model are clearly well within the margin of error for the range of possible pitch profile sizes.

The big peak wavelength transition for low numbers of layers in the early stages is used as additional evidence that the numerical model uses a pitch profile similar to the one responsible for the optical response in its key characteristics. Over the first few additional pitches of the modelled development, the peak wavelength undergoes a strong red shift. Pitch variation within a low number of pitch repeats dramatically changes the peak wavelength that is reflected. This is demonstrated in figure 4.26 where a redshift is seen both in the case of a transition from a series of short pitches to a series of long ones, and in the case where the initial pitches are shorter only within a random distribution. No change in peak wavelength is seen in reflection from a uniform pitch profile.

Similar strong redshifts were seen in the experimental observation of many of the early stage cells, which are shown in figure 4.27. As the effect was particularly prominent in the earliest and lowest intensity peaks, where the characteristics are most difficult to identify, and not as part of a linear trend with the changes observed in the rest of the cell development, these early changes were not included in the linear fits of the cells in the previous analysis.

In the model multilayer reflection, the change occurs only over the first five pitches, after which the peak wavelength stabilises or varies slowly with additional peaks. It may be that the effect can account for some of the early changes observed in the cells.

However, the similarity between the appearance of the two effects is circumstantial and although it suggests there might be a physical correspondence, more evidence

is required to confirm the link via measuring the cell wall anatomy and the optical response of the same cell wall.

It should be noted that the changes in the peak intensity and wavelength observed in the development of *P. condensata* cells fall within the range of observed behaviour of the model of the cell as a helicoidal multilayer building gradually each pitch consecutively from cellulose layers.

4.6.9 Conclusions

Conclusions about the transition in *P. condensata* follow naturally from those in *P. japonica* in which it was found that a significant degree of structural colour is reflected from cells in the earliest stages, long before the fruit appears to be coloured other than chlorophyll green. The pitches of the profiles were also found to have been laid down in permanent configuration from the earliest development.

Both of these conclusions are also drawn for the *P. condensata*. In this study I demonstrated the measurement of structural colour peaks of increasing intensity. In these cells a considerable continuous variation in the peak wavelength was measured. I have demonstrated that this is explained by variation in the pitch length within a single pitch profile, and therefore the cell growth is consistent with the explanation developed for the *P. japonica* cells.

I found no evidence of a consistent red or blue shift in cells that were either increasing or stable in intensity, and no difference between the left and right handed cells. The conclusion from chapter 2 that the right handed cells in *P. condensata* have a longer peak wavelength than left handed cells in the same fruit was reaffirmed, and found to be true from the earliest development.

Crucially, the extremely highly differentiated cell wall of *P. condensata* did not show a significant difference in its development from the *P. japonica* which presents a less extreme adaptation. Both were simulated using the same optical model, although the parameters were slightly different. The degree of difference in the measurement techniques, and the level of accuracy intended in the numerical model I believe makes quantitative comparison between the two parameters for the two different models inconclusive at this stage.

Like *P. japonica*, the *P. condensata* cells pass through stages of development of very different appearance, and yet the structural colour responsible for their final appearance starts to appear much earlier than it dominates the light reflected. Unlike *P. japonica*, the *P. condensata* cells are not hollow or filled with other material in their mature state. This means that the appearance of the final fruit retains the point-like 'pixelated' reflection that makes it appear shimmery, rather than the additional scattering cavity reflection that is observed in the *P. japonica*. The fruit epicarp, as

discussed in chapter 2 has many more layers of structurally coloured cells. The development period of the fruit observed both in the lab and by Dr Rebecca Karanja in the field was markedly longer than that of *P. japonica*.

Chapter 5

Structural Colour in the Genus *Viburnum*

5.1 Introduction

This chapter uses the same optical analysis techniques explored in detail in the previous chapters on *Pollia* to investigate an unusual non-pigmentary colouration mechanism in two species' fruits, *Viburnum tinus* and *Viburnum davidii*. Although related, the fruits produced by the plants have quite different colour appearance and mechanisms for structural colour production.

This chapter takes a significantly different approach to the analysis of structural colour. In the previous species, the material responsible for the colouration had already been confirmed, and analysis was undertaken to understand its development. For the species in this chapter, the study was concerned with analysing the optical response and identifying the structure and materials responsible for it. The optical response and morphological analysis of *V. tinus* are presented. Development of the fruits is then discussed in general terms, rather than taking the individual cell approach in the previous chapters. The optical response and the morphological characteristic of *V. tinus* are compared to other fruits in the genus, and particularly to *V. davidii*.

5.1.1 Experimental detail - Optical Microscopy

Viburnum tinus and *V. davidii* fruits were harvested at maturity from shrubs in Cambridge at Newnham and Pembroke College gardens, and transferred to the lab within ten minutes. The identities of the shrubs were confirmed by Dr Edwige Moyroud and Miranda Sinnott-Armstrong. Other species were picked in Cambridge University Botanic Gardens: *V. hupehense*, *V. lobophyllum*, *V. opulus* and *V. cylindricum*, Arnold Arboretum (Boston, USA): *V. rhytidophyllum* and East Rock Park (New Haven, CT USA): *V. acerifolium*. Thin cross-sections of the fruit, were cut using

a clean scalpel blade to peel the fleshy meso- and exocarp for microscopic analysis. To achieve very thin cross-sections, the fruit's epidermis was placed between two flat pieces of crosslinked silicone dental wax, tightly bound with an elastic band. Thin slices of the moulding rubber and pericarp were cut and the fruit slices transferred into filtered (milli Q Type 1) water on a glass microscope slide. The thin section was then trapped in water under a glass coverslip and examined in an optical microscope.

5.2 *Viburnum tinus*

5.2.1 Introduction

Viburnum tinus is an evergreen shrub native to southern Europe and widely planted in gardens [184] for its year-round flowering cycle, producing pink-white flowers and fruits even in the middle of winter, and unusual metallic-blue fruits [185]. These are single-seeded drupes consisting of a hard endocarp ('stone') with a very thin fleshy mesocarp (flesh) and smooth exocarp (skin). The fruits mature from immature creased narrow green shapes, through a 'shimmery' reddish colouration to a bright metallic blue, widening to oval ellipsoids about 0.5 cm wide. The fruits grow in clusters of 5 – 30 and after reaching maturity remain on the stem, retaining their metallic blue colouration with only minor dulling even into the next fruiting season unless picked off by frugivores. Known consumers include small birds like Robins and Blackcaps. [186]

Inspired by use of *V. tinus* extracts in traditional medicine previous studies have focused on chemical analysis including iridoids, [187] [188] and anthocyanins [189] and other constituents. [190] Some observation of an apparent structural colour cause in *V. tinus* was reported in 1985, [191] however a clear correlation between the morphological characteristics and the optical response which was not analysed, is not previously reported.

Most studies of pigments in *Viburnum tinus* have focused on the leaves [192] and wood [193] rather than the fruits, although a multi-species study on anthocyanins demonstrated the inclusion of a pigment common to other *Viburnum* species. However, the study does not correlate the pigments extracted from the fruit with its observed colour. In fact, the fruits of the other species with pigmented anthocyanins in common do not share the lustrous bright blue colour of *V. tinus* drupes. No previous study has demonstrated the pigments or other mechanism responsible for the striking colour of *V. tinus* drupes. This chapter intends to fill that gap, investigating an unusual non-pigmentary colouration mechanism demonstrating unexpected similarities between this and unrelated species.

FIGURE 5.1: Photo of *V. tinus* fruits on an ornamental garden shrub at Newnham College, Cambridge in November. The orientation of the photo is accurate, the fruit sprigs are often pointing upwards and sometimes shaded under leaves. Flowers and fruits are often visible simultaneously.

V. tinus fruits are unusual within and outside of their genus for their 'metallic' appearance (see photo in figure 5.1).

Such unusual metallic appearance is generally an indication of a structural component of the colour as the metallic appearance is due to directional reflection. This distinguishes it from the generally matte appearance of pigmented colouration in which light is scattered in every direction.

After being picked the fruits retain their metallic blue colouration for a couple of weeks if kept refrigerated and hydrated, although lose their colour and turn black and wrinkled over just a couple of days if allowed to dry out. Their blue appearance can be restored by submerging in water for a couple of hours. This reversible colour change may be repeated by redrying and rewetting several times, the limits of this were not explored as some pigment appears to leak out into the water after several reimmersions. Images of this phenomenon are shown in figure 5.2.

Reversible colour change is not definitively associated with structural colouration, as pigments can also produce colour change on rehydration. However, when hydration does affect structural colour, this may be because the structure deforms so that blue is no longer reflected when dry, and then swells after immersion in water to reflect again as before. In this hypothesis, the change indicates that the material from which the structure is made is hydrated, fluid or otherwise fragile and replaceable with water.

FIGURE 5.2: The left-hand image shows two *V. tinus* fruits which had been left to dehydrate at room temperature for 8 months. The image on the right shows the same two fruit 24 hours later after floating under the surface of tap water at room temperature. The water remained clear.

5.2.2 Optical and Electron Microscopy

Under a microscope, *V. tinus* cells have an unusual variegated and glittery or patchy appearance, with very small domains reflecting bright, discontinuous colours at a wide range of wavelengths, as seen in figure 5.3. Epidermal cells are also seen to have well defined edges with dark borders round every cell, similarly to the cells of *P. japonica*.

Cross-section

Cross-sections through the epidermal cell layers in optical and electron microscopy reveal the different areas of the cell contributing to the optical effect. A schema in figure 5.4 A indicates the observed components in the epidermal cells in each of the measured cross-sections. The outer cell wall of the epidermal cells is observed to be

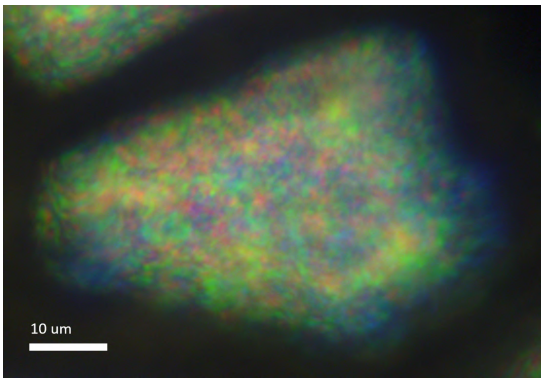

FIGURE 5.3: Water immersion optical microscope image of a *V. tinus* cell imaged from above without polarisation, showing bright and highly varied reflection.

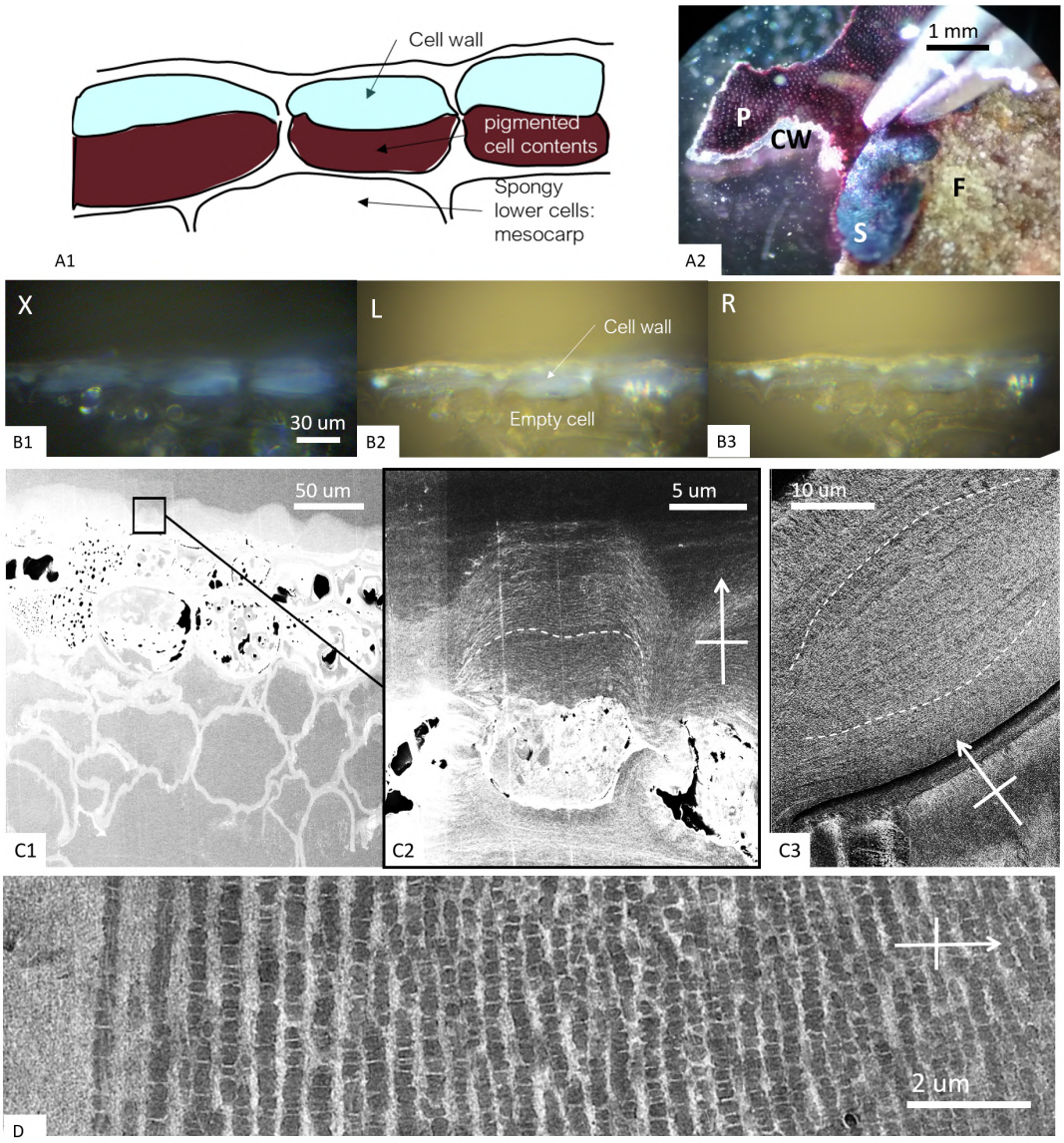

FIGURE 5.4: A1. Labelled schematic of the structurally coloured and pigmented cells, A2. A stereomicroscope image of tweezers holding in place two pieces of broken epidermal skin in water. S. is a scrap of the epidermis top surface seen as on the fruit. CW,P and F are layers of the epidermis viewed from underneath with different parts removed. CW shows only the upper epidermal cell walls without pigment. P is the dark pigmented cells and F is the deeper spongy yellow flesh cells. B1-3. Water immersion optical cross-section through the epidermal cell layer showing depigmented cells in B1: crossed polarisation, B2: Left circular polarisation B3: right circular polarisation. Parallel polarisation looks the same as left and right circular polarised images. C1-C2: Increasing magnification of SEM of microtomed cross-section through embedded *V. tinus* epidermis. C3: cryo-SEM of thickened cell wall cross-section. D: TEM through embedded cell wall showing globular inclusions arranged in layers and lower unstructured cell wall. Arrows where shown point to the outside of the fruit epidermis. White dashed lines in C2 and C3 are shown to indicate the layers

extremely thickened and adapted. The epidermal cell cavity is pigmented. There are seen to be a number of layers of pigmented cells below the epidermal layer, but there is no deeper structurally- reflecting material.

Optical and electron microscopy images of thin slices through the cross-section are presented in figure 5.4. The cells in the optical microscopy cross-section B1 - B3 have been cut open and the dark red pigment released and washed away in the water. The pigment contents are observed in other cross-sections, and during cutting is observed to leak from the cells. The thick blue-reflecting cell wall material remains visible in the optical cross-section and is therefore apparently solid. For this reason it is described as part of the cell wall. Given the observation above that the structural colour is dependent on hydration, it should be noted that the cross-section was kept immersed in water during this experiment.

The SEM cross-section images 5.4 C1, C2 and D, show an extended region of the epicarp fixed in resin which may be correlated with the cells in image A2 of the same figure. The large spongy cells in the SEM are the same as the yellowish large cells labelled F. In the same image, they are scratched off in one area to expose the pigmented cells labelled P, and the pigment of the cells has been drained to expose the thickened cell walls in area CW.

The electron microscope and optical microscope images both show that two thirds of the outer epidermal cells' volume is taken up by a strikingly thickened cell wall. The adapted cell wall, which is optically blue reflecting is visible in C3, a higher magnification cryo-SEM image which shows that the material has a nanostructure made up of quasi-uniform layers throughout the thickened region.

Image D in figure 5.4 shows the globular vesicles or layers in high resolution TEM cross-section. An observation made about the structures during many iterations of EM imaging by Dr Paula Rudall, Miranda Sinnott-Armstrong and Dr Yu Ogawa, was that under some fixing and staining conditions, the inclusions appeared as empty cavities in the matrix, filled with embedding resin. An explanation for this is that under the wrong buffer and fixation conditions, solubilisation and diffusion of the original material which fills the layered inclusions in mature fruit occurs, leaving the layers of inclusions apparently vacant. Immidazole buffer and staining with osmium tetroxide (OsO4) was shown to fix the material making up layers containing inclusions properly. In the image this successful technique is shown and the staining shows high electron absorption, and the inclusions are therefore dark in the image.

Polarised Optical Response

Polarisation filters were used to understand the polarisation characteristics of the fruit's epicarp and therefore the origin of the colour. Images taken with different

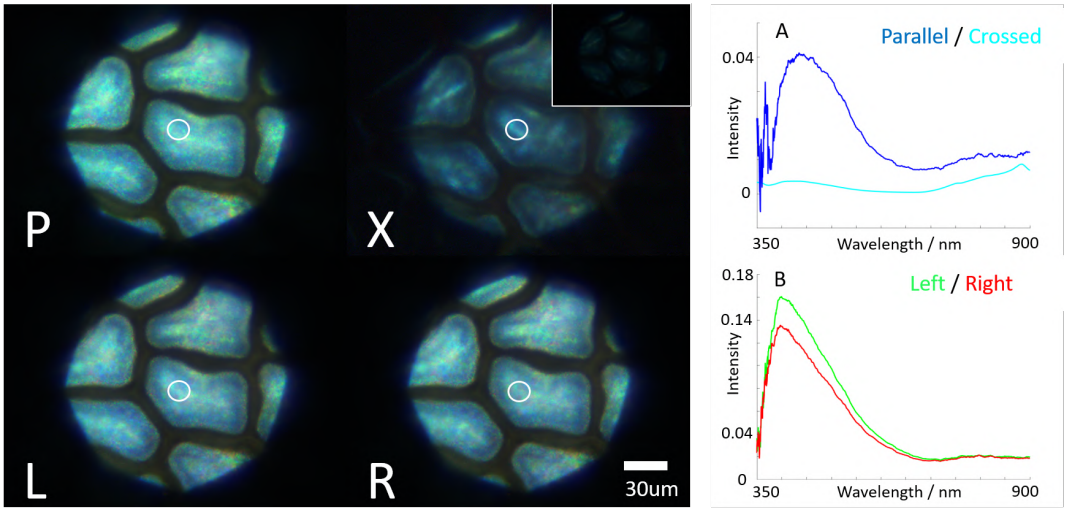

FIGURE 5.5: The four microscope images show the same group of upper epidermal cells imaged in water immersion by simply placing the unbroken fruit under the microscope. The letters on each image refer to the polarisation filter applied before imaging. L,R, and P are left and right circular and parallel polarisers respectively, and X is from crossed polarisers with an increased exposure time. The true relative intensity of the X image to the others is shown by the inset. The spectra on the right show a comparison of the light intensity for each polarisation with the same exposure time. The intensity is given relative to the total incident light. The parallel polarised reflected intensity is demonstrated to be much greater than the crossed polarisation. A small discrepancy between left and right circular polarised signals is also evident. All spectra are taken from the same location, indicated by the white circle.

polarisation are presented in 5.5.

Spectra in graph B show that there is only a very small difference in the intensity. This difference is characteristic and found at many positions on the fruit, although without a systematic bias to the right or the left circular polarisation. However, the existence of even a small difference between the two circular polarisations is not usually observed in ordinary pigmented materials. No difference in L/R is measured when a very small collection spot (close to the domain size of a coloured patch) is used and focused on the variegated parallel-polarised colouration in high magnification.

The light reflected in the crossed linear polarisation imaging is much less intense, the photograph inset in the X image in figure 5.5 shows an image taken with the same integration time as the image taken with parallel polarisers. The relative intensity can also be examined in plot A. The light that is reflected in crossed polarisers is very distinct from the parallel polarised light. It is a diffuse blue reflection with cell-scale structures like lines and bands that don't align with features seen in parallel polarisation. It is likely that this light is reflected also in the parallel polarisation but is not visible due to its low intensity compared with the polarisation-retained reflection.

Looking at the optical response in cross-section from figure 5.4 B1-B3, a blue reflection is observed from the thick outer epidermal cell-wall. The reflection is unusual because it cannot be focused straightforwardly to identify a blue surface. The colour coming from the cross-section of the thickened cell wall in the epidermal cell layer is also not uniform through the cell wall region. It is reflected in all polarisations without a distinctive difference. The blue light reflected orthogonally is therefore seen to be unpolarised, weak and not angularly-dependent. It is dominant in cross-section due to the lack of bright reflection observed form the surface in parallel and left and right circular polarisations.

5.2.3 Interpretation

Polarisation-retained Reflection - Parallel Polarisers

The fact that the outer epidermal cells have a glittery appearance only when observed with parallel linear polarisation filters indicates either a thin-film-interference-like or a multilayer-like reflection.

Thin film interference can be an evolutionary adaptation to reflect coloured light, as in some butterflies like the Buckeye, [194] however it generally reflects a less bright colour than multilayer mechanisms. Identification of thin-film vs multilayer effects are sometimes evident, as thin-film interference can have a characteristic 'oil-slick' appearance, and some multilayer reflection is much brighter than can be achieved

from thin film interference. Some of these differences were discussed in section 1.1.3. However, that is not always the case, and both effects may be observed in the same material. Colouration in either case is dependent on the characteristic lengthscale of the material. Therefore the diverse range of colours reflected in patchy coloured parallel polarisation indicates the presence of domains of varying characteristic lengthscale.

The electron microscope images show a very thick multilayer present in the adapted cell wall. The layers on the TEM are approximately 160-200 nm thick, which, assuming typical biological material refractive indices of anywhere between 1.45 [195] - 1.6 [196], increases our confidence in the optical multilayer hypothesis. Applying Bragg's law, the optical wavelength reflected would be around 460 - 720 nm, which is in agreement with the colouration observed in the optical image.

In order to understand whether the material composition is consistent with the model, the components of the multilayer and their refractive indices were assessed by Dr Yu Ogawa and Miranda Sinnott-Armstrong. The staining of the sample in the TEM with OsO4, indicates that it is likely the dark areas of the image are made of lipids or a similar molecule. *Viburnum tinus* fruits are known to have a high lipid content and the possibility that these lipids are stored in the epidermal skin and related directly to the fruit's appearance is of significant interest, as it would link the iridescent visual marker directly with the fruit's nutritional value. This research is ongoing.

The matrix material is apparently the same as the cell wall, with which it appears continuous under all electron microscopy. The cell wall has features common to other cell walls and the matrix is therefore assumed to be similar to non-structurally coloured plant cell walls. Additionally, in contrast to simple Bragg stack systems, a large amount of disorder is observed in the unusual globular structure constituting what we define layers (as seen in 5.4 C1 - D). In order to analyse the impact of such disorder on the reflection finite-element analysis via numerical modelling would also be required.

Circular Polarised Reflection

The almost complete suppression of the reflection in the crossed-polarisers case demonstrates that the variegated colour reflection is not due to a helicoidal structures as in the *Pollia* cells described in earlier chapters. However, the spectra shown in figure 5.5 demonstrates a slight discrepancy between left and right handed circularly polarised light depending on the cell and location observed. There was no clear pattern of disparity favouring one handedness over the other, or regarding the intensity of the difference in the reflected intensities. However, this difference is significant and not ordinarily found in simple pigmented materials, in which it is generally

straightforward to demonstrate identical left and right handed circular polarisation reflection intensities. This circular birefringence of the outer epidermal layer is supported by evidence of some helicoidal structure in the TEM cross-sectional images. However, it does not appear to play an important role in generation or modification of the fruit's colour.

Cross-polarisation Reflection

Although the majority of the light reflected from the top surface of the fruit cells is suppressed by the use of crossed polarisers, there remains a low-intensity signal, which is not attributed to experimental error. Instead of the bright 'glittery' look of the polarisation-retained image, the cross-polarisation image includes a 'blue glow' with larger-scale structures apparent in the reflection that do not seem to correspond to the cell shape or the dominant structures in the polarisation-retained light.

Signal observed in the cross-polarised configuration can indicate either a structural or pigmentary scattering mechanism, or a structurally coloured chiral reflection. The fact that the reflection is inhomogeneous indicates that the phenomenon is localised. This could be by organelles which restrict a reflecting or absorbing pigment, or scattering material in specific locations within the cell. Another possibility is that if the reflection relies on reflection by a planar material, this is not aligned with the surface of the cell and therefore normal to the optical axis, except in the reflecting areas.

The optical reflection from the cross-section is surprising. It does not look like the specular-type reflection that was dominant when the cell is viewed from above in parallel polarisers. The colour looks like it arises from structural scattering because it is robust to cutting the cell when the rest of the pigment is washed away, and because no pigmented organelle or planar location in the cell is seen to be responsible for the diffuse reflection. This would suggest that the effect is the result of a structure within the cell wall itself. The blue reflection occurs from the material where the layers of inclusions are observed.

Disorder

The TEM cross-section of the fruits, their pixelated appearance and the different polarisation behaviour contributions to the optical response, which are inhomogeneous within the same cell, indicate that it is important to consider the role of disorder in the structure.

Total disorder in nanostructured material causes multiple scattering at all wavelengths and is responsible for producing very highly reflecting white materials, both in nature and artificial structures. [197] Depending on the size of the particles, these

disordered scatterers can increase the proportion of blue reflected wavelengths due to single scattering phenomena. [198]

A slight increase in disorder in very highly ordered structures produces a 'quasi-order' in which some aspects of structurally coloured reflection may be preserved in addition to characteristics of disordered scattering. Angular independence is frequently enhanced by quasi-order dominating over perfect order. This allows for a non-iridescent structural colour, as seen in some bird feathers [199] [200] and mammalian skin. [46] In many cases of isotropically reflecting structural colour, it has been proposed that the colouration arises from constructive interference of light in a photonic crystal that has a photonic characteristic length scale but is isotropic over a larger scale of the material. [201] Disorder is also responsible for the higher angular independence, and predominance of blue colouration responsible for the blue halo on petals discussed briefly in chapter 2. [67]

Whilst extremely highly ordered structures are seen in nature, such as the uniformity of layers in some beetle elytra, [166], there are also numerous examples of natural quasi-order responsible for enhanced characteristics in structural colour. It has been demonstrated that disorder can be responsible for the optical appearance of tissues with low angular dependency, [202] and limited wavelength range reflected. [203]

It is proposed that as well as the ordered planar reflection responsible for part of the colouration in *V. tinus* fruits, a secondary effect occurs due to deviation in the structure from perfect order. This effect, as seen in other occurrences of the same phenomenon is predominantly blue.

The characteristic length scales in the material fall within the lengthscales associated with the Mie scattering regime [204], which has been suggested as responsible for disordered blue colouration. However, Mie scattering theory applies directly to spherical particles, and it is not clear that the layered inclusions seen in this instance can be perfectly described. In order to confirm that Mie scattering, or on the other hand isotropic constructive interference as the cause of the blue colouration in this fruit, better measurements of the globular inclusions' 3D shape is required.

These disorder hypotheses should be further examined to understand whether it is an important contribution. Further work should concentrate on the optical simulation of the structure and material involved. In order to do this, the composition and refractive indices of the inclusions and the matrix should also be precisely identified. This work is a subject of ongoing inquiry in collaboration with Dr Yu Ogawa and Miranda Sinnott-Armstrong, in order to define the material composition of the different materials that make up the adapted cell wall.

5.2.4 Conclusion

This analysis suggests that the majority of the reflection from the *Viburnum tinus* cells is from a lipid-like/cellulose Bragg-type multilayer, where the lipid component is assumed to have a refractive index around 1.48 which is characteristic of lipids. [205] The multilayer also appears to have a third dimension or structure, reflecting diffuse and scattered polarisation light in the plane of the multilayer, as seen in the optical cross-section. This does not appear to be due to pigments, but disorder in the globular multilayer itself. In order to confirm this, further work is required to identify the lipid component, and to model the globular layers in order to demonstrate that the identified lengthscales can be used to predict the measured spectra.

This work used optical analysis to demonstrate structural colour, which is confirmed by electron microscopy revealing a refractive index contrast and a periodic structure on the scale of a Bragg multilayer. However, the exact mechanism for the reflection of the light remains unidentified and is the subject of ongoing investigation.

5.2.5 The Role of Pigment

Further investigation of the interaction of pigment and structure was made by partially removing the pigment.

The epicarp was cut using a razor blade in an oblique cross-section and viewed in reflection and transmission. On cutting, the lower part of the epicarp cells containing pigment partially or completely released it when the walls were broken by the cut, as observed during the preparation of the 'empty' cross-section in figure 5.4 B1-B3. This is particularly clear in figure 5.6 A and B, in which the outer cells of the cut have been emptied whilst the inner cells which were not cut remain pigmented. Figure A is imaged in reflection and transmission light simultaneously and the central pigmented cells are shown to be reflective and opaque due to the absorbing pigment.

The optical effect of the pigment on the cells in reflection is demonstrated in Figure 5.6. Spectra reflected from neighbouring pigmented and unpigmented cells were recorded, the spectra, averages and average difference between filled and unfilled cells plotted. The difference line therefore represents the 'visually effective' reflection (above 0) and absorption (below 0) of the pigment. The pigment is shown to absorb light between 380 and 650 nm, increasing the proportion of blue light in the reflected total. This 'contrast' effect is responsible for the increased blue appearance of the pigmented cells. The spread of error due to measuring different locations for the pigmented and unpigmented cells indicates that the pigment is not implicated in reflecting at the blue peak.

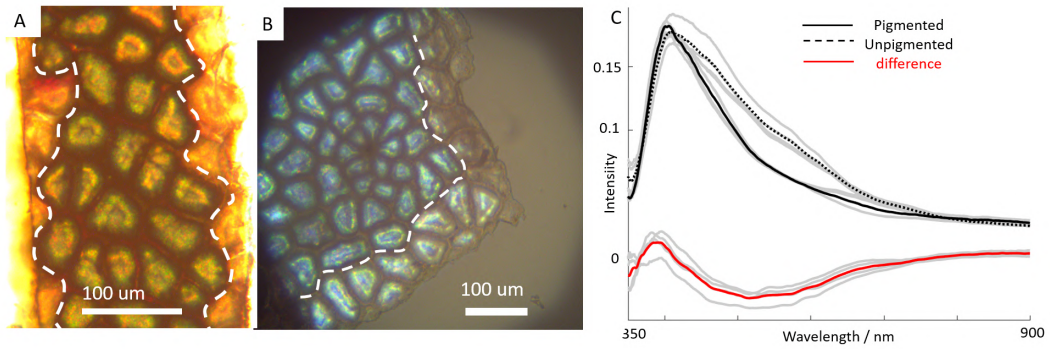

FIGURE 5.6: A and B were taken in water immersion optical microscopy using a 40x objective lens. Both show sections of *V. tinus* epidermal tissue imaged from above. The tissue edge cells have been broken and the pigment contents emptied, the boundary between the pigmented and unpigmented areas are shown with dashed white lines. A is illuminated simultaneously in transmission and reflection. The pigmented cells block the transmitted light, and therefore make the reflected light more pronounced. In B the brighter blue colour is seen reflected from the pigmented cells. In fact, both pigmented and unpigmented cells reflect the blue light, but the pigment absorbs other wavelengths making the blue more evident. Spectra taken from adjacent pigmented and unpigmented cells are shown in plot C.

The pigment absorption above 380 nm is its important visual contribution. However, the visually effective absorption does not necessarily give the pigment's actual absorption spectrum. The high degree of reflection in the blue peak occurs from the layered tissue located above the pigmented area, and may itself mask the absorption profile of the underlying pigment.

5.2.6 Development in *V. tinus*

A development study like the *Pollia* studies previously described was impractical because the plant specimens we have access to are large outdoor shrubs. However, the plants are widespread in Cambridge (UK), and the fruits regular and abundant, making a destructive technique suitable.

The fruits were observed by eye on the plant during their maturation and seen to transition from a small green stage through a red-brown to the final mature blue metallic stage. Fruits were picked representing different points on the maturation spectrum. Images of fruits in these different stages are shown in figure 5.7 along with microscope images showing the parallel and crossed-polariser filtered appearances.

The cross-polarisation image is dominated by the pigment contribution until the final stage, passing from very bright green and red reflection to a mature state with

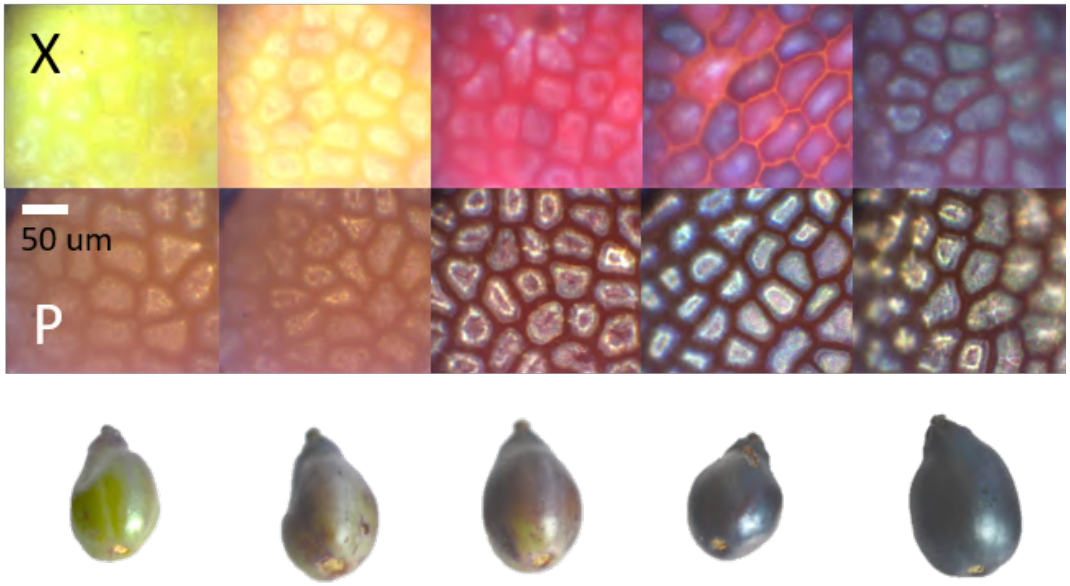

FIGURE 5.7: Images of the development stages with increasing maturity left to right shown in water immersion microscopy from crossed polarisers (top row X), parallel polarisers (middle row P) and a photo of the whole fruit. Images were not taken of the same area in each pair. However cells were characteristic of the fruit.

a dark background and bluish foreground reflection. The parallel-polarised images show that the bright variegated polarisation-retaining structures are also visible from early in the fruit development. Again the background pigmentation of the cells appears to get darker while the foreground colouration gets brighter.

Interpretation of the optical images of the *Viburnum tinus* indicates that the structurally coloured component of the cell wall develops starting from the green phase, significantly before the fruit is visibly blue. Earlier in the development process during the green and red phases, a 'sheen' is visible which appears to be the macroscopic effect of the latent structural colour. However, the non-absorbed light reflected from the pigment in the cells makes it non-dominant.

Fruits at the different stages, green, red and blue were embedded in resin and microtome cross-sectioned and imaged for TEM. Micrographs of the three sections are shown in figure 5.8. The electron microscope images confirm what the optical microscopy indicates, that the structurally coloured layer, identified as the thickened cell wall section at the top of the outer epidermal cells, is developed early on.

Measuring the thickness of these three specimens shows that the cell walls of the green, red and blue stages are 14 um, 19 um and 18.5 um respectively, providing a good indication that at least the majority of the structurally coloured material is developed by the green stage. Moreover, the material composition and nanostructure visible on the TEM do not appear to differ in the three cases.

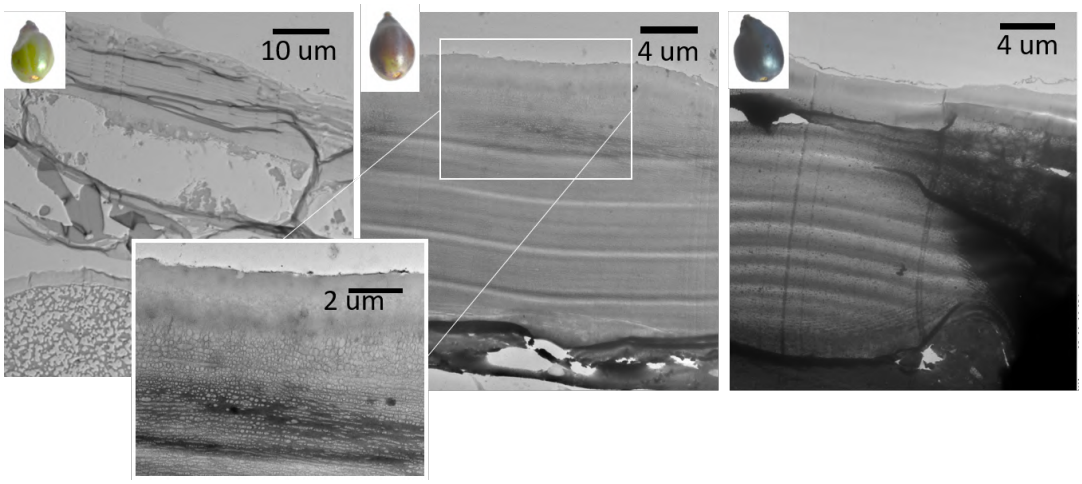

FIGURE 5.8: TEM images taken by Dr Paula Rudall of microtomed sections of resin-embedded *V. tinus* fruits at different maturation stages indicated by the fruit photo. There is some tearing and slight folding in each image, for example the smooth widely spaced lines across the red and blue stages. However, the early development of a thick cell wall in the green stage is distinguishable.

5.3 Other *Viburnum* Species

In collaboration with Miranda Sinnott-Armstrong, (Donoghue lab, Yale), a number of different species from the very extensive and varied *Viburnum* genus were observed. Parallel and crossed polarisation images of each of the fruits are compared in figure 5.9 for six species. The fruits on the right hand side of the figure show no evidence of structural colour analogous to that in *V. tinus*. This analysis was made using reasoning outlined in 5.2.3. However, the *V. dentatum* shows a very slight amount of 'blue haze' reflection, and *V. davidii* showed a much more enhanced colouration. This optical measurement indicates a significant role for structural colouration in the fruit, and the species was therefore further investigated for indications of a primary role for structural colour.

Figure 5.9 also shows a very small amount of blue reflection in crossed polarisation from *V. cylindricum*, this was not widespread on the fruit's surface although was observable by surveying a larger area. Even on optimising collection of this signal, the blue peak was negligible in the spectrum, and appeared to arise from a thin film interference on some cells. Additional species which showed no evidence of structural colour but were investigated in detail were *V. opulus*, *V. acerifolium*, *V. rhytidophyllum*. These results are not included in this report because of their lack of interest with regards to structural colour. They all appeared red or black and had no colour apparent in parallel or crossed polarisation beyond the pigment and cuticle reflection as in the fruits in the right hand column of figure 5.9.

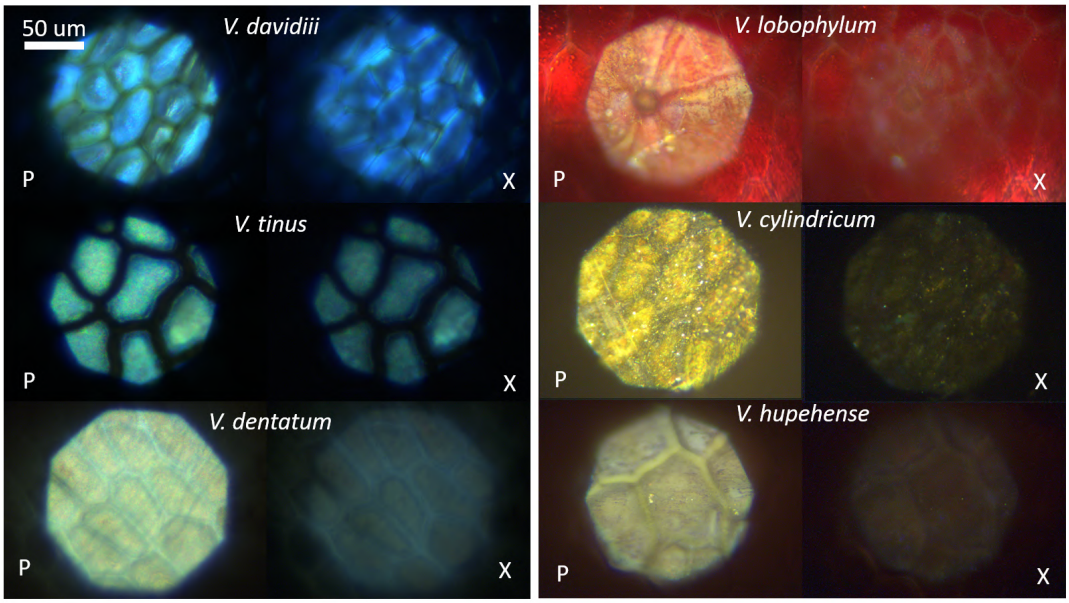

FIGURE 5.9: Left, top to bottom: *V. davidii*, *V. tinus*, *V. dentatum*. Right: *V. lobophyllum* , *V. cylindricum*, *V. hupehense*. Each fruit is imaged in parallel (P) and crossed (X) polarisation. Fruits other than *V. tinus* and *V. davidii* were collected and all fruits identified by Miranda Sinnott-Armstrong

5.4 *Viburnum davidii*

V. davidii is a closely related species to *V. tinus*, it is an evergreen shrub which grows best without prolonged exposure to high intensity sunlight. It is dioecious – having separate male and female plants, which must cross-pollinate for the female plant to bear fruit. [206] *V. davidii* fruit appears a brighter blue and less 'metallic' than *V. tinus*. This close relation, its differentiation and even stronger blue colouration make an interrogation of this species informed by our understanding of *V. tinus* a productive study. The fruits' appearance is an unusually vivid blue, they do not release a blue pigment when cut. The species is a popular ornamental garden plant. Samples for this study were taken from Pembroke College gardens and a private garden in Cambridge and are photographed in figure 5.10.

Optical microscope images of *V. davidii* show that its cells have a different appearance depending on measurement in parallel or cross-polarised configuration. The cells also have numerical-aperture dependent reflection streaks visible from the top of the cell - see figure 5.11 . The numerical aperture dependent reflection spots suggest a structural effect and a curved multilayer interface responsible for the reflection.

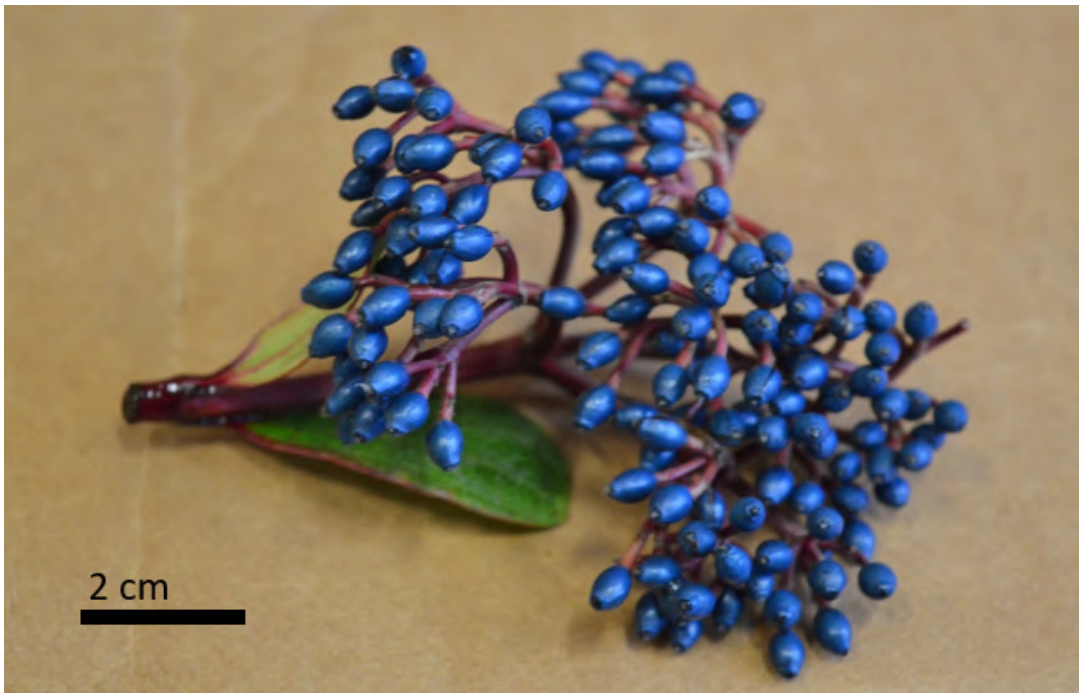

FIGURE 5.10: *V. davidii* is a popular ornamental garden plant, this was picked from a garden in Cambridge, UK.

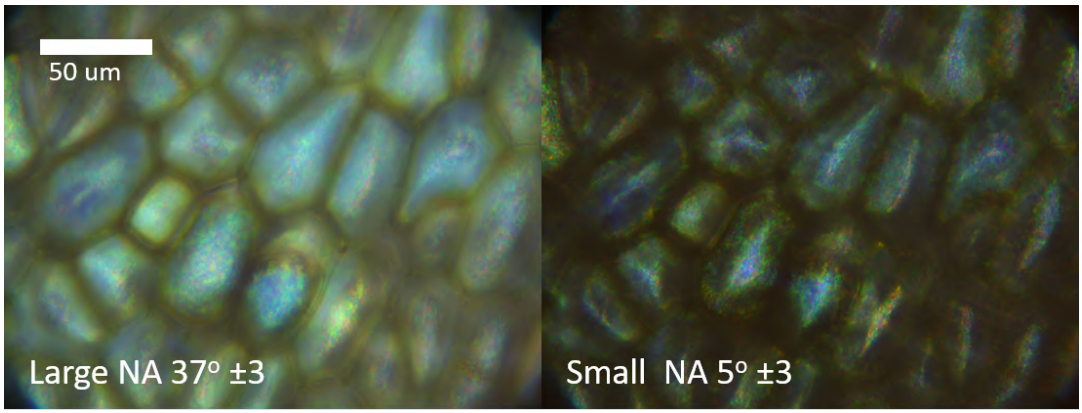

FIGURE 5.11: *V. davidii* has more prominently and uniformly curved cells than *V. tinus*. This curvature means that light is only reflected from a central area in the middle of the cell, whose width depends on the numerical aperture (NA). This feature is shared with *P. condensata* as shown and explained in figure 1.10. Numerical aperture-dependent localisation of reflection is a signifier of a likely structural origin of the colour.

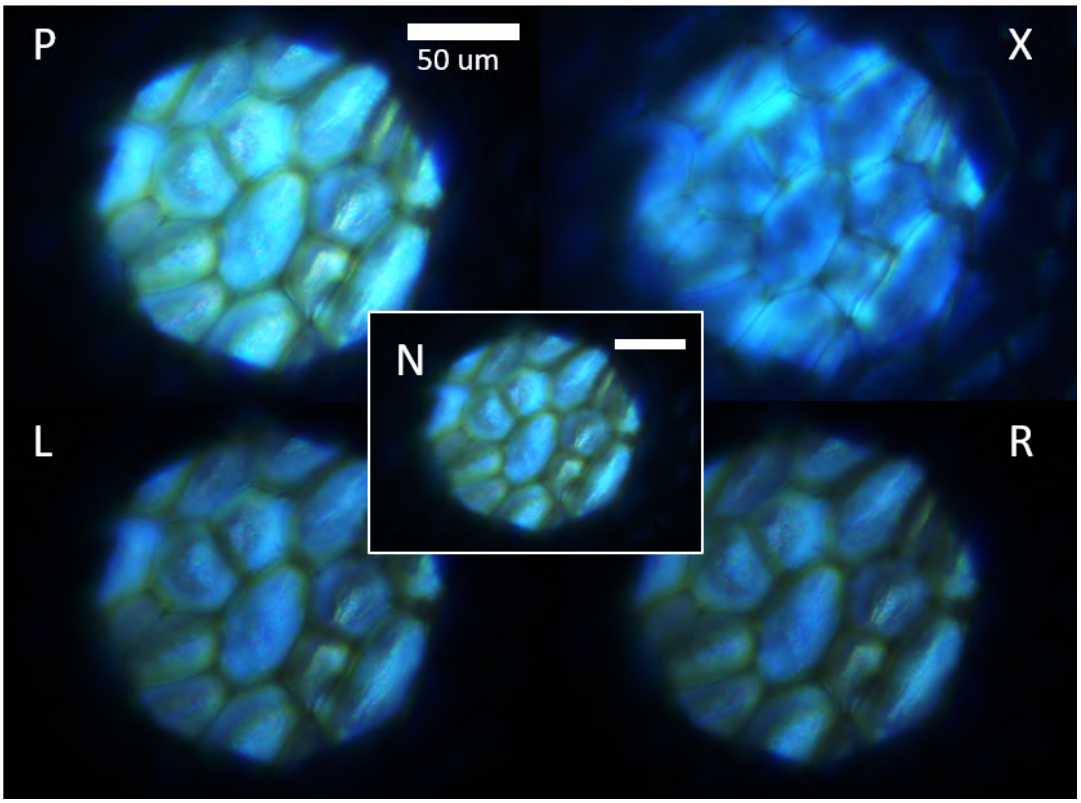

FIGURE 5.12: *V. davidii* imaged under different polarisations: parallel polarisers (P), crossed polarisers (X), left (L) and right (R) circular polarisation and no polarisation filter (N).

5.4.1 Cross-section

The outer epidermal cells of *V. davidii* shares similarities with *V. tinus*. A bright multicoloured reflection is visible in parallel-polarisation and not cross-polarisation - see 5.12. A thickened cell wall is also seen in the top section of the outer cells when cut in cross-section for water immersion optical microscopy - see 5.13. In this preparation technique, any water soluble pigment within the dissected cells is dispersed into the microscopy medium as for *V. tinus*. The very highly thickened upper cell wall layer is seen to be retained and to reflect brightly orthogonal as well as parallel to the surface normal as shown in figure 5.12 and 5.13.

Polarised spectral profiles are shown for pigmented and pigment-drained cells of *V. davidii* and compared to the same measurements on cells of *V. tinus* in figure 5.14. From these plots, the cross-polarised reflection is seen to be brighter in *V. davidii*, and the parallel-polarised less bright. The intensity of light reflected in the different measured polarisations is therefore closer in *V. davidii*. The left and right circular polarisations again show a slight difference but not systematically biased to one handedness. The effect of pigment appears similar in *V. davidii* to that described previously. Spectral peaks taken without pigment are broader, showing increased reflection at longer wavelengths.

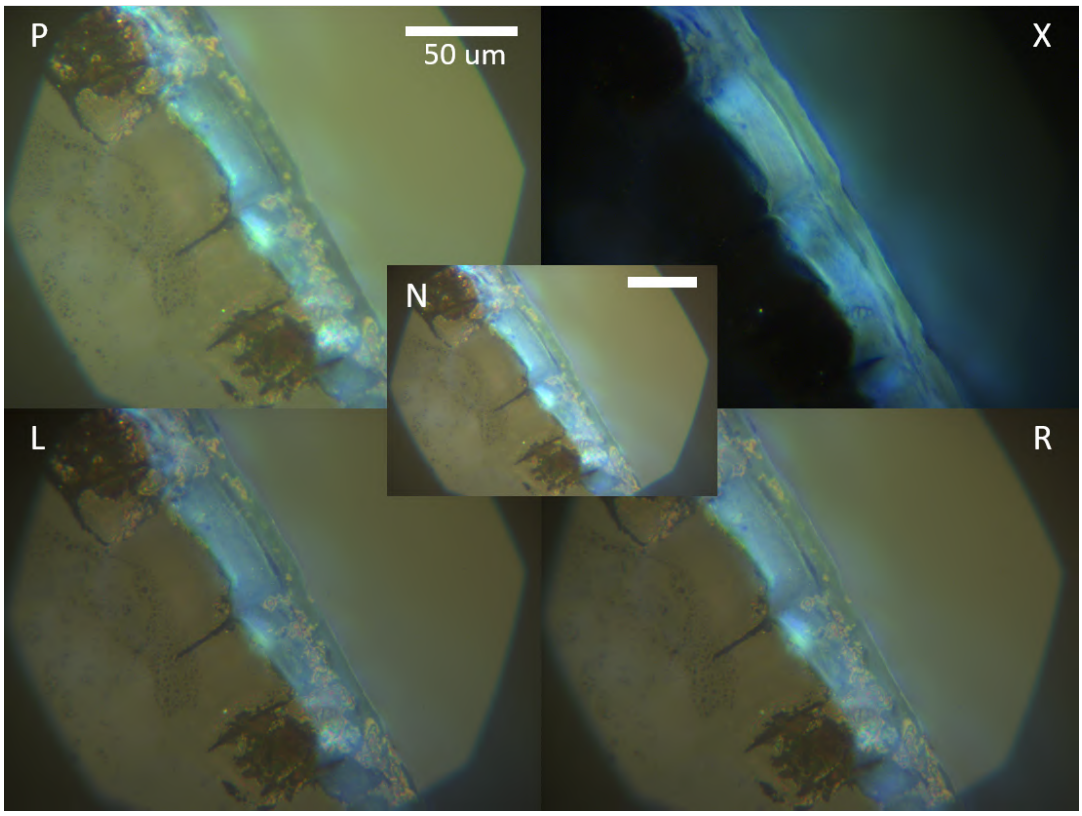

FIGURE 5.13: The water-immersed optical cross-section of the *V. davidii* shows a diffuse blue reflection from the thickened outer cell wall similar to the same observation in *V. tinus*. There appears to be no effect on the intensity in any polarisation (P-parallel, X - crossed, L-left, R- right, N - no filter).

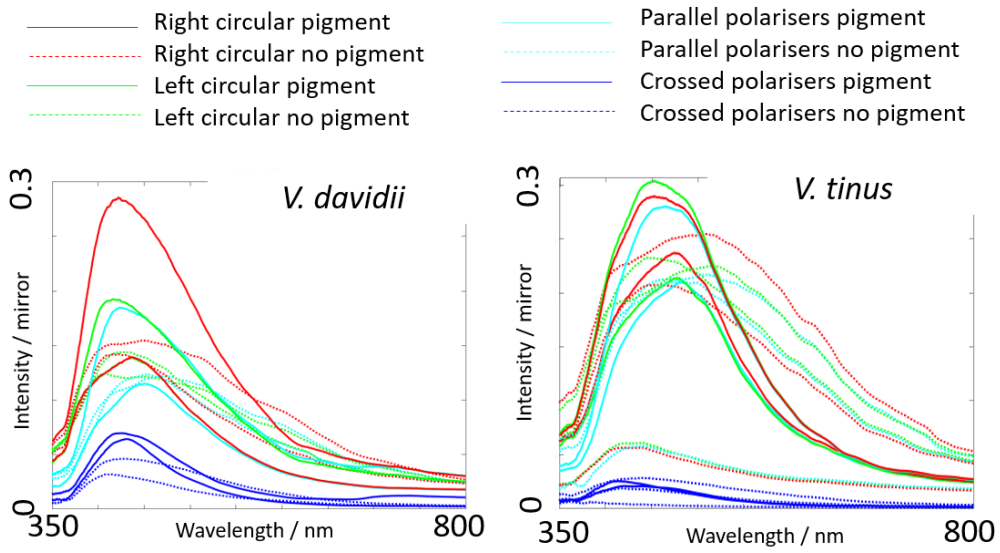

FIGURE 5.14: Plots of spectra measured from *V. davidii* and *V. davidii* with different polarisation filters for pigmented and pigment-drained cells.

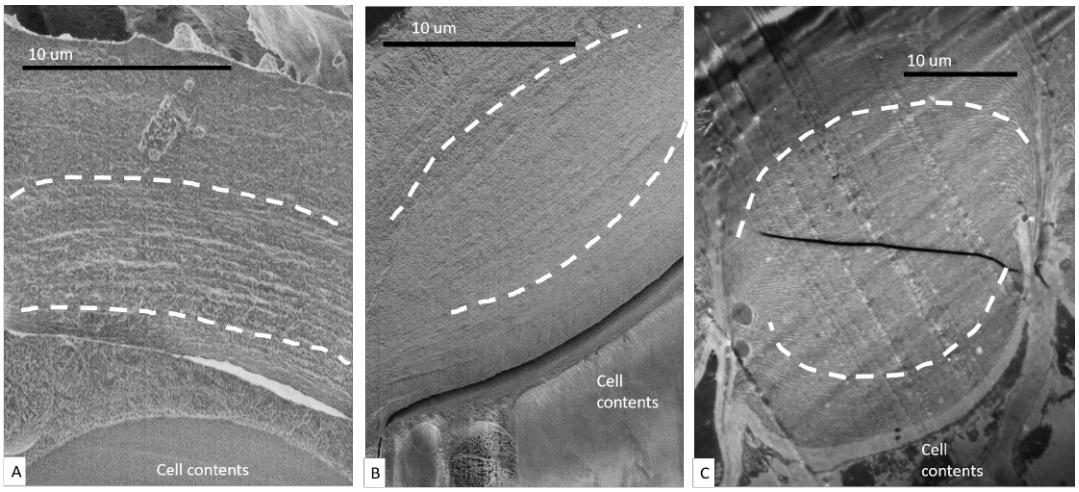

FIGURE 5.15: Cryo-SEM images(A,B) and TEM (C) taken by Dr Yu Ogawa of A. *V. dentatum*, B. *V. tinus* and C. *V. davidii*. White dashed lines are used to emphasise the curvature of the inclusion layers. A: *V. dentatum* has a much less thick cell wall, making this image characteristic. C: A greatly increased curvature in the *V. davidii* is also observed generally. The thickness of *V. tinus*(B) and *V. davidii* is variable and a high number of cells were not measured due to lack of embedded samples.

SEM images of *V. davidii* reveal a very highly curved reflecting cell wall, as shown in figure 5.15. Initial measurements of cell wall thickness from SEM and TEM of embedded tissues estimate the *V. davidii* iridosome to be approximately 30 um thick, while *V. tinus* iridosomes tend to be less thick and highly curved as shown in the comparative electron microscopy images. However, these figures should be treated cautiously as a low number of cells were measured. Again, the SEM reveals layers on a photonic lengthscale, made up of a globular material.

5.5 Conclusion

In this chapter optical and electron microscopy was used to investigate an unusual visual effect from common garden shrubs in the UK *Viburnum tinus* and *Viburnum davidii*. The techniques, analysis and structural colour assumptions used to interpret biological microscopy were the same as those used in the previous chapter on *Pollia*. The fruit itself also has a slight resemblance to the *Pollia* fruits, being approximately the same size and colour. However, the structure and material were shown to be very different in this case.

The structural colour is reflected from planar assemblies of lipid globules in a cell wall matrix. These planes are arranged in thickened adapted cell walls. *V. davidii*, *V. tinus* and *V. dentatum* were shown to have varying intensities of reflected structural colour corresponding to different thicknesses of the adapted cell wall tissue.

Light was reflected orthogonally from these planes, and was shown to retain its incident linear polarisation. Unusually, the multilayers when cut were demonstrated to reflect unpolarised light normal to the cross-section. In *V. davidii*, which was the most intensely reflecting of the measured species, the planes of the multilayer curved round the edges of the cell steeply, making the in-plane reflection a significant part of the overall reflected light. Structural colour had never previously been reported in *V. davidii*.

It was noted that the structural colour in *V. tinus*, as also found in the *Pollia* development series, develops much earlier than the structural colour effect becomes the dominant optical characteristic. This is due to the lack of absorbing pigments in the early stages which allow the non-structural reflection to dominate. Furthermore, under diffuse illumination, pigmentary colour is scattered in all directions. This is more easily visible macroscopically than in microscope analysis, in which the low-angle control of the light incidence tends to promote observation of non-scattering effects. The importance of underlying absorptive pigments in the mature stage was demonstrated. A small degree of extra absorption in the pigmented cells in figure 5.6 changed the appearance of the cell, by better defining the width of the blue peak reflected from the cell. The insight into pigmentation and its role in the visibility and potential for exploitation of structural colour is discussed further in chapters 6 and 7.

5.5.1 Impact and Further Work

In order to fully model the optical response of the materials in both species, the refractive index of the two components of the cell wall must be analysed. This is an ongoing project.

Understanding the tissue growth processes in *Viburnum tinus* might give insights into other structurally coloured plants and fruits, many of which are likely to be unreported due to the sparse study of structural colour in plants. An ongoing collaboration investigates the material from which the structure is formed. As previously mentioned the shrub is extremely common in gardens in the UK and elsewhere, and forms a part of frugivorous birds' diets. Understanding the interaction of the chemical make-up and the fruit signalling via coloured appearance with the birds' diet could therefore give new insight into the ecological needs of UK wildlife. Work forthcoming by Miranda Sinnott-Armstrong will compare the nutritional content, colouration and phylogenetic relation of highly differentiated species in the *Viburnum* genus in order to understand how the colouration of the fruit is a signal adapted to communicate with seed-dispersers. The optical analysis of *Viburnums* presented here will provide evidence for this work.

Finally, study of the different optical effects and structures in the plant has resonance for design of structurally coloured materials. This soft, hydrated tissue is capable of reflecting a lustrous metallic blue sheen. By understanding the material and structure required for this effect, we may be able to reproduce similar biomimetic materials for use in food, cosmetics, fabrics and colourants.

The materials which make up this fruit epicarp appear to be lipids, cellulose-based cell wall and anthocyanin absorbing pigments. These materials on their own are not colourful, but the colouration produced in the plant through combining them in a nanostructure is capable of reflecting a 'metallic' sheen appearance, and an extremely vivid and robust blue through structural variation. Mimicking this tissue could potentially give us biomaterial-based surfaces with the same properties. This is a potential route to sustainable colour engineering.

Comparison with Structurally Coloured Fruits in other Clades

The colouration mechanism exploited in *Viburnum* is similar to what was observed in other blue fruits. *Delarbrea michieana* [82] is a blue fruit (see figure 2.3) whose nanostructure is reproduced from a previous report in figure 5.16. The multilayer observed in this fruit is anatomically very similar to the one described in *V. tinus*. Although this multilayered structure was identified as an iridosome and it was described as responsible for the bright blue colour, a quantitative correlation between the anatomy of the fruits and the optical response was missing for the *Delarbrea* fruits and the components of the architecture were not described. This observation is particularly interesting as it might indicate an example of convergent evolution as despite the apparent similarity of the two materials, and the visual appearance of the fruits, they are not closely related phylogenetically, their clades are shown in 5.17.

Another similar architecture is found in the fruits of *Elaeocarpus angustifolia*, [81] figure 5.16. This blue fruit has also been reported as structurally coloured and shows a very similar epidermal cell shape. Lee [81] identified as the nanostructure responsible for the blue colouration the one reproduced in figure 5.16 B4. Given the apparent similarity of several structures in the *Viburnum* species presented in this chapter, there is a good basis on which to re-analyse both *Delarbrea michieana* and *Elaeocarpus angustifolia* in order to compare the blue iridosomes in these other fruits more fully.

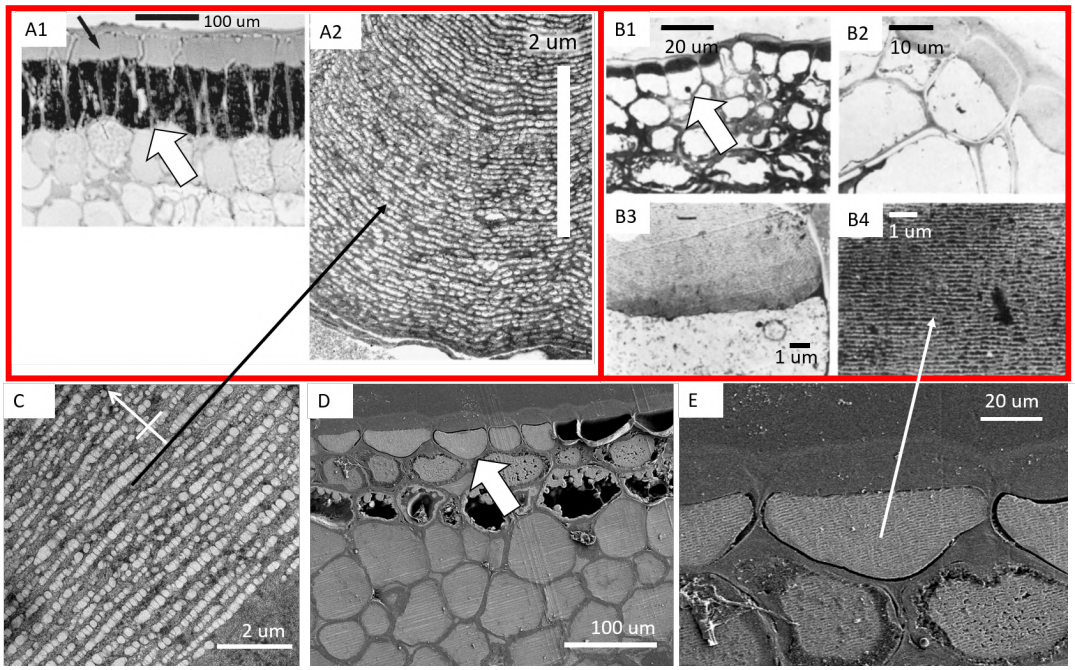

FIGURE 5.16: Comparison of *Delarbrea michieana* (A1-2) [82] and *Elaeocarpus angustifolia*(B1-4) [81] with *Viburnum tinus* (C,D,E). A1 and B1 show light microscope images of the epicarp cross-section. A2, B2,B3,B4,C show TEM sections through the embedded epicarp, D and E show SEM images of the embedded fruit. Large white arrows in A1, B1 and D indicate the lower wall of an external, structurally coloured cell. C and A2 are compared. E and B4 are compared.

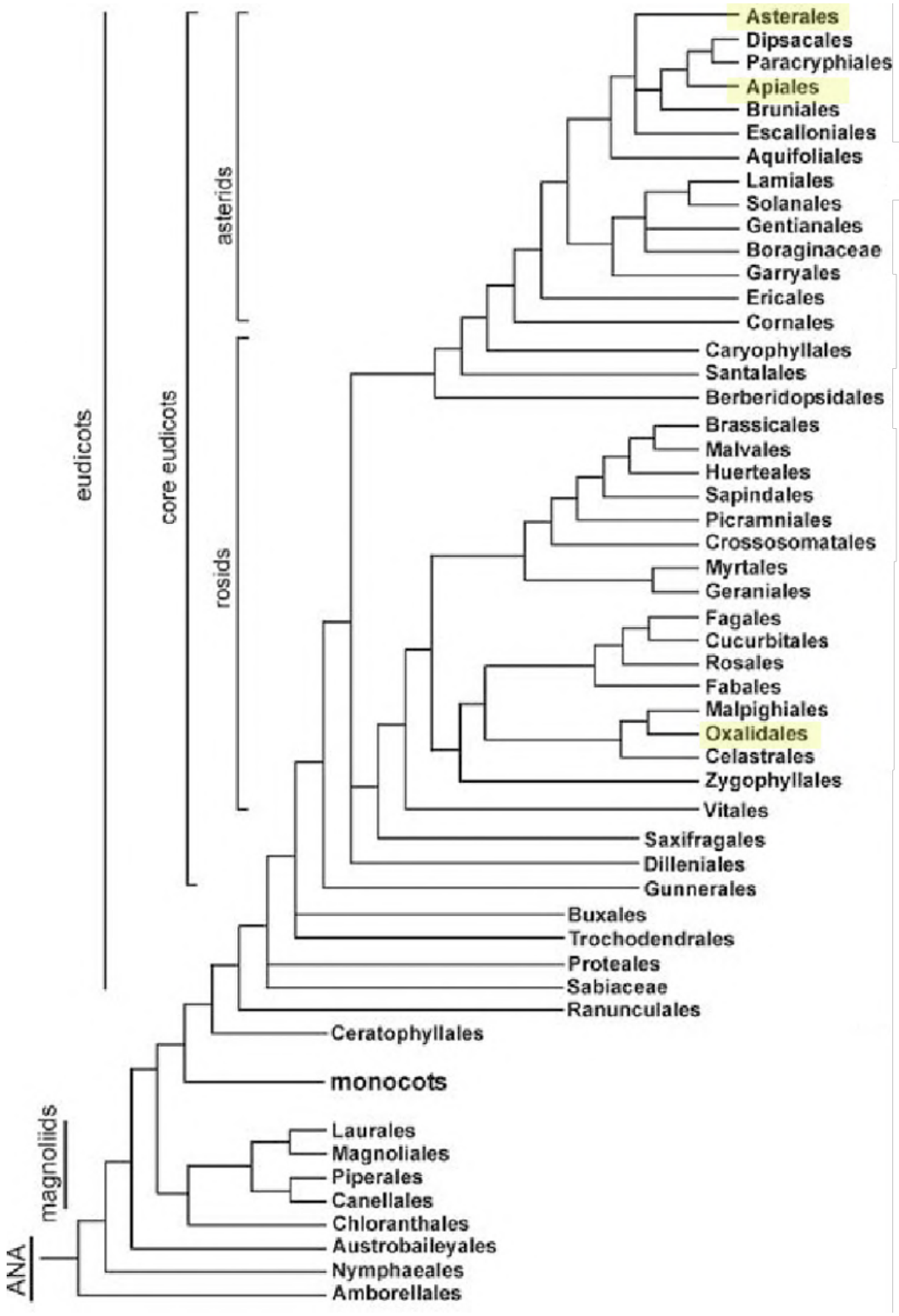

FIGURE 5.17: Eudicot phylogenetic tree of orders [207] showing the orders containing the structurally coloured fruits mentioned here highlighted. Asterids -Dipsacales: *Adoxaceae: Viburnum* and -Apiales: *Araliaceae: Delarbrea* [82] and Rosid: Oxalidales *Eleaocarpaceae: Elaeocarpus*. [81]

Chapter 6

Artificial Structural Colour

6.1 Biomimetic Helicoids: Cellulose Nano Crystals

As discussed in section 3.1.2, several colloids extracted directly from natural biopolymers such as collagen, [162] chitin [208] and cellulose [163] have been demonstrated to self-assemble into chiral nematic structures. These systems are particularly interesting as they promise the potential for development of sustainable techniques for artificial structurally coloured materials. Here, cellulose-based materials are discussed, however the same principles might be directly applied to the other biomaterials mentioned above.

The many routes to produce structural colour architectures can be characterised as top-down or bottom-up. This divides materials that are designed and built up by sequentially controlled processes like material deposition, etching or writing, and materials that result from chemical reactions, or self-assembly of smaller building blocks interacting to reach the configuration states of lowest free energy.

Chiral materials with an anisotropic and circularly asymmetric geometry are difficult to fabricate with top-down processes. [209] In the last few decades, cellulose nanocrystals (CNCs) have been demonstrated to be a convenient system to produce photonic materials. Water suspensions of CNCs spontaneously organise into a chiral nematic architecture that is maintained when dried and that strongly resembles the helicoidal structure observed in the *Pollia* genus and other helicoidal cellulose cell walls, as discussed in chapter 3.

CNCs are very high aspect ratio crystallite particles extracted from any type of natural cellulose fibres. CNCs can be extracted from fibres by acid hydrolysis. Before extraction these crystallites serve in natural cellulose fibres to stiffen the cell wall. Ordinary cellulose fibrils are constituted of cellulose polysaccharide chains that are semi-crystalline, in which the crystalline parts are connected to one another with amorphous material. The amorphous parts of cellulose fibrils are less dense than the crystalline regions and therefore can be dissolved rapidly by acid hydrolysis. On exposure to sulphuric acid, the fibrils are stripped to leave only the crystallites or

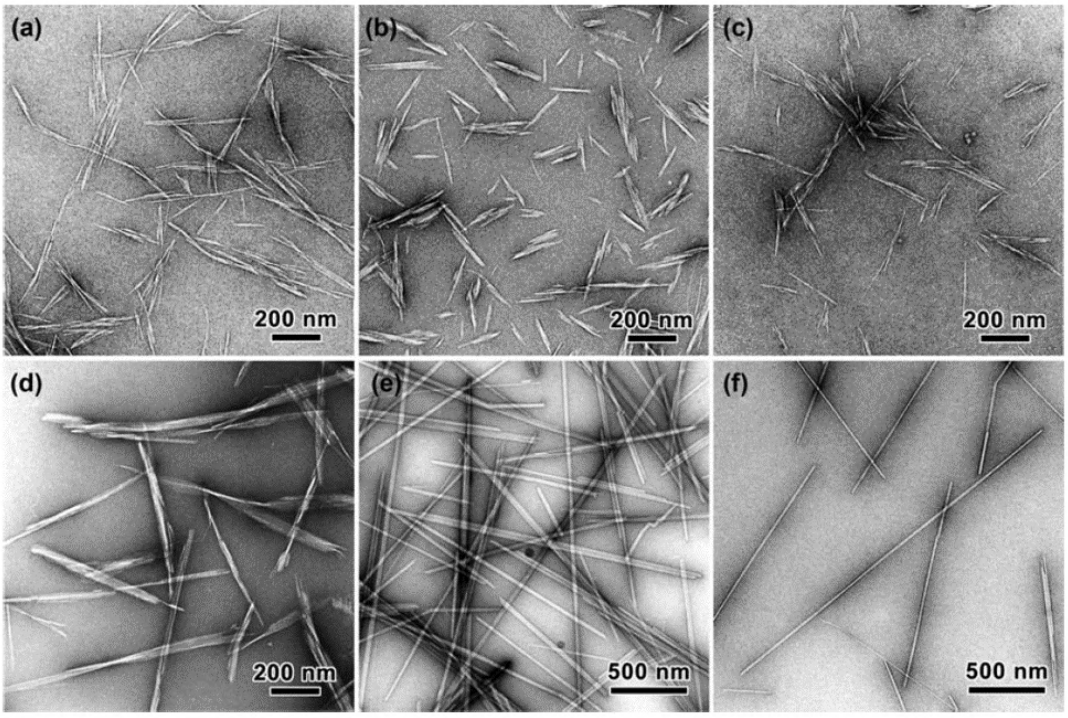

FIGURE 6.1: TEM micrographs of CNCs taken from a. Wood, b. Cotton, c. Bamboo, d. Bacteria, e. Algae, f. Tunicates. Reproduced from [210]

CNCs. [163] The extent of hydrolysis and therefore the morphology of the CNCs is controlled by the strength and length of time of acid exposure. The form of the crystallites is also strongly influenced by the biological source of the cellulose from which they were extracted - see figure 6.1.

Water suspensions of CNCs are stabilised by control of the charges on the crystals and in the liquid through further treatment such as temperature change, sonication and the addition of salts and solvents. [39]

CNC suspensions are known to spontaneously form a chiral nematic liquid crystalline phase. The formation of this phase is described by Onsager [211] and SLO theory. [212] This description predicts the observed phase transition between isotropic and liquid crystalline phases. The transition occurs at a threshold of the volume fraction of crystals in suspension where orientational order in the crystals is entropically favourable due to the excluded volume in the suspension, rather than entropy favouring disorder in the crystals. The phase transition is seen in nucleation and growth of discrete localised areas of chiral nematic phase called tactoids. Tactoids may be observed under a microscope between crossed polarisers due to their birefringence. [163] Provided the rate of evaporation is not too fast, which causes jamming of the non-aligned crystallites in an isotropic arrangement, the tactoids coalesce and grow to fill the entire volume. Finally, the evaporation of the fully chiral nematic suspension compresses the tactoids and brings them into alignment with

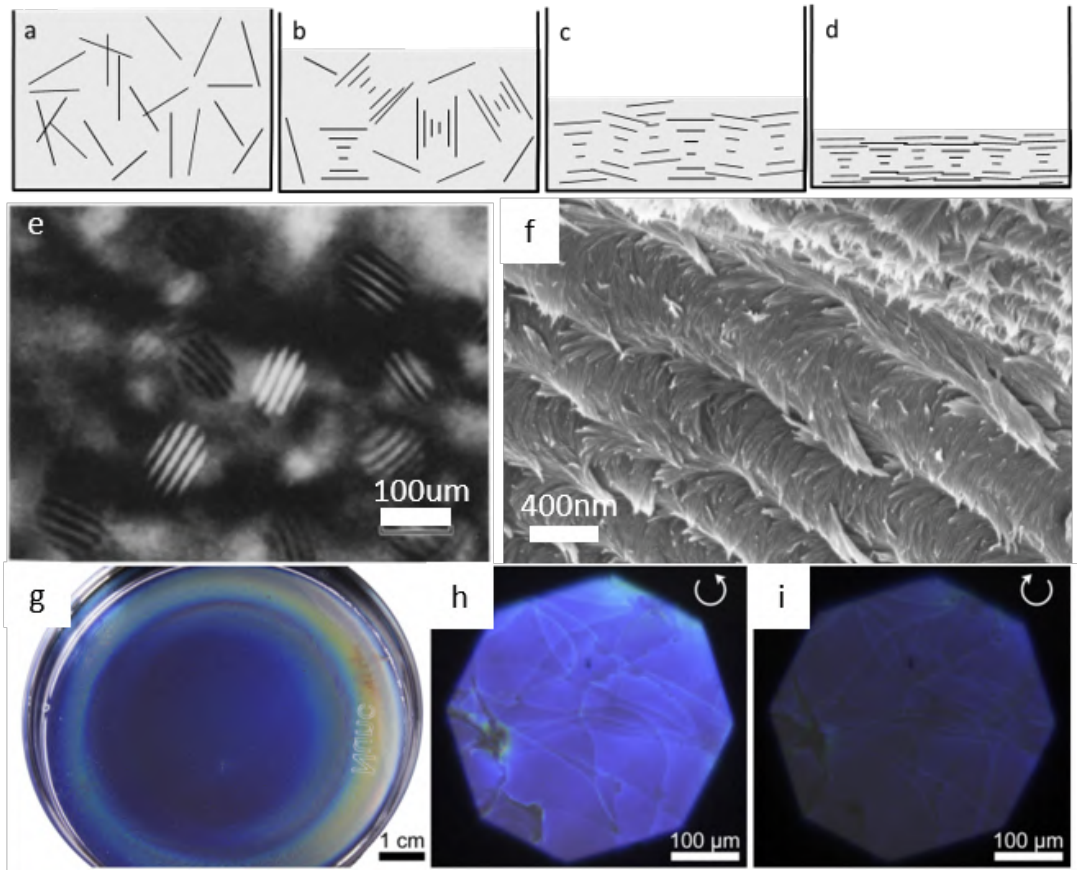

FIGURE 6.2: a-d. Schematic of CNC film assembly from suspension. e. The first optical image of CNC tactoids in suspension reproduced from [163]. f. SEM image of an oblique fracture through a dry optical-wavelength CNC film. g-i. Reproduced from [215]. g. Photo of CNC film. h & i. Optical microscope images taken in left and right handed polarised light respectively.

each other and the plane of the substrate. [213] [38]

Cellulose nanocrystals are anisotropic, and have a birefringent refractive index reported as $n_e/n_o = 1.53/1.58$, [214], which is small enough to be appropriately treated with the optical model from Berreman expanded in chapter 1. The pitch of the resulting helicoidal film can be controlled and designed to reflect a band of visible light, as shown in figure 6.2. [32] The self-assembled helicoid of the CNCs is left handed and conforms to the optical theory reflecting left circularly polarised light in the pseudo-Bragg condition.

The control of CNC film formation has reached maturity in the last fifteen years, [216] and applications of the photonic films, like sensors, [217] are increasingly a focus of research. CNC films have been demonstrated as excellent candidates for templating, [218] and composites [219] transferring their chiroptical properties into materials with enhanced refractive index contrast and stability.

The cellulose films themselves show promise as security papers, [220] [221] displays [222] and pigments. [223]

Cellulose nanocrystal films can be tuned to reflect any colour in the visible range and combined to give mixed colours, potentially replacing any ordinary chemical colouration. The challenges limiting the applicability of this system in an industrial context lie in achieving control independent of CNC source, the speed of self-assembly, [223] and the strong iridescence in CNC films that makes the colouration too angularly dependent to produce a consistent visual impression. The optical response of a CNC film is from a one-dimensional multilayer, making the visible colour angle dependent. This iridescence presents challenges for its use in replacement of traditional pigments.

Furthermore, in order to apply the proposed CNC coating, the film must either be formed in situ by evaporating to form a film on the substrate (which is not practical in most cases due to surface unsuitability, film assembly time and film stiffness), or the film must be isolated in fragments. [223] Self-assembly in confined geometry to directly obtain coloured particles, [224] [225] or grinding down films into smaller flakes are potential routes to achieving this. Each approach however introduces its own challenges, as the droplets must be dried in such a way as to avoid 'coffee-ring' and other edge-effects, where the CNCs don't assemble into substrate-aligned helicoids. Equally grinding must avoid the creation of unnecessary mechanical scarring and surface roughness, which increases scattering, and therefore decreases colour purity.

Even after overcoming technical challenges for the creation of CNC pigment powders, the application of the particles must be controlled to align the film fragments with the substrate on which they are applied, in order to avoid a mix of reflected colours destroying the target colour. By overcoming these challenges, a CNC pigment would be feasible, but still limited by the one-dimensional multilayer responsible for the structural reflection creating an iridescent colouration. In the next section I will discuss a geometrical strategy to overcome this problem.

6.1.1 Curved Geometries for Structural Colour

Structurally coloured materials generally are attractive because of their great brightness, which is enhanced thanks to the absorption-free reflection mechanism. Another very attractive feature is iridescence, allowing a material to have more than one colour appearance. However, both the lack of absorption and the reflection of multiple wavelengths pose engineering challenges of their own and must be carefully tuned and manipulated to exploit their desirable qualities.

For an iridescent material, controlling the angle of reflection observed by the viewer is one way to control the effective colour of the material, and is a strategy deployed for example in the feathers of rock doves which have pink and green stripes reflected around their necks. The optical appearance is controlled by the strong curvature of

the barbules which works to reflect the pink and green selectively from different points on the feather barbules. [226]

Looking at structurally coloured materials beyond the CNC films discussed above, there have been multiple attempts to confine photonic crystals in spherical geometry in order to overcome the problems associated with the strong directionality typical of structural colour. Photonic crystals have been confined in spheres by using self-assembly of spherical nanoparticles to form periodic FCC lattices via microfluidics, resulting in inverse silica balls [227] and silica opal Janus particles. [228] Further attempts have been made using droplets to give magnetic particles, [229] coating large spheres with smaller ones [230] and formation of large scale spheres. [231] Macroscopic angular independence thanks to the confinement of spherical domains in spheres has been demonstrated [232] albeit to a limited extent.

One attempt to create photonic spheres from assemblies of smaller polymer nanoparticles, shown in figure 6.3, is successful in confining an ordered and high quality photonic crystal within a solid sphere that could be potentially used in a pigment. [233] The work demonstrates a single coloured spot that is seen to be reflected from the centre of the ball, and enhanced by gold nanoparticle absorption. An unintended diffraction grating effect is also demonstrated on photonic balls formed from larger PEG colloidal spheres. Extra reflections from unwanted wavelengths are a major obstacle in the production of photonic balls, as the hugely increased surface area scatters light unpredictably, or reintroduces colours that in bulk materials are easily reflected out of the optical axis.

There has been some research into the optics of solid multilayer-shell systems in a cylindrical case through rolling and stretching a dielectric multilayer, [90] which was linked to the structure of *Margaritaria nobilis* fruit cell walls, although without reference to their helicoidal structure. [91]

As well as these non-chiral 3D colloidal clusters, confined geometry has also been demonstrated in a system of chiral cholesteric liquid crystal [234], showing coloured crosstalk originating from multiple reflections between neighbouring spheres, shown in figure 6.3. Notably these effects were shown in this system only for liquid droplets.

The same principle has been applied by using a water CNC suspension with microfluidics to obtain a curved multilayer. [39] This study showed that the cellulose nanocrystals can be confined and assemble quickly in liquid droplets, as in the cholesteric droplets in [234]. They also showed that the layering and chirality of the cellulose nematic could be retained during the drying process. However, unfortunately buckling occurred during drying, resulting in a flattened and wrinkled solid geometry which prevented an optical response analogous to the fruit cells.

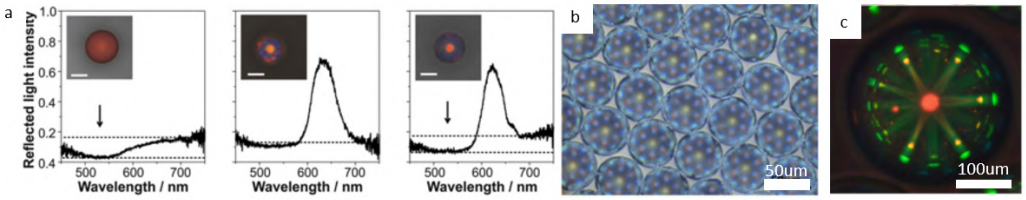

FIGURE 6.3: a. Reproduced from [233], a single structural colour reflected from the centre of each photonic ball made of a 3D assembly of 200 and 250 nm polymer nanoparticles in cases of disorder, order, and additional absorbance from gold nanoparticles. b. A solid photonic ball formed from larger 610 nm PEG particles reflecting a central multilayer spot and additionally a grid of diffraction grating reflections. c. Liquid droplets of highly oriented cholesteric liquid crystal showing multiple reflections of colours at different locations due to cross-talk with neighbouring spheres from [234] .

Finally, a collection of materials take the principles of geometrical manipulation to enhance structural colour effects without attempting to create discrete particles, avoiding the encapsulation and scattering problems. These have been overtly biomimetic and top-down approaches, as in the use of microcavities with atomic layer deposition of alternating metals to mimic the reflective pits of a butterfly's scales [235] in a non-biological material. Another use of a non-flat substrate was in the mimicry of a Morpho butterfly wing [203] through the deposition of alternating layers of titanium and silicon dioxide on silica spheres. Although this approach does not explicitly set out to create spherical-based multilayers, it is intended to take advantage of an increase in the disorder of the multilayer, as the butterfly biomaterial itself does, and for this the spherical geometry is an excellent starting point.

This chapter is a report of a successful engineering of a highly curved CNC film geometry. This approach mimics the *Pollia* cell wall shapes to enhance the angular independence of the CNC film.

6.2 Hierarchical Architecture for Artificial Structural Colour

The previous chapters of this thesis have focused on the structurally coloured material found in epidermal cells of several different species of fruit. The *Pollia* and *Viburnum* cell wall architectures were extensively discussed. Biological tissue's inherent cellular compartmentalisation in these fruits makes the characteristics of the tissular material distinct from the bulk processes currently used in engineering artificial structurally coloured materials.

As previously described, key features of the *Pollia condensata* cell optics are a single colour reflected by each cell, from a small central spot of each cell when illuminated with low angle incident light. The discretised biomaterial defines a colour in each cell which may differ between cells reflecting a brighter and richer spectrum.

These features are all directly related to the discrete ellipsoidal cell shapes which define the multilayer cell wall material. This material architecture, that is structured not only on the scale of optical wavelengths, but also on a larger geometrical-optics scale, is referred to as hierarchical. The challenge of reproducing such a material is a step towards recreating the attractive optical appearance of the fruit. This would be a useful exploitation of structural colour by opening the door to an extension of artificial optical materials towards those found in nature. Reproducing the optical effects in an artificial model is also profitable from a theoretical perspective as it allows us to confirm the conclusions drawn from observation of natural material.

Finally, the artificial materials discussed above in which the reflection is controlled through confinement in spherical geometries show a very similar approach to that in cell wall ellipsoids. The aim of mimicking cell wall ellipsoids therefore is identified with the development of geometrical confinement as an artificial material fabrication technique.

In this chapter, I present a novel templating method to hierarchically structure self-assembled CNC material. I show that self-assembly and structural colour can be retained in the CNC material even when assembled in curved templates. I briefly present four regimes for curved structures which are indicated in figure 6.4.

1. low relief hemisphere arrays
2. hemisphere array films
3. sphere array films
4. individual spheroids

I show that hemisphere arrays can be formed from well-ordered CNC multilayers. Then I demonstrate the recreation of the central reflection spot observed in *P. condensata*, and a measurably increased angle of reflection from an individual spheroid and finally I discuss outlooks for this.

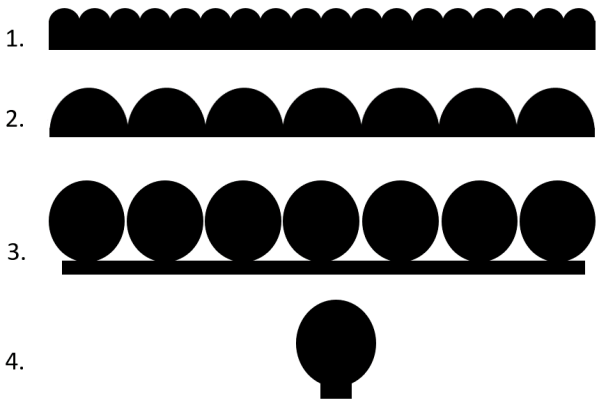

FIGURE 6.4: Schematic showing the four structures introduced in this chapter: 1. Low relief monolayer opal 2. Hemisphere array 3. sphere array 4. individual spheroid structure.

6.2.1 CNC films

Optical analysis of a flat optically reflecting CNC film is given in figure 6.5. The film shows a bright fairly uniform green colour in left handed circular polarisation and very little light reflected in right handed polarisation. Some additional colour mixed domains are seen in both polarisations, due to defects. Additional defects are seen as flow lines on the left circular polarisation image. Imaging the film in reciprocal space, it is shown in image C that the shorter wavelength blue light is reflected at higher angles and further from the centre in K space. This angle-dependent colouration is a visualisation of the iridescence of the material. Application of the Berreman formulation for a helicoidal multilayer reflector as described in section 6.1 has been demonstrated to correctly reproduce this optical reflection. [38]

It is proposed that the hierarchical structure might also be used, in addition to replicating the *Pollia* cell features, to increase the angular independence and high-angle reflection from the material.

6.2.2 Novel CNC Film Templating Procedure

A new technique for constructing hierarchically structured CNC films was developed and is schematised in 6.6.

This technique takes a master shape which is the same as the target desired for the CNC film. In this chapter, I use variations on an array of close-packed sphere shapes on a flat surface, although the technique was also successfully used with a number of other shapes, not shown here.

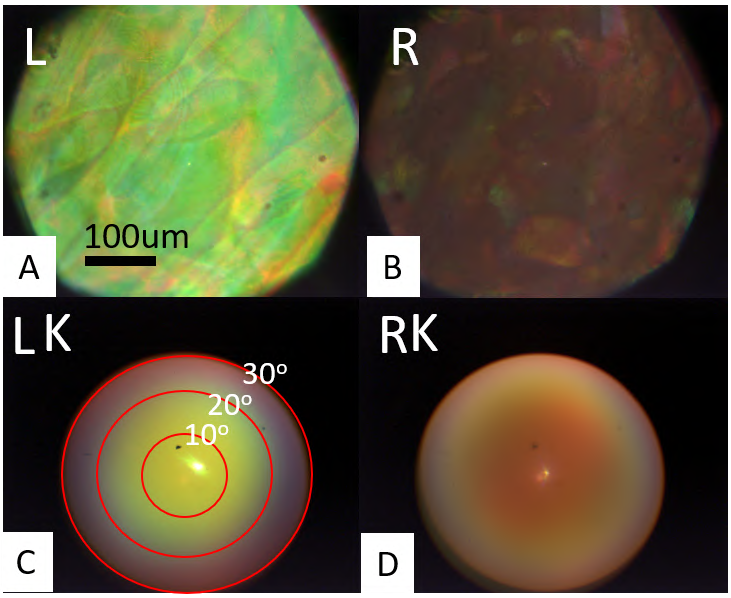

FIGURE 6.5: A & B. Bright field, real-space images of a flat film in left and right circular polarised light. The same area is seen in both. The film colour is fairly uniform and seen to be primarily reflecting in left circular polarisation, although some domains are seen as patches of other colours in both polarisations. Flow line defects are also seen in the left circular polarisation filter. C & D. K-space images of the same area. The light is visualised in terms of angular dependency. In the left circular polarisation, image C, the bright green colour is reflected only at angles up to 20°. Lower wavelength blue light is reflected at higher angles. In right polarisation, image D, the intensity of the light reflected is much lower. Light reflected in right circular polarisation is the result of multiple reflection from defects.

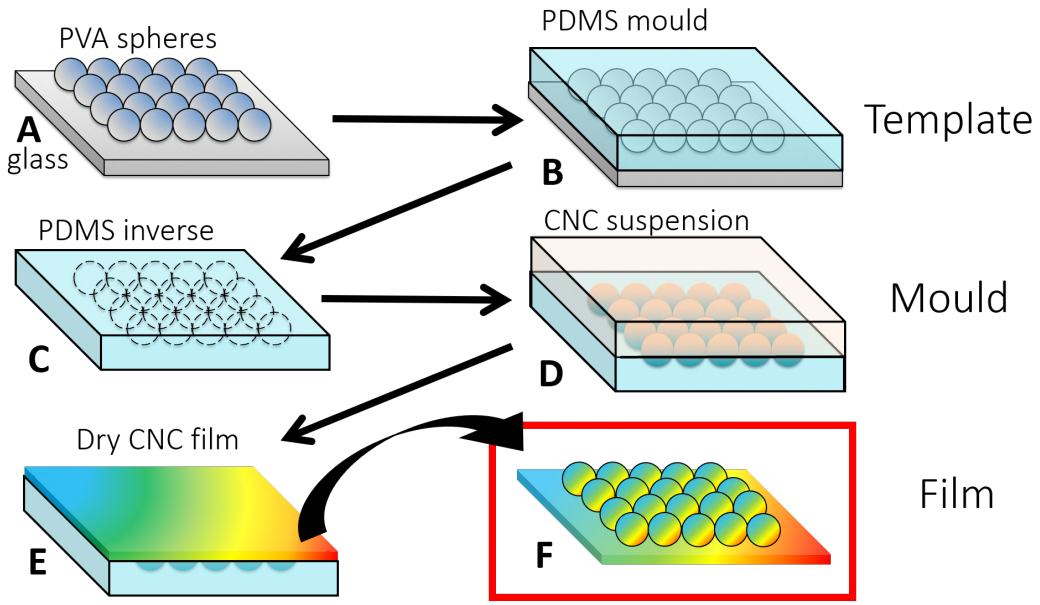

FIGURE 6.6: The schematic shows the templating procedure. A. Master template is assembled. B. PDMS is cast onto the master and hardened. C. PDMS is removed from master-shape, inverted and cleaned to remove residual material. D. CNC suspension is cast into mould and left to evaporate slowly. E-F. Dry film is peeled from PDMS mould which may be used again.

Master Shapes for Templating

A number of different shapes were used in templating the CNC film, in order to develop the technique, and explore the robustness of the CNC self-assembly in non-flat geometry. Excellent reproduction of the moulds by well organised helicoidal layers was demonstrated in all the shapes attempted. An example is given in figure 6.11. In this case, the mould used was a Fresnel lens. The image shows a cross-section through the array of prisms making up the lens, and through a single triangular prism made of CNC multilayer. The layers are well aligned on each side of the prism.

In order to mimic the curvature of the cellular structure, the cells were modelled as spheres. Figure 6.7 schematises this design principle, indicating the use of curvature to reflect light from every angle in three dimensions, which is realistic in diffuse ambient illumination. Image A is an SEM image of a cross-section through a mature *P. condensata* cell showing curved multilayers forming a flattened elliptical cross-section. Image B is a simplistic diagram indicating the principle of uniform reflection from multiple angles. *Pollia* cells are embedded within an epidermal tissue and are only visible from one direction. For the design to work in structures that may be indiscriminately applied to a surface, it is desirable that the model extends the bio-inspired concept to a higher curvature structure.

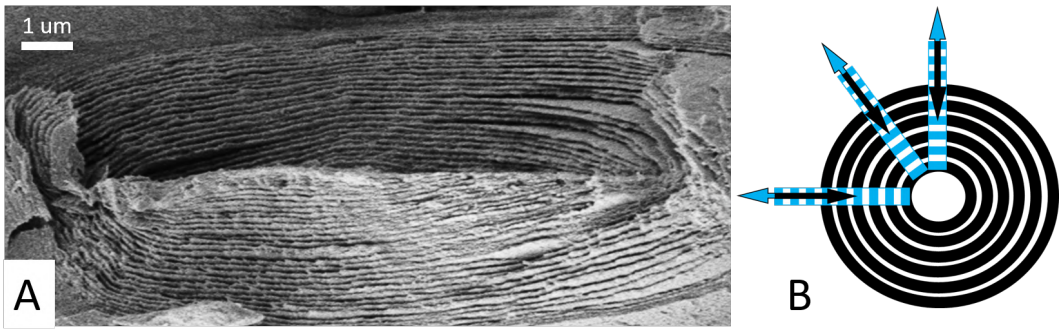

FIGURE 6.7: Comparison of an SEM cross-section through a structurally coloured *Pollia condensata* cell (A) and a bio-inspired schematic of a curved geometry multilayer (B). A shows that the cell has an ellipsoidal multilayer geometry. B shows a blue wave with wavelength matching the pitch of the multilayer no matter what angle it is incident at, introducing the conceptual basis for the bio-inspired strategy.

Sphere Production and Alignment Master structures for structuring the templates were produced by assembling polystyrene (PS) or Polyvinylacrylate (PVA) spheres onto a glass slide in an ordered hexagonal lattice. Spheres of diameter 10 um or less were made by Dr Yang Lan from PS via a nucleated growth mechanism. They were centrifuged to obtain the spheres from the reagents and redispersed via vortex agitation in water. Spheres of 50-70 um diameter were made from PVA by Dr Richard Parker by a microfluidic technique using fluorous oil (FC-40) as the suspension medium.

The PVA spheres were made by microfluidic co-flow of 10 wt% PVA (13-23 kDa, 87-89% hydrolysed) in milliQ water and 2 wt% XL171 surfactant (Sphere Fluidics) in FC-40 (3M) fluorous oil. The flow rate was aqueous solution: oil flow = 300:600 uLh^{-1}. The spheres were washed with FC-40 to partially remove the surfactant.

For sphere diameters from 350 nm - 10 um, the deposition in an ordered lattice was achieved via a home-made doctor blade system. [236] The doctor blade consists of a one dimensional stage (Thorlabs) electronically controlled directly by cube controller (Thorlabs TDC001) via a pen screw motor (Thorlabs, Z825B). A glass coverslip (25 mm square) was used as the coating blade. It is taped to the stage and its trailing edge is adhered to the substrate by the surface tension of the droplet which is dragged across the substrate, coating it. A small quantity of the colloidal suspension was dropped onto one end of a glass slide and the spreading blade used to slowly drag the colloid across the slide. This method allows the deposition of a uniform monolayer of spheres onto the glass slide. The colloidal particles self-assemble to a close-packed arrangement through convective deposition by the capillary force as the droplet is moved away from the evaporation line. The physical principles are the same as assembly by vertical evaporation, [230] but the speed of the blade coater must match the speed of evaporation and therefore movement of the evaporation

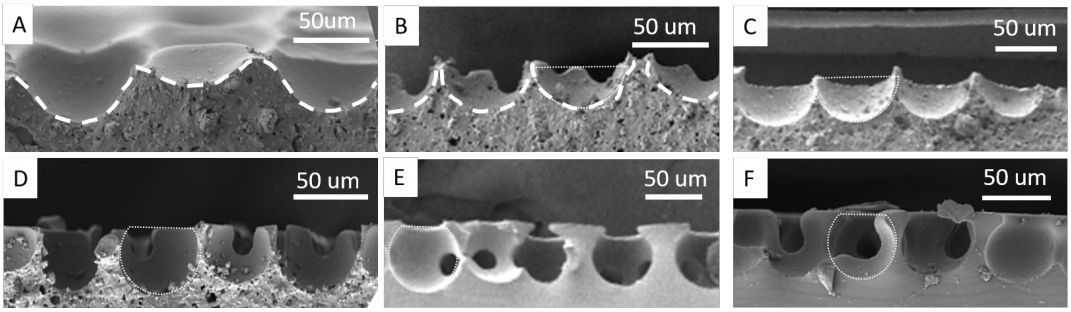

FIGURE 6.8: Moulds from PVA spheres (percentage of sphere moulded) A. Dental Wax(DW) over spheres which had been washed and swelled with water/ethanol, see figure 6.10 (25%) B. DW mould from unwashed spheres. (30%) C. DW mould from washed spheres swelled with ethanol. (45%) D. DW on washed spheres. (80%) E. PDMS on washed spheres swelled with ethanol. (90%) F. PDMS on washed spheres. (95%)

line for a coating of any given thickness.

Larger PVA 60 um spheres are not suitable for aligning with the doctor blade or convective deposition technique as they are too large and heavy to be assembled by the capillary force. However, they still assemble in suspension due to surface charges and and can be induced to form well packed monolayers by slowly drying the suspension.

After drying some surfactant was left bridging and around the base of the spheres. In order to make hemisphere and sphere arrays, the degree of coalescence and the infiltration of the moulding material were calibrated. Figure 6.8 compares the degree of penetration of the moulding material around the curvature of spheres after different treatment. Washing with fluorous oil is used to remove the surfactant residues and increase the degree of inter-sphere penetration. Slight swelling with ethanol is used to decrease the moulding depth. Dental wax, which when unset is a very viscous gel is seen to have a much lower degree of penetration than PDMS which is a relatively low viscosity fluid prior to setting. Heating at 80, 90, 110 and 130 ^{o} did not cause coalescence of the PVA spheres, as shown in figure 6.9. Only a slight flattening of the spheres was seen. Spheres were not heated.

In order to create hemisphere arrays, the unwashed PVA spheres were swollen with a water - ethanol mixture. This was effective in removing the gaps between adjacent spheres. Higher water-content increased the coalescence of the spheres. The calibration is shown in SEM and optical images in figure 6.10. The figure shows that an ethanol fraction of 70-80 % is effective in swelling and joining the adjacent spheres to one another to create a coalesced hemisphere array. Dental wax was used in order to mould the inverse of this array. This was the method used to create the hemisphere array templates used in this chapter. Whole sphere array moulds were created by using the PVA sphere arrays without swelling or washing, templated in PDMS.

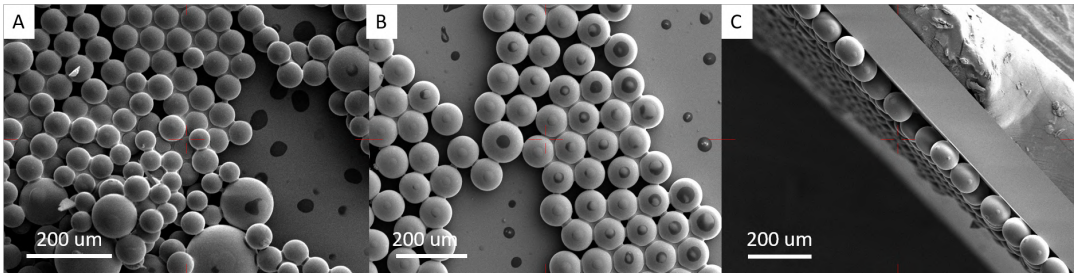

FIGURE 6.9: SEM showing PVA spheres array after A. 60 minutes at 80° B and C. 10 minutes at 130°, the ordinarily white sample went brown.

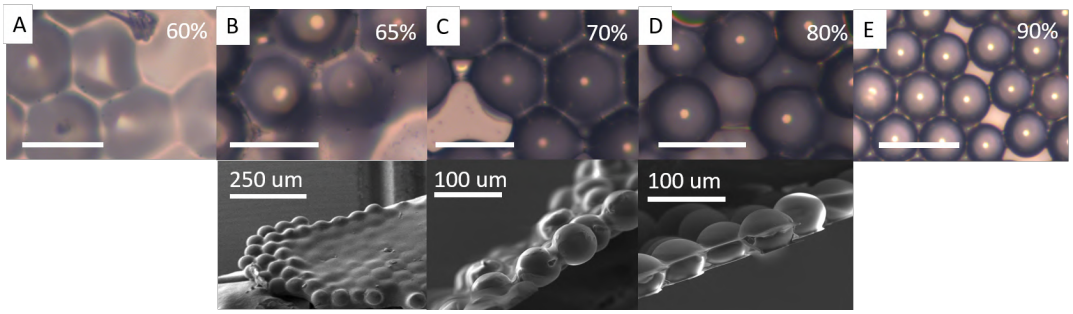

FIGURE 6.10: PVA sphere arrays after treatment with mixture of ethanol:water. The proportion of ethanol is given in the top right hand corner. Top row: optical reflection microscope images, scale bar 50 um. Bottom row: SEM images. A and E were not measured in SEM because it was clear the very high and low degree of coalescence were clear by optical analysis.

For the low-relief patterns, Monolayers of monodisperse PS and PVA colloids of 350 nm, 500 nm, 750 nm, 3 um and 10 um were deposited onto clean glass coverslips and templated in PDMS according to the process described in the scheme in 6.6.

Different categories of structures are assessed: low relief structures made from templated spheres of 10 um or less, hemisphere arrays, sphere arrays and the analysis of single spheres.

Moulding Technique

The master is mounted on a detachable base and submerged in moulding material. Two moulding materials were used in the experiments presented in this chapter. For low relief nanostructures, and for high relief close-to-full spheres, freshly mixed liquid Polydimethylsiloxane (PDMS (Sylgard 184 9:1 base:curing agent, Sigma Aldrich). The unset PDMS was degassed by repeated evacuation with a vacuum pump, until no further bubbles were visible in the PDMS. This is important to ensure that the PDMS has fully infiltrated the structure rather than trapping pockets of air which disrupt the desired template. The PDMS and mould was then cured at 80°C for 2-3 hours and left to cool.

For moulding the hemisphere arrays, Elite HD+ Light Body Fast Set, a two part mixture dental impression silicone was applied to the top of the mould and flattened off on top. The dental silicone sets within 10 minutes of mixing.

The master template was cut out and removed from the elastomer leaving a lip around the edge of about 0.5-1 cm. The resulting PDMS/silicone mould was sonicated in acetone or hot (30°) water for two hours to remove the residues of the master template which remain embedded in the mould, and washed five times.

Film Casting

Finally, the mould was filled with a depth of approximately 0.5 cm CNC suspension at 3 % concentration. The mould was covered with a Petri dish tilted to allow a small air-exchange opening and placed in a drying cabinet (cabinet with silica drying beads). The suspension was left to dry without disturbance in the mould for 10-14 days or until dry and no longer undergoing mass loss through evaporation. The resulting free-standing film is manually removed from the mould.

The CNC suspensions for each templated film, including non-structurally-coloured cases, were prepared and their optical characteristics manipulated and characterised prior to use. The CNC suspensions were prepared by acid hydrolysis from filter paper by Dr Bruno Frka-Petešić, [39] Dr Giulia Guidetti [237] and Cyan Williams. The suspension was maintained at 3% concentration. It was heat treated at 60° in an

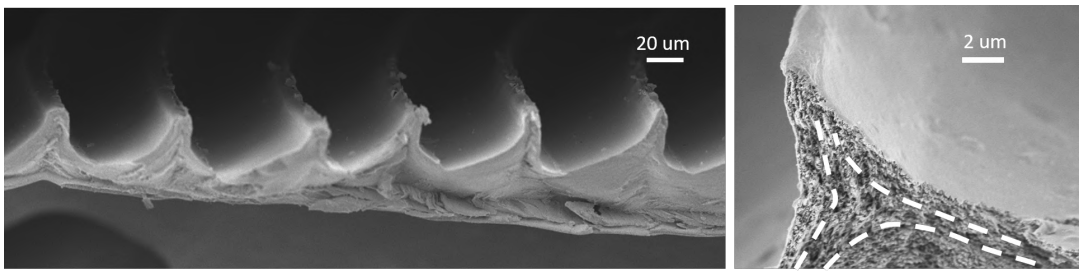

FIGURE 6.11: SEM image of a cross-section through a Fresnel microlens pattern made of helicoidal assembled CNC. The CNC planes reproduced the full structure, and the planes remained aligned to the steep edges as seen in the right hand image, with dashed guidelines.

oil bath for 28 hours and tip sonicated at 2000J/g. No salt was added. It was filtered with a 0.7 um vacuum filter and kept refrigerated.

6.3 Ellipsoidal Geometries

6.3.1 Low-Relief Structures

Figure 6.12 is a demonstration of the successful templating in the CNC films of opal monolayer structures on a range of scales. The three columns show: left - a left handed circularly polarised microscope image, centre - a right handed circularly polarised image and right - an SEM image of the templated film.

The bright left handed circularly polarised reflection images compared to the dark right handed ones indicate that left handed helicoidal self-assembled structure was present in every case. Some domain boundaries, flow lines and some light reflected in right handed circular polarisation indicate the presence of defects which are also observed in flat geometry. [238]

Templating successfully reproduces the intended shape and its use does not appear to induce additional defects so the colour uniformity can be in principle improved by treating the suspension as for a flat film. [39]

The SEM images confirm that the templating was successful even down to the scale close to the size of the nanocrystals themselves. In the SEM cross-section (inset) of the 3 um diameter hemispheres, the planes of the helicoidal crystals seem to be essentially unaffected and still align well with the bulk of the film. The SEM images confirm that the size and tight packing of the spheres with respect to the CNCs meant that the templating was effectively of a hemisphere array, rather than of the entire sphere.

The success of these architectures demonstrated the ability to hierarchically pattern CNC films with a curved template. The method also retained self-assembled structural colour. The technique therefore works to produce a hierarchical geometry material.

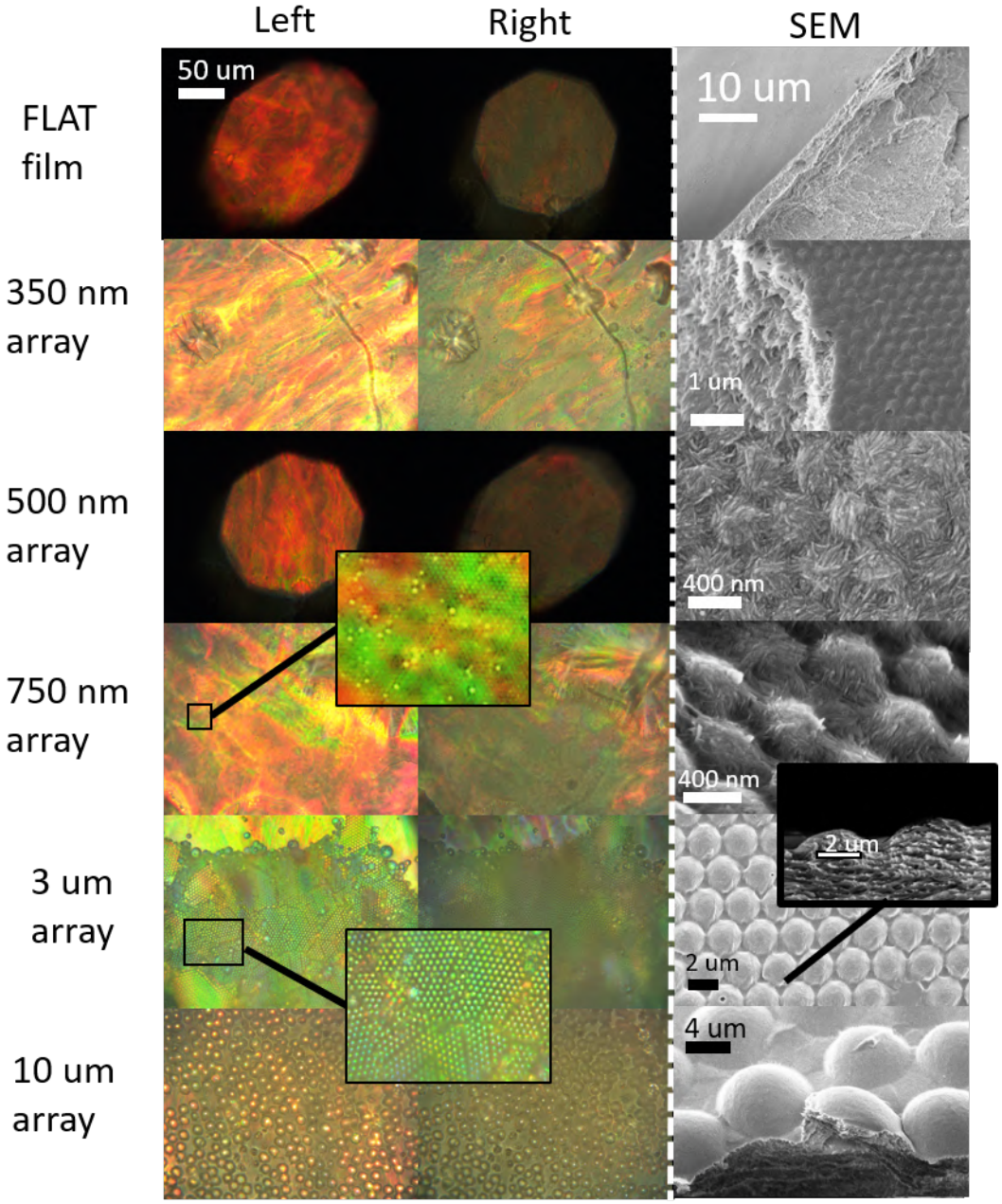

FIGURE 6.12: Five different sizes of very small sphere arrays are shown. Each row shows an array of a different size sphere. The sample is imaged in left and right to show the degree of order and disorder. The samples are also imaged in SEM in the right-hand column.

6.3.2 Hemisphere Arrays

Larger ellipsoidal master templates were created with spheres of a diameter directly analogous to the scale of *Pollia* cells. Spheres of a uniform 60-70 um were assembled by Dr Richard Parker.

The hemisphere array was intended to introduce a large scale plane reorientation, mimicking the *P. condensata* cell curvature, whilst maintaining continuity with the flat connective base film. The curved hemisphere film has potential to combine the positive characteristics of the curved film - including adapted optical effects, and the flat film - the ease of formation, alignment and manipulation. This could potentially be exploited by fragmenting the structured film in order to create a powder.

Results

Structured free-standing films were produced in which structural colour retained in the final structure, shown in figure 6.13. The structurally coloured film is imaged in polarisation optical microscopy incident on the curved structures (A and B) and from the flat connecting film side (C and D). Comparison between the left and right handed circularly polarised reflection pairs show that the helicoidal structural colour is preserved. Image A shows red and green reflection from the hemisphere surface. The image is taken using a small numerical aperture, and a point-like reflection spot is observed reflected from the centre of the curved surface as seen from *Pollia* cell walls.

Figure 6.13 images C and D show the same film from the opposite or 'flat' side, again in left and right circular polarisation. The base-film colour is seen to be predominantly blue. Each hemisphere is marked by a bright central reflection spot of green, and a surrounding dark area. The dark area around the bright green spot is caused by a dip in the flat film where the CNC layering sinks into the hemisphere, making the layers off-angle to the surface such that the light is no longer collected by the objective lens aperture. This mimics a similar structure seen in dimpled beetle elytra as reported in [240], figure 7. There are green streaks visible between the hemisphere reflection spots, caused by multiple reflections between the symmetrical angled layers in the concave hemispherical reflectors, as expected in radially assembled cholesteric structures. [239]

SEM image E 6.13 confirms that the hemisphere mould produces an array of smooth, well curved hemispheres. Image F is of a broken cross-section that shows that alignment of the helicoidal layers inside the hemisphere follows the outer surface throughout the internal structure. The internal planes are continuous with the outside of the film but also with the base film which is curved into the hemisphere shape.

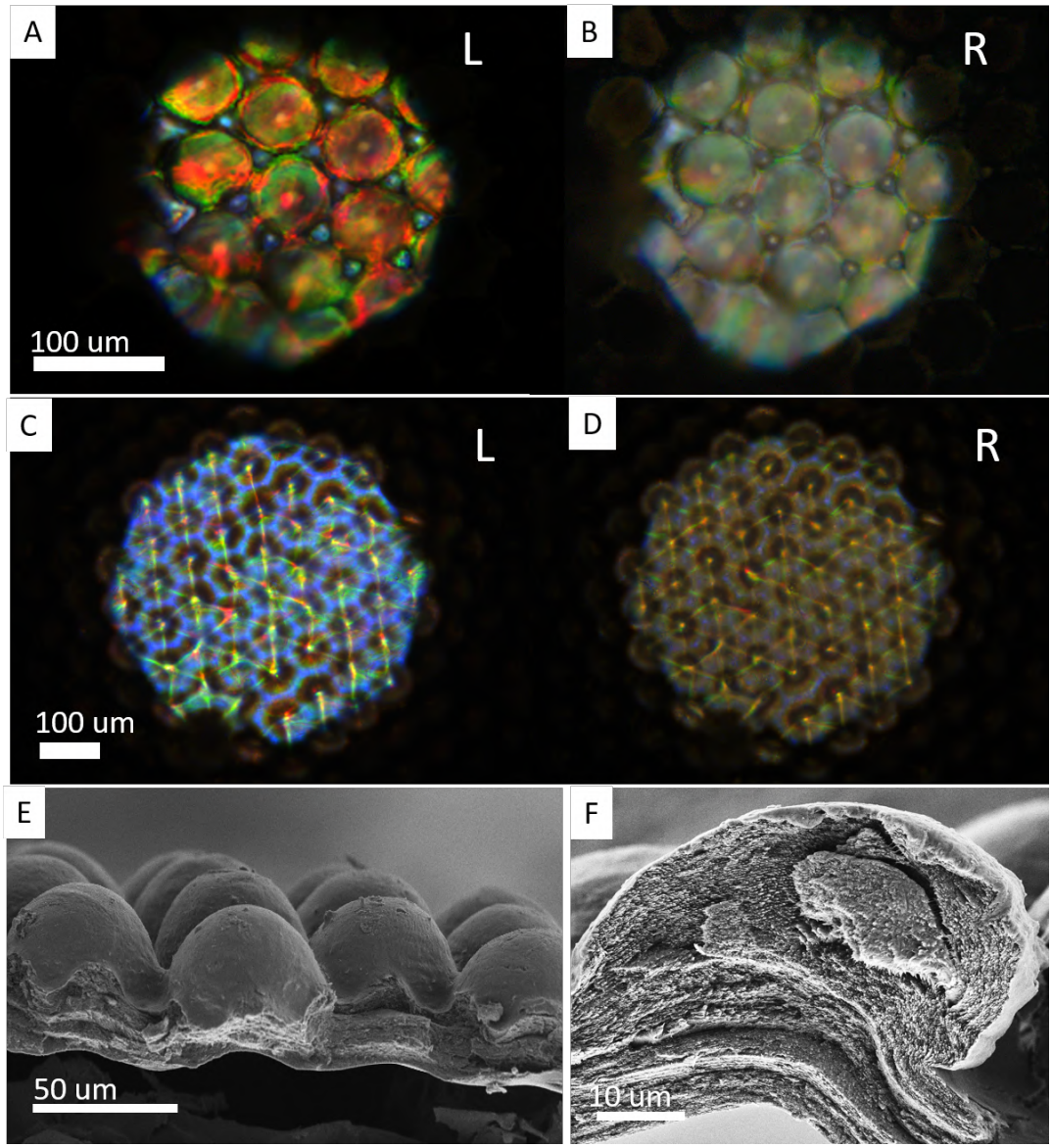

FIGURE 6.13: A & B. Hemisphere array film imaged from the patterned side in left (L) and right (R) circularly polarised light. C & D. The same film imaged from the flat side in left and right circularly polarised light. The colour of the patterned side is seen to be red-shifted with respect to the flat side of the film. In C, each of the hemispheres is visible as a dark spot with a central bright reflection spot. There is also significant cross-talk between the concave structures. [239] E & F. SEM images of the same array. E shows multiple hemispheres in an array, F shows a cross-section through a single hemisphere, showing alignment of the layers around the curved surface, and advection of the layering from the flat side of the film.

The film is dried with the hemispheres pointing down, below the 'base film' and evaporation occurs from above. The hemisphere outer edge is therefore in place and compressed towards the smooth outer edges during evaporation. Advection draws the flat film layer into the hemisphere vacancies as the water evaporates.

Unlike in *Pollia* cells, the central reflection point in A and B is not the only reflection from the hemispheres, which also generate a less intense red and green reflection throughout the hemisphere. It is proposed that this is the result of the thick area of CNC film which fills the hemisphere and joins it to the flat film. Unlike in a spheroid structure which has a strong layer curvature throughout, this filling area has a decreasing angle with respect to the hemisphere surface in its internal layering. The existence of low-angle helicoidal pitches therefore reflects light from throughout the hemisphere, at positions other than the central location.

Reflection from the flat film can be distinguished from the reflection originating in the hemisphere due to the red-shifted wavelength of light reflected from the helicoidal pitches within the hemisphere.

6.3.3 Sphere Arrays

The hemisphere array template was extended to an array with structures close to a full sphere. The same method was used to create the master template, but the surfactant was washed off the spheres leaving them in contact with the substrate and one another over a much smaller surface area. Templating the film using this mould formed a '3D monolayer' of spheres, with each spheroid shape attached to the 'base film' as before, but with a much narrower neck. The template was made in PDMS in order to get a greater infiltration around the edges of the spheres.

Templating a true 3D sphere in this way has inherent limitations related to the size of the contact area between the spheres and the surface, and between the spheres. If the contact of the sphere to the surface is too small, the CNC suspension is not introduced into the cavity, either because surface tension makes it energetically unfavourable, or if the contact zone is even smaller, because the nanocrystals are longer than the contact zone diameter. The spheres were not therefore washed entirely clean of the fluorous oil in order to retain some connectivity. After the suspension was introduced into the template, the assembly was placed briefly under weak vacuum in order to drive the air out of the mould, where it was otherwise trapped in the confined spheres.

Additionally the diameter of the solid CNC sphere places a further restriction on the narrowness of the sphere neck, due to difficulty in removing the film with the spheres intact. It was demonstrated that spheroids remaining attached to the film could be assembled and removed from the PDMS mould provided the structure was

strong enough to stretch the PDMS mould around the widest part of the spheroid without breaking.

Results

Microscopic Figure 6.14 shows bright and dark field images of the successful 3D array and an SEM cross-section through a single structure. Images A and B show the left and right circularly polarised images of the spheroid array in bright field. Notable is the reflection of a spot in the centre of the structure much smaller than the outer edge. The wavelength of the multilayer reflected from the confined spheroid is, as before, longer than film it is attached to. In this spheroid array however, small domain, right circular polarisation reflection and colour variability defects appear to be located predominantly in the film rather than the spheroids. Where colour mixing is present in the spheroids, the effect is isolated within one spheroid rather than over many neighbouring structures.

Images C and D from the same figure show the dark field reflection in left and right circular polarisation. The higher angle light reflection is visible in rings around the location of the bright reflected spot in bright field. The reflection of light at low and high angles from the spheroid structures in the right circular polarisation is negligible showing that the self-assembly is robust in this tightly confined geometry.

The SEM cross-section in image E shows that the top layers of the helicoids follow the outside of the sphere as before. The dissimilarity is where the very strongly advected layers from the base film form a stalk shape protruding into the curved top half, like the shape of a mushroom. A dashed line is used as an indicator of the geometry.

Macroscopic The structured part of the film looks opaque and highly scattering macroscopically. This is due to scattering outside the film itself on the additional surfaces created by the 3D structure, making the surface appear rough. In order to attempt to reduce the scattering effect, refractive index matching oil (Cargille refractive index series AAA-1/2) with n = 1.52 was applied. The observed outcome of the addition of refractive index matching oil with n = 1.52 is shown in image B in figure 6.15. Compared to the area of structured film in air, there is a reduction in the extent of scattering, but not sufficient to suppress the scattering-dominance in the overall appearance. This indicates that there is insufficient infiltration or matching of this refractive index oil with the cellulose material.

The spheroid array was imaged with a large depth of field and focused area (Keyence digital microscope). This image is shown in figure 6.15 B. The central reflected spots of light are clearly visible from the centre of each of the spheroids. What is visible in this image is that the overall appearance of the spheroids on the film is

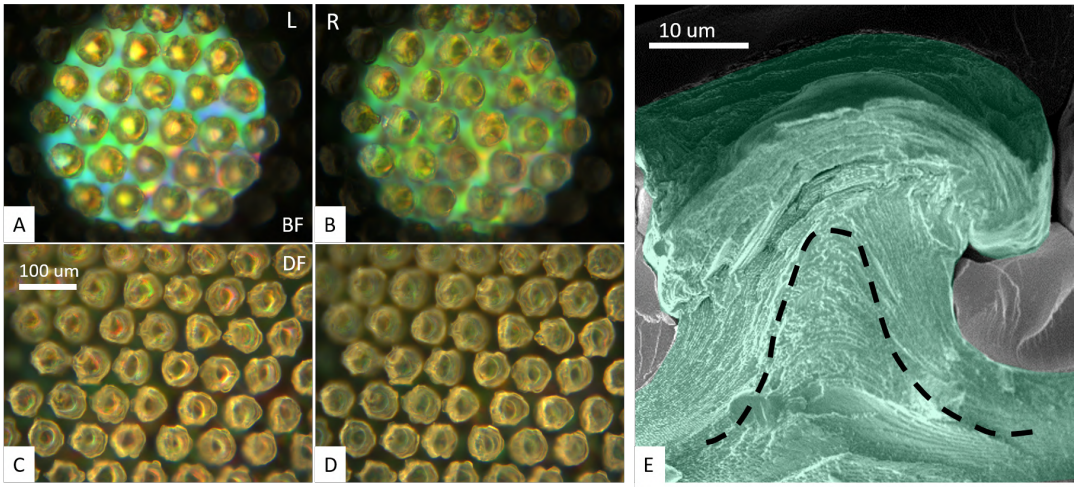

FIGURE 6.14: A & B. Sphere array film imaged in bright field with a large numerical aperture of 37° in left (A) and right (B) circular polarisation. The coloured reflection spots on the sphere structures are visible on in the left circular polarisation filter. The same film is imaged using dark filed illumination in C & D. Coloured rings are visible on each structure in C and not D. E. SEM of a cross-section through an embedded sphere-structure. The CNC periodic layered patterns are seen to be aligned with the outer curvature, with strong advection from the flat film, giving a 'stem', indicated by the dashed line.

dominated by the film colour, and that a significant amount of light is scattered by the spheroids. Each of the spheroids appears dark except for the central reflection in this image, indicating that no light is reflected normally, but more crucially, that light reflected from the surface is scattered in a different direction.

Discussion

The microscope images of the spheroid array on the film in figure 6.14 show that the curved cellulose helicoid held to be responsible for the unusual appearance of *Pollia* cells was reproduced using this artificial technique and material. In images A-D, a low occurrence of colour-mixing depolarising defects was observed on the spheroid structures. Imaging in the right circular polarisation demonstrated a very low degree of non-left circular polarised reflection from the spheroids in either bright or dark field illumination.

The film connected to the spheroids, in the background of figure 6.14, image A did however have a high degree of colour mixing and multiple reflection defects. These defects appear to be somewhat correlated to the confined spheroids which are locally adjoined. A cross-section through the multilayer spheroid shows in figure 6.14 that there appears to be a significant advection of material in the stem of the spheroid structure, indicating an interaction between the spheroid structure and the connecting film.

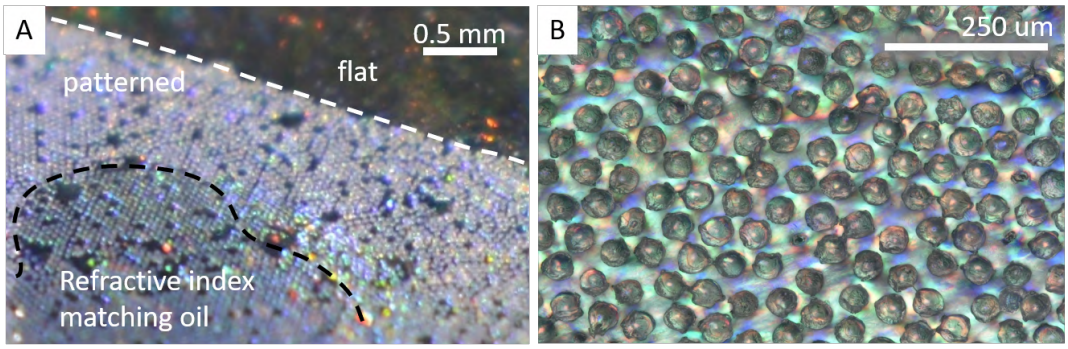

FIGURE 6.15: A. Refractive-index-matching oil droplet on patterned film. The black dashed line indicates the edge of the oil droplet. The white dashed line indicates the edge of the patterned area on the film. B. The sphere-patterned film imaged using a Keyence digital microscope to obtain a wide field of view, wide angle of illumination and collection and extended focal depth.

The SEM of the structure in image E indicates the plane orientation and demonstrates that a high degree of curvature is reproduced as desired in the spheroid structured 'cap', but the formation does not close into a full sphere with both a convex and concave side, as in the shape observed in the cell wall. This means that some aspects of the cell architecture are reproduced, but not the ellipsoid in its entirety.

Nevertheless, a comparison between the hemisphere array and spheroid array films in figures 6.13 and 6.14 respectively show that the central reflection spot is better isolated in the spheroid array than in the hemisphere array. Comparing the SEM cross-sections of the two architectures, it is suggested that this is due to greater angles of tilt between the internal planes in the structure and the surface. In the spheroid there is a greater disconnect between the stem and cap of the spheroid array than in the gradual merging of the hemisphere array with the flat film.

The macroscopic visual impact of the hierarchical array is shown in figure 6.15 A. The aim of the project was to mimic the *Pollia* cell wall optical signatures. This forms part of a larger ambition, not directly addressed in this thesis, to develop techniques for improved angular robustness in CNC film macroscopically, so that it may be exploited as a pigment. Understanding the differences between the optical response of natural and biomimetic materials therefore indicates the direction for further development towards this aim.

Inspection of the whole film in the deep field microscope image in figure 6.15 B shows that the majority of the light reflected is from the flat connecting film, rather than the small spots of light reflected from the centre of each spheroid. Although the confined structures have clear and well-defined bright reflection spots, the curved structure actually decreases the amount of light reflected back from the material, because a greater proportion of the light is scattered away from the incident angle.

Addition of extra light reflected from behind the target structure reduces the optical impact as the overall visible appearance is of the mixed reflection. The additional reflection therefore prevents an optical impact from the spheroid reflections. In order to eliminate this undesirable reflection, a number of approaches could be taken. The spheroid structures could be removed from the connecting film via mechanical abrasion and resuspended in a pigmented or transparent medium. An additional pigment could be applied to the top of the flat part of the film blocking its reflection, for example by preparing the flat areas of the mould prior to templating. Alternatively, the pitch of the flat area of the film could be tuned to reflect non-optical UV wavelengths which do not contribute to the reflection. The longer pitch induced by confinement would make the spheroid structures optically reflective. This technique should be explored in conjunction with the addition of pigment. The most important contribution to the macroscopic optical appearance, as demonstrated in figure 6.15 A is the high degree of scattering making the structured area look white overall. A pigmentation technique is required as well as index matching in order to stop the scattering of stray light. Pigmentation could be included as part of the multilayer structure, within the spheroid structures, or associated to the connecting film. The integration of pigment with the structurally coloured material is discussed further at the end of the chapter.

Production of this hierarchically structured film is a successful demonstration of the principles of reflection from the curved multilayer architecture in *Pollia* cells. A significant curvature was introduced to the helicoidal multilayer, and observed to change the reflection appearance. However, in this system, multiple additional air-interface surfaces were introduced, enhancing surface scattering. The loose packing of the spheroids and use of a well-ordered visibly-reflecting attachment film caused additional coloured reflection to be a significant contributing factor in the overall film appearance.

Further work could decrease or vary the evaporation rate in order to reduce the film defects and change the planar orientation induced in advection. A pigment such as carbon black could also be added to the film in order to suppress the scattering, or the entire array embedded in a polymer matrix to resolve the refractive index boundary scattering. In order to apply the film array, the ellipsoids could be further isolated from the film and one another by reducing the volume of CNC in the mould. A method to systematically scratch the spheres from the film, or to otherwise separate the sphere array into a useful powder, could be developed.

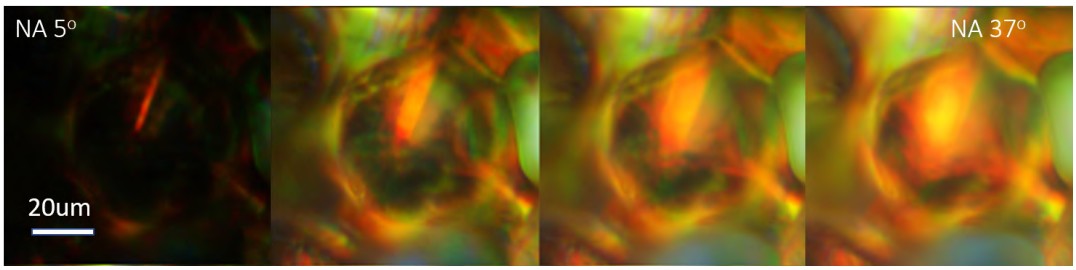

FIGURE 6.16: left to right: images of the same spheroid structure with increasing numerical apertures from 3° to 37°. The size of the reflection spot in the centre of the spheroid structure is seen to increase with increasing numerical aperture. This reproduces an effect observed in *Pollia condensata* and is discussed in section 1.5.1 and figure 1.10.

6.3.4 Single Spheres

The deeper sphere-array template allowed the formation of entire spheroid shapes. These were then removed from the film by manual pressure from tweezers. The confined spheroid structures in the array were therefore addressed individually as single curved multilayer components. Individual spheres were characterised to understand the way in which the optical response is modified for each individual curved structure.

Results

The size of the reflection spot in the centre of the cell may be controlled by closing and opening the numerical aperture, see figure 6.16, as demonstrated for the *Pollia* fruit cells. As the numerical aperture is dilated, the width of the reflection spot increases.

Three exfoliated spheroids are shown in 6.17. Image A, shows the attachment of a spheroid to flat film, B shows a broken cross-section, C shows the smooth top of a spheroid. The outer pitches and cross-section show a good uniformity and smooth well ordered multilayer with a pitch reflecting visible wavelengths.

A single spheroid was rotated through 180° over the curved top section. The results of the spectral measurement are shown in figure 6.18 and compared with a flat film rotated through its reflective range. The sphere reflected a double peaked profile, some reflection could be measured between 40-180° with a good uniformity in the spectral profile between 100-180°. This range shows a significant increase in the range of reflection in comparison to the flat film, which was shown to reflect a peak only over the range 140-170°. Further investigation is needed to understand the cause of the double-peaked spectral profile.

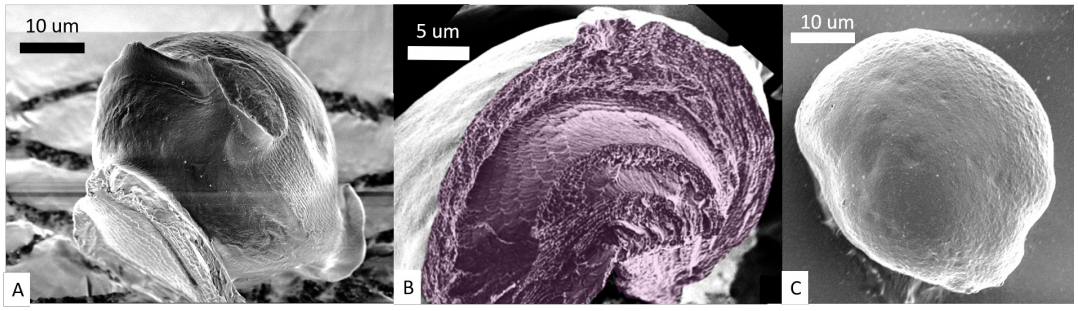

FIGURE 6.17: Three SEM images of individual cellulose spheroids. A. Structure with base film fragment attached and evidence of bridges to other structures, no stem visible. The outer surface is smooth with evidence of layering around the middle. B. Cross-section through a spheroid showing uniform period structure throughout, very little buckling. C. Spheroid seen from above, exposing smooth unbuckled surface.

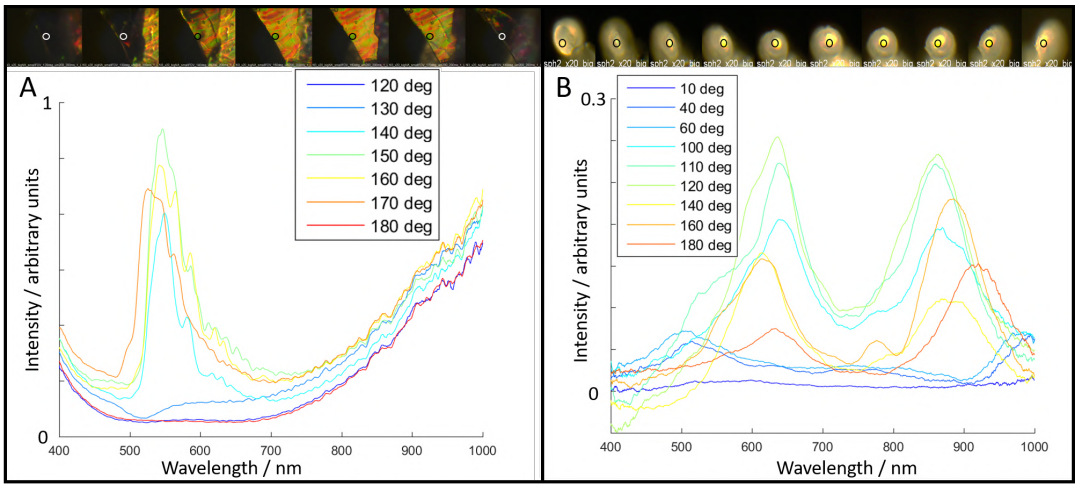

FIGURE 6.18: A. Flat CNC sample rotated through 60º and the same spatial location measured at each angle. Spectra are plotted and images of the film shown above. B. A single spheroid structure mounted on a needle and rotated through 170º. The collection spot location and diameter is indicated on each of the images above.

Discussion

The production of single spheroid multilayer structures was successfully demonstrated using the templating technique. The numerical aperture-dependent central reflection spot is a good demonstration that the analysis of the *Pollia* cell appearance was well founded, and that the glittery impression of the cell assembly in the *Pollia* outer shell is potentially reproducible.

Rotation The light intensity measured by taking a spectrum of the central reflected spot in rotation through 180^o was even more striking, as the angle at which light was reflected was increased from 30^o for a flat film to 140^o. This was only measured over the curved side as the effect of templating using the spheroid structure was to create asymmetric particles with a highly curved spheroid cap and a 'stem' side in which the multilayer does not lie parallel to the curvature of the sphere.

Comparison The attempt to produce single spherical CNC multilayer particles has been reported [224] using microfluidics to form a suspension droplet which then assembles and dries out in a non-aqueous medium. The results from this method are reproduced in figure 6.19. Image A shows the final result of the microfluidic technique under SEM, the originally spherical droplet is buckled and collapsed by the drying process due to the low volume of CNCs with respect to the volume of the droplet. Image B is the outer edge of part of the dry buckled particle, showing layers of helicoidal cellulose with twice the pitch indicated as 'p'. The organised layers are retained in the buckled particle, although the pitches were shown to be longer than visible wavelength, making them non-reflecting in visible light.

The demonstration of CNC helicoid hierarchical structuring and confinement presented in this thesis compares favourably with these previously reported results. The templating technique is demonstrated to produce visible-wavelength reflecting pitches, solid filled spheroids with a uniform shape and size, and smooth, well-aligned high-curvature multilayer surfaces. This is achieved in both the spheroid and hemisphere shapes due to the reservoir of CNC suspension in the continuous film to which the spheres are attached. For the microfluidic technique, the fundamental limitation is that the low concentration of the suspension required to allow CNCs to assemble means that the final volume of dry CNCs is much smaller than the volume of the sphere. Having assembled at the outer edge of the droplet, where the water leaves the droplet and the CNCs align at the interface, the drying droplet collapses. In the templating technique, the layers are built up at the target curved interface, and as the suspension becomes more concentrated, additional volume of suspension is drawn into the structure from above, filling the shape, and continuing the layered architecture.

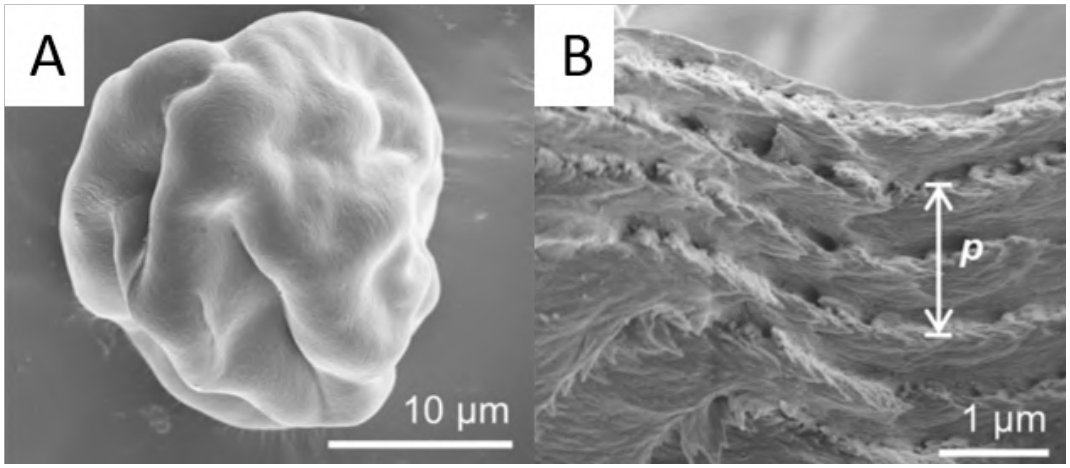

FIGURE 6.19: SEM images reproduced from [224], the microfluidic technique produces buckled structures (A) and pitch distances longer than the visible wavelength.

The pitch of the confined spheroid in templating is lengthened, but not longer than visible wavelengths. An explanation for the increased pitch is advanced in the work discussed above from [224]. In this analysis the pitch is measured to expand according to an inverse cube of the concentration. The concentration is changed in the system as the droplets dry from their surface in three dimensions decreasing the volume of the droplet until kinetic arrest.

In the novel templating technique, the concentration of CNCs in the confined area should increase during assembly only as the water evaporates from the top surface. It should not undergo as strong an increase in concentration during assembly as in the microfluidic technique. The less extreme elongation in the pitch observed in the templating technique is consistent therefore with the model proposed in the previous work. However, it is not clear whether and why the concentration in the templated spheroids during self-assembly would be higher than that of the flat film. Optical analysis and modelling of the film drying in the template would be necessary to understand the evolution of the pitch length in the film to its final configuration. Understanding when during the drying process the stem CNCs are drawn into the cavity is crucial to understanding the concentration transition in the suspension, and therefore the explanation that should be advanced to explain the lengthened pitch.

6.4 Prospects for Further Work

Limitations in the work presented in this chapter are largely a feature of the defects found in CNC self-assembled film material.

Techniques and materials described in this chapter are considered here for their prospects for future progress.

Defects The work presented here has not been optimised for the removal of defects, which requires additional control of evaporation rates, addition or suppression of salts, heating, additional magnetic fields and sonication. However, the levels of defects demonstrated in the different structures do not appear higher than in flat films, in which defects may be suppressed through optimisation. [39] Optimisation of the self-assembly technique therefore represents a feasible and important future challenge.

In the 3D spheroid structures, the appearance of defects in the curved films looks significantly reduced due to the single-spot reflection. The extent and mechanism by which the influence of defects on the appearance of the spheroids can be diminished in hierarchical architecture would be valuable.

The shape and internal structure of the spheroids is a particular form of defect which should be investigated. The surface of the spheroids is extremely smooth and well-formed, especially in comparison with alternative processes. However, the connection of the spheres and hemispheres to one another and the film prevents the reproduction of a perfect sphere.

Controlling the orientation and defect resistance in spheroid structures represents a novel challenge with respect to the previous defect-control investigation that has been based on flat films. Further investigation should be carried out into the suppression of the 'stem' effect as multilayers advected into the well-ordered top hemisphere as shown in 6.14 conform to the orientations of both the top curvature and the underlying base layer. Prospects for an increase in humidity allowing for a second stage of tactoid reorientation should be tested.

Pitch Control This investigation into the relative orientation of the different parts of the spheroid would also be usefully generalised to a broad understanding of the effect of confinement on the structurally coloured multilayer. The increase in the pitch length in confinement has been noted in this technique. Quantification of this effect would allow a fully characterised flat-film producing suspension to be used in the templating technique to achieve well defined optical wavelengths for pigment design.

It may be that the juxtaposition of the different multilayer orientations within the spheroid structure are an inherent element in the fabrication technique. This is not necessarily a problem as the orientations might be tuned to reflect complementary peaks. Quantification, modelling and demonstration of spectral peak design would be a valuable tool for future exploitation of the technique.

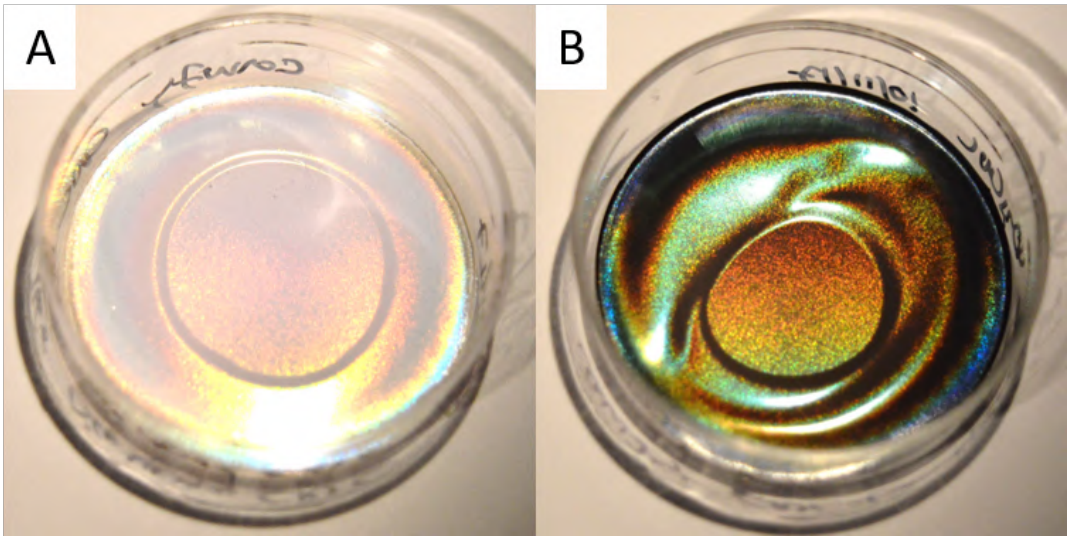

FIGURE 6.20: Photographs of flat self-assembled CNC films approximately 3 cm in diameter. A. Pure CNC film. B: 6 wt% graphene. All work by Cyan Williams, unpublished.

Applications The reflection from structurally coloured material is extremely bright, versatile and has the capacity to replace and enhance colourants in all areas of industrial production. Entirely structural-derived colour is responsible for the most beautiful of natural optical phenomena, and biomimicry is a profoundly important method for understanding and manipulating colouration. However, the characteristic of structural colour that is responsible for the intensity and purity of the colours achievable, its lack of absorption, also represents a challenge. The transparency of structural coloured materials means that additional absorption of the unreflected light by a uniformly dark pigment is important in order to allow structural colour to dominate.

The most important feature of the design for exploitation and improvement of understanding of this structure is the addition of pigment both internally to the helicoid multilayer and as a background, and the use of an embedding matrix. A dark absorbing pigment acts as a contrast to reduce back reflection which diminishes the dominance of the structural effect. The refractive index matching matrix is vital to avoid additional scattering within the material. These colouration concepts were not touched upon in the investigation carried out in this chapter.

Current research into CNC film optimisation is demonstrating the potential for combination of successfully ordered CNCs with absorptive pigments such as carbon black and graphene to improve colouration. The effect of addition of 6 wt% graphene is seen in figure 6.20 in work by Cyan Williams. Addition of the light-absorbing graphene makes the films appear dark, but improves the visibility of the structural colour. The optimisation of this effect in combination with hierarchical structure should be the focus of future work extending the project reported in this chapter.

6.5 Conclusion

In this chapter, a new templating technique was developed and described, and applied successfully to different configurations of the ellipsoidal structure. A small scale, low-relief array was used to show that the non-disrupted assembly of the film in the structure was accomplished. Assembled CNC films were then shown in hemisphere and sphere arrays and the optical response of individual spheroids demonstrated.

Both the hemisphere and spheroid array were shown to reproduce the structurally coloured reflection from the centre of the curved surface, directly mimicking the appearance of cells in *Pollia condensata*. The spheroid structures were shown to better isolate this reflection through the alignment of helicoidal pitches in the rest of the structure away from the plane parallel to the surface. Individual spheroid architecture of the CNC film was shown to dramatically increase the angles at which the spectrum was reflected with respect to a flat film. This represents an improvement in currently reported techniques to create highly curved cellulose multilayers.

The macroscopic effects of the innovative technique remain to be optimised for use as a colourant. For application it is necessary to enhance the material through the addition of an absorption pigment or other method for the suppression of the scattering from other surfaces which dominates the overall reflection. The technique should also be optimised for larger scale production of isolated structures which may be applied as a structurally coloured pigment.

Chapter 7

Conclusion

7.1 Research Questions

The field of structural colour research generates interest as an object of cultural fascination. Evolution in organisms has produced an exquisite range of materials, colours and extraordinary optical effects. Understanding how these work and the unexplored complexities of the natural world contributes a cultural benefit to society, and provides an accessible route for non-scientists to scientific theories, like wave optics, that enrich our understanding of the world. The development of charismatic interdisciplinary research of this kind is a vital part of a society that values scientific research as a cultural good. As publicly funded research, the study presented in this thesis attempted to address this need.

One challenge in assessing structurally coloured material is that the architecture responsible for producing the reflection is necessarily similar to or below the wavelength of visible light. This makes observation of the structure possible only through electron microscopy, which requires destructive preparation. However, due to the intimate link between the structurally coloured material and the reflection spectrum it generates, modelling and analysis of structural colour profiles provides a way to use non-destructive optical spectroscopy to observe the sub-wavelength material that generates it. This approach uses the sensitivity of interference reflection to overcome the limits of optical resolution and material transparency and generate information about sub-wavelength structures. Due to the non-invasive and non-destructive approach, it also allows us to carry out this analysis on developing materials without interrupting their growth.

Nevertheless, very few studies of structural colour have made use of this approach to understand how the architecture develops. This study intended to bridge the gap and demonstrate the application of the physical understanding of structural colour and materials to optically characterise sub-wavelength biological development. This offers a different perspective on cell wall growth, the study of which remains a focus of research in contemporary biology and biochemistry.

The extent of structural colouration in plants remains unclear, as well as how and with what functional adaptation it has evolved, and how it is used as a tool by plants for visual appearance in their environment. These factors have relevance for understanding ecological interactions, plant biology and animal vision. The extension of our understanding to *Pollia* and *Viburnum* in this report therefore represents a useful advance.

Another benefit that may be directly conveyed by publicly funded research is the development of engineering solutions for widespread application. The study of natural materials provides a solution to challenges through biomimesis, in which principles from the evolution-honed responses to engineering problems are extracted and applied. This research intended to understand tissues making up structurally coloured fruits as advanced optical materials and for artificial mimicry. Inspiration from plants suggests the possibility of producing beautiful and brightly coloured materials that are also biodegradable, biocompatible and sustainable.

One such material which has generated significant interest in the possibility of its exploitation for pigmentation is cellulose nanocrystal (CNC) helicoidal self-assembled film. This material has a strong structural and optical resemblance to the structure in *Pollia* cells. Research into the adaptation of optically reflecting cellulose cell wall material was proposed to gain insight directly on manipulation of CNC films. The theory developed to model CNC films in turn was applied to understand the development of the cell wall material. This interdisciplinary approach was designed to enhance the progress of both fields.

7.2 Results

A significant proportion of the research presented, described in chapters 2 - 4 is focused on *Pollia*. I demonstrated the exploitation of a structurally coloured helicoidal cellulose by four species in the genus using varying cell configurations to create different different visual appearances. I demonstrated the particularly unusual existence of right handed helicity existing in only one of the four species, *P. condensata* and showed that cells with this handedness also exhibit a longer pitch. The importance of right handed helicoidal cellulose material in this species is of particular interest because right handed architectures do not self-assemble in artificial CNC materials. This result indicates that in *P. condensata* the existence of right handed architecture is associated with a modified material or growth process.

In chapters 3 and 4 I used the model of optically reflecting helicoidal cellulose to directly observe cell wall development. The use of a series of optical cell-by-cell observations over the course of fruit maturation produced an understanding of the spectral transition undergone by cell walls. Modelling of this change showed that the

transition could be described by a build up of the cell wall in layers laid down with a permanent configuration. A gradual growth in the intensity of the light reflected, associated with no change in the peak wavelength in *P. japonica* was observed. In *P. condensata* a similar gradual increase in the intensity of the cells was observed. The peak wavelength was seen to vary slightly more over the maturation time. However no consistent red- or blue-shift was observed in the cells in general.

The development of the structurally coloured peak was modelled as a helicoidal cellulose photonic crystal with variable pitch lengths. This variation of pitches was demonstrated to be able to account for the changes in peak wavelength seen in the development of structural colour in *P. condensata*. No difference was observed between the development of left and right handed cells of *P. condensata* beyond the reaffirmation of a consistently longer average wavelength reflected by the measured right handed cells. However, a significantly greater variation of peak wavelength during maturation was observed in the *P. condensata*, as well as a much wider variation in the range of peak wavelengths measured between cells.

A particularly striking outcome of the development studies was that in both cases the structurally coloured material developed independently of the pigmented component of the fruit's appearance. Dominance of the fruits' appearance by structural colour did not occur until a further change in pigmentation as dark pigments developed underneath the structurally coloured cells and absorbed the scattered light that had previously dominated the reflection.

A further unanticipated observation made during the development of *P. japonica* was the transition to its final appearance, which happens in each cell quickly and from the perspective of the cells' visual appearance, reversibly, via dehydration of the cells' internal cavity. The existence of a different internal phase within the cell wall cavity distinguishes the *P. japonica*'s overall appearance from the other *Pollia* species studied, which are entirely filled with cell-wall material. The dehydration causes a scattering effect which makes the appearance of most cells a more scattering matte pale blue, rather than the distinct 'pixelated' reflections observed from the centre of cells in *P. condensata*.

Electron microscopy was used to compare cell cross-section morphology in the two *Pollia* species at different stages of development with the optical analysis. The cell-wall cross-sections were consistent with the optical analysis and theory proposed, within the limitations of the electron microscopy techniques. Significant cell wall thickness was shown to be present in intermediate stages of both fruits. Use of profiles extracted from the electron microscopy cross-sections was able to produce numerically modelled optical profiles in line with observed peaks, although there was a small discrepancy in the *P. japonica* cell, which was attributed to the resolution limitation of the electron microscopy images and accepted limits of accuracy in the TEM preparation technique.

As well as the studies on *Pollia*, optical analysis of structural colour in fruits was extended to two species commonly found as ornamental plants in UK gardens, *Viburnum tinus* and *Viburnum davidii*. The existence of structural colour effects reflecting light with a retained linear polarisation, and also with a scattered polarisation were shown. A periodic globular layered structure within a specialised cell wall was identified as the source of the structural colour.

A similarity shared by the *V. davidii* and *P. condensata* is the reflection under low-angle illumination in a microscope from only a central region of the cell. This was attributed in both cases to the curvature of the reflecting layer structure.

This optical response was successfully replicated in the hierarchical structuring of CNC film. Successful fabrication of this material was shown using a novel technique to template CNC film with the biomimetic shape and size of the fruit cells described in the earlier chapters. The circularly polarised structural colour of the film was retained and successfully adapted by the technique to partially resemble the appearance of the individual *P. condensata* fruit cells. The shape was also shown to enhance the angular independence of the film, a feature not directly addressed in studies of the fruit due to the inaccessibility of cells embedded within the epicarp surface.

7.3 Implications

7.3.1 Structural Colour in Nature

The research presented contributes to the body of knowledge on structural colour in plants by extending the species, materials and optical responses known. The use of structural colour by plants may be less ostentatious than the most famous of the structural colours in peacocks and butterflies, but it nevertheless produces distinctive appearances in fruits. Fruit colourations are generally signals to seed dispersers and therefore often show enhancements to detectability [241] or indication of nutritional content. [242] The evolution of complex optical materials in both genera studied is evidence that structural colour may be a common feature in plant materials, and play a crucial role in signalling between plant species and the animal seed-dispersers as the intended recipients of the signal.

The work described in this thesis used circular polarisation optical microscopy to analyse the unique known occurrence of right handed helicoidally structured cellulose, indicating the possibility that biochemical analysis of the right handed helicoid could identify an extra material component which could allow for the artificial construction of right handed helicoidal cellulose.

Analysis of the development of structurally coloured cell walls in *Pollia* fruit cell walls of two different species showed observation of cell maturation and cell wall growth in living species. The development of cell walls in *Pollia* fruit cell walls was shown to be consistent with the model for assembly in which layers of cellulose-based fibrils are laid down gradually and that the relative spacing and alignment of the microfibrils assemblies is permanent. Significant movement of cellulose microfibrils after cell wall construction was rejected. This observation should be considered in the development of general models for cell wall growth.

7.3.2 Colouration Engineering Principles

As our understanding of natural structural coloured phenomenon increases, the imaginative and technical toolbox at our disposal for the design and creation of artificial structural colour improves. This thesis draws out a number of themes in the natural exploitation of structural colour, discussed here as qualitative phenomena.

Geometrical Optics

One dimensional Bragg multilayers reflect light with an angular-dependent wavelength, making them iridescent. Three dimensional photonic crystals [243] have higher symmetry and therefore can decrease the dependence of the wavelength on the viewing angle, depending on the level of symmetry within the structure. [244] [245] As mentioned in chapter 3, three dimensional photonic crystals, although known in animals, have only been reported in algae [66] but no higher plants.

Instead of employing a true three dimensional photonic crystal, the use of an additional hierarchical curvature in combination with a one- dimensional planar multilayer extends the dimensionality of the structurally coloured reflection. The use of curvature in photonic structures within cells I have demonstrated, both through identifying the curved cell walls, and reproducing the effect in artificial material, is important to its optical response.

Pixelation

Associated with the cell curvature that is identified as a design principle above is the separation of optical material into discrete structures. Cellular confinement is a feature of all living organisms, and many of the biomaterials they generate. For this reason it might be dismissed again as an accidental or unfortunate side-effect of natural growth processes. However, discrete processing and formation of materials in tiny volumes gives natural tissues benefits too. Gyroids in butterfly wings are

formed under carefully controlled conditions thanks to their cellular origin, and with domains whose different orientation add a disorder and robustness to the angular reflection from the butterfly scales. [246]

The fruit *P. condensata* also benefits from the discreteness of the helicoidal envelopes that make up its cells. Although the helicoidal pitches within each cell reflect a single waveband, the separate reflection from different cells means that cells may differ completely from their neighbours. The cells in the fruit's epidermis are large enough that the distinct colours reflected from them give the fruit's appearance a rich glittery texture, [92] a visual effect that is potentially desirable and attractive in optical design. [247] This can be contrasted with the visual effect produced by the *P. japonica* in which the cells have a narrow range of wavelengths and the cells' point-like optical response is suppressed by scattering. The resulting appearance of the fruit is flat and continuous rather than compartmentalised.

Traditionally, artificial materials are produced in bulk processes with an emphasis on homogeneity and smooth texture. However, large-scale microfluidics [248] and bio-inspired engineering [249] make cellular and compartmentalised materials desirable and attainable. The extension of biomimetics to incorporate cellular design has potential to provide new solutions to pigmentation, such as the attractive 'pixelation' effect of *P. condensata*. Moreover, the ubiquity of electronic screens makes the use of pixelated discretised visual stimuli a natural optical tool.

Scattering and Absorbing Pigment

The most important theme running adjacent to the main conclusions in each of the chapters of this thesis is the importance of scattering and absorbing pigments when combined with structural colour.

Structural colour relies on the constructive interference of reflected waves to produced a brilliant reflection. Any light that is not constructively reflected is allowed to pass through the material. This means that structurally coloured materials are essentially transparent, allowing light to pass through both sides. Moreover, there may be many scattering surfaces in a hierarchically structured material, reflecting a bright broadband spectrum which obscures the structurally coloured peak, or underlying pigments or features that reflect light themselves. Structurally coloured materials without a dark absorptive pigment can therefore appear relatively uninteresting without closer inspection. The addition of a dark pigment absorbs all stray scattering and stops transmitted light, dramatically enhancing the brilliance of the structural colour. This principle is seen in natural structural coloured materials wherever they are found, whether in feathers [199] butterflies [250] or fruits, as discussed in this thesis.

In exploiting structural colour, a dark background is essential for us to see its potential vibrancy. This principle is being used in the engineering of structurally coloured materials through the addition of carbon black nanoparticles [251] [252] and plasmonic nanoparticles [253] like gold. [233] Few studies take a systematic approach to the issue of absorptive pigments for structural colour. Despite success in replicating the optical response of curved helicoidally reflecting cellulose reported in chapter 6, the material produced did not replicate the macroscale effects seen in the whole *Pollia* epicarp. This shortfall is the outcome of an insufficient extent of biomimesis. The geometry includes reflection from prominent low-angle planes in the film which contribute additional scattering. In addition, unlike in the fruits, or in the mimetic materials mentioned above, no absorbing pigmented was included in the design. The reflection is therefore dominated by a significant degree of scattering.

Different structural and chemically pigmented colours complement one another in many biological materials, combining multiple effects beyond just dark pigmentation. [254] The impact and visibility of these effects should be considered when assessing whether the colouration is really an adaptive function; the difference between the display function played by the peacock's tail compared to the apparently accidental by-product of pearlescence visible on the inside of oyster shells. Understanding pigment spectra [255] is not enough to assess the colouration mechanisms employed by biological organisms because of the diversity and complexity of visual responses. The broader context of ocular and neurological factors, psychological and contextual contrast stimuli is vital, for example in the case of blue halo iridescence previously described. [78] The possibility of combining multiple optical effects is an inherent feature of structural colour, due to the selective interaction with only part of the visible spectrum. This suggests a richness of engineering possibilities in combining scattering, pigment and reflective materials.

7.4 Challenges

Working with the developing fruits in this research project required a careful and labour-intensive strategy. The optical technique is transposed from materials and photonics research, and had to be optimised for working with a living specimen. The difficulty of accounting for biological variation presented a challenge to understanding the behaviour of the cells. A significant number of cells were observed in order to make the results meaningful and generalisable beyond individual cells. However, the challenge inherent in finding and measuring the cells made the study imbalanced, and did not generate a large-scale evaluation of right handed cells. A study focused on right handed cells would be a valuable approach to develop understanding of the more unusual architecture. Moreover, an optimised microscopy set-up in which the plant may be allowed to grow underneath the microscope, rather

than be moved in and out of position would radically improve the observations made.

A further challenge to the conclusions drawn is a better understanding of how the TEM samples presented fit into the conclusions. TEM images present a deceptively clear image of sub-wavelength structures. The images produced are very high definition, but in their analysis suggests that the process of embedding, staining, cutting and imaging introduces variable errors depending on the material and technique, as discussed in section 3.6.3. This makes comparison of their analysis difficult. A more in-depth investigation into the effect of the microscopy preparation and imaging would be challenging but would allow for the assessment of the consistency or otherwise of the electron and optical microscopy results to a greater degree of resolution. Optical measurement and modelling of cells before and after preparation for TEM should be used to better understand the effect of resin embedding.

A key area of extension for the questions asked in this thesis is in the development of a more advanced numerical model for immature *Pollia* cells. The model adopted to analyse the biological tissues in this thesis is intentionally simplistic, treating the cell wall material as analogous to an artificial film. However, this model is clearly limited in its capacity to predict the exact spectral response of cellular biological materials, it is treated instead as a demonstration of the theoretical model which is applied to understand the cell wall growth. A much better understanding of the cell growth might be achieved if a model could be developed taking into account the curvature and spatial extent of the cell wall. Additionally, the model should include the effect of pigment and scattering from below or internal to the reflecting cells, and also light reflected from the outer cuticular surface. This model, along with a further optimised experimental approach could allow the structural observation to give a clearer insight into the rate of cell wall growth throughout the maturation process. A model which was able to incorporate these elements would also have significant application in design of structurally coloured artificial materials, by incorporation of other elements.

7.5 Future Perspectives

Further research on the material components and characteristics of right handed cellulose might provide an insight into its occurrence biologically and the possibility of its exploitation. This could be transformative in understanding cell wall development, and potentially for artificial materials too, and is a clear direction for future research. Focus on the early growth and differentiation of cells associated with the septa and vascular tissue, via biological approaches suggest themselves as potential directions.

A full understanding of the relationship between the artificial self-assembled CNC material and its biological analogue is yet to be fully developed. This subject, which this thesis has only alluded to, is a complex biological and biochemical question, but its answer would provide us with a toolbox for understanding how some cell walls become helicoidal, how amongst those, some become structurally coloured, and also potentially provide a toolbox for the creation of other structurally coloured materials from biological or entirely lab synthesised components. This research might also tackle helicoidal structures in nature found in chitin and collagen. These structures, analogous to those in cellulose, are widespread across the natural world, and are adapted to perform many of the same functions. One question might be whether the development patterns seen in these structures is the same as for cellulose, despite their different material. Understanding this would give insight into each material and their development processes.

The parallels with other biological materials, fulfilling in some cases the same function, for example the brightly reflective chitin helicoids in beetles [256] indicate that the structural colour has evolved separately in chitin and cellulose to perform the same role. What exactly this role is in both cases remains unclear. The evolutionary and ecological role of structural colour in different environments, genera and species would be a productive application of the study of this physical and anatomical phenomenon to understanding ecosystems. In the cases of the fruits studied in this thesis, the fruit dispersers of *Pollia* remain unconfirmed, and how the appearance of the fruits works to attract these species is of particular interest. Previous work has suggested a mimicking role for the fruit colouration, [257] although in the environment of many of the *Pollia* species, there is no clear mimicry target. A not entirely understood aspect of the fruits' appearance is whether adaptation in the visual systems of fruit dispersers is sensitive to circularly polarised light, and therefore the circular polarisation itself acts as a conspicuous signal, either for fruits displaying a single or combined handedness.

The fruit dispersers of *Viburnum* are better known, as the species are much better studied. The role of the colouration in attracting these species has not been confirmed. However, Blackcaps, small birds which are known dispersers [186] of *Viburnum tinus* have been investigated for their preferences when choosing other berries to eat. Studies have demonstrate the importance of both anthocyanins [258] and lipids [259] to these birds in their diet. Anthocyanins have been demonstrated to enhance Blackcaps' immune systems [258] and lipid-rich foods are especially important in migration and during winter. [259] In these two studies, Blackcaps were shown to selectively choose fruits with higher anthocyanin and lipid content with 'reasonable accuracy' based on their appearance. In both cases an increase in the target nutrient was associated with a darker appearance in the fruits investigated, differences which were shown at a local level. *V. tinus* fruits have been shown to

contain both anthocyanins [189] and high levels of lipids. [260] Both of these materials are implicated in the proposed structure responsible for the bright metallic blue colour of the fruit. Research into whether colouration is an honest signal for the nutritional value of the fruit in either or both components, and can be used as such by Blackcaps would be useful for understanding plant-animal communication.

Finally, the exploitation of the biomimetic technique demonstrated in templating of CNC film in combination with dark pigmentation and scattering in line with the principles outlined would be a productive line of research. Beyond that optimisation for industrial application is both feasible and foreseeable. The opportunity to replace chemical pigments with structurally coloured ones is a chance to improve the quality and environmental impact of artificial colouration in everyday life. We should welcome structural colour engineering soon bearing fruit.

Appendix A

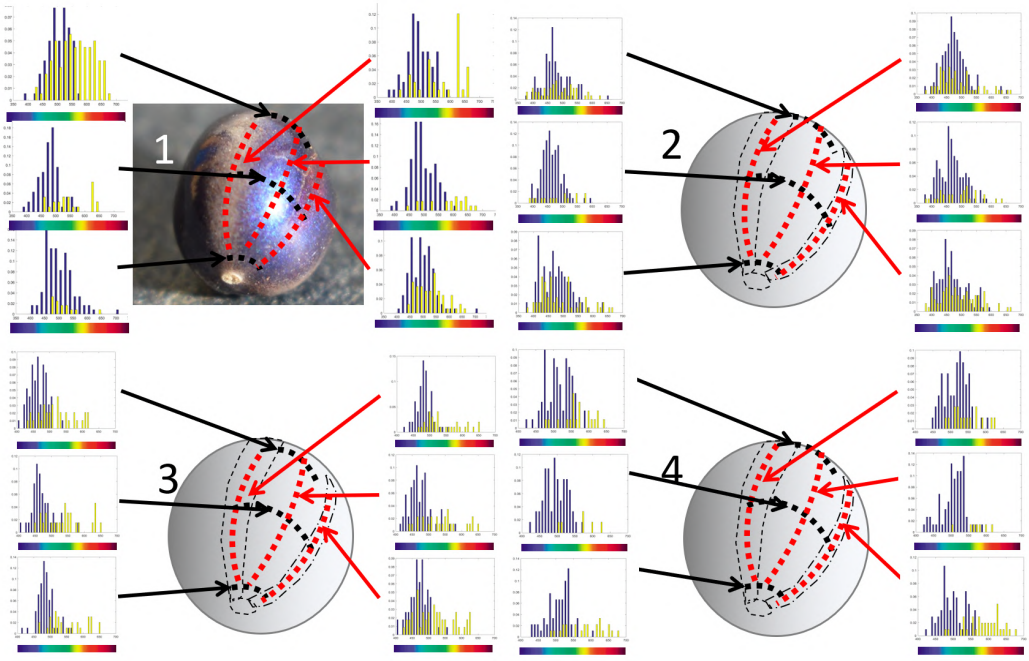

FIGURE 1: Four fruits were surveyed to understand the distribution of polarisation and spectral range on the epidermal cell layers. Fruit 1 was shown in figure 2.12 and is shown again here. The cells are shown as a histogram, the number of left handed cells is shown in blue bars, the number of right handed cells are shown in yellow bars. Cells were surveyed using nine locations on each of the fruits, at the front, middle and back along two adjacent stripes, and between the stripes. The histograms show a very patchy distribution, with locations of strongly varying numbers of right handed cells, which tend but not always to be red-shifted with respect to the left handed circularly polarised cell spectra.

Appendix B

Initially measurements took approximately half an hour and were repeated up to four-five times a day, during which time the target area was exposed to focused white light from the microscope lamp. After five days a pigmented line developed through the area, clearly the result of damage to the fruit from light exposure. This sort of pigmentation was not visible anywhere else on this or any other fruit. Unfortunately this mean that the last few measurements had to be abandoned, and the observation reinitialised on a different fruit. Furthermore, the overexposure of the fruit demonstrated a need to reduce the time the fruit was exposed to the light in order to measure a full maturation. For this reason, the target cells in part two were measured at most twice a day, and the intensity and aperture were reduced as far as possible whilst still maintaining a clear characterisation of the reflected spectrum.

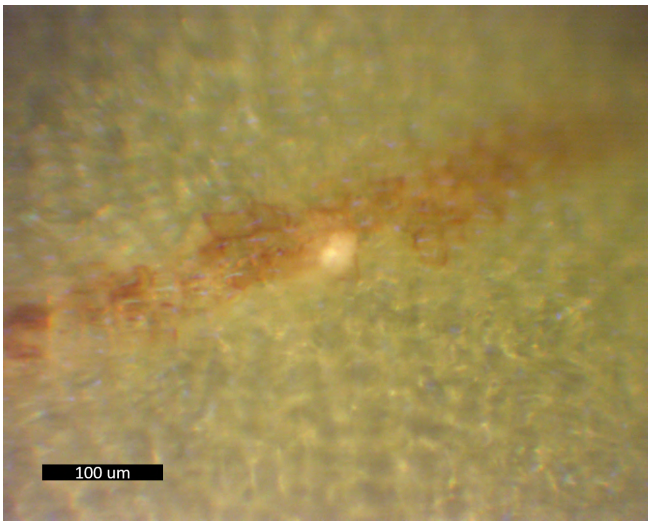

FIGURE 2: The same area shown in figure 3.9 after overexposure to focused light over the period of one week, damage is visible in the form of a brown pigmented line.

Appendix C

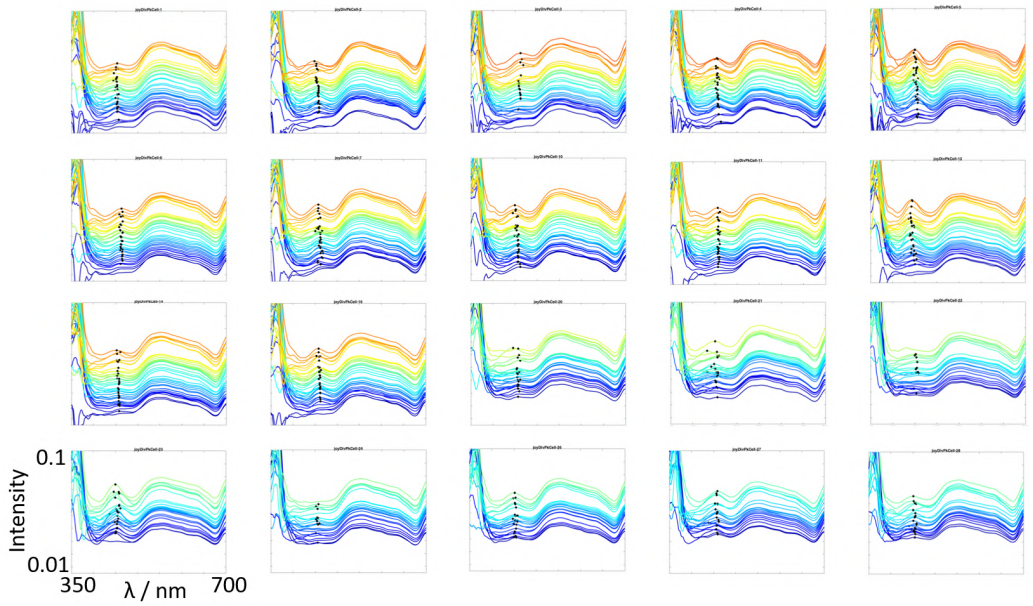

FIGURE 3: Each of the cells measured in the first part of the *P. japonica* development study presented in chapter 3 are represented here by one graph. Each spectral measurement is plotted. Increasing time is indicated in the line colour changing from blue to red, and an offset on the y axis. The identified structurally coloured peak is indicated with a black dot. Axes indicated are uniform for all plots.

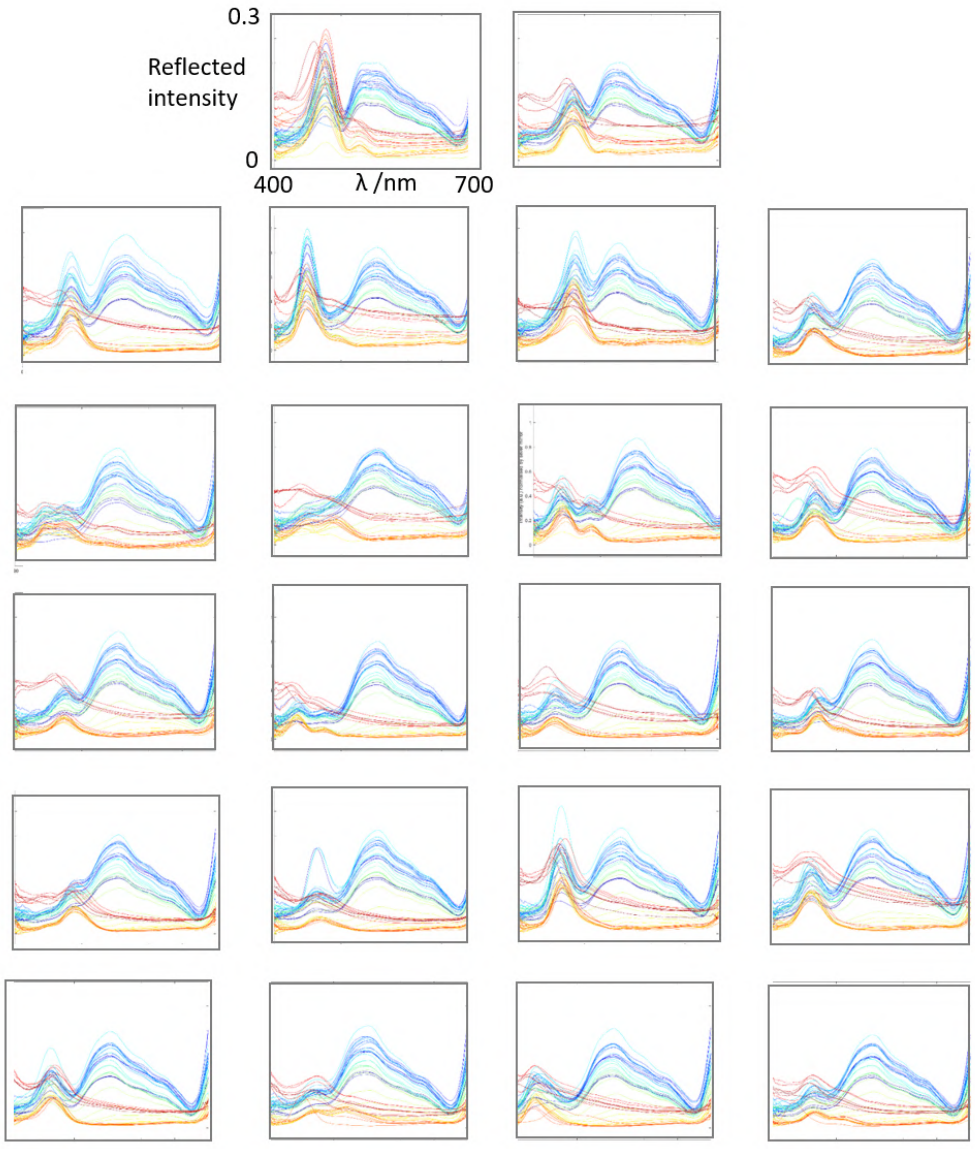

FIGURE 4: The progression of every monitored *P. japonica* cell during 'part 2' i.e. maturation after the first week. The spectra are colour coded chronologically with blue being the earliest scan, and red the latest. The key features of the scans are the structurally coloured peak below 500 nm wavelength, and the chlorophyll signal which is the majority of the spectrum above 500 nm. Axes indicated are uniform for all plots.

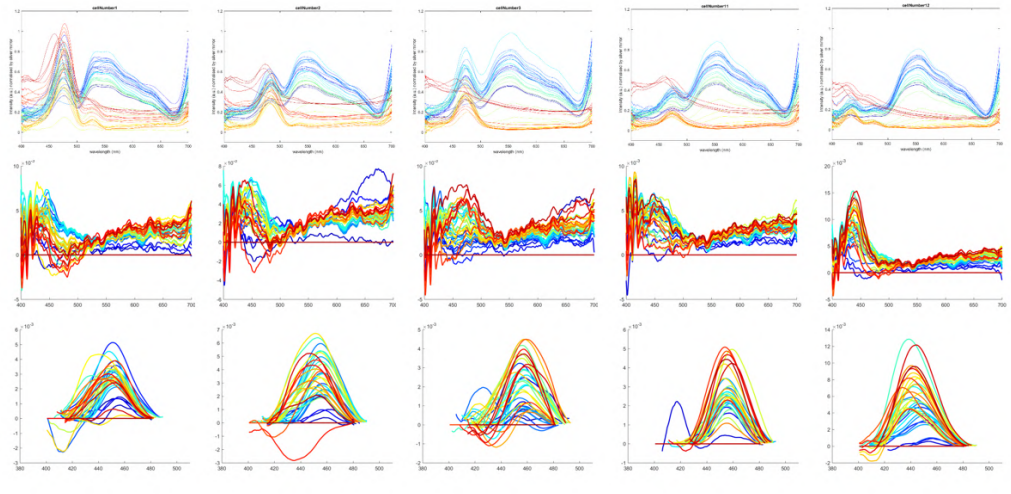

FIGURE 5: A number of cells are considered, the top row shows the original data set. The second row shows the same data with the subtraction of a chlorophyll profile scaled by the cell intensity. The third row shows the peaks only with a subtraction assuming a linear component of the chlorophyll between the turning points on either side of the structural coloured peak.

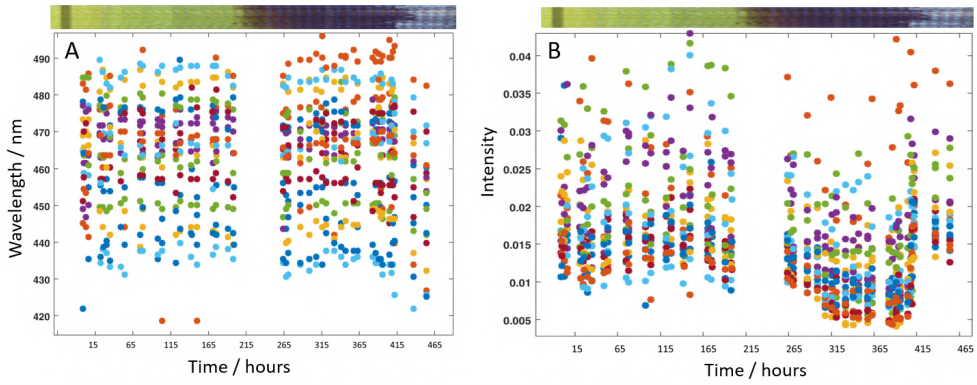

FIGURE 6: After processing by assuming a linear pigmented baseline, the structural colour peaks were analysed for each cell and plotted over time in terms of peak wavelength (left plot) and peak intensity (right plot). The montage of all cell images is shown over the top of the spectra indicating the transitions between the different stages. The intensity measurement clearly correlates to the overall intensity of the cell image, which is dominated by the pigment contribution, indicating tat the attempt to remove the impact of the chlorophyll was unsuccessful.

Appendix D

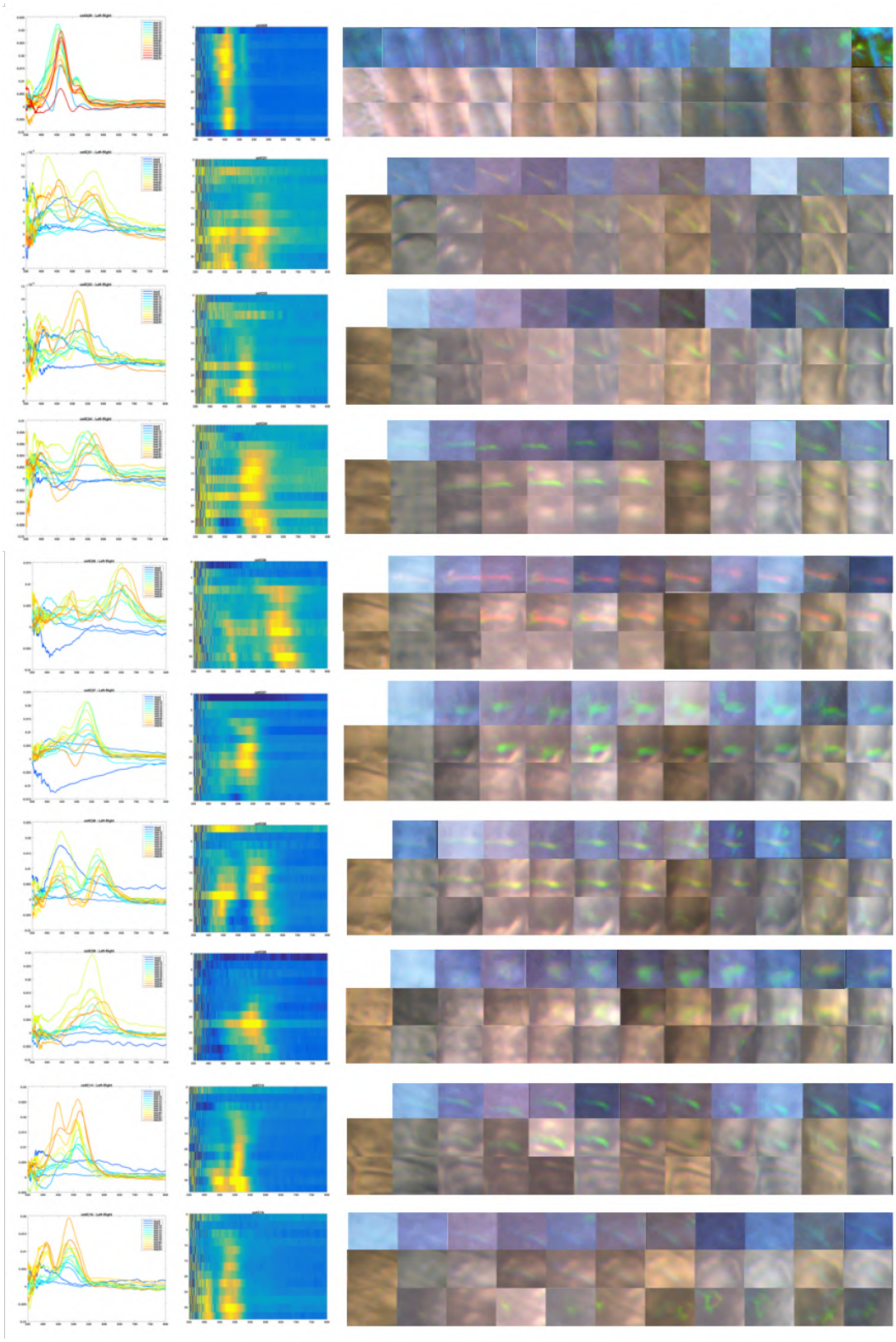

FIGURE 7

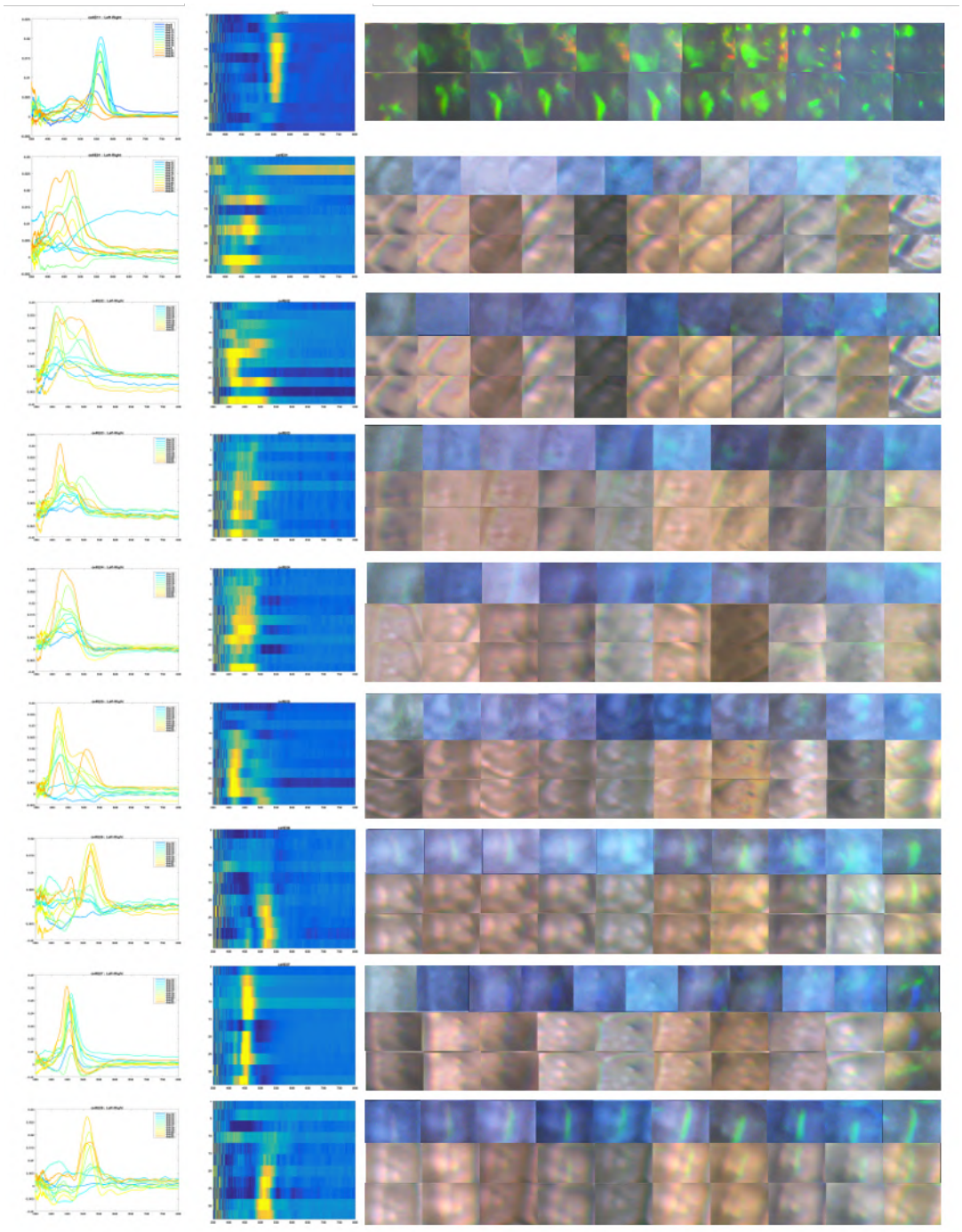

FIGURE 8

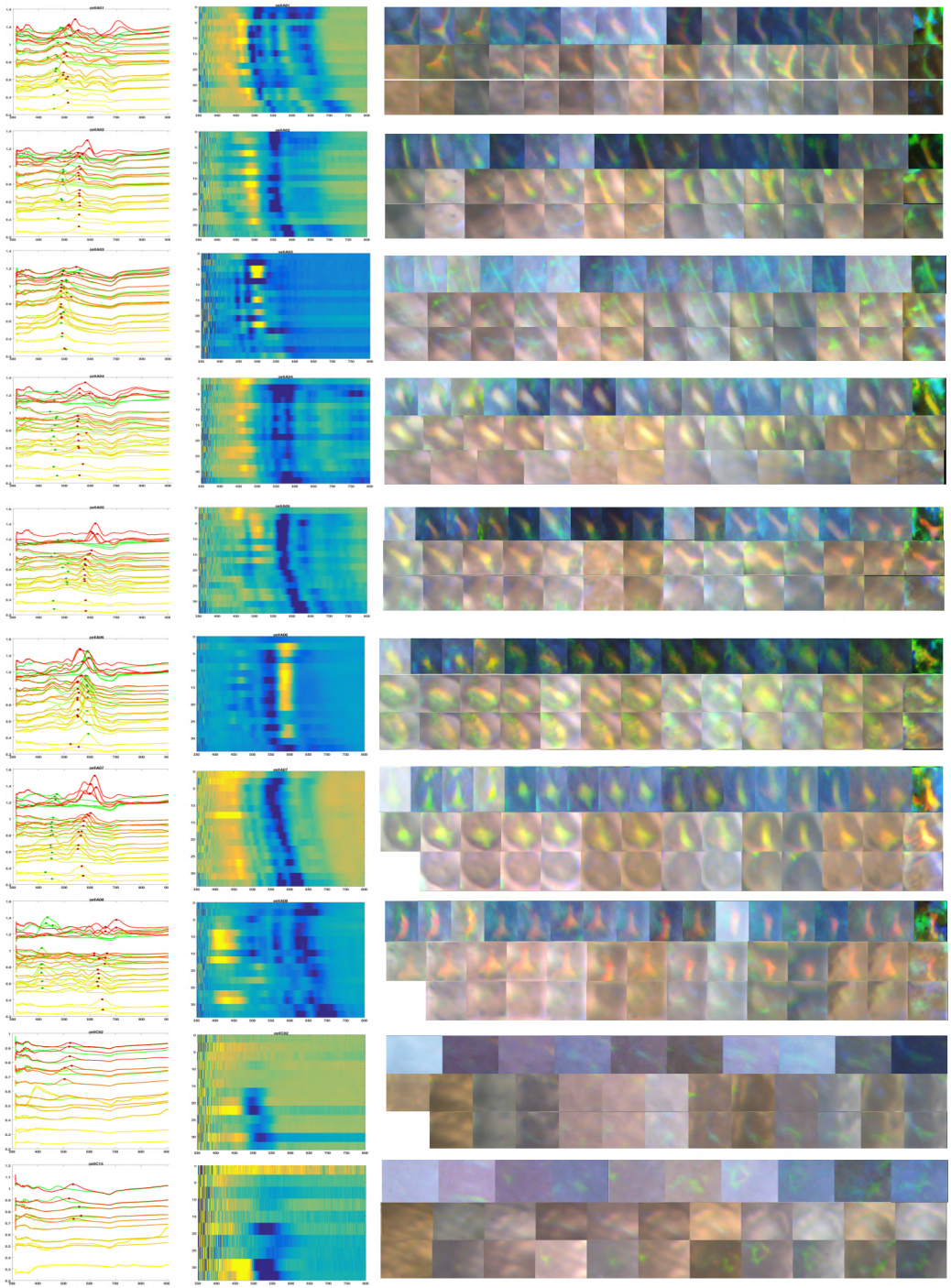

FIGURE 9

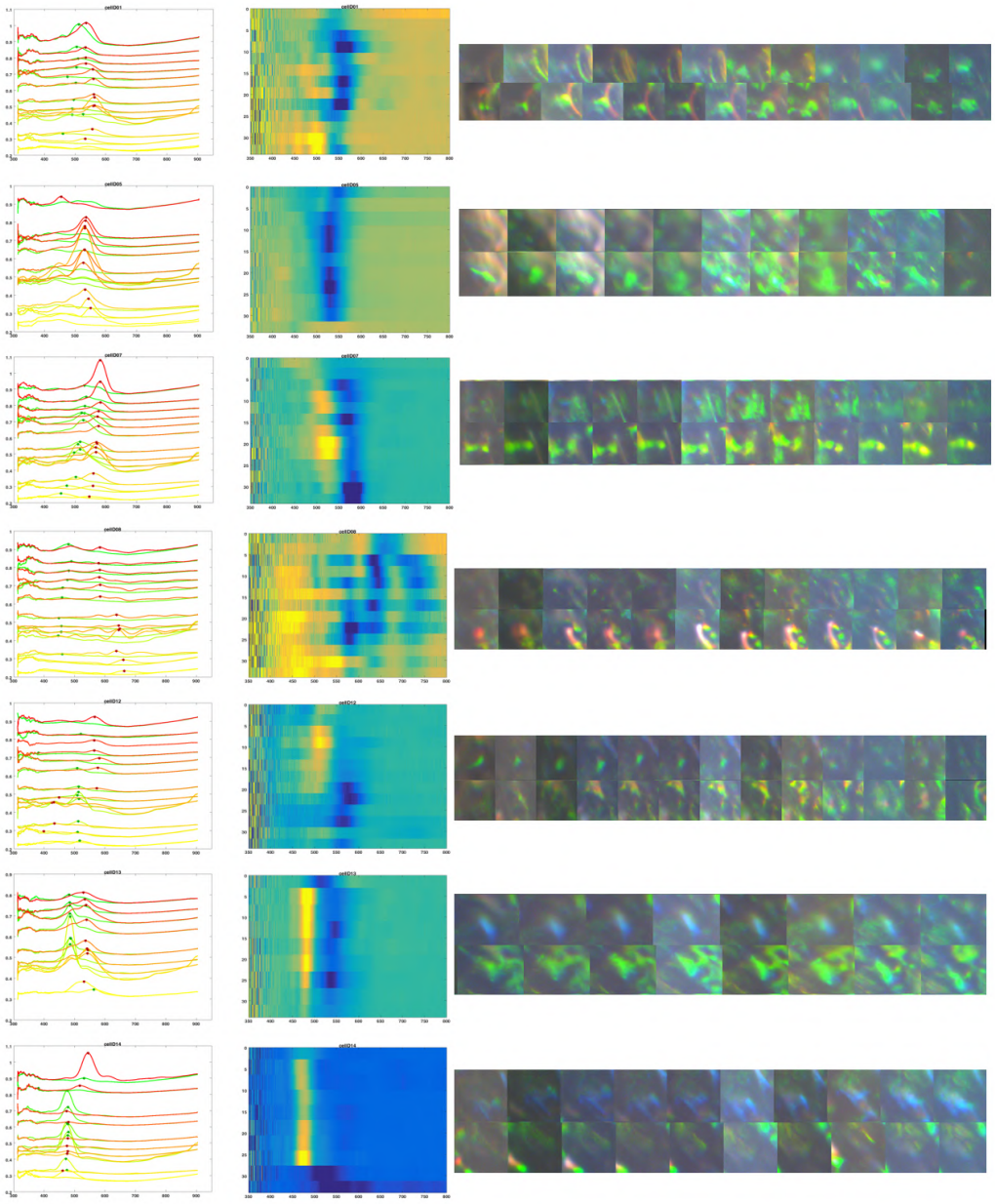

FIGURE 10

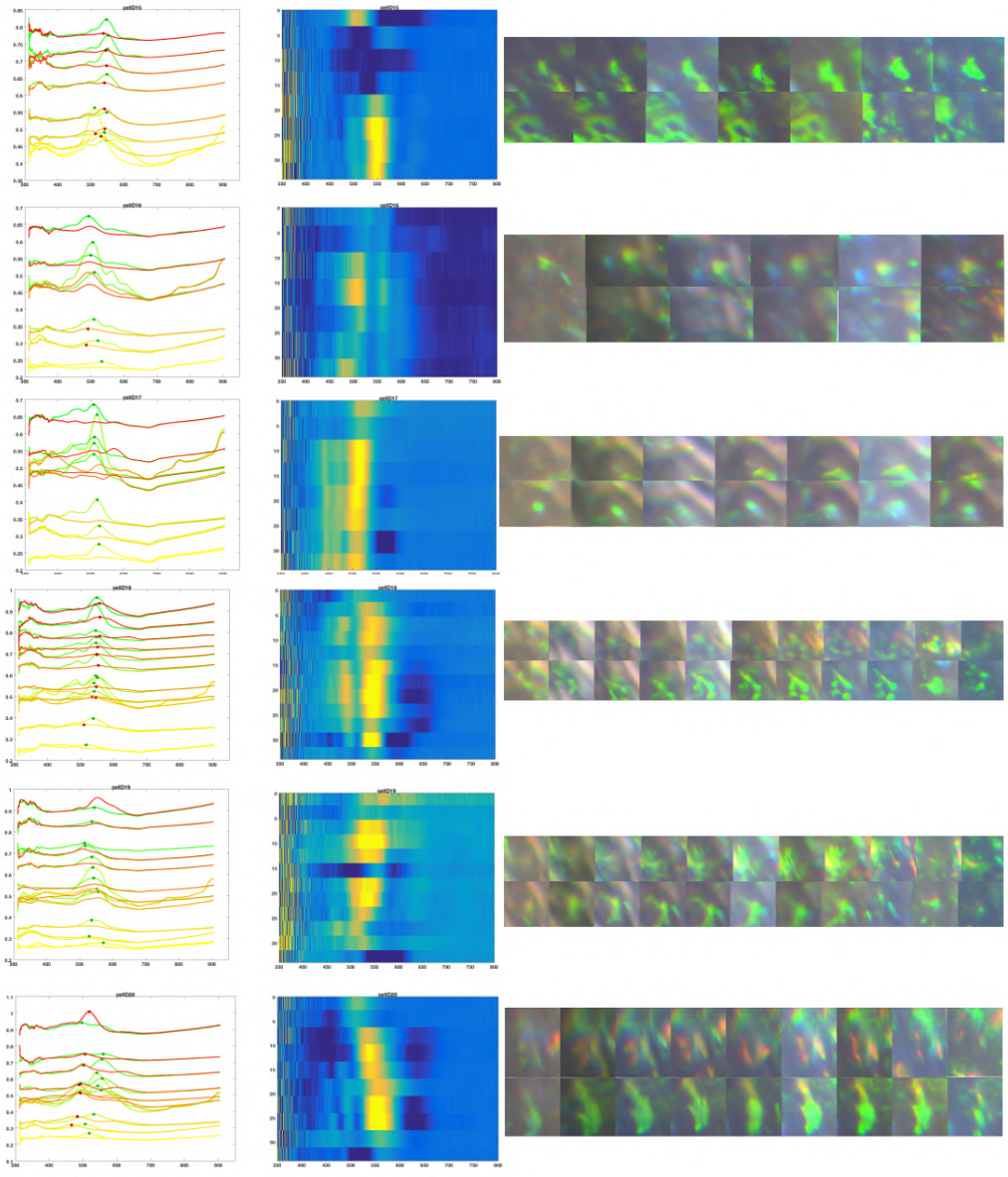

FIGURE 11

Bibliography

[1] Horst Schulze. *Researchers from Cambridge University Visit Kenya to Study 12 Million Year Old Fossil Microscope donation from ZEISS enables examination of valuable specimens in National Museums of Kenya (NMK), Nairobi*. 2016. URL: https://blogs.zeiss.com/microscopy/news/en/researchers-from-cambridge-university-visit-kenya-to-study-12-million-year-old-fossil/.

[2] Pochi Yeh. *Optical Waves in Layered Media*. Ed. by Bahaa E. A. Saleh. Hoboken: John Wiley & Sons, 1998. ISBN: 0-471-73192-7.

[3] R. de L. Kronig and W.G. Penney. "Quantum Mechanics of Electrons in Crystal Lattices". In: *Proc. Roy. Soc.* 139 (1931), p. 499.

[4] J. Korringa. "On the calculation of a the energy of a Bloch wave in a metal." In: *Physica* 13.6 (1947), pp. 392–400.

[5] S. Satpathy, Ze Zhang, and M.R. Salehpour. "Theory of photon bands in three-dimensional periodic dielectric structures". In: *Physical Review Letters* 66.3 (1991), p. 393. ISSN: 00319007. DOI: 10.1103/PhysRevLett.66.393.

[6] Daniel M. Mittleman et al. "Optical properties of planar colloidal crystals: Dynamical diffraction and the scalar wave approximation". In: *Journal of Chemical Physics* 111.1 (1999), pp. 345–354. ISSN: 00219606. DOI: 10.1063/1.479276.

[7] K.M. Ho, C.T. Chan, and C.M. Soukoulis. "Existence of a Photonic Gap in Periodic Dielectric Structures". In: *Physical Review Letters* 65.25 (1990), pp. 3152–3155.

[8] E. Yablonovitch, T. J. Gmitter, and K. M. Leung. "Photonic band structure: The face-centered-cubic case employing nonspherical atoms". In: *Physical Review Letters* 67.17 (1991), pp. 2295–2298. ISSN: 00319007. DOI: 10.1103/PhysRevLett.67.2295.

[9] E. Yablonovitch. "Photonic band-gap structures". In: *Journal of the Optical Society of America B* 10.2 (1993), p. 283. ISSN: 0740-3224. DOI: 10.1364/JOSAB.10.000283. URL: http://www.opticsinfobase.org/abstract.cfm?URI=josab-10-2-283{\%}0A.

[10] Sajeev John. "Strong localization of photons in certain disordered dielectric superlattices". In: *Physical Review Letters* 58.23 (1987), pp. 2486–2489. ISSN: 00319007. DOI: 10.1103/PhysRevLett.58.2486.

[11] Naemi Waeselmann. "Structural transformations in complex perovskite-type relaxor and relaxor-based ferroelectrics at high pressures and temperatures". PhD thesis. University of Hamburg, 2012.

[12] W.H. Bragg and W.L. Bragg. "The reflection of X-rays by crystals". In: *Proc. R. Soc. Lond. A* 88.605 (1913), pp. 428–438.

[13] S. Kinoshita, S. Yoshioka, and J. Miyazaki. "Physics of structural colors". In: *Reports on Progress in Physics* 71.7 (2008), p. 076401. ISSN: 0034-4885. DOI: 10.1088/0034-4885/71/7/076401. URL: http://stacks.iop.org/0034-4885/71/i=7/a=076401?key=crossref.3afb50a9a9544f56b392e59620e5d674.

[14] Max Born and Ernst Wolf. *Principles Of Optics*. Pergamon Press, 1959.

[15] Shuichi Kinoshita. *Structural Colors in the Realm of Nature*. World Scientific Publishing Co. Singapore, 2008, pp. 076401–076431. ISBN: 9789812707833.

[16] Gerhard Pfaff and Peter Reynders. "Angle-Dependent Optical Effects Deriving from Submicron Structures of Films and Pigments". In: *Chem. Rev.* 99 (1999), pp. 1963–1981. DOI: 10.1021/cr970075u.

[17] R. Clark Jones. "I . Description and Discussion of the Calculus". In: *J.O.S.a.* 31 (1941), pp. 488–493. DOI: http://dx.doi.org/10.1364/JOSA.31.000488.

[18] Dave3457. *Diagram of circular polarization*. 2013. URL: https://en.wikipedia.org/wiki/Circular{_}polarization.

[19] Garth J. Simpson. *Nonlinear optical polarisation analysis in chemistry and biology*. cambridge: Cambridge University Press, 2017, pp. 1–16. DOI: 10.1017/9781139019026.001.

[20] Friedrich Reinitzer. "Contributions to the knowledge of cholesterol". In: *Liquid Crystals* 5.1 (1888), pp. 7–18. ISSN: 13665855. DOI: 10.1080/02678298908026349.

[21] C. W. Oseen. "The Theory of Liquid Crystals". In: *Trans Faraday Soc* 29.l (1932), p. 833.

[22] Hl. de Vries. "Rotatory power and other optical properties of certain liquid crystals". In: *Acta Crystallographica* 4.3 (1951), pp. 219–226. ISSN: 0365-110X. DOI: 10.1107/S0365110X51000751.

[23] Harry Coles. "Chiral Nematics: Physical Properties and Applications". In: *Handbook of Liquid Crystals*. Wiley-VCH Verlag GmbH, 1998, pp. 335–409.

[24] E. I. Kats. "Optical Properties of Cholesteric Liquid Crystals". In: *Soviet Physics JETP* 32.5 (1971), pp. 1004–1007.

[25] Rajaram Nityananda. "On the Theory of Light Propagation in Cholesteric Liquid Crystals". In: *Molecular Crystals and Liquid Crystals* 21 (1973), pp. 315–331. ISSN: 0026-8941. DOI: 10.1080/15421407308083326. arXiv: 1709.07277. URL: http://arxiv.org/abs/1709.07277.

[26] Cécile Malgrange, Christian Ricolleau, and Michel Schlenker. "Rotatory Power and Optical Activity". In: *Symmetry and Physical Properties of Crystals*. Dordrecht: Springer Netherlands, 2014, pp. 385–406. ISBN: 978-94-017-8993-6. DOI: 10.1007/978-94-017-8993-6_18. URL: https://doi.org/10.1007/978-94-017-8993-6{_}18.

[27] C. Elachi and C. Yeh. "Stop bands for optical wave propagation in cholesteric liquid crystals". In: *Journal of the Optical Society of America* 63.7 (1973), p. 840. ISSN: 0030-3941. DOI: 10.1364/JOSA.63.000840. URL: http://www.opticsinfobase.org/abstract.cfm?URI=josa-63-7-840.

[28] P. S. Hauge, R. H. Muller, and C. G. Smith. "Conventions and formulas for using the Mueller-Stokes calculus in ellipsometry". In: *Surface Science* 96.1-3 (1980), pp. 81–107. ISSN: 00396028. DOI: 10.1016/0039-6028(80)90296-4.

[29] A. C. Neville. *Biology of Fibrous Composites*. Cambridge University Press, 1993. ISBN: 0-521-41051-7.

[30] Gary H. Conners. "Electromagnetic Wave propagation in cholesteric materials". In: *J. of the Opt. Soc. of America* 58.7 (1968), pp. 875–879.

[31] A. C. Neville and B. M. Luke. "Form optical activity in crustacean cuticle". In: *Journal of Insect Physiology* 17 (1971), pp. 519–526. ISSN: 00221910. DOI: 10.1016/0022-1910(71)90030-8.

[32] R. Middleton, U. Steiner, and S. Vignolini. "Bio-mimetic Structural Colour using Biopolymers". In: *Bio-Inspired Polymers*. Royal Society of Chemistry, 2016. Chap. 17, pp. 561–591. ISBN: 978-1-78262-413-4. DOI: 10.1039/9781782626664-00555.

[33] D. W. Berreman. "Optics in Stratified and Anisotropic Media: 4x4-Matrix Formulation". In: *Journal of the Optical Society of America* 62.4 (1972), pp. 502–510. ISSN: 0030-3941. DOI: 10.1364/JOSA.62.000502.

[34] H. G. Yoon and H. F. Gleeson. "Accurate modelling of multilayer chiral nematic devices through the Berreman 4 × 4 matrix methods". In: *Journal of Physics D: Applied Physics* 40.12 (2007), pp. 3579–3586. ISSN: 0022-3727. DOI: 10.1088/0022-3727/40/12/006.

[35] Doekele G. Stavenga et al. "High refractive index of melanin in shiny occipital feathers of a bird of paradise". In: *Light: Science & Applications* 16.November 2014 (2015), pp. 1–6. ISSN: 2047-7538. DOI: 10.1038/lsa.2015.16.

[36] Jun Xu and Zhiguang Guo. "Biomimetic photonic materials with tunable structural colors". In: *Journal of Colloid and Interface Science* 406 (2013), pp. 1–17. ISSN: 00219797. DOI: 10.1016/j.jcis.2013.05.028. URL: http://dx.doi.org/10.1016/j.jcis.2013.05.028.

[37] Hua Zhu. "A Biogeographical Comparison Between Yunnan, Southwest China, and Taiwan, Southeast China, with Implications for the Evolutionary History of the East Asian Flora". In: *Annals of the Missouri Botanical Garden* 101.4 (2016), pp. 750–771. ISSN: 0026-6493. DOI: 10.3417/2011037. URL: http://www.bioone.org/doi/10.3417/2011037.

[38] Ahu Gumrah Dumanli et al. "Controlled, bio-inspired self-assembly of cellulose-based chiral reflectors". In: *Advanced Optical Materials* 2.7 (2014), pp. 646–650. ISSN: 21951071. DOI: 10.1002/adom.201400112.

[39] Richard M. Parker et al. "The Self-Assembly of Cellulose Nanocrystals: Hierarchical Design of Visual Appearance". In: *Advanced Materials* 1704477 (2017), p. 1704477. ISSN: 09359648. DOI: 10.1002/adma.201704477. URL: http://doi.wiley.com/10.1002/adma.201704477.

[40] H. H. Mollenhauer. "Artifacts casued by dehydration and epoxy embedding in transmission electron microscopy". In: *Microscopy research and technique* 26.1 (1993), pp. 496–512.

[41] Caroline A. Schneider, Wayne S. Rasband, and Kevin W. Eliceiri. "NIH Image to ImageJ: 25 years of image analysis". In: *Nature Methods* 9.7 (2012), pp. 671–675. ISSN: 15487091. DOI: 10.1038/nmeth.2089. arXiv: arXiv:1011.1669v3. URL: http://dx.doi.org/10.1038/nmeth.2089.

[42] Johannes Schindelin et al. "Fiji: An open-source platform for biological-image analysis". In: *Nature Methods* 9.7 (2012), pp. 676–682. ISSN: 15487091. DOI: 10.1038/nmeth.2019. arXiv: 1081-8693.

[43] Caleb Q. Cook and Ariel Amir. "Chirped photonic crystals: a natural strategy for broadband reflectance". In: (2016). arXiv: 1608.05831. URL: http://arxiv.org/abs/1608.05831.

[44] S. Yoshioka and S. Kinoshita. "Effect of Macroscopic Structure in Iridescent Color of the Peacock Feathers". In: *Forma* 17 (2002), pp. 169–181.

[45] T. J. Wardill et al. "Neural control of tuneable skin iridescence in squid". In: *Proceedings of the Royal Society B: Biological Sciences* 279.1745 (2012), pp. 4243–4252. ISSN: 0962-8452. DOI: 10.1098/rspb.2012.1374.

[46] Richard O. Prum and Rodolfo H. Torres. "Structural colouration of mammalian skin: convergent evolution of coherently scattering dermal collagen arrays." In: *The Journal of experimental biology* 207.Pt 12 (2004), pp. 2157–2172. ISSN: 0022-0949. DOI: 10.1242/jeb.00989.

[47] Dvir Gur et al. "Structural Basis for the Brilliant Colors of the Sapphirinid Copepods". In: *Journal of the American Chemical Society* (2015), p. 150626131826007. ISSN: 0002-7863. DOI: 10.1021/jacs.5b05289. URL: http://pubs.acs.org/doi/abs/10.1021/jacs.5b05289.

[48] Andrew R. Parker et al. "Structural colour: opal analogue discovered in a weevil." In: *Nature* 426.December (2003), pp. 786–787. ISSN: 0028-0836. DOI: 10.1038/426786a.

[49] Villads Egede Johansen et al. "Genetic manipulation of structural color in bacterial colonies". In: *Proceedings of the National Academy of Sciences* (2018), p. 201716214. ISSN: 0027-8424. DOI: 10.1073/pnas.1716214115. URL: http://www.pnas.org/lookup/doi/10.1073/pnas.1716214115.

[50] Tomasz M. Trzeciak and Peter Vukusic. "Photonic crystal fiber in the polychaete worm Pherusa sp." In: *Physical Review E - Statistical, Nonlinear, and Soft Matter Physics* 80.6 (2009), pp. 1–6. ISSN: 15393755. DOI: 10.1103/PhysRevE.80.061908.

[51] Trevor Williams. "Natural invertebrate hosts of iridoviruses (Iridoviridae)." In: *Neotropical entomology* 37.6 (2008), pp. 615–632. ISSN: 1519-566X. DOI: 10.1590/S1519-566X2008000600001.

[52] Ling Li et al. "A highly conspicuous mineralized composite photonic architecture in the translucent shell of the blue-rayed limpet". In: *Nature Communications* 6 (2015), pp. 1–11. ISSN: 20411723. DOI: 10.1038/ncomms7322. URL: http://dx.doi.org/10.1038/ncomms7322.

[53] P. Vukusic et al. "Quantified interference and diffraction in single Morpho butterfly scales". In: *Proc. R. Soc. Lond. B* 266.April (1999), pp. 1403–1411.

[54] Ainsley E. Seago et al. "Gold bugs and beyond: a review of iridescence and structural colour mechanisms in beetles (Coleoptera)." In: *Journal of the Royal Society, Interface / the Royal Society* 6 Suppl 2.October 2008 (2009), S165–S184. ISSN: 1742-5689. DOI: 10.1098/rsif.2008.0354.focus.

[55] J. V. Sanders. "Diffraction of light by opals". In: *Acta Crystallographica Section A* 24.4 (1968), pp. 427–434. ISSN: 16005724. DOI: 10.1107/S0567739468000860.

[56] C. V. Raman and A. Jayaraman. "The Structure of Labradorite and the origin of its iridescence." In: *Proceedings of the Indian Academy of Science* A32 (1950), pp. 1–16.

[57] Robert Hooke. *Micrographia*. Royal Society, 1665.

[58] Pete Vukusic and J. Roy Sambles. "Photonic structures in biology." In: *Nature* 424.August (2003), pp. 852–855. ISSN: 0028-0836. DOI: 10.1038/nature01941.

[59] M. F. Land. "The physics and biology of animal reflectors." In: *Progress in biophysics and molecular biology* 24 (1972), pp. 75–106. ISSN: 00796107. DOI: 10.1016/0079-6107(72)90004-1.

[60] V. L. Welch and J.-P. Vigneron. "Beyond butterflies—the diversity of biological photonic crystals". In: *Optical and Quantum Electronics* 39.4-6 (2007), pp. 295–303. ISSN: 0306-8919. DOI: 10.1007/s11082-007-9094-4. URL: http://link.springer.com/10.1007/s11082-007-9094-4.

[61] Jiyu Sun, Bharat Bhushan, and Jin Tong. "Structural coloration in nature". In: *RSC Advances* 3.35 (2013), p. 14862. ISSN: 2046-2069. DOI: 10.1039/c3ra41096j. URL: http://xlink.rsc.org/?DOI=c3ra41096j.

[62] Marion I. Newbigin. *Colour in Nature*. London: Annals and Magazine of Natural History, 1898.

[63] Priscilla Simonis et al. "Cylindrical Bragg mirrors on leg segments of the male Bolivian blueleg tarantula Pamphobeteus antinous (Theraphosidae)." In: *Optics express* 21.6 (2013), pp. 6979–96. ISSN: 1094-4087. DOI: 10.1364/OE.21.006979. URL: http://www.ncbi.nlm.nih.gov/pubmed/23546081.

[64] Jérémie Teyssier et al. "Photonic crystals cause active colour change in chameleons". In: *Nature Communications* 6 (2015), p. 6368. ISSN: 2041-1723. DOI: 10.1038/ncomms7368. URL: http://www.nature.com/doifinder/10.1038/ncomms7368.

[65] Beverley J. Glover and Heather M. Whitney. "Structural colour and iridescence in plants: the poorly studied relations of pigment colour." In: *Annals of botany* 105.4 (2010), pp. 505–511. DOI: 10.1093/aob/mcq007.

[66] Martin Lopez-Garcia et al. "Light-induced dynamic structural color by intracellular 3D photonic crystals in brown algae". In: *Science Advances* 4.April (2018), pp. 1–9. DOI: 10.1126/sciadv.aan8917.

[67] Edwige Moyroud et al. "Disorder in convergent floral nanostructures enhances signalling to bees". In: *Nature* 550.7677 (2017), pp. 469–474. ISSN: 0028-0836. DOI: 10.1038/nature24285. URL: http://dx.doi.org/10.1038/nature24285.

[68] Kumi Yoshida, Mihoko Mori, and Tadao Kondo. "Blue flower color development by anthocyanins: From chemical structure to cell physiology". In: *Natural Product Reports* 26.7 (2009), pp. 884–915. ISSN: 02650568. DOI: 10.1039/b800165k.

[69] Katherine R. Thomas et al. "Function of blue iridescence in tropical understorey plants." In: *Journal of the Royal Society Interface* 7.53 (2010), pp. 1699–707. ISSN: 1742-5662. DOI: 10.1098/rsif.2010.0201. URL: http://rsif.royalsocietypublishing.org/content/7/53/1699.

[70] Silvia Vignolini et al. "The mirror crack'd: Both pigment and structure contribute to the glossy blue appearance of the mirror orchid, Ophrys speculum". In: *New Phytologist* 196.4 (2012), pp. 1038–1047. ISSN: 0028646X. DOI: 10.1111/j.1469-8137.2012.04356.x.

[71] Elizabeth Bradshaw et al. "Comparative labellum micromorphology of the sexually deceptive temperate orchid genus Ophrys: Diverse epidermal cell types and multiple origins of structural colour". In: *Botanical Journal of the Linnean Society* 162.3 (2010), pp. 504–540. ISSN: 00244074. DOI: 10.1111/j.1095-8339.2010.01033.x.

[72] S. Vignolini et al. "Directional scattering from the glossy flower of Ranunculus: how the buttercup lights up your chin". In: *Journal of The Royal Society Interface* 9.71 (2012), pp. 1295–1301. ISSN: 1742-5689. DOI: 10.1098/rsif.2011.0759.

[73] Heather Whitney et al. "Floral Iridescence, Produced by Diffractive Optics, Acts as a cue for animal pollinators". In: *Science* 323.January (2009), pp. 130–133. DOI: 10.1126/science.1166256.

[74] Susete N. Fernandes et al. "Structural Color and Iridescence in Transparent Sheared Cellulosic Films". In: *Macromolecular Chemistry and Physics* 214.1 (2013), pp. 25–32. ISSN: 10221352. DOI: 10.1002/macp.201200351. URL: http://doi.wiley.com/10.1002/macp.201200351.

[75] Karin Kjernsmo et al. "Iridescence impairs object recognition in bumblebees". In: *Scientific Reports* (2018), pp. 6–10. ISSN: 2045-2322. DOI: 10.1038/s41598-018-26571-6. URL: http://dx.doi.org/10.1038/s41598-018-26571-6.

[76] Heather M. Whitney et al. "Flower iridescence increases object detection in the insect visual system without compromising object identity". In: *Current Biology* 26.6 (2016), pp. 802–808. ISSN: 09609822. DOI: 10.1016/j.cub.2016.01.026. URL: http://dx.doi.org/10.1016/j.cub.2016.01.026.

[77] De Premorel et al. "Higher iridescent-to-pigment optical effect in flowers facilitates learning , memory and generalization in foraging bumblebees". In: *Proc. R. Soc. Lond. B* 284 (2017), p. 20171097. DOI: 10.1098/rspb.2017.1097.

[78] Silvia Vignolini et al. "The flower of Hibiscus trionum is both visibly and measurably iridescent". In: *New Phytologist* (2014), n/a–n/a. ISSN: 1469-8137. DOI: 10.1111/nph.12958. URL: http://dx.doi.org/10.1111/nph.12958.

[79] Chris J. Chandler et al. "Structural colour in Chondrus crispus". In: *Scientific Reports* 5 (2015), pp. 1–10. ISSN: 20452322. DOI: 10.1038/srep11645. URL: http://dx.doi.org/10.1038/srep11645.

[80] Matthew Jacobs et al. "Photonic crystal structure of Begonia chloroplasts enhances photosynthetic efficiency". In: *Nature Plants* October (2016), p. 16162. ISSN: 2055-0278. DOI: 10.1038/nplants.2016.162.

[81] David W. Lee. "Ultrastructural Basis and function of iridescent blue colour of fruits in Elaeocarpus". In: *Nature* 349 (1991), pp. 260–262.

[82] David W. Lee, George T. Taylor, and Anthony K. Irvine. "Structural Fruit Coloration in Delarbrea michieana (Araliaceae)." In: *International journal of plant sciences* 161.2 (2000), pp. 297–300. ISSN: 1058-5893. DOI: 10.1086/314249. URL: http://www.ncbi.nlm.nih.gov/pubmed/10777454.

[83] Greg Strout et al. "Silica nanoparticles aid in structural leaf coloration in the Malaysian tropical rainforest understorey herb Mapania caudata". In: *Annals of Botany* 112.6 (2013), pp. 1141–1148. ISSN: 03057364. DOI: 10.1093/aob/mct172.

[84] Kevin S. Gould and David W. Lee. "Physical and Ultrastructural Basis of Blue Leaf Iridescence in Four Malaysian Understory Plants". In: *American Journal of Botany* 83.1 (1996), pp. 45–50.

[85] Rita M. Graham, David W. Lee, and Knut Norstog. "Physical and Ultrastructural Basis of Blue Leaf Iridescence in Two Neotropical Ferns". In: *American Journal of Botany* 80.2 (1993), pp. 198–203.

[86] A. Nasrulhaq-Boyce and J. G. Duckett. "Dimorphic epidermal cell chloroplasts in the mesophyll-less leaves of an extreme–shade tropical fern, Teratophyllum rotundifoliatum (R. Bonap.) Holtt.: a light and electron microscope study". In: *New Phytologist* 119.3 (1991), pp. 433–444. ISSN: 14698137. DOI: 10.1111/j.1469-8137.1991.tb00044.x.

[87] Chiou Rong Sheue et al. "Bizonoplast, a unique chloroplast in the epidermal cells of microphylls in the shade plant Selaginella erythropus (Selaginellaceae)". In: *American Journal of Botany* 94.12 (2007), pp. 1922–1929. ISSN: 00029122. DOI: 10.3732/ajb.94.12.1922.

[88] Han Zhou et al. "Bio-Inspired Photonic Materials: Prototypes and Structural Effect Designs for Applications in Solar Energy Manipulation". In: *Advanced Functional Materials* 1705309 (2017), p. 1705309. ISSN: 1616301X. DOI: 10.1002/adfm.201705309. URL: http://doi.wiley.com/10.1002/adfm.201705309.

[89] Charles Hebant and David W. Lee. "Ultrastructural Basis and Developmental Control of Blue Iridescence in Selaginella Leaves". In: *American Journal of Botany* 71.2 (1984), pp. 216–219.

[90] Mathias Kolle et al. "Bio-inspired band-gap tunable elastic optical multilayer fibers". In: *Advanced Materials* 25 (2013), pp. 2239–2245. ISSN: 09359648. DOI: 10.1002/adma.201203529.

[91] Silvia Vignolini et al. "Structural colour from helicoidal cell-wall architecture in fruits of Margaritaria nobilis". In: *Journal of The Royal Society Interface* 13.124 (2016), p. 20160645. ISSN: 1742-5689. DOI: 10.1098/rsif.2016.0645. URL: http://rsif.royalsocietypublishing.org/lookup/doi/10.1098/rsif.2016.0645.

[92] Silvia Vignolini et al. "Pointillist structural color in Pollia fruit." In: *Proceedings of the National Academy of Sciences of the United States of America* 109.39 (2012), pp. 15712–5. ISSN: 1091-6490. DOI: 10.1073/pnas.1210105109.

[93] Ken Fern. *Tropical Plants Database: Margaritaria discoidea*. (Visited on 08/06/2018).

[94] Christopher R. Hardy, Dennis Wm. Stevenson, and Helen G. Kiss. "Development of the gametophytes, flower, and floral vasculature in Dichorisandra thyrsiflora (Commelinaceae)". In: *American Journal of Botany* 87.9 (2000), pp. 1228–1239. ISSN: 00029122. DOI: 10.2307/2656715.

[95] D. W. Stevenson and S. J. Owens. "Some aspects of the reproductive morphology of Gibasis venustula (Kunth) D. R. Hunt (Commelinaceae)". In: *Botanical Journal of the Linnean Society* 77.3 (1978), pp. 157–175. ISSN: 10958339. DOI: 10.1111/j.1095-8339.1978.tb01397.x.

[96] Robert B. Faden. "Pollia Thunb . (Commelinaceae): The First Generic Record From the New World". In: *Missouri Botanical Garden* 65.2 (1978), pp. 676–680.

[97] Oliur Harhman and Abul Hassan. "New angiospermic taxa for the flora of bangladesh m. o". In: *Bangladesh J. Plant Taxon.* 24.2 (2017), pp. 165–171.

[98] Somporn Putiyanan and J. F. Maxwell. "Survey and Herbarium Specimens of Medicinal Vascular Flora of Doi Mae Soi". In: *CMU Journal of natural sciences* 5.August 1978 (2006), pp. 169–178.

[99] Kannika Panyaphu et al. "Medicinal plants of the Mien (Yao) in Northern Thailand and their potential value in the primary healthcare of postpartum women". In: *Journal of Ethnopharmacology* 135.2 (2011), pp. 226–237. ISSN: 03788741. DOI: 10.1016/j.jep.2011.03.050. URL: http://dx.doi.org/10.1016/j.jep.2011.03.050.

[100] Benjamin Thomas. "The psychoactive flora of papua new guinea". In: *Journal of Psychoactive Drugs* 35.2 (2003), pp. 285–293. ISSN: 21599777. DOI: 10.1080/02791072.2003.10400011.

[101] J. Bokdam. "Contribution a l'Etude ethnobotanique des Wagenis de Kisangani, Zaire". In: *Mededelingen Landbouwhogeschool, Wageningen* 39.675 (1975).

[102] A. C. Neville. "A pipe-cleaner molecular model for morphogenesis of helicoidal plant cell walls based on hemicellulose complexity". In: *Journal of Theoretical Biology* 131 (1988), pp. 243–254. ISSN: 00225193. DOI: 10.1016/S0022-5193(88)80241-8.

[103] N. C. Carpita and D. M. Gibeaut. "Structural models of primary cell walls in flowering plants: consistency of molecular structure with the physical properties of the walls during growth." In: *The Plant journal : for cell and molecular biology* 3 (1993), pp. 1–30. ISSN: 0960-7412. DOI: 10.1111/j.1365-313X.1993.tb00007.x.

[104] S. Wang et al. "PNAS Plus: Helical insertion of peptidoglycan produces chiral ordering of the bacterial cell wall". In: *Proceedings of the National Academy of Sciences* 109 (2012), E595–E604. ISSN: 0027-8424. DOI: 10.1073/pnas.1117132109.

[105] S. Caveney. "Cuticle Reflectivity and optical activity in scarab beetles and the role of uric acid". In: *Proc. Roy. Soc. Lond. B.* 178 (1971), pp. 205–225.

[106] A. Akinsoji et al. "Evaluation and Flora Diversity of Gashaka Gumti National Park-1 Gashaka Sector, Taraha State, Nigeria". In: *Ethiopian Journal of Environmental Studies and Management* 9.6 (2016), pp. 713–737. DOI: 10.4314/ejesm.v9i6.5.

[107] James A. Comiskey et al. "Vegetation Assessment of Takamanda Forest Reserve, Cameroon". In: *Takamanda : The biodiversity of an African Rainforest*. 2003. Chap. 3, pp. 10–19. ISBN: 1893912124.

[108] D.J. Greenland and J.M.L. Kowal. "Nutrient content of the moist tropical forest of Ghana". In: *Plant and soil XII* 2 (1960), pp. 154–174. ISSN: 0032079X. DOI: 10.1007/BF01377368.

[109] John Giobaguan Iyawe. "The ecology of small mammals in Ogba Forest Reserve, Nigeria". In: *Journal of Tropical Ecology* 5.1 (1989), pp. 51–64. ISSN: 14697831. DOI: 10.1017/S0266467400003217.

[110] E W Jones. "Ecological Studies on the Rain Forest of Southern Nigeria: IV. The Plateau Forest of the Okomu Forest Reserve". In: *The Journal of Ecology* 44.2 (1955), pp. 83–117. ISSN: 00220477.

[111] J. M. Moutsambote et al. "Vegetation and List of Plant Species Identified in the Nouabalé-Ndoki Forest, Congo". In: *Tropics* 3.4 (1994), pp. 277–293.

[112] H. Terashima, M. Ichikawa, and I. Ohta. "Catalog of Useful Plants of Tropical Africa". In: *African Study Monographs* 16 (1991), pp. 1–195.

[113] Jonathan Timberlake et al. "The Biodiversity and Conservation of Mount Chiperone, Mozambique". In: July (2007).

[114] Jacob Willie, Nikki Tagg, and Luc Lens. "Diversity and community composition of herbaceous plants in different habitat types in south-east Cameroon". In: *African Journal of Ecology* June (2017), pp. 1–11. ISSN: 01416707. DOI: 10.1111/aje.12454. URL: http://doi.wiley.com/10.1111/aje.12454.

[115] Hideaki Terashima and Mitsuo Ichikawa. "A Comparative ethnobotany of the Mbuti and Efe hunter-gatherers in the Ituri forest, Democratic Republic of Congo". In: *African Study Monographs* 24.2003-03 (2003), pp. 1–168. DOI: 10.14989/68220.

[116] Martin T Walsh and David C Moyer. *Hehe Botanical Dictionary*. 2002.

[117] Peter J. Fashing and Marina Cords. "Diurnal primate densities and biomass in the Kakamega Forest: An evaluation of census methods and a comparison with other forests". In: *American Journal of Primatology* 50.2 (2000), pp. 139–152. ISSN: 02752565. DOI: 10.1002/(SICI)1098-2345(200002)50:2<139::AID-AJP4>3.0.CO;2-N.

[118] James D. Paurson. "Aspects of Diet , Foraging , and Seed Predation in Ugandan Forest Baboons". In: (1976).

[119] B. F. Jacobs and C. H. S. Kabuye. "An extinct species of Pollia thunberg (commelinaceae) from the miocene ngorora formation, Kenya". In: *Review of paleobotany and palynology* 59 (1989), pp. 67–76.

[120] Maria E. Mcnamara. "The taphonomy of colour in fossil insects and feathers". In: *Palaeontology* 56.3 (2013), pp. 557–575. ISSN: 00310239. DOI: 10.1111/pala.12044.

[121] Marie-Madeleine Giraud-Guille. "Plywood structures in nature". In: *Current Opinion in Solid State and Materials Science* 3.3 (1998), pp. 221–227. ISSN: 13590286. DOI: 10.1016/S1359-0286(98)80094-6.

[122] T. Yamamoto et al. "Twisted plywood structure of an alternating lamellar pattern in cellular cementum of human teeth." In: *Anatomy and embryology* 202.1 (2000), pp. 25–30. ISSN: 0340-2061. DOI: 10.1007/PL00008241.

[123] J. C. Weaver et al. "The Stomatopod Dactyl Club: A Formidable Damage-Tolerant Biological Hammer". In: *Science* 336.6086 (2012), pp. 1275–1280. ISSN: 0036-8075. DOI: 10.1126/science.1218764.

[124] J. C. Roland et al. "Morphogenesis of plant cell walls at the supramolecular level: Internal geometry and versatility of helicoidal expression". In: *Protoplasma* 140 (1987), pp. 75–91. ISSN: 0033183X. DOI: 10.1007/BF01273716.

[125] Bharath Natarajan and Jeffrey W. Gilman. "Bioinspired Bouligand Cellulose Nanocrystal Composites: A Review of Mechanical Properties". In: *Philosophical Transactions A* 376 (2017). DOI: 10.1098/rsta.2017.0050.

[126] Y. Bouligand. "Twisted fibrous arrangements in biological materials and cholesteric mesophases." In: *Tissue & cell* 4.2 (1972), pp. 189–217. ISSN: 00408166. DOI: 10.1016/S0040-8166(72)80042-9.

[127] Yves Bouligand. "Liquid crystals and biological morphogenesis: Ancient and new questions". In: *Comptes Rendus Chimie* 11.3 (2008), pp. 281–296. ISSN: 16310748. DOI: 10.1016/j.crci.2007.10.001.

[128] Michel Mitov. "Cholesteric liquid crystals in living matter". In: *Soft Matter* (2017). ISSN: 1744-683X. DOI: 10.1039/C7SM00384F. URL: http://xlink.rsc.org/?DOI=C7SM00384F.

[129] Woo-Jae Chung et al. "Biomimetic self-templating supramolecular structures". In: *Nature* 478.7369 (2011), pp. 364–368. ISSN: 0028-0836. DOI: 10.1038/nature10513. URL: http://dx.doi.org/10.1038/nature10513.

[130] A. C. Neville and S. Levy. "Helicoidal orientation of cellulose microfibrils in Nitella opaca internode cells: ultrastructure and computed theoretical effects of strain reorientation during wall growth". In: *Planta* 162 (1984), pp. 370–384. ISSN: 00320935. DOI: 10.1007/BF00396750.

[131] Ting Wang, Heather E Mcfarlane, and Staffan Persson. "The impact of abiotic factors on cellulose synthesis". In: *Journal of Experimental Botany* 67.2 (2016), pp. 543–552. DOI: 10.1093/jxb/erv488.

[132] Thomas H. Giddings and L. Andrew Staehelin. "Spatial relationship between microtubules and plasma-membrane rosettes during the deposition of primary wall microfibrils in Closterium sp." In: *Planta* 173 (1988), pp. 22–30. ISSN: 00320935. DOI: 10.1007/BF00394482.

[133] Robert J. Moon et al. *Cellulose nanomaterials review: structure, properties and nanocomposites.* Vol. 40. 7. 2011, pp. 3941–94. ISBN: 1765496829. DOI: 10.1039/c0cs00108b. URL: http://www.ncbi.nlm.nih.gov/pubmed/21566801.

[134] Antoinette O'sullivan. "Cellulose: the structure slowly unravels". In: *Cellulose* 4.3 (1997), pp. 173–207. ISSN: 09690239. DOI: ChemistryandMaterialsScience. URL: http://dx.doi.org/10.1023/A:1018431705579.

[135] Anne Mie C. Emons and H. Kieft. "Winding threads around plant cells Applications of the geometrical model for microfibril deposition". In: *Protoplasma* 180 (1994), pp. 59–69. ISSN: 0033-183X. DOI: 10.1007/BF01379224.

[136] D. P. Delmer and Y. Amor. "Cellulose biosynthesis." In: *The Plant cell* 7.July (1995), pp. 987–1000. ISSN: 0066-4294. DOI: 10.1146/annurev.pp.38.060187.001355.

[137] Anne Mie C. Emons and Bela M. Mulder. "How the deposition of cellulose microfibrils builds cell wall architecture". In: *Trends in Plant Science* 5.1 (2000), pp. 35–40. ISSN: 13601385. DOI: 10.1016/S1360-1385(99)01507-1.

[138] Martin Bringmann et al. "Cracking the elusive alignment hypothesis: The microtubule-cellulose synthase nexus unraveled". In: *Trends in Plant Science* 17.11 (2012), pp. 666–674. ISSN: 13601385. DOI: 10.1016/j.tplants.2012.06.003. arXiv: 84868206947. URL: http://dx.doi.org/10.1016/j.tplants.2012.06.003.

[139] J. Chan. "Microtubule and cellulose microfibril orientation during plant cell and organ growth". In: *Journal of Microscopy* 247.November 2011 (2012), pp. 23–32. ISSN: 00222720. DOI: 10.1111/j.1365-2818.2011.03585.x.

[140] Alexander R. Paredez, Christopher R. Somerville, and David W. Ehrhardt. "Visualization of cellulose synthase demonstrates functional association with microtubules." In: *Science (New York, N.Y.)* 312.June (2006), pp. 1491–1495. ISSN: 0036-8075. DOI: 10.1126/science.1126551.

[141] Y Watanabe et al. "Visualization of cellulose synthases in Arabidopsis secondary cell walls." In: *Science (New York, N.Y.)* 350.6257 (2015), pp. 198–203. ISSN: 1095-9203. DOI: 10.1126/science.aac7446. URL: http://www.ncbi.nlm.nih.gov/pubmed/26450210.

[142] Charles T Anderson et al. "Real-Time Imaging of Cellulose Reorientation during Cell Wall Expansion in Arabidopsis Roots". In: *Plant Physiology* 152.February (2010), pp. 787–796. DOI: 10.1104/pp.109.150128.

[143] H. Buschmann et al. "Helical Growth of the Arabidopsis Mutant tortifolia1 Reveals a Plant-Specific Microtubule-Associated Protein". In: *Current Biology* 14 (2004), pp. 1515–1521. ISSN: 0950-1991. DOI: 10.1016/j.cub.2004.08.033.

[144] S. Mizuta et al. "Possible involvement of membrane fluidity in helicoidal microfibrillar orientation in the coenocytic green alga, Boergesenia forbesii". In: *Protoplasma* 180 (1994), pp. 82–91. ISSN: 0033183X. DOI: 10.1007/BF01379226.

[145] T. I. Baskin. "On the alignment of cellulose microfibrils by cortical microtubules: A review and a model". In: *Protoplasma* 215 (2001), pp. 150–171. ISSN: 0033183X. DOI: 10.1007/BF01280311.

[146] David R. Smyth. "Helical growth in plant organs : mechanisms and significance". In: *The company of biologists* 143 (2016), pp. 3272–3282. DOI: 10.1242/dev.134064.

[147] Alejandro D. Rey. "Liquid crystal models of biological materials and processes". In: *Soft Matter* 6.15 (2010), p. 3402. ISSN: 1744-683X. DOI: 10.1039/b921576j. URL: http://xlink.rsc.org/?DOI=b921576j.

[148] Kerwyn Casey Huang, David W. Ehrhardt, and Joshua W. Shaevitz. "The molecular origins of chiral growth in walled cells". In: *Current Opinion in Microbiology* 15.6 (2012), pp. 707–714. ISSN: 13695274. DOI: 10.1016/j.mib.2012.11.002.

[149] A. C. Neville and S. Caveney. "Scarabaeid beetle exocuticle as an optical analogue of cholesteric liquid crystals." In: *Biological reviews of the Cambridge Philosophical Society* 44 (1969), pp. 531–562. ISSN: 1464-7931.

[150] A. C. Neville and B. M. Luke. "A two-system model for chitin-protein complexes in insect cuticles." In: *Tissue & cell* 1.4 (1969), pp. 689–707. ISSN: 00408166. DOI: 10.1016/S0040-8166(69)80041-8.

[151] A. C. Neville, D. C. Gubb, and R. M. Crawford. "A new model for cellulose architecture in some plant cell walls". In: *Protoplasma* 90 (1976), pp. 307–317. ISSN: 0033183X. DOI: 10.1007/BF01275682.

[152] Anthony Charles Neville. “Molecular and mechanical aspects of helicoid development in plant cell walls”. In: *BioEssays* 3.1 (1985), pp. 4–8. ISSN: 0265-9247. DOI: 10.1002/bies.950030103. URL: http://doi.wiley.com/10.1002/bies.950030103.

[153] J. C. Roland, D. Reis, and B. Vian. “Liquid crystal order and turbulence in the planar twist of the growing plant cell walls”. In: *Tissue and Cell* 24.3 (1992), pp. 335–345. ISSN: 00408166. DOI: 10.1016/0040-8166(92)90050-H.

[154] G. De Luca and A. D. Rey. “Monodomain and polydomain helicoids in chiral liquid-crystalline phases and their biological analogues”. In: *European Physical Journal E* 12.2 (2003), pp. 291–302. ISSN: 12928941. DOI: 10.1140/epje/i2002-10164-3.

[155] Danièle Reis and Brigitte Vian. “Helicoidal pattern in secondary cell walls and possible role of xylans in their construction”. In: *Comptes Rendus - Biologies* 327 (2004), pp. 785–790. ISSN: 16310691. DOI: 10.1016/j.crvi.2004.04.008.

[156] U. Kutschera. “The growing outer epidermal wall: Design and physiological role of a composite structure”. In: *Annals of Botany* 101 (2008), pp. 615–621. ISSN: 03057364. DOI: 10.1093/aob/mcn015.

[157] B. Vian et al. “Cholesteric-like crystal analogs in glucuronoxylan-rich cell wall composites: Experimental approach of acellular re-assembly from native cellulosic suspension”. In: *Protoplasma* 180 (1994), pp. 70–81. ISSN: 0033-183X. DOI: 10.1007/BF01379225.

[158] A. C. Neville and B. M. Luke. “A biological system producing a self-assembling cholesteric protein liquid crystal.” In: *Journal of cell science* 8.1 (1971), pp. 93–109. ISSN: 0021-9533.

[159] J. H. M. Willison and R. M. Abeysekera. “A liquid crystal containing cellulose in living plant tissue”. In: *Journal of Polymer Science: Polymer Letters Edition* 26.2 (1988), pp. 71–75. ISSN: 03606384. DOI: 10.1002/pol.1988.140260202. URL: http://doi.wiley.com/10.1002/pol.1988.140260202.

[160] J. Chan et al. “The rotation of cellulose synthase trajectories is microtubule dependent and influences the texture of epidermal cell walls in Arabidopsis hypocotyls”. In: *Journal of Cell Science* 123.20 (2010), pp. 3490–3495. ISSN: 0021-9533. DOI: 10.1242/jcs.074641. URL: http://jcs.biologists.org/cgi/doi/10.1242/jcs.074641.

[161] B. Satiat-Jeunemaitre. “Spatial and Temporal Regulations in Matrices : Helicoidal Extracellular Comparison Between Plant and Animal”. In: *Tissue and Cell* 24.3 (1992), pp. 315–334.

[162] Marie Madeleine Giraud-Guille. "Liquid crystallinity in condensed type I collagen solutions. A clue to the packing of collagen in extracellular matrices". In: *Journal of Molecular Biology* 224.3 (1992), pp. 861–873. ISSN: 00222836. DOI: 10.1016/0022-2836(92)90567-4.

[163] J. F. Revol et al. "Helicoidal self-ordering of cellulose microfibrils in aqueous suspension." In: *International journal of biological macromolecules* 14 (1992), pp. 170–172. ISSN: 01418130. DOI: 10.1016/S0141-8130(05)80008-X.

[164] Marie Madeleine Giraud-Guille, Laurence Besseau, and Raquel Martin. "Liquid crystalline assemblies of collagen in bone and in vitro systems". In: *Journal of Biomechanics* 36.10 (2003), pp. 1571–1579. ISSN: 00219290. DOI: 10.1016/S0021-9290(03)00134-9.

[165] E. Belamie et al. "Possible transient liquid crystal phase during the laying out of connective tissues: α-chitin and collagen as models". In: *Journal of Physics: Condensed Matter* 18.13 (2006), S115–S129. ISSN: 0953-8984. DOI: 10.1088/0953-8984/18/13/S08.

[166] Gonzague Agez, Chloé Bayon, and Michel Mitov. "Multiwavelength micromirrors in the cuticle of scarab beetle Chrysina gloriosa". In: *Acta Biomaterialia* (2016). ISSN: 17427061. DOI: 10.1016/j.actbio.2016.11.033. URL: http://linkinghub.elsevier.com/retrieve/pii/S1742706116306298.

[167] Danièle Reis et al. "Cellulose-glucuronoxylans and plant cell wall structure". In: *Micron* 25.2 (1994), pp. 171–187. URL: http://www.sciencedirect.com/science/article/pii/0968432894900418.

[168] Andrew R. Parker and Helen E. Townley. "Biomimetics of photonic nanostructures." In: *Nature nanotechnology* 2.6 (2007), pp. 347–353. ISSN: 1748-3387. DOI: 10.1038/nnano.2007.152.

[169] Kathryn D. Feller et al. "Selection of the intrinsic polarization properties of animal optical materials creates enhanced structural reflectivity and camouflage". In: *Phil. Trans. R. Soc. B* 372 (2017), p. 20160336. DOI: 10.1098/rstb.2016.0336.

[170] H. T. Ghiradella. "Structure and Development of Iridescent Butterfly scales: lattices and laminae". In: *Journal of Morphology* 202 (1989), pp. 69–88.

[171] H. T. Ghiradella. "Light and color on the wing : structural colors in butterflies and moths". In: *Applied optics* 30.24 (1991), pp. 3492–3500.

[172] H. T. Ghiradella and M. W. Butler. "Many variations on a few themes: a broader look at development of iridescent scales (and feathers)". In: *Journal of The Royal Society Interface* 6.Suppl_2 (2009), S243–S251. ISSN: 1742-5689. DOI: 10.1098/rsif.2008.0372.focus. arXiv: arXiv:1011.1669v3.

[173] R. O Prum et al. "Development of colour-producing -keratin nanostructures in avian feather barbs". In: *Journal of The Royal Society Interface* 6.Suppl_2 (2009), S253–S265. ISSN: 1742-5689. DOI: 10.1098/rsif.2008.0466.focus. URL: http://rsif.royalsocietypublishing.org/cgi/doi/10.1098/rsif.2008.0466.focus.

[174] Olimpia D. Onelli et al. "Development of structural colour in leaf beetles". In: *Scientific Reports* 7.1 (2017), pp. 1–9. ISSN: 20452322. DOI: 10.1038/s41598-017-01496-8. URL: http://dx.doi.org/10.1038/s41598-017-01496-8.

[175] Susan L. Ustin et al. "Retrieval of foliar information about plant pigment systems from high resolution spectroscopy". In: *Remote Sensing of Environment* 113.SUPPL. 1 (2009), S67–S77. ISSN: 00344257. DOI: 10.1016/j.rse.2008.10.019. URL: http://dx.doi.org/10.1016/j.rse.2008.10.019.

[176] Daniele Pugliese. *Chlrophyll Absorption Spectra graphic*. 2008. URL: https://commons.wikimedia.org/wiki/File:Chlorophyll{_}ab{_}spectra2.PNG.

[177] R. H. Baayen, D. J. Davidson, and D. M. Bates. "Mixed-effects modeling with crossed random effects for subjects and items". In: *Journal of Memory and Language* 59.4 (2008), pp. 390–412. ISSN: 0749596X. DOI: 10.1016/j.jml.2007.12.005. arXiv: arXiv:1011.1669v3. URL: http://dx.doi.org/10.1016/j.jml.2007.12.005.

[178] William R. Heinson, Amitabha Chakrabarti, and Christopher M. Sorensen. "Crossover from spherical particle Mie scattering to circular aperture diffraction". In: *Journal of the Optical Society of America A* 31.11 (2014), p. 2362. ISSN: 1084-7529. DOI: 10.1364/JOSAA.31.002362. URL: https://www.osapublishing.org/abstract.cfm?URI=josaa-31-11-2362.

[179] Andrew R. Parker, David R. McKenzie, and Maryanne C. J. Large. "Multilayer reflectors in Animals using Green and Gold Beetles as Contrasting Examples". In: *The Journal of Experimental Biology* 201 (1998), pp. 1307–1313.

[180] M. V. King. "Dimensional changes in cells and tissues during specimen preparation for the electron microscope." In: *Cell biophysics* 18 (1991), pp. 31–55. ISSN: 0163-4992. DOI: 10.1007/BF02990514.

[181] Allan S. Jones, Bruce K. Milthorpe, and C. Rolfe Howlett. "Measurement of microtomy induced section distortion and its correction for 3-dimensional histological reconstructions". In: *Cytometry* 15.2 (1994), pp. 95–105. ISSN: 10970320. DOI: 10.1002/cyto.990150203.

[182] Paul Derbyshire et al. "Cell elongation in Arabidopsis hypocotyls involves dynamic changes in cell wall thickness". In: *Journal of Experimental Botany* 58.8 (2007), pp. 2079–2089. ISSN: 00220957. DOI: 10.1093/jxb/erm074.

[183] Beverley J. Glover. "Differentiation in plant epidermal cells." In: *Journal of experimental botany* 51.344 (2000), pp. 497–505. ISSN: 14602431. DOI: 10.1093/jexbot/51.344.497.

[184] Lubica Feriancová Maryam I.S. Alkurdi, Jan Supuka and Mária Bihunová. "Viburnum tinus L. as a new Mediterranean element for central Europe urban landscapes". In: *IOSR Journal of Agriculture and Veterinary Science (IOSR-JAVS)* 7.6 (2014), pp. 50–58. URL: http://www.iosrjournals.org/iosr-javs/papers/vol7-issue6/Version-1/K07615058.pdf.

[185] Laila M. Karlsson et al. "Complex combination of seed dormancy and seedling development determine emergence of Viburnum tinus (Caprifoliaceae)". In: *Annals of Botany* 95.2 (2005), pp. 323–330. ISSN: 03057364. DOI: 10.1093/aob/mci029.

[186] M. Debussche and P. Isenmann. "Bird-Dispersed Seed Rain and Seedling Establishment in Patchy Mediterranean Vegetation". In: *OIKOS* 69.3 (1994), pp. 414–426.

[187] Lamberto Tomassini et al. "Iridoid glucosides from Viburnum tinus". In: *Phytochemistry* 38.2 (1995), pp. 423–425. ISSN: 14786419. DOI: 10.1080/14786410500056678.

[188] Klaus Bock et al. "Iridoid allosides from Viburnum opulus". In: *Phytochemistry* 17.December 1978 (1978), pp. 753–757. DOI: 10.1016/S0031-9422(00)94220-1.

[189] Monica Jordheim, Nils Harald Giske, and Øyvind M. Andersen. "Anthocyanins in Caprifoliaceae". In: *Biochemical Systematics and Ecology* 35.3 (2007), pp. 153–159. ISSN: 03051978. DOI: 10.1016/j.bse.2006.09.010.

[190] Mona A. Mohamed et al. "Phytochemical constituents and hepatoprotective activity of Viburnum tinus". In: *Phytochemistry* 66.23 (2005), pp. 2780–2786. ISSN: 00319422. DOI: 10.1016/j.phytochem.2005.07.019.

[191] Zvonimir Devide. "Über die ursache des blauglanzes der früchte von Viburnum tinus L." In: *Acta Bot. Croat.* 45 (1986), pp. 97–100.

[192] M. G. Sajilata, R. S. Singhal, and M. Y. Kamat. "The carotenoid pigment zeaxanthin - A review". In: *Comprehensive Reviews in Food Science and Food Safety* 7.1 (2008), pp. 29–49. ISSN: 15414337. DOI: 10.1111/j.1541-4337.2007.00028.x.

[193] Gertrude Maud Robinson and Robert Robinson. "A survey of anthocyanins. Notes on the distribution of leuco-anthocyanins". In: *Biochemical Journal* 25.5 (1932), p. 1687.

[194] Doekele G. Stavenga, Hein L. Leertouwer, and Bodo D. Wilts. "Colouration principles of nymphaline butterflies – thin films , melanin , ommochromes and wing scale stacking". In: *Journal of Experimental Biology* March (2014). DOI: 10.1242/jeb.098673.

[195] Chen Ma et al. “Supported lipid bilayers lifted from the substrate by layer-by-layer polyion cushions on self-assembled monolayers”. In: *Colloids and Surfaces B: Biointerfaces* 28.4 (2003), pp. 319–329. ISSN: 09277765. DOI: 10.1016/S0927-7765(02)00175-3.

[196] R. A. Paterson et al. “Polarized Light Microscopy: An Old Technique Casts New Light on Māori Textile Plants”. In: *Archaeometry* 59.5 (2017), pp. 965–979. ISSN: 14754754. DOI: 10.1111/arcm.12281.

[197] Bodo D. Wilts et al. “Evolutionary-Optimized Photonic Network Structure in White Beetle Wing Scales”. In: *Advanced Materials* 30.19 (2018), pp. 1–6. ISSN: 15214095. DOI: 10.1002/adma.201702057.

[198] Hans Moosmüller and W. Patrick Arnott. “Particle optics in the rayleigh regime”. In: *Journal of the Air and Waste Management Association* 59.9 (2009), pp. 1028–1031. ISSN: 21622906. DOI: 10.3155/1047-3289.59.9.1028.

[199] Matthew D. Shawkey and Geoffrey E. Hill. “Significance of a basal melanin layer to production of non-iridescent structural plumage color: evidence from an amelanotic Steller’s jay (Cyanocitta stelleri).” In: *The Journal of experimental biology* 209.Pt 7 (2006), pp. 1245–1250. ISSN: 0022-0949. DOI: 10.1242/jeb.02115. URL: http://jeb.biologists.org/cgi/doi/10.1242/jeb.02115.

[200] Heeso Noh et al. “How noniridescent colors are generated by quasi-ordered structures of bird feathers”. In: *Advanced Materials* 22.26-27 (2010), pp. 2871–2880. ISSN: 09359648. DOI: 10.1002/adma.200903699. arXiv: 0912.4487.

[201] R. O. Prum. “Anatomically diverse butterfly scales all produce structural colours by coherent scattering”. In: *Journal of Experimental Biology* 209.4 (2006), pp. 748–765. ISSN: 0022-0949. DOI: 10.1242/jeb.02051. URL: http://jeb.biologists.org/cgi/doi/10.1242/jeb.02051.

[202] Shuichi Kinoshita, Shinya Yoshioka, and Kenji Kawagoe. “Mechanisms of structural colour in the Morpho butterfly : cooperation of regularity and irregularity in an iridescent scale”. In: *Proc. R. Soc. Lond. B* 269 (2002), pp. 1417–1421. DOI: 10.1098/rspb.2002.2019.

[203] Bokwang Song, Seok Chan Eom, and Jung H. Shin. “Disorder effect on broad-angle reflection from Morpho-inspired structures”. In: *2015 11th Conference on Lasers and Electro-Optics Pacific Rim, CLEO-PR 2015* 3 (2016). DOI: 10.1109/CLEOPR.2015.7376454.

[204] Hugo J. van Staveren et al. “Light scattering in lntralipid-10% in the wavelength range of 400–1100 nm”. In: *Applied Optics* 30.31 (1991), p. 4507. ISSN: 0003-6935. DOI: 10.1364/AO.30.004507. arXiv: arXiv:1011.1669v3. URL: https://www.osapublishing.org/abstract.cfm?URI=ao-30-31-4507.

[205] Sönke Johnsen. “Lifting the Cloak of Invisibility: The Effects of Changing Optical Conditions on Pelagic Crypsis 1 ¨”. In: *Integr. Comp. Biol.* 590.43 (2003), pp. 580–590.

[206] *Missouri Botanical Garden*. 2018. URL: http://www.missouribotanicalgarden.org/PlantFinder/PlantFinderDetails.aspx?kempercode=d284 (visited on 03/09/2018).

[207] Claudia Erbar. "Nectar secretion and nectaries in basal angiosperms, magnoliids and non-core eudicots and a comparison with core eudicots". In: *Plant Diversity and Evolution* 131.2 (2014), pp. 63–143. ISSN: 18696155. DOI: 10.1127/1869-6155/2014/0131-0075.

[208] J. F. Revol and R. H. Marchessault. "In vitro chiral nematic ordering of chitin crystallites". In: *International Journal of Biological Macromolecules* 15.6 (1993), pp. 329–335. ISSN: 01418130. DOI: 10.1016/0141-8130(93)90049-R.

[209] S. R. Kennedy et al. "Optical activity of chiral thin film and liquid crystal hybrids". In: *Liquid Crystals* 28.12 (2001), pp. 1799–1803. DOI: 10.1080/02678290110076399.

[210] Madhu Kaushik et al. "Transmission Electron Microscopy for the Characterization of Cellulose Nanocrystals". In: *The Transmission Electron Microscope - Theory and Applications, Intech*. 2015. Chap. Chapter 6: pp. 129–163. DOI: 10.5772/60985.

[211] L. Onsager. "The effects of Shape on the interation of colloidal particles". In: *Annals New York Academy of Sciences* (1949), pp. 627–659.

[212] A. Stroobants, H. N. W. Lekkerkerker, and T. Odijk. "Effect of Electrostatic Interaction on the Liquid Crystal Phase Transition in Solutions of Rodlike Polyelectrolytes+". In: *Macromolecules* 19 (1986), pp. 2232–2238.

[213] J.-F. Revol, L. Godbout, and D. G. Gray. "Solid Self-Assembled Films of Cellulose with Chiral Nematic Order and Optically Variable Properties". In: *Journal of Pulp and Paper Science* 24.5 (1998), pp. 146–149. ISSN: 0826-6220. URL: http://cat.inist.fr/?aModele=afficheN{\&}cpsidt=2259862.

[214] D. Klemm et al. *Comprehensive Cellulose Chemistry*. Wiley-VCH Verlag GmbH & Co. KGaA, 2004, pp. 9–29.

[215] B. D. Wilts et al. "Invited Article: Chiral optics of helicoidal cellulose nanocrystal films". In: *APL Photonics* 2.4 (2017), p. 040801. ISSN: 2378-0967. DOI: 10.1063/1.4978387. URL: http://aip.scitation.org/doi/10.1063/1.4978387.

[216] Jan P F Lagerwall et al. "Cellulose nanocrystal-based materials: from liquid crystal self-assembly and glass formation to multifunctional thin films". In: *NPG Asia Materials* 6.1 (2014), e80. ISSN: 1884-4057. DOI: 10.1038/am.2013.69. URL: http://dx.doi.org/10.1038/am.2013.69.

[217] Michael Giese et al. "Functional Materials from Cellulose-Derived Liquid-Crystal Templates". In: *Angewandte Chemie International Edition* 54.10 (2015), pp. 2888–2910. ISSN: 14337851. DOI: 10.1002/anie.201407141. URL: http://doi.wiley.com/10.1002/anie.201407141.

[218] Kevin E. Shopsowitz, Wadood Y. Hamad, and Mark J. MacLachlan. "Flexible and iridescent chiral nematic mesoporous organosilica films." In: *Journal of the American Chemical Society* 134.2 (2012), pp. 867–70. ISSN: 1520-5126. DOI: 10.1021/ja210355v. URL: http://www.ncbi.nlm.nih.gov/pubmed/22188398.

[219] Ariella Lukach et al. "Coassembly of Gold Nanoparticles and Cellulose Nanocrystals in Composite Films Myriam Me t". In: *Langmuir* 31 (2015), pp. 5033–5041. DOI: 10.1021/acs.langmuir.5b00728.

[220] Yu Ping Zhang et al. "Nanocrystalline cellulose for covert optical encryption". In: *Nanophotonics* 6.1 (2012), p. 825808. ISSN: 1934-2608. DOI: 10.1117/12.906770. URL: http://nanophotonics.spiedigitallibrary.org/article.aspx?doi=10.1117/1.JNP.6.063516.

[221] Shenglong Shang et al. "Fabrication of magnetic field induced structural colored films with tunable colors and its application on security materials". In: *Journal of Colloid and Interface Science* 485 (2017), pp. 18–24. DOI: 10.1016/j.jcis.2016.09.016.

[222] Yuqian Zhao et al. "Artificial Structural Color Pixels : A Review". In: *Materials* 10.944 (2017). DOI: 10.3390/ma10080944.

[223] Raphael Bardet, Naceur Belgacem, and Julien Bras. "Flexibility and Color Monitoring of Cellulose Nanocrystal Iridescent Solid Films Using Anionic or Neutral Polymers". In: *Applied Materials and Interfaces* 7 (2015), pp. 4010–4018. DOI: 10.1021/am506786t.

[224] Richard M. Parker et al. "Hierarchical Self-Assembly of Cellulose Nanocrystals in a Confined Geometry". In: *ACS Nano* 10.9 (2016), pp. 8443–8449. ISSN: 1936086X. DOI: 10.1021/acsnano.6b03355.

[225] Tianheng Zhao et al. "Printing of Responsive Photonic Cellulose Nanocrystal Micro-Film Arrays". In: *Advanced Functional Materials* (2018).

[226] Shinya Yoshioka, Eri Nakamura, and Shuichi Kinoshita. "Origin of two-color iridescence in rock dove's feather". In: *Journal of the Physical Society of Japan* 76.1 (2007), pp. 1–4. ISSN: 00319015. DOI: 10.1143/JPSJ.76.013801.

[227] J.H. Moon et al. "Electrospray-assisted fabrication of uniform photonic balls". In: *Advanced Materials* 16.7 (2004), pp. 605–609+575. ISSN: 09359648. DOI: 10.1002/adma.200305446.

[228] Shin Hyun Kim et al. "Optofluidic assembly of colloidal photonic crystals with controlled sizes, shapes, and structures". In: *Advanced Materials* 20.9 (2008), pp. 1649–1655. ISSN: 09359648. DOI: 10.1002/adma.200703022.

[229] Wei Luo et al. "Rotating 1-D Magnetic Photonic Crystal Balls with Tunable Lattice Constant". In: *Nanoscale* (2017). ISSN: 2040-3364. DOI: 10.1039/C7NR03335D. URL: http://pubs.rsc.org/en/Content/ArticleLanding/2017/NR/C7NR03335D.

[230] Xiaoming Yang et al. "Production of Structural Colors with High Contrast and Wide Viewing Angles from Assemblies of Polypyrrole Black Coated Polystyrene Nanoparticles". In: *Applied Materials and Interfaces* (2016). DOI: 10.1021/acsami.6b03739.

[231] Yuanjin Zhao et al. "Bio-inspired variable structural color materials". In: *Chemical Society Reviews* 41.8 (2012), p. 3297. ISSN: 0306-0012. DOI: 10.1039/c2cs15267c. URL: http://xlink.rsc.org/?DOI=c2cs15267c.

[232] Shin Hyun Kim et al. "Optofluidic synthesis of electroresponsive photonic janus balls with isotropic structural colors". In: *Advanced Materials* 20.21 (2008), pp. 4129–4134. ISSN: 09359648. DOI: 10.1002/adma.200801167.

[233] Nicolas Vogel et al. "Color from hierarchy: Diverse optical properties of micron-sized spherical colloidal assemblies". In: *Proceedings of the National Academy of Sciences* 112.35 (2015), p. 201506272. ISSN: 0027-8424. DOI: 10.1073/pnas.1506272112. URL: http://www.pnas.org/lookup/doi/10.1073/pnas.1506272112.

[234] Yong Geng et al. "High-fidelity spherical cholesteric liquid crystal Bragg reflectors generating unclonable patterns for secure authentication". In: *Scientific Reports* 6.May 2016 (2016), p. 26840. ISSN: 2045-2322. DOI: 10.1038/srep26840. URL: http://www.nature.com/articles/srep26840.

[235] Mathias Kolle et al. "Mimicking the colourful wing scale structure of the Papilio blumei butterfly." In: *Nature nanotechnology* 5.7 (2010), pp. 511–515. ISSN: 1748-3387. DOI: 10.1038/nnano.2010.101. URL: http://dx.doi.org/10.1038/nnano.2010.101.

[236] Hongta Yang and Peng Jiang. "Large-scale colloidal self-assembly by doctor blade coating". In: *Langmuir* 26.16 (2010), pp. 13173–13182. ISSN: 07437463. DOI: 10.1021/la101721v.

[237] Giulia Guidetti and Supervisor Silvia Vignolini. "Cellulose photonics : designing functionality and optical appearance of natural materials". PhD thesis. 2018.

[238] Partha Saha and Virginia A. Davis. "Photonic Properties and Applications of Cellulose Nanocrystal Films with Planar Anchoring". In: *Applied Nano Materials* (2018). DOI: 10.1021/acsanm.8b00233.

[239] JungHyun Noh et al. "Tuneable multicoloured patterns from photonic cross-communication between cholesteric liquid crystal droplets". In: *Journal of Materials Chemistry C* 2.5 (2014), p. 806. ISSN: 2050-7526. DOI: 10.1039/c3tc32055c. URL: http://xlink.rsc.org/?DOI=c3tc32055c.

[240] Jinxiang Chen et al. "Review of beetle forewing structures and their biomimetic applications in China: (I) On the structural colors and the vertical and horizontal cross-sectional structures". In: *Materials Science and Engineering: C* 55 (2015), pp. 605–619. ISSN: 09284931. DOI: 10.1016/j.msec.

2015.05.064. URL: http://linkinghub.elsevier.com/retrieve/pii/S0928493115301132.

[241] H. Martin Schaefer, Veronika Schaefer, and Misha Vorobyev. "Are Fruit Colors Adapted to Consumer Vision and Birds Equally Efficient in Detecting Colorful Signals?" In: *The American Naturalist* 169.S1 (2007), S159–S169. ISSN: 0003-0147. DOI: 10.1086/510097. URL: http://www.journals.uchicago.edu/doi/10.1086/510097.

[242] H. Martin Schaefer, Veronika Schaefer, and Douglas J. Levey. "How plant-animal interactions signal new insights in communication". In: *Trends in Ecology and Evolution* 19.11 (2004), pp. 577–584. ISSN: 01695347. DOI: 10.1016/j.tree.2004.08.003.

[243] Ayaka Kawamura et al. "Full-Color Biomimetic Photonic Materials with Iridescent and Non-Iridescent Structural Colors". In: *Scientific Reports* 6.August (2016), p. 33984. ISSN: 2045-2322. DOI: 10.1038/srep33984. URL: http://www.nature.com/articles/srep33984.

[244] James A. Dolan et al. "Optical Properties of Gyroid Structured Materials: From Photonic Crystals to Metamaterials". In: *Advanced Optical Materials* 3.1 (2015), pp. 12–32. ISSN: 21951071. DOI: 10.1002/adom.201400333. URL: http://doi.wiley.com/10.1002/adom.201400333.

[245] E. Pavarini et al. "Band structure and optical properties of opal photonic crystals". In: *Physical Review B - Condensed Matter and Materials Physics* 72.4 (2005). ISSN: 10980121. DOI: 10.1103/PhysRevB.72.045102. arXiv: 0505068 [cond-mat].

[246] K. Michielsen and D. G. Stavenga. "Gyroid cuticular structures in butterfly wing scales: biological photonic crystals." In: *Journal of the Royal Society, Interface / the Royal Society* 5.18 (2008), pp. 85–94. ISSN: 1742-5689. DOI: 10.1098/rsif.2007.1065.

[247] G. F. Grether, G. R. Kolluru, and K. Nersissian. "Individual colour patches as multicomponent signals". In: *Biological Reviews* 79.2004 (2004), pp. 583–610. DOI: 10.1017/S1464793103006390.

[248] Takasi Nisisako and T. Torii. "Microfluidic large-scale integration on a chip for mass production of monodisperse droplets and particles". In: *Lab on a Chip* 8.2 (2008), pp. 287–293. ISSN: 14730189. DOI: 10.1039/b713141k.

[249] George Mayer and Mehmet Sarikaya. "Rigid biological composite materials: Structural examples for biomimetic design". In: *Experimental Mechanics* 42.4 (2002), pp. 395–403. ISSN: 00144851. DOI: 10.1177/001448502321548229.

[250] Radwanul Hasan Siddique et al. "Colour formation on the wings of the butterfly Hypolimnas salmacis by scale stacking". In: *Scientific Reports* 6 (2016), p. 36204. ISSN: 2045-2322. DOI: 10.1038/srep36204. URL: http://www.nature.com/articles/srep36204.

[251] Otto L. Pursiainen et al. "Nanoparticle-tuned structural color from polymer opals". In: *Optics Express* 15.15 (2007), p. 9553. ISSN: 1094-4087. DOI: 10.1364/OE.15.009553. URL: http://www.opticsinfobase.org/abstract.cfm?URI=oe-15-15-9553.

[252] Yukikazu Takeoka et al. "Production of colored pigments with amorphous arrays of black and white Colloidal particles". In: *Angewandte Chemie - International Edition* 52.28 (2013), pp. 7261–7265. ISSN: 14337851. DOI: 10.1002/anie.201301321.

[253] Natalie Koay et al. "Hierarchical structural control of visual properties in self-assembled photonic-plasmonic pigments". In: *Optics Express* 22.23 (2014), p. 27750. ISSN: 1094-4087. DOI: 10.1364/OE.22.027750. URL: https://www.osapublishing.org/oe/abstract.cfm?uri=oe-22-23-27750.

[254] Matthew D. Shawkey and Geoffrey E. Hill. "Carotenoids need structural colours to shine". In: *Biology Letters* 1.2 (2005), pp. 121–124. ISSN: 1744-9561. DOI: 10.1098/rsbl.2004.0289. URL: http://rsbl.royalsocietypublishing.org/cgi/doi/10.1098/rsbl.2004.0289.

[255] Casper J. van der Kooi et al. "How to colour a flower: On the optical principles of flower coloration". In: *Proceedings of the Royal Society B: Biological Sciences* 283.1830 (2016). ISSN: 14712954. DOI: 10.1098/rspb.2016.0429.

[256] Luke T Mcdonald et al. "Circularly polarized reflection from the scarab beetle Chalcothea smaragdina : light scattering by a dual photonic structure". In: *Interface focus* 7 (2017), p. 20160129. DOI: 10.1098/rsfs.2016.0129.

[257] Silvia Vignolini et al. "Analysing photonic structures in plants". In: *J R Soc Interface* 10.July (2013), p. 20130394. DOI: 10.1098/rsif.2013.0394.

[258] H. Martin Schaefer. "Why fruits go to the dark side". In: *Acta Oecologica* 37.6 (2011), pp. 604–610. ISSN: 1146609X. DOI: 10.1016/j.actao.2011.04.008. URL: http://dx.doi.org/10.1016/j.actao.2011.04.008.

[259] H. Martin Schaefer, Alfredo Valido, and Pedro Jordano. "Birds see the true colours of fruits to live off the fat of the land". In: *Proceedings of the Royal Society B: Biological Sciences* 281.1777 (2014). ISSN: 14712954. DOI: 10.1098/rspb.2013.2516.

[260] Christophe Thebaud and Max Debussche. "A Field Test of the Effects of Infructescence Size on Fruit Removal by Birds in Viburnum tinus". In: *OIKOS* 65.3 (2017), pp. 391–394.